Sub-wavelength microscopy techniques in the TeraHertz frequency range

Gizem Soylu

THÈSE

Pour obtenir le grade de

DOCTEUR DE LA COMMUNAUTE UNIVERSITE GRENOBLE ALPES

Spécialité : **OPTIQUE ET RADIOFREQUENCES**

Arrêté ministériel : 25 mai 2016

Présentée par

Gizem SOYLU

Thèse dirigée par **Jean-Louis COUTAZ,** et
codirigée par **Emilie HÉRAULT**,
et **Alessandro MONFARDINI**

préparée au sein du **L'Institut de Microélectronique, Electromagnétisme et Photonique - Laboratoire d'Hyperfréquences et de Caractérisation**
dans **l'École Doctorale Electronique, Electrotechnique, Automatique, Traitement du Signal (EEATS)**

Techniques de microscopie sous-longueur d'onde aux fréquences TéraHertz

Sub-wavelength microscopy techniques in the TeraHertz frequency range

Thèse soutenue publiquement le **24 juillet 2020**,
devant le jury composé de :

Monsieur JEAN-LOUIS COUTAZ
Professeur Emérite, Université Savoie Mont Blanc, Directeur de Thèse
Monsieur ALESSANDRO MONFARDINI
Directeur de Recherche, CNRS Délégation Alpes, Codirecteur de Thèse
Monsieur GUILHEM GALLOT
Directeur de Recherche, CNRS Île-De-France Gif-sur-Yvette, Rapporteur
Monsieur SUKHDEEP DHILLON
Directeur de Recherche, CNRS Délégation Paris-Centre, Rapporteur
Madame PASCALE ROY
Directrice de Recherche, CNRS Ile-De-France Gif-sur-Yvette, Présidente
Madame EMILIE HÉRAULT
Maître de Conférences, Université Savoie Mont Blanc, Invitée

Acknowledgements

First of all, I would like to express my sincere gratitude and appreciation to my Ph.D. advisors Prof. Jean-Louis Coutaz, Dr. Emilie Hérault and Dr. Alessandro Monfardini. I would like to thank Prof. Jean-Louis Coutaz for giving me this opportunity to work with him. It has been an honour to be his Ph.D. student, I had fruitful and inspiring discussions on physics with you. You are a great scientist! Additionally, I learned a lot of laboratory skills from Dr. Emilie Hérault, that helped progress the project. Thank you for your brilliant ideas and your encouragement during this journey, which was not always easy but you were always there to help me. Also, I am very glad to have worked with Dr. Alessandro Monfardini for his help and advice, which helped me to develop the experiments in the Néel Institute.

I would also like to thank Dr. Guilhem Gallot and Dr. Sukhdeep Dhillon for accepting the work of rapporteur and for the interest you took in the work carried out, as well as Dr. Pascal Roy for her role as examiner and for coming to the defence in Le-Bourget-du Lac during the pandemic.

I am grateful to the French Research Agency (ANR) through the LabEx FOCUS ANR for the financial and technical opportunities provided for the completion of this thesis.

I would like to thank Dr. Guy Vitrant for his support during my Ph. D. and for introducing me to Prof. Jean-Louis Coutaz. I am very grateful to work with Dr. Jean-François Roux for all the discussions and suggestions he provided when writing our paper. I would like to thank Dr. Gwenaël Gaborit for supplying crystals and his remarkable ideas.

I would like to thank to Dr. Giorgos Georgiou and Dr. Federico Sanjuan, your enthusiasm for being scientists is inspirational. I appreciated how much time you spend for me to make some simulations on COMSOL, thank you Giorgos! Also, thank you for letting us to share the femtosecond laser! I am very pleased to work with you Federico, you are a such a cheerful and easy person to work with, thank you for giving me nice tricks when I needed to build an experimental setup! They were precious.

Sometimes, I needed some professional hands especially in the clean room, thank you Aude Bouchard for spending your time with me to make my samples! I would like to thank Dr. Magali Astic for helping me with my experiments when I needed her. Thank you also to Dr. Guillermo Martin, who helped us find a way to fabricate our cone shaped samples.

I suppose the experiments in Néel Institute would be impossible without the help of Dr. Florence Lévy-Bertrand and Dr. Martino Calvo. Thank you for all supports and encouragements!

Sometimes there were times that we needed distraction from the lab and in these times I was surrounded by great friends: Bastien Muller, Farah Aljammal and Dongwei Zhai and Hasti Vakili Mohadeseh. Thank you for your valuable friendship and your motivation.

Last but not least, I would like to thank my parents Leyla and Rüknettin, my brother Meriç, and my best friend and husband Jamie for their endless love and their encouragement. I am sure that I would not come this point without you. Thank you.

Table of Contents

Abstract

Imaging in the Terahertz frequency range at sub-wavelength resolution has gained a great interest for certain studies which cannot be carried out with other parts of the electromagnetic spectrum. However, classical optical schemes cannot be employed to obtain micrometre-range resolution for THz microscopy as diffraction limits the resolution to about 100 µm. In this thesis, we present two different original sub-wavelength THz microscopy techniques. In the first technique, the THz beam is screened by a thin metallic sheet in which a sub-wavelength hole has been made. The sample is placed against the sheet and moved over the hole to perform a raster image. The expected resolution is then equal to the hole size. The second technique presented in this thesis is based on generated a THz signal directly from the sample. When a laser beam is focused in the sample, the illuminated region, if non-centrosymmetric, can generate THz signals through optical rectification. The raster image is obtained by recording this THz signal while the laser beam is moved over the sample. The expected resolution is then close to the laser spot size.

Both technique might involve weak THz signals. That is why we investigated on the possibility to measure them with a very sensitive detector, usually used for astronomy, named kinetic inductance detector (KID). This manuscript presents its principle as well as the study that was carried on. On a "classical" time domain spectroscopy setup, signal as low as 0.2 fW were thus recorded, demonstrating the interest of such detectors.

The two last chapters are dedicated to the two microscopy techniques themselves. For the first one, a simulation model using a finite element model solver is used to design the most efficient aperture to enhance the transmission through a sub-wavelength hole. The results show that a conically tapered hole has a higher transmission than a classical cylindrical hole. Our attempts at using the KIDs camera for the first time for THz microscopy are discussed and first encouraging results are presented.

Finally, the ORTI (Optical Rectification Terahertz Imaging) technique is investigated. An image with a 10 µm spatial resolution (λ/214 for 0.14 THz) was obtained while scanning the ferroelectric domains of a crystal of PPKTP. We show that the resolution of the image depends only on the laser spot size and not on the generated THz frequency. In addition, we showed that ORTI image can be used to scan a poly-crystalline sample as well as a crystal with different thickness areas. Lastly, the limitations of the spatial resolution of ORTI images are discussed in detail.

Résume

La microscopie dans le domaine Terahertz (de facto sub-longueur d'onde) suscite un fort intérêt pour compléter les techniques déjà existantes aux autres longueurs d'onde. Cependant, la limite de diffraction empêche, par des schémas optiques classiques, d'atteindre des tailles de faisceaux THz, et donc des résolutions d'image, inférieurs à quelques centaines de micromètres. Dans cette thèse, nous proposons deux techniques de microscopie originales. La première consiste à écranter le faisceau THz à l'aide d'une fine plaque de métal percé d'un trou dont le diamètre est sub-longueur d'onde. L'échantillon est placé contre la plaque et déplacé devant le trou afin de faire une image point à point. La résolution attendue pour l'image est de l'ordre de grandeur de la taille du trou.

La deuxième technique présentée ici consiste à générer un signal THz directement dans l'échantillon. Lorsqu'un faisceau laser est focalisé dans l'échantillon, la région illuminée peut, dans le cas où elle est non centrosymmétrique, générer un signal THz par rectification optique. Une image point à point est obtenue en scannant l'échantillon avec le faisceau laser. La résolution d'image attendue est alors proche de la taille du faisceau laser.

Les signaux THz en jeu dans ces deux techniques sont potentiellement faibles. C'est pourquoi nous avons étudié la possibilité de les mesurer avec des détecteurs très sensibles, habituellement utilisé en astronomie : les KIDs (kinetic inductance detector). Après avoir présenté les principes physiques mis en jeu dans de tels détecteurs, ce manuscrit décrit la caractérisation qui a été faite d'une caméra KIDs. A l'aide d'un montage « classique » de spectroscopie dans le domaine temporel, nous avons pu mesurer des puissances de signal très faibles, de l'ordre de 0.2 fW, démontrant les performances de tels détecteurs.

Les deux derniers chapitres sont dédiés aux deux techniques de microscopie elles-mêmes. Pour la première, une simulation à base d'éléments finis a été utilisée afin de rechercher la forme d'ouverture permettant d'obtenir la meilleure transmission d'un trou sub-longueur d'onde. Les résultats montrent qu'une ouverture conique est plus performante qu'un trou cylindrique. Une analyse des résultats encourageants obtenus lors des premières expériences de microscopie THz à travers un trou et impliquant une caméra KIDs est présentée.

Finalement, la technique dite ORTI (Image Terahertz par Rectification Optique) est étudiée. Une image de 10 µm de résolution spatiale ((λ/214 à 0.14 THz) a été obtenue en scannant les domaines ferroelectriques d'un cristal de PPKTP. Il est démontré que la résolution de l'image dépend uniquement de la taille du faisceau laser et non pas de la fréquence THz générée. De plus, il est montré que cette technique peut être utilisée pour imager un échantillon poly-cristallin ou encore un échantillon présentant des zones géographiques de différentes épaisseurs. Enfin, ce manuscrit se conclue sur les paramètres limitant la résolution spatiale des images ORTI.

General introduction

Nowadays, imaging and microscopy techniques are important in our laboratories to visualize, diagnose or identify the samples. These techniques use electromagnetic radiation to make an image. When electromagnetic radiation interacts with an object, what is seen is the image results of the interaction of that radiation with the atoms of the object. Scientists are continuously looking for new methods to exploit parts of the electromagnetic spectrum for imaging: one of the most interesting and the recently discovered regions is Terahertz (THz) radiation. Because of several unique properties, Terahertz imaging gained great attention. They can probe spectral signatures, phonon resonances and vibrational and rotational energy levels of the materials. Therefore, there is a great interest on THz microscopy, in fields of nanotechnology, biology, microelectronics and medicine. However, THz microscopy suffers from poor resolution. The resolution is limited by the diffraction limit which is 150 µm for 1 THz. Such resolution restricts the possible future applications of terahertz microscopy. Therefore, the aim of this thesis is to develop new ideas to reach subwavelength THz resolution.

One idea to reach subwavelength THz resolution is to use the nonlinear property of the materials, which originates from the second harmonic generation (SHG) imaging method. In this technique, the laser light interacts with a non-centrosymmetric material and generates a new photon with the double of its frequency. These SHG images are of high quality since the resolution is still limited by the diffraction limit of the laser light which is much smaller than the THz ones (500-1000 nm). In the same process of generating second harmonic waves, THz waves are generated as well. This method is known as optical rectification. In this thesis, a THz microscopy technique is demonstrated by scanning the sample with a laser beam and detecting these generated THz waves in the sample with optical rectification, so the subwavelength resolution of THz microscopy is achieved by the spot size of the laser beam on the sample. We call this technique optical rectification terahertz imaging (ORTI).

In this thesis ORTI is used to image some nonlinear crystals and the parameters limiting its resolution are discussed. It is a unique technique comparing to the other commonly used subwavelength THz microscopy techniques such as scanning near field microscopy (SNOM) and aperture-based microscopy because the crystal itself generates the terahertz waves due to its nonlinear properties. However, the generated THz wave energy is 1000 times smaller than SHG waves, and if this technique is to be applied for imaging crystals or biological tissues with a low nonlinear coefficient, then there is a certain need for a highly sensitive detector. For this, we use kinetic inductance detectors (KIDs) which is a superconducting detector. For the first time to our knowledge, the KIDs camera will be used for THz microscopy in this thesis. In order to demonstrate the KIDs camera could be used in THz microscopy, some preliminary studies are performed such as detecting weak THz pulses. Then, a THz microscopy technique using the KIDs camera as a detector is shown by using an aperture based technique: a thin sample is located against a metal sheet which has a hole, and the THz image is obtained by moving the sample over the hole which is fixed. The subwavelength THz resolution is achieved with this technique by making the hole smaller. Firstly, to estimate the light transmission passing through the hole, a finite element solver HFSS is used. With this solver, a more complex aperture can be designed instead of designing an ordinary cylindrical hole.

This thesis is organized as follows:

Chapter 1 begins with a brief introduction to the historical and technical information of the terahertz domain. The advantages of using THz waves for imaging together with the application areas will be discussed. Next, the research problems of THz microscopy are described with some examples: diffraction limit and subwavelength resolution. The commonly used different techniques for subwavelength THz microscopy are also summarized in this chapter. The last part of this chapter highlights the obtained primarily result and the objectives of this thesis.

Chapter 2 presents the theory of different methods used in this project to generate and to detect THz pulses. It concludes with a basic concept of the THz time domain spectroscopy technique.

In Chapter 3, kinetic inductance detectors are introduced by giving a basic theory to understand their response to light. The multiplexing of these detectors to form them in a matrix are described here briefly. The following of the chapter presents the experimental results which were published in a journal [1]. This work includes the minimum THz pulses measured by using KIDs in this project.

Chapter 4 focuses on simulation results performed in HFSS and experimental results for THz microscopy by using the KIDs camera. The presented simulation results show the estimated light transmission through a hole used for THz microscopy. The aperture performance is investigated using HFSS simulations, and the results are discussed. The THz microscopy setup is presented as well as the first experimental images. Different apertures are used for imaging the samples using the KIDs camera as a detector. Difficulties encountered during the experiments are discussed.

Chapter 5 is dedicated to the ORTI technique on the diffraction of THz waves. The experimental results obtained with two different setups are presented in 1D and 2D at different generated THz frequencies. Imaging of a periodically poled KTP crystal is exposed theoretically and experimentally. The parameters, which have an influence on the image resolution, are discussed at the end of the chapter.

The thesis conclusions and outlook for the future are discussed in Chapter 6.

1. Bibliographic review on sub-wavelength terahertz imaging

1.1 Introduction to terahertz

Terahertz (THz) radiation is commonly defined as electromagnetic waves whose frequencies spread from 0.1 THz to 10 THz, which corresponds to the wavelength range between 3000 µm and 10 µm [2,3]. One terahertz frequency ($\nu = 1$ THz) corresponds to a period ($\tau = 1/\nu$) of 1 ps, a wavelength ($\lambda = c/\nu$, c is the speed of light) of 300 µm, a wavenumber of 33 cm^{-1} ($k = 1/\lambda$) , a photon energy ($E = h\nu$, h is the Planck constant) of 4.1 meV, and an equivalent temperature ($T = h\nu/k_B$, k_B is the Boltzmann constant) of 47.6 K. As shown in Figure 1.1, THz radiation bridges the gap between the electronic world (starting from microwave and going to lower frequencies) and the photonics world (starting from infrared and going to higher frequencies), which are defined by the nature of the related sources and detectors. Unfortunately, in the THz range, neither electron based devices nor optical techniques were efficient until the late 1970s and early 1980s. That is why this region is called the 'THz gap'. However, this gap has been filled over the last three decades with a lot of development in techniques of generation and detection of THz. From the high frequency edge of the THz range, photonic technologies have seen much progress, and the electronic technologies have also developed for the low frequency edge.

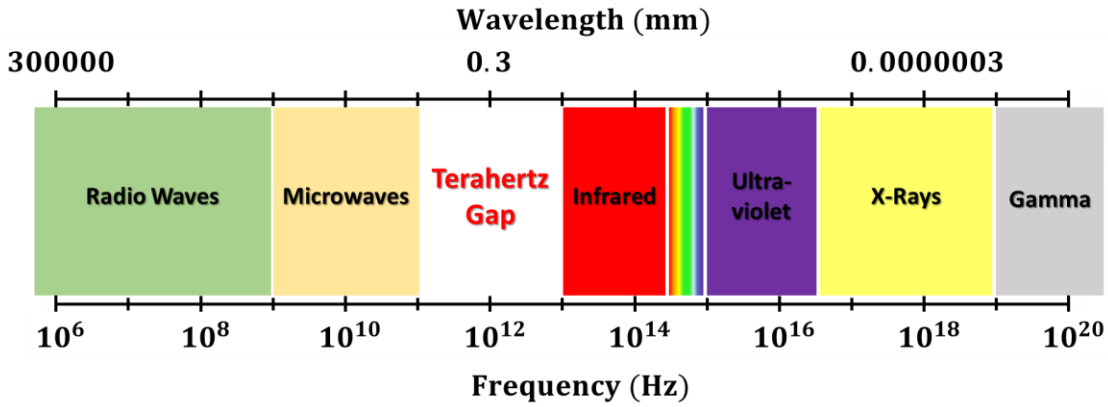

Figure 1.1: The electromagnetic spectrum in terms of frequency and wavelength

After the invention of ultrafast mode-locked lasers, pioneering work came with the study of the response of photoconductive dipole antennas to generate electrical signals with a time resolution of a few picoseconds in 1975 [4]. The first prototype of photoconductive antennas as an emitter and a detector was first used in the late 1980s [5,6]. This led to the development of THz time-domain spectroscopy (THz-TDS) which is a powerful technique for generating and detecting THz pulses [7,8]. After this, different initial mechanisms for the generation and detection of THz radiation have been exploited such as second order nonlinear effect in an electro-optic crystal ($LiTaO_3$) for generating Cerenkov-like THz beams (optical rectification) [9], complete THz system with optical rectification generation in a nonlinear medium (ZnTe crystal) and detection by electro-optical Pockels effect using the same crystal [10], and more recently generating THz radiation by the focusing of high-intensity

laser pulses into gas (plasma generation) [11] and detecting the THz signal by a four-wave mixing effect in the photo-induced gas plasma [12].

As a consequence of growing research in this field, THz radiation now has a wide range of prospective applications: for imaging in the field of security, in biological science, in food industry, in semiconductor technology, in art; for analysing chemical components in the pharmaceutical industry; for communication in wireless technology; for monitoring in the paper and polymer industry and in earth and space science [13–15].

1.2 Application of terahertz imaging

There are numerous advantages of using THz radiation to form images. First of all, as terahertz is a given frequency range in the electromagnetic spectrum, THz imaging can provide supplementary information to imaging systems in other frequency ranges, like microwaves, infrared, visible, ultraviolet and X-rays. However, comparing to microwaves, THz has smaller wavelengths so the spatial resolution is better. Also, most of the common materials like paper, clothes, cardboard are transparent, while they are opaque at optical wavelengths. On the other hand, metals are opaque to THz radiation and highly reflective while the plastic is partially transparent. These qualities make it possible to detect the inside of packaging in the THz (cardboard, plastic) to avoid faulty pieces. This can solve the one of the most significant issues in the food industry; there might be some possibly damaging materials in the packaging such as glass, metal, wood. It has been demonstrated that the foreign bodies with a less than 1 mm spatial resolution can be identified in a chocolate bar using THz technology [16] (see Figure 1.2). There are also other applications in food industry to detect foreign bodies in flour sample [17], in noddle [18] , in powdered milk [19], etc.

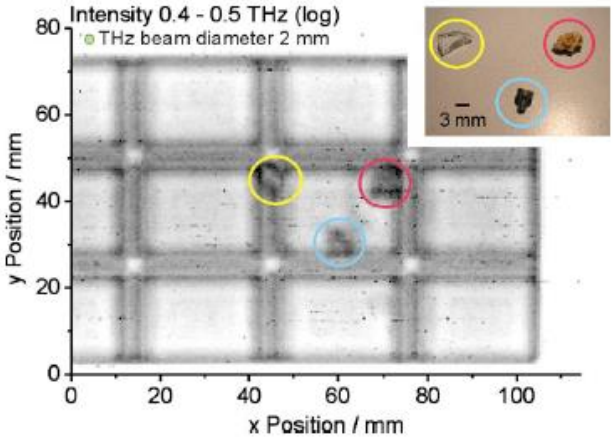

Figure 1.2: THz image of chocolate bar with three different contaminations: a glass splinter (yellow circle), a small stone (red circle) and a metal screw (blue circle). (Image is taken from [16])

Terahertz technology is also a topic in the field of defence and security. For the detection of exploited materials, terahertz imaging has an excellent ability to detect explosive materials [20,21]. The main concept is that many molecules have different fingerprint in terahertz frequencies so it can be used to distinguish some chemical component and to analyse these materials. For example, terahertz imaging can be used to analyse quantitatively (by measuring water content) the mixture of

the petroleum products; one of these products, kerosene, is a serious problem to make illegal fuel with mixing diesel [22]. In additionally, in security application, the illicit drugs can be identified in a packages [23,24] since non-metallic and non-polar materials are transparent to THz. Although the metallic objects are not transparent to THz, dangerous metallic items like guns and knives can be visible because of their shapes [25].

THz photon energy is lower than X-ray (for 1 THz, the photon energy is 1 million times weaker than X-ray photons). It is a non-ionizing radiation, and it is not hazardous to living tissues in general. Although the depth of penetration into living tissues is small (about 100 µm), various promising diagnostic solutions have been studied. This feature makes it possible to perform medical imaging without any damage to tissues. For instance, we can identify different types of tissues such as muscle, fat, kidney and vein by using terahertz spectral data [26,27]. Other alternative medical imaging techniques are the teeth structure and more specifically identifying dental caries [26,28]. Dentists try to detect patient's tooth decay by using visual inspection or X-ray radiography. These two methods are difficult to use to identify the early phase of the tooth decay. The tooth decay happens when the dentine is destroyed by acid in the mouth. This result in a reduction of the mineral content of the enamel. Since these regions are absorbent in terahertz, they can be clearly observed by using terahertz-pulse imaging [26]. Figure 1.3 shows two tooth decays (pointed by red squared frames in Figure 1.3(a) and Figure 1.3 (b)) in visible and in terahertz.

(a) (b)

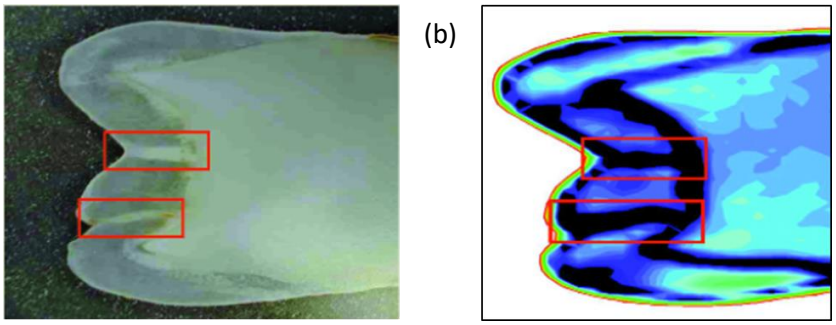

Figure 1.3 Photography of two tooth decays in visible (a) and in terahertz (b). (Image taken from [26])

THz waves are highly absorbed by water. Therefore, in biology, terahertz radiation can be applied to distinguish between cancerous and healthy cells since the water content in those cells are significantly different [29–31]. One example showing us the comparison between the image of breast tissue in THz and the visible is shown in Figure 1.4. The breast tumor is visible in terahertz region (see Figure 1.4 (b)). In this work, they also studied the absorption coefficient and refractive index of the normal tissues and cancerous tissues [32]. The results show that both properties in THz are higher in cancerous cells than the normal ones.

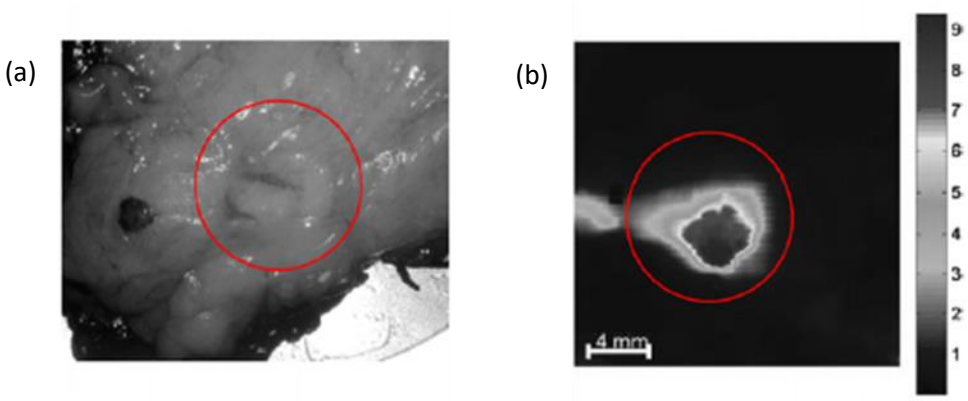

Figure 1.4: Image of tumor in human breast in visible (a) and (b) in terahertz (Image taken from [32])

Terahertz imaging techniques can be applied for imaging and analysing the artworks and the historical objects. Comparing to mid-infrared band, terahertz spectroscopy gives more clear and direct information to identify the compositions of different types of paint layer including the pigments, binders and their mixtures [33,34]. In addition, terahertz reflection imaging can give information on the thickness of the hidden paint layers in painting on a canvas while X-ray and infrared reflectography is limited by the penetration depth to high density pigments such as lead-white paint used commonly in historical paintings [35]. These indicate the potential use of THz imaging for art historians, as well as in restoration of historical objects and paints for conservators and conversation scientists [36,37].

In nanoscale regime, terahertz radiation gives information about biological samples which cannot be easily obtained by other wavelengths. Since a 1 THz corresponds to a period of 1 ps, it can interact with phenomena fluctuating in time scale of picosecond and sub-picosecond. For example, breaking and reforming hydrogen bonds between the water molecules occur in this scale. In addition, vibrational modes of biomolecules which includes DNA modes can be visible in this scale, and the chemical recognition of nanostructured materials can be recognized based on their THz fingerprint. THz spectroscopy techniques can sense the conformational changes in biomolecules [38]. Electrons in nanostructures resonate at THz frequencies, so the dynamic changes in charge carriers can be characterized [39]. In semiconductor industry, the THz microscopy techniques can be used for integrated circuits to detect any fault in the circuit [40] or for evaluating the performance of solar cells [41]. The opportunities with imaging in THz is limitless.

1.3 Classical terahertz microscopy: 'T-ray imaging'

The lack of sources and detectors in the terahertz region has been one of the biggest challenges to take up. Thanks to the development of far-infrared gas lasers, the first terahertz image was recorded in 1976 [42] by Hartwick *et al*. They used this gas laser to generate continuous terahertz waves in the wavelength region of 300 – 1000 µm. The THz images were recorded both in the transmission and reflection modes by using a liquid helium cooled GaAs detector. Figure 1.5 shows the visible and the terahertz images of a key, and the key was successfully imaged in the terahertz even when it is enclosed in a small cardboard box filled with foam rubber (see Figure 1.5 (b)).

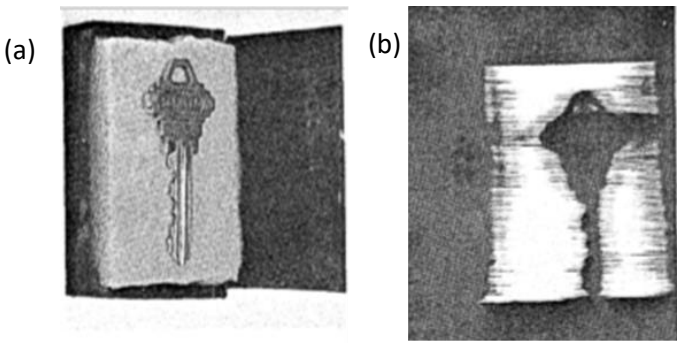

Figure 1.5: (a) Image of a key in the visible region and (b) image of a key enclosed in a box using a wavelength of 300 µm – 1000 µm created by using far infrared gas laser (image taken from [42])

One of the reasons for the interest in terahertz imaging is related to the terahertz time-domain spectroscopy, or THz-TDS [43]. The key components of a THz-TDS system are a femtosecond laser, an emitter, a detector and a delay-producing stage. Ultra-fast optical pulses can generate sub-ps terahertz pulses in the emitter, which can be detected by the detector whose integration time is longer than the terahertz pulse length, because the THz signal is read only when the receiver is triggered by the laser probe pulse. The obtained information is in the time domain and can be converted to frequency domain by Fourier transform. The first image produced by using THz-TDS was obtained by Hu and Nuss in 1995 [44]. In their setup, they used photoconductive antennas: one for THz emission and the other for THz detector, and they obtained transmission THz images by raster scanning. Figure 1.6 (a) shows the THz image of a semiconductor integrated circuit in a package which shows that terahertz imaging can be used for package inspection in industry. The next two images were obtained from a fresh leaf just after it was cut and the same leaf after 48 hours (see Figure 1.6 (b)). The leaf image changed after 48 hours because the water concentration decreased gradually due to the evaporation, and THz waves are strongly absorbed by watery materials. This is also quite a useful property of terahertz to examine chemical compositions in the materials. Hu and Nuss named this method as 'T-ray' imaging [45]. These first terahertz images made a huge impact on the scientific communities working on terahertz imaging systems and lead to subsequent development of terahertz microscopy techniques.

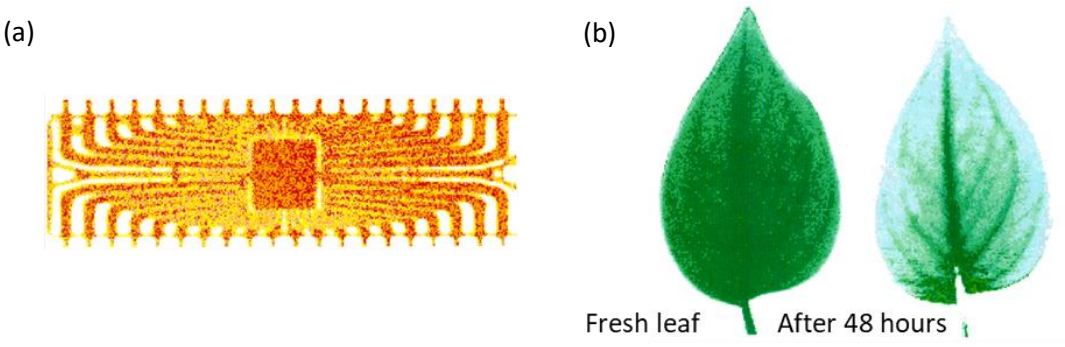

Figure 1.6: THz images of a packaged semiconductor integrated circuit (a) and the fresh leaf and the same leaf after 48 hours (b) (Image is taken from [44])

1.4 Sub-wavelength terahertz microscopy

1.4.1 Limitations of sub-wavelength Terahertz microscopy

Terahertz imaging has evolved differently in many fields. As a consequence, the developments in macroscopic imaging have made possible performing microscopy at THz wavelength, and the interest to image microscopic objects using THz waves has increased as well. However, there are some difficulties which limit the performance of terahertz imaging of microscopic objects [46]. The major problem for THz sub-wavelength microscopy is diffraction, because the long THz wavelength limits the spatial resolution to 100's of µm when employing classical microscopy techniques.

1.4.1.1 The diffraction limit

When light passes through a circular aperture of any size, it diffracts, bends around the corner of the hole and interferes constructively and destructively. Instead of a sharp edge spot, the image becomes a center bright spot surrounded with less intense concentric rings. This diffraction limited spot is the Airy disk. In Figure 1.7, light passes through a hole with a diameter of *D* and the diffraction pattern appears on a screen at a distance from the hole marked as *L*. The first minimum in the pattern occurs at an angle θ_A=$1.22\,\lambda/D$ (the angle is defined as regards to the optical axis, and thus it corresponds to the radius of the first minimum circle), *i.e.* at a position $1.22\,\lambda\,L/D$ from the center if the distance between the hole and the screen is L.

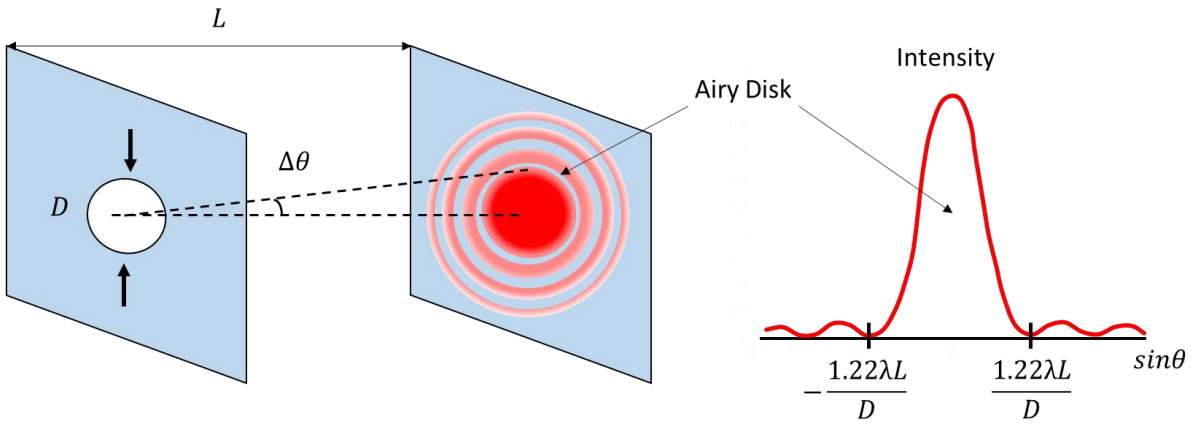

Figure 1.7: Diffraction occurs when light passes through the hole.

The problem when resolving two neighbouring objects (assuming here two circular light sources) comes from the distance between them. If they are too close, their diffraction patterns overlap and the image becomes unresolved. If the maxima of the diffraction patterns are separated, they can be resolved as shown in Figure 1.8. But what can be the minimum opening angle between these object to resolve? The criterion was proposed by Rayleigh in the 19th century which states that two objects can be distinguished if the maximum of one diffraction pattern falls onto the first minimum of other one. This is known as Rayleigh criterion for diffraction-limited imaging systems. So the minimum resolvable angle is $\theta_{min} = 1.22\,\lambda\,/D$.

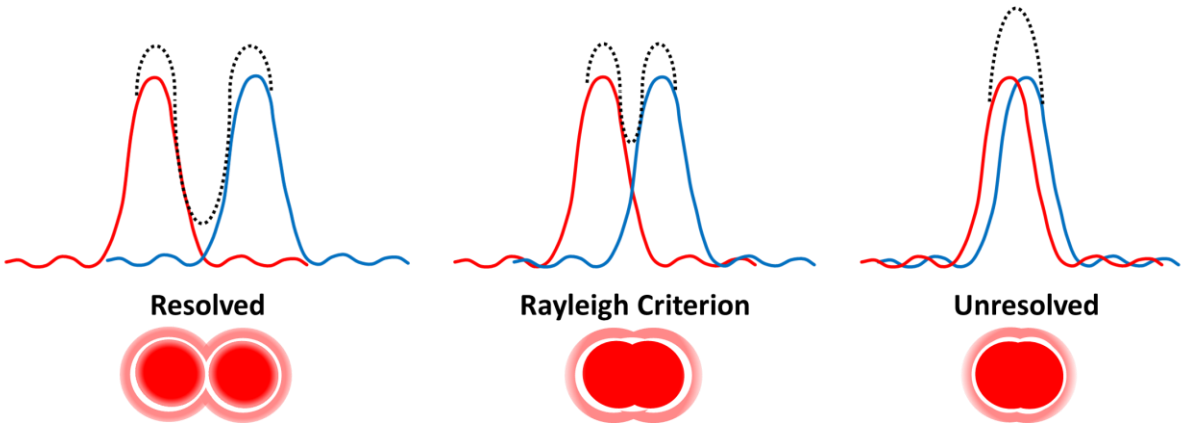

Figure 1.8: Resolved: two images are resolved because the airy disks do not overlap. Rayleigh criterion: the images are just resolvable because the minimum separation between them is the radius of their airy disk. Unresolved: the images are not resolved because their airy disks overlap.

The same criterion can be applied for a focused laser beam; whose profile is a Gaussian one. At the focal plane of a lens, which is supposed to be big enough to neglect diffraction by the lens aperture, two parallel laser beams of equal intensity are focused down a waist of radius ω. The two spots can be distinguished if the two Gaussian shapes cross at half their maxima. It corresponds to a distance from the centre of the first spot equal to $\omega\sqrt{ln2}$ and thus to a lateral resolution $\delta = 2\omega\sqrt{ln2}$. Let us notice that both resolutions (Airy disks and focused Gaussian beams) are rigorously not exactly the same, since the Rayleigh criterion corresponds to Airy disk curves crossing at ~ 0.37 instead of 0.5.

1.4.1.2 Sub-wavelength resolution

Spatial resolution is one of the limitations of all kind of microscopic techniques. For example, in classical optical THz microscopy, lenses and objectives are limited by construction to a numerical aperture $NA = D/2L = D/2F \approx 1{\sim}1.5$ (in microscopes, the distance L between the lens and the sample is equal to the focal length F). Therefore the best resolution restrained by diffraction is $1.22\,\lambda\,L/D = 1.22\,\lambda/2NA \approx \lambda/2$, *i.e.* half of the wavelength (for example 150 µm for 1 THz). Although this spatial resolution is adequate in some applications [47,48], it restrains the application of THz imaging to large objects. For example, terahertz has a unique property to excite low-frequency internal molecular motions including the weakest hydrogen bonds and other weak interactions. The weakest hydrogen bonds are quite essential for biological cell processes and are required for the function of DNA, enzymes, proteins and others [49]. They can be directly detected by terahertz radiation and not by IR, UV and visible radiation. Therefore, a terahertz absorption spectrum plays an important role in cancer diagnoses. The imaging of these vibrational resonances in micrometre-size biological cells is only possible by achieving a sub-wavelength terahertz resolution.

There have been different techniques developed to reach the sub-wavelength resolution in terahertz. To image a sub-wavelength object, it is necessary to collect not only the propagating waves but also the evanescent waves. This can be possible when the distance between the object and the source (or the detector in some cases) is smaller than the wavelength. This technique is called near-field imaging. There have been a variety of techniques developed for near-field imaging. The first terahertz near-field imaging was demonstrated in 1998 [50] and since then this technique became a

very popular research area. Some of the cases just implemented the optical techniques to the terahertz domain while others were only developed particularly for terahertz imaging. The other approach is to use a sub-wavelength aperture. A smaller aperture results in weaker transmission. However, there has been some research showing that special design of holes can enhance the transmission through the hole. The detailed studies for near-field techniques and sub-wavelength aperture is discussed in the next section.

1.4.2 Different sub-wavelength terahertz microscopy techniques

In 1928, E. H. Synge suggested for imaging small objects to use a small (sub-wavelength) size hole constructed in a metal plate illuminated and scanned very close to the sample surface [51]. To understand how much the size of the cylindrical hole could be minimized, the first study was developed by Bethe [52]. According to Bethe's prediction, the transmission of a single sub-wavelength cylindrical aperture in a perfectly conducting and infinitely thin metal sheet is proportional to $(r/\lambda)^4$, where r is the radius of the hole and λ is the wavelength of incident radiation [52]. The transmission is quite weak when $r \ll \lambda$. If the metal has a finite thickness, the surface waves and surface plasmons play an important role and contribute the transmission. This can be observed for subwavelength apertures ($r \ll \lambda$) since the near-field effects contribute to the transmission [53]. This extraordinary light transmission (known as EOT phenomenon) was first experimentally demonstrated for subwavelength hole arrays by Ebbesen *et al.* [54]. Afterwards, it was numerically solved for a single cylindrical hole by Garcia de Abajo [55]. In his model, the hole was considered to be filled with a high-index dielectric material and Maxwell's equations are solved by using the boundary element method. This EOT phenomenon indicates that for a certain wavelength, the normalized transmission efficiency with cross section of hole area exhibits more light than a larger transmission hole. However, if the hole is considered as a cylindrical waveguide whose length is bigger than the incident wavelength, there exists indeed a cut-off frequency. Below this frequency, the transmitted light is strongly diminished because of the cut-off effect in the aperture [56,57]. It can be formulized as [58]:

$$f_c = \frac{1.841\ \mathrm{c}}{\pi\ \mathrm{D}} \tag{1.1}$$

where D is the diameter of the circular aperture. For example, for a circle aperture with a diameter of 100 µm, the cut off frequency of the equivalent circular metallic waveguide is equal to 1.76 THz. It means that below this frequency, the transmitted power is reduced thus the spatial resolution will be limited by this loss. But the metal sheet in most experiment is rather thin, so the transmission is not null thanks to surface wave excited on both sides of the sheet. The contributions of surface plasmon-polaritons and surface waves are more interesting for the subwavelength apertures because the near-field effects contribute to the transmission through the aperture [59].

In addition, there is a straightforward relationship between the cut-off frequency and the cross section of the hole. It has been shown that one way to achieve high power throughout is to use different shapes of aperture rather than using a circular shape, such as siemens star [60], tapered [61], bow-tie[62], H- [63] , C- [64], I- [65] shaped apertures. Another design is a metal with a single hole surrounded by periodic grooves [62,66]. This will enhance the transmission associated with the excitation of coupled surface plasmon polaritons [67,68]. When a sample is put in contact to the metal

plate, it absorbs a part of the light transmitted by the hole, and also it changes the transmission efficiency of the hole, because it strongly perturbs the evanescent waves that are excited at the hole edge and in the vicinity of the hole. Thus the far field light signal transmitted through both the hole and the sample contains the signature of the sample material. Therefore, working in the near field region of the hole allows one to break the diffraction limit [50]. Another way of efficiently producing localized evanescent waves is to make use of a sharp tip, and to locate the sample nearby the tip, which permits to reach the nanometer scale [69].

In summary, two ideas can generally be applied for THz near-field imaging. One approach is to use small hole by following the original idea of Synge, known as scanning near field microscopy (SNOM). The other is to use a metallized tip, or apertureless SNOM. Beside these classical techniques, nonlinear optics may help in breaking the diffraction limit. These latter methods are based on producing a THz emission through a high power optical excitation of the sample. Here the lateral resolution is given by the laser spot size, which could be much smaller that the THz wavelength. Let us notice that these nonlinear techniques do not deliver a THz transmission image of the sample, but a map of its THz generation efficiency, which is related to the refractive index and absorption at THz frequency, and also the nonlinearity of the sample material. This last one depends on the chemical composition of the sample, and of its crystallinity, as it will be explained later on.

1.4.2.1 Aperture-based near-field techniques

The simplest method to achieve a better resolution is to reduce the size of the incoming radiation at the sample. This can be done by making a sub-wavelength hole in a metal sheet and placing the hole in front of the object. In its simplest form, the object is illuminated only with light which comes from the sub-wavelength aperture and scanned point by point. Since only the transmitted light through this aperture is detected, the spatial resolution of this system is determined by the size of the sub-wavelength aperture. For this approach, Mitrofanov *et al.* developed a collection mode detector which has a square aperture of 30 x 30 μm^2 in a gold film (with a thickness of 600 nm) deposited on a Gallium Arsenide (GaAs) photoconductive antenna [70] (see Figure 1.9). In this experiment, to generate the THz beam another GaAs photoconductive antenna was used. The transmitted THz waves were measured by the detector which was placed at a distance of 10-15 µm behind the object. In their other work, a silicon lens was placed on the top of the aperture and they reached a spatial resolution of 7 µm ($\lambda/200$) for the frequency range from 0.2 to 2.5 THz [71]. The reason why this method works and there is no obvious cut-off effect observed is because the waveguide is short so the many non-propagating modes reach the end of the waveguide.

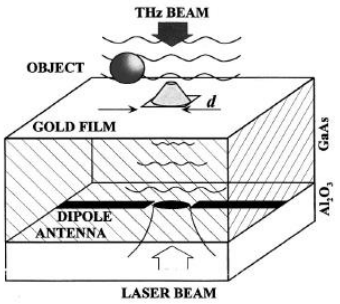

Figure 1.9: Representation of aperture-type near field THz detector used in Mitrofanov *et al.* experiment (Image is taken from [70])

Other methods were explored previously to guide the wave into the aperture. The first demonstration of waveguide aperture for terahertz imaging was performed by Hunsche *et al.* [50].They used a tapered metal tip with a sub-wavelength exit in a standard THz spectrometer to scan a test sample (see Figure 1.10) . They observed the sample with a spatial resolution of 50 μm ($\lambda/4.4$) at 1.36 THz. After the work by Hunsche *et al.,* the near field technique became popular. For example, Schade *et al.* studied a conical aperture based technique to image a leaf by applying synchrotron radiation [72]. The image was obtained in a near-field region by putting the leaf in front of the exit aperture by an adjustable ring, and the spatial resolution for this image was 130 μm ($\lambda/6$) at 0.36 THz radiation. Additionally, Liu *et al.* tried something else with the conically tapered hole by cutting the hole in a half and allowing a gap between the two pieces: this structure allows broadband THz propagation [57].

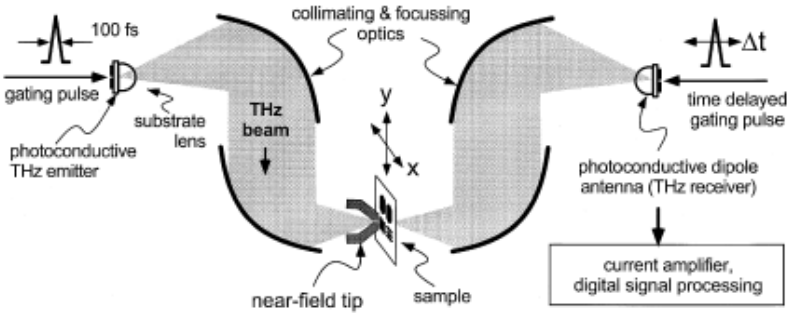

Figure 1.10: The experimental setup used by Hunsche *et al.*(Image is taken from [50])

Normally, the incident Gaussian beam at the focus is larger than the size of the aperture. The coupling problem between the incident THz wave and the aperture hole can be solved by decorating the hole with surrounding periodic structures. This results in the incident wave coupling to the surface mode then propagating to the centre of the hole [66]. Therefore, the transmission light through the hole is increased. Until now, many different designs have been shown. For example, a single circular hole surrounded by concentric periodic groves was used to image a metal pattern in near field region with a spatial resolution of 50 μm ($\lambda/4$) under 1.5 THz radiation [73]. Instead of using a circular hole at the center of concentric groves, Ishihara *et al.* used a bow-tie shaped aperture shown in Figure 1.11 [62]. They achieved a spatial resolution of 12 μm ($\lambda/17$) for THz radiation with a frequency of 1.4 THz.

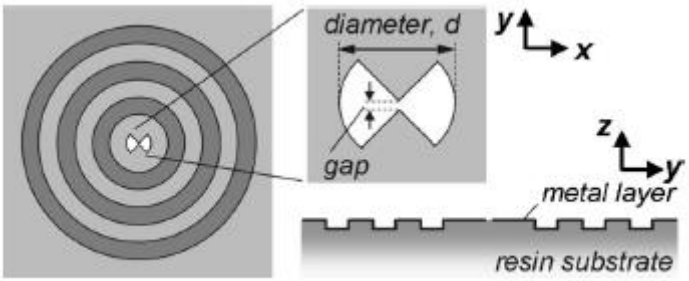

Figure 1.11: The demonstration of bow tie aperture surrounded by concentric groves (Image is taken from [62])

Another method using a Bull's eye aperture in combination with a fiber-scanning near field imaging in THz was studied by Chiu *et al.* [74]. The fiber, used to guide the THz waves, brings the

incident waves to the corrugated aperture. The enhanced coupling light passing through the aperture was focused on breast tissues, and a spatial resolution was achieved to 210 μm ($\lambda/4$).

1.4.2.2 Aperture-less near-field techniques

High resolution THz microscopy can be achieved by using aperture-less near-field imaging techniques. This method was based on a scattering-type scanning near-field microscope (s-SNOM), firstly developed for microwaves [75]. The technique consists of a sharp metal tip which enhances the local electric field in a close distance to the sample to be imaged. With an illuminated terahertz beam, the tip scatters some portion of the light proportionally to the polarizability of the material below the tip. This technique can achieve a sub-wavelength resolution since that one is determined by the size of the tip apex and not by the illumination light. The disadvantage of this method is that it generally suffers from a poor signal-to-noise ratio but this can be optimized by designing longer tips [76]. The first demonstration of this technique in terahertz was done by Van der Valk *et al* [77], who imaged an electro-optic crystal (GaP) with a sharp copper tip. They detected the near field component of the scattered electric field with a lock-in system synchronized with the probe pulse that illuminating from underneath the region of the sample and tip (see Figure 1.12). The achieved spatial resolution for the image was 18 μm ($\lambda/110$) for 0.15 THz.

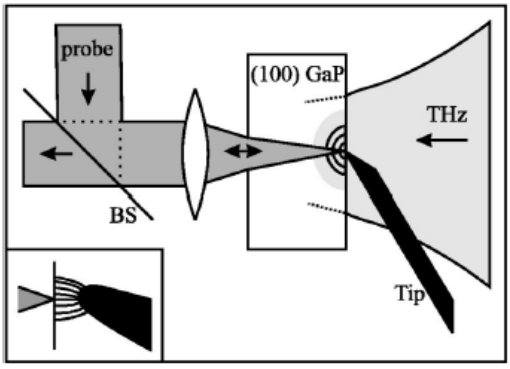

Figure 1.12: Schematic illustration the experimental setup used by Van der Valk *et al.* The inset shows the electric field lines near the tip (Image is taken from [77])

With the same technique, Chen *et al.* [78] managed to reach a nanometer resolution in the far field collection of the scattered field. In their technique, they used a metal tip of an atomic force microscope (AFM) in a combination with a THz-TDS setup. As seen in Figure 1.13, the incident THz pulses cause a dipole moment in the tip-surface system, so some of the THz radiation is scattered and absorbed. The transmitted THz pulse is detected by electro-optic sampling or a bolometer. They scanned a semi-insulated silicon with a resolution of 150 nm ($\lambda/1000$).

From then, the scattering near-field techniques started to be popular in terahertz imaging; there have been a lot of research to increase the resolution and develop the technique. For example, Moon *et al.* [79] demonstrated that even though the metallic gratings were embedded in a dielectric film, they could image them with a spatial resolution of 90 nm ($\lambda/3300$) at 1 THz. Probably the most impressive resolution by using tip scattering of near field was achieved by Eisele *et al.* [80]. They imaged a single nanoparticle with a spatial resolution of 10 nm. In their work, they combined the nano-tip with a fast femtosecond pump probe (10 fs).

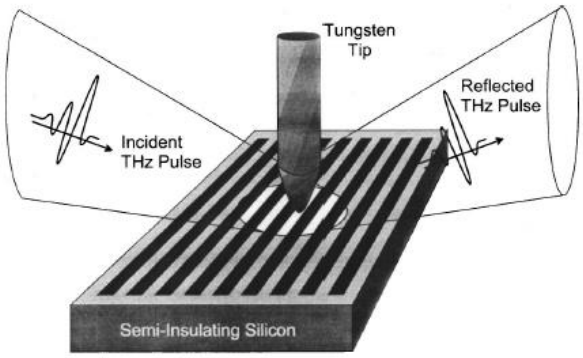

Figure 1.13: Illustration of the experimental method used in Chen *et al.* (Image is taken from [78])

In an alternative method to s-SNOM, Wachter *et al.* fabricated a tapered photoconductive THz field probe-tip mounted on a wedge with a 30° inclination [81]. The electrodes (two tapered planer wires) are based on a triangular shaped low temperature grown GaAs, and the gap between them is 1.8 µm, presented in Figure 1.14. Because of the electrode configuration, the two perpendicular polarization states (x and y directions) have different spatial resolutions which are 5 µm (λ/600) for a frequency range from 0.1 to 3 THz and 7 µm (λ/428) for the other one.

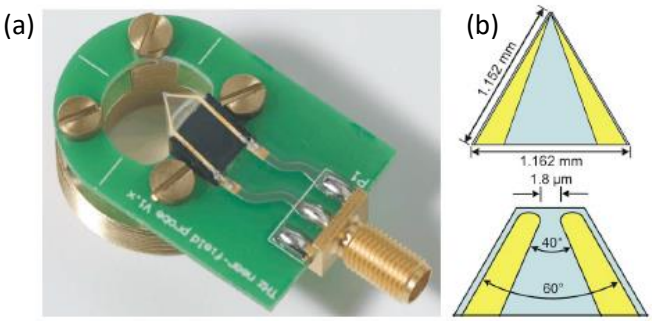

Figure 1.14: (a) Picture of the tapered photoconductive probe (b) The upper image is for the schematic of probe tip and the below one is zoom image for the demonstration of the inner of the probe (Images are taken from [81])

The last terahertz imaging technique using a tip is scanning tunnelling microscopy (STM). In STM design, the tip is brought very close the sample and a small voltage is applied. Then a quantum tunnelling happens when the electrons of the sample move to the tip. The image of the sample is formed by this tunnelling current. This technique allows to image the structure at an atomic level. In THz-STM design, the ultrafast terahertz pulses are focused onto the tip and produce a transient voltage that drives a tunnelling current. With this technique, Cocker *et al.* imaged InAs nanodots grown on GaAs wafer with a spatial resolution of 2 nm (λ/150000) at 1 THz [82]. Thereafter, they also imaged a pentacene molecular orbital (the resolution is about 0. 6 Å) [83].

1.4.2.3 Terahertz emission imaging technique

Another sub-wavelength imaging technique is Laser-Terahertz Emission Microscopy (LTEM) technique. The sample to be imaged is a semiconductor material or device that is illuminated by

femtosecond laser pulses. The semiconductor-laser interaction results in generating and possibly accelerating photo carriers. This terahertz emission can be detected by the optoelectronic techniques. For example, a photoconductive antenna can be the sample to be imaged. Femtosecond pulses generate terahertz pulses in the area where the antenna is illuminated. This emitted pulse gives information about the physical properties of the illuminated area of the antenna. When the sample scan is performed by changing the position of the laser beam, the image of the sample is obtained. Therefore, the resolution depends mostly on the spot size of the laser beam and not so much on terahertz wavelength. One of the first images was reported by Brener and his colleagues in 1996 [84]. They studied an emission efficiency of emitters composed of electrodes designed in different shapes on a GaAs wafer. Basically, in their technique, they used femtosecond pulses to excite biased photoconductive switches and scanned point by point at the side of the anodes. The terahertz emission was collected by a pair of off-axis paraboloids, and the waveforms recorded with THz dipole antenna grown on LT GaAs. They obtained the image of one of the anode with a spatial resolution of 2 µm which is shown in Figure 1.15.

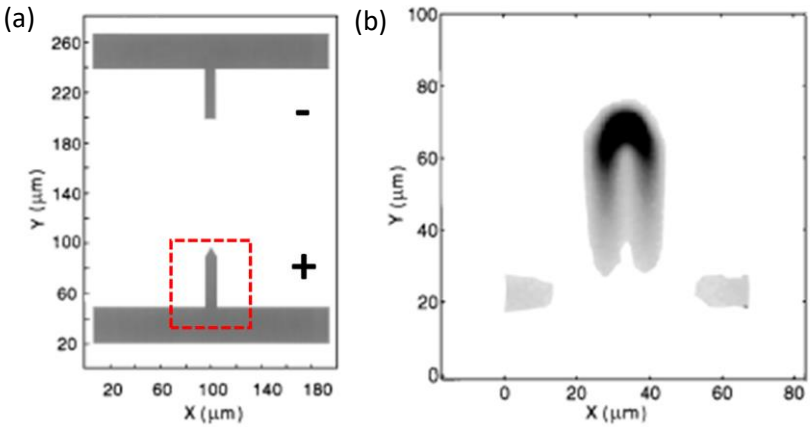

Figure 1.15: Photography of electrodes of emitter and the red dashed square shows the scanned anode (a). Terahertz emission image of the anode and indicating the sharp edge of the electrode (b). (Image was taken from the article [84] and a little modification was done)

LTEM technique can be applied in imaging integrated circuit (IC) chips. For example Kiwa *et al.* [40,85] studied IC chips to image the electrical faults with a spatial resolution of 3 µm. They built a backscattering-type LTEM, in which the terahertz emission is backward. This emission was generated by femtosecond pulses which scan the sample placed on motorized stages. The authors indicated that the generated waveforms depend on the design and photocarriers lifetimes of the semiconductor wafer. This makes it possible to investigate any structural default. Figure 1.16 shows the image of wafers without and with default. After applying a certain voltage to this circuit, the electric field distribution changes remarkably and the difference can be easily seen in LTEM images.

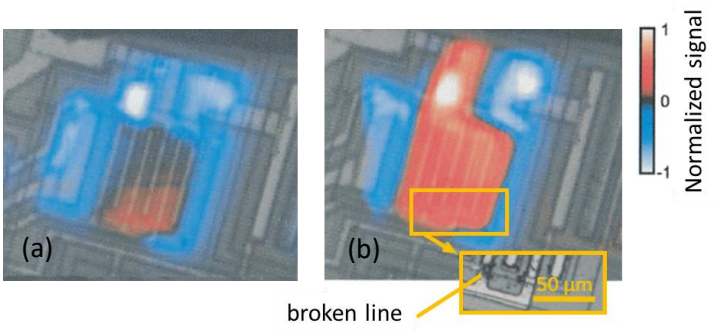

Figure 1.16: LTEM image of normal circuit (a) and false circuit (b) (Image is taken from [40])

1.4.2.4 Near-field nonlinear optical techniques

These techniques are based on the emission by optical rectification or detection by electro-optic effect in a nonlinear crystal wafer on which the sample to be studied is located. The sample modifies the emission or detection in the crystal through its near-field presence.

The emission technique was developed by Lecaque *et al.* [86] and their setup is shown in Figure 1.17 (a). In the experiment, they place a sample to be imaged on a nonlinear ZnTe crystal. The femtosecond pulses are focused with a microscope objective to the crystal that generates THz and IR waves by optical rectification. The broadband emitted waves are transmitted through the sample and are collected by an objective. These waves are then detected by different detectors according to the selected frequencies (THz or IR). They imaged a human eyebrow and improved the resolution (30 µm $\sim \lambda/10$) by performing a deconvolution procedure, which is a classical microscopy technique. The complementary detection technique was proposed by Blanchard *et al.* [87]. In this method, strong THz pulses generated by tilted $LiNbO_3$ illuminate widely the sample. Unlike Lecaque *et al.*'s method [86], this time the sample is on the top of the thin electro-optic crystal, and the probe beam is used to interact directly with this thin crystal and read the scattering and diffracting THz pulses by the sample. The 370 µm x 420 µm area image was obtained at 35 frames per second with a spatial resolution of 14 µm ($\lambda/10$ at the center frequency of 0.7 THz).

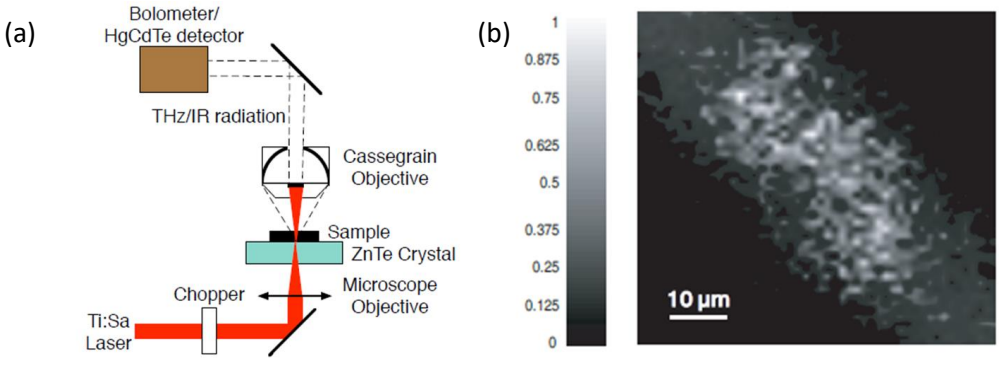

Figure 1.17: (a) The experimental setup (b) The THz image of human eyebrow. (Images taken from [86])

Recently, the spatial resolution of LTEM was improved to the nanoscale range by combining it with a s-SNOM approach [88]. Klarskov *et al.* used femtosecond pulses to excite a commercial AFM

tip (see Figure 1.18).). Here, the tip enhances the localized fields generated by the optical pulse in the sample interaction volume, which are Raman and nonlinear process signals [89].Therefore, the generation of THz signal is underneath the tip. They detected the laser light backscattered with a photodiode, the forward-scattered THz signal with the electro-optic detector and the LTEM signal by chopping the femtosecond laser pulses. Figure 1.185 (b), (c) and (d) show the image of the nanogold wire in the three different spectral regions. These three images all have the same spatial resolution of about 20 nm.

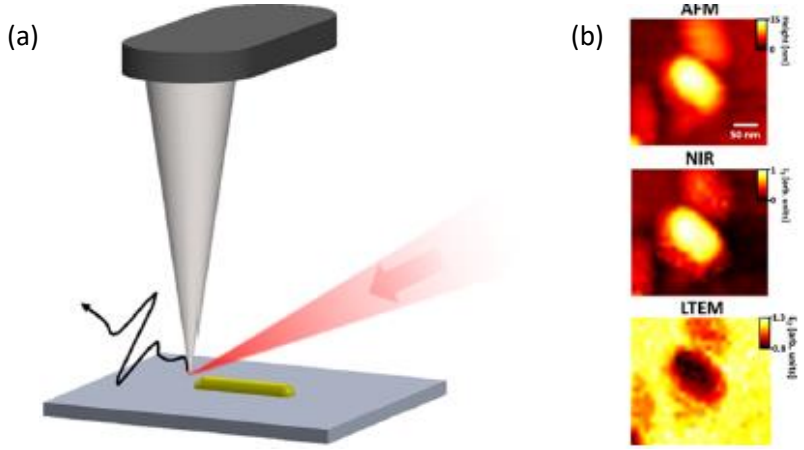

Figure 1.18: (a) Demonstration of LTEM imaging. (b) AFM, NIR and LTEM images of nanogold. (Images taken from [88])

1.5 Thesis Objectives and Primary Results

1.5.1 Primary Results of ORTI technique

The Optical Rectification Terahertz Imaging (ORTI) is based on generating terahertz waves in a nonlinear material through optical rectification: the short pulse beam illuminates a small spot at the sample surface. A THz signal is generated by this excited spot through optical rectification, and a terahertz image of the sample is obtained by scanning the sample in the laser beam. This technique was firstly used to image the ferroelectric domain walls of ferroelectrics [90–92]. The main reason for mapping the ferroelectric domains with terahertz imaging is to determine the polarization directions of the domains which cannot be determined by mapping second-harmonic generation intensities. Therefore, the main aim of the study was not microscopy. However, the ORTI technique was later demonstrated by Sanjuan *et al.*, a study proving its microscopic ability [93]. Figure 1.19 shows the obtained sugar grain image with ORTI technique. The reason they preferred to image a sugar grain is because sugar is a cheap and efficient nonlinear material. For this image, they recorded the peak values of terahertz signals as a function of position in the crystal.

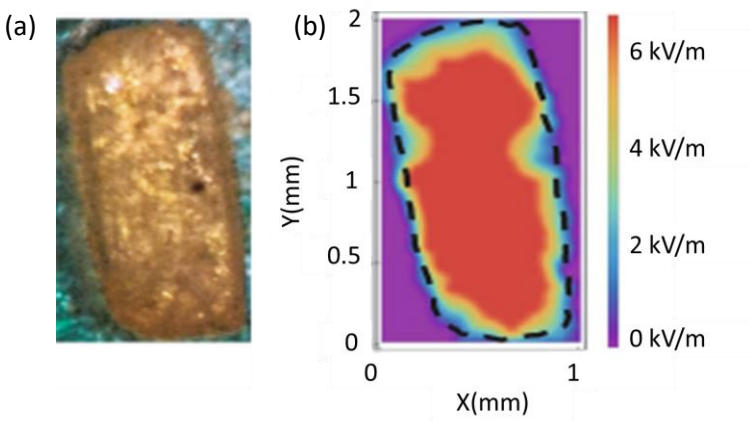

Figure 1.19: (a)Photography of a sugar grain. (b) ORTI image of sugar grain with a spatial resolution of 50 µm (Image is taken from [93] and numbers and texts were reformatted)

Figure 1.20 shows the experimental setup used for the first ORTI technique. An amplified laser system (Cohorent Libra) emits optical pulses of 50 fs duration with an energy of 5 mJ at 800 nm, and at a repetition rate of 1 kHz. The minimum lateral resolution of the ORTI technique results from a balance between focusing hardly the laser beam and destroying the sample due to the huge laser power density at the focused. This will be described in details in Chapter 5 of this manuscript. In the work reported [93], in the resolution was 50 µm, *i.e*. of the order of $\lambda/12$.

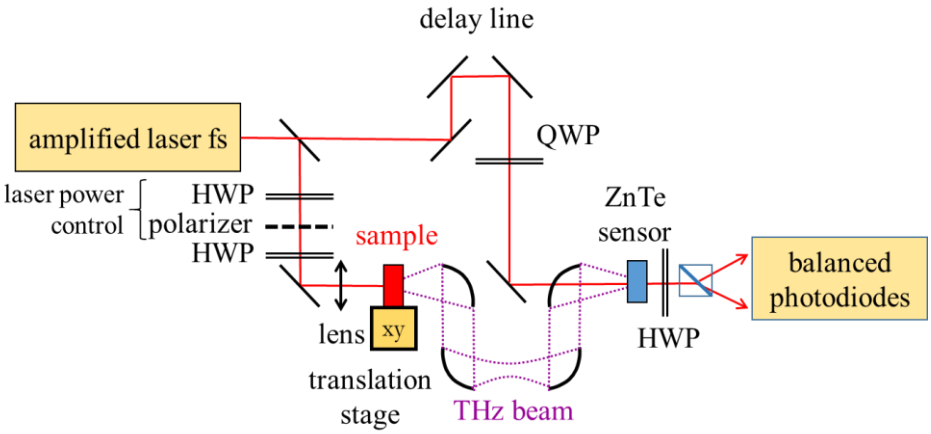

Figure 1.20: The experimental setup (Image is taken from [93])

1.5.2 Objectives

The work by Sanjuan *et al.* [93] has validated the principle of ORTI. However, these preliminary results merit additional studies and improvements. In this PhD project, we focus on the development of the ORTI technique. Simultaneously, we will address microscopy based on super-transmission through a sub-wavelength size hole in a metallic sheet, which is a more classical microscopy technique, in the sense it does not involved nonlinear phenomena in the sample. Finally, we will compare the performance, advantages and drawbacks of both techniques.

The super-transmission technique is using a hole made in a metallic sheet, and the sample will be located against the sheet and moved over the hole. The hole transmission will be perturbed by the

sample, giving the image of the sample opacity with a spatial resolution corresponding to the hole diameter. To reach the sub-wavelength resolution with hole, a reduction in the size of the aperture is required, which obliges to detect weak THz signals. Therefore, to overcome this problem, in this PhD, highly sensitive detectors (typically $NEP \sim 10^{-17}$ W/ $Hz^{1/2}$) called Kinetic Inductance Detectors (KIDs) are employed to detect weak THz waves for the first time for THz microscopy. In addition, we also aim to measure minimum THz pulse power can be detected by using KIDs.

The second part of this PhD project is based on ORTI technique. A sample, whose material is not centro-symmetric, can generate THz waves under femtosecond laser beam illumination. The imaging of these samples will be done by moving the sample at the focus point of the laser so the resolution is limited by the near field infrared diffraction. Here again, the weak expected THz signal could request the ultra-sensitive KID matrix as a detector in case of using not highly-nonlinear material, *e.g.* organic samples. Although, this technique was showed before [93], some studies and improvements have to be done, for example reducing the spatial resolution, recording THz waveforms (imaging in different THz frequencies, in the primary result there was no spectral information) and showing the capability of this technique by using different samples like imaging ferroelectric domains of ferroelectric samples.

2. **Terahertz Pulses**

Femtosecond lasers play an important role in generating and detecting of terahertz pulses. In this chapter, generation of THz pulses with femtosecond laser pulses is introduced, as well as the related detection technique. The most widely used optoelectronic devices for THz generation are photoconductive antennas and nonlinear crystals. The same laser beams are also used to detect these THz pulses by a time-equivalent method based on either electro-optic crystals or photoconductive antennas. These detectors and emitters are well suited to terahertz time domain spectroscopy (THz-TDS) systems, which will be discussed at the end of this chapter. In addition, other terahertz detectors used in this work are discussed; these detectors are sensitive to the power of the terahertz signal, and thus they cannot be used in a simple way in time-domain systems.

The generation of terahertz pulses depends on the antenna or the nonlinear crystal, the laser pulse duration and energy. The pulse duration limits the temporal resolution of the generated THz bandwidth [94]. The energy carried by optical waves in the antenna is described by the Poynting vector $\vec{\mathrm{P}}$. The electromagnetic field consists of electric ($\vec{\mathrm{E}}$) and magnetic fields ($\vec{\mathrm{H}}$), so the Poynting vector is:

$$\vec{\mathrm{P}} = \vec{\mathrm{E}} \times \vec{\mathrm{H}} \tag{2.1}$$

In general, the density of optical power per unit area (D) normal to the propagation direction, is the time average of the Poynting vector, which is defined as:

$$\mathrm{D} = \int_{\mathrm{time}} \left|\vec{\mathrm{P}}\right| \mathrm{dt} = \int_{\mathrm{time}} \left|\vec{\mathrm{E}} \times \vec{\mathrm{H}}\right| \mathrm{dt} = \frac{\left|\vec{\mathrm{E}} \times \vec{\mathrm{H}}^{*}\right|}{2} \tag{2.2}$$

Here, $\vec{\mathrm{H}}^{*}$ is the complex conjugation of $\vec{\mathrm{H}}$. Considering a plane wave (with an electric field magnitude E_0) passing through the medium, Equation (2.2) becomes [94]:

$$\mathrm{D} = \sqrt{\frac{\varepsilon}{\mu}} \frac{\mathrm{E}_0 \, \mathrm{E}_0^{*}}{2} = \frac{\mathrm{E}_0^2}{2\mathrm{Z}} \tag{2.3}$$

where Z is the characteristic impedance (response) of the transmission medium. Commonly used femtosecond laser systems to generate pulsed THz radiation have a pulse duration less than 100 fs, and their centre wavelength is 800 nm. Another essential parameter of the laser pulse is its optical peak intensity. In an ultrashort time period, a high laser peak intensity can be concentrated. These intense and short pulses excite the THz antennas and the THz output generation increases with the peak power density of the laser pulse. The peak power is described as

$$\widehat{\mathrm{P}}_{\mathrm{laser}} = \frac{\overline{\mathrm{P}}_{\mathrm{laser}} \tau_{\mathrm{rep}}}{\Delta \mathrm{t}_{\mathrm{pulse}}} \tag{2.4}$$

where Δt_{pulse}, $\overline{P}_{laser}$ and τ_{rep} are the pulse duration, the average power and the repetition time rate of the laser pulse, respectively. When the laser interacts with the illuminating area of the antenna, the peak density of the laser $\widehat{D}_{laser}$ is equal to ratio of the peak power of the laser $\widehat{P}_{laser}$ and the illuminating area S_{laser}, which is:

$$\widehat{D}_{laser} = \frac{\widehat{P}_{laser}}{S_{laser}} = \frac{\left(\widehat{E}_{laser}\right)^2}{2Z} \tag{2.5}$$

where $\widehat{E}_{laser}$ is the peak magnitude of the laser electric field.

2.1 Generation of terahertz pulses

This section explains two main methods to generate THz pulses used in this work. These are optical rectification and photoconduction commonly used in THz-TDS setup. These sources have in common that they are exposed to femtosecond laser pulses to generate THz radiation. The average THz power obtained from these sources ranges from nanowatts up to microwatts, depending on the pump laser power [95].

2.1.1 Optical rectification

The bound valence electrons in a matter can be forced to oscillate by an external applied electromagnetic field. The movement of electrons result in an emitting radiation. Since the influence of magnetic field is almost negligible on a material [2], the response of electrons can be described by electric polarization. The classical Lorentzian model is known to give a good description of the relationship between the external field and the polarization in matter. The details of this model can be read in the following sources : [2,96,97].

When the applied field magnitude is much weaker than the intra-atomic field, the induced polarization $\vec{P}(t)$ is proportional to the electric field $\vec{E}(t)$ and to the first order of electric susceptibility $\overleftrightarrow{\chi}^{(1)}$. However, at higher intensities, the polarization is driven into the nonlinear regime and is expanded in power series of the electric field:

$$\begin{aligned}\vec{P}(t) &= \varepsilon_0 \overleftrightarrow{\chi}^{(1)} : \vec{E}(t) + \varepsilon_0 \overleftrightarrow{\chi}^{(2)} : \vec{E}(t) : \vec{E}(t) + \varepsilon_0 \overleftrightarrow{\chi}^{(3)} : \vec{E}(t) : \vec{E}(t) : \vec{E}(t) + \cdots \\ &= \vec{P}^{(1)}(t) + \vec{P}^{(2)}(t) + \vec{P}^{(3)}(t) + \cdots\end{aligned} \tag{2.6}$$

where $\overleftrightarrow{\chi}^{(n)}$ is the n-th order nonlinear susceptibility, and $\vec{P}^{(n)}(t)$ is the n-th order polarization. Let us consider the circumstance for a second order nonlinear medium which is excited by two optical fields oscillating angular frequencies at ω_1 and ω_2, namely $\vec{E}_1(t) = \vec{E}(\omega_1)\cos(\omega_1 t)$ and $\vec{E}_2(t) = \vec{E}(\omega_2)\cos(\omega_2 t)$. It is important to remind that the second order polarization can only occur in a non-centrosymmetric crystals otherwise $\overleftrightarrow{\chi}^{(2)}$ is zero identically in centrosymmetric ones [97]. So the second order nonlinear polarization is in a form of

$$\vec{P}^{(2)}(t) = \frac{\varepsilon_0}{2}\overleftrightarrow{\chi}^{(2)}(\omega_1+\omega_2,\omega_1,\omega_2):\vec{E}(\omega_1).\vec{E}(\omega_2)\cos((\omega_1+\omega_2)t) + \frac{\varepsilon_0}{2}\overleftrightarrow{\chi}^{(2)}(\omega_1-\omega_2,\omega_1,-\omega_2):\vec{E}(\omega_1).\vec{E}(\omega_2)\cos((\omega_1-\omega_2)t) \quad (2.7)$$
$$= \vec{P}^{(2)}_{\omega_1+\omega_2} + \vec{P}^{(2)}_{\omega_1-\omega_2}$$

As a result, the second order polarization has two terms: $\vec{P}^{(2)}_{\omega_1+\omega_2}$ for the summation of the frequencies and $\vec{P}^{(2)}_{\omega_1-\omega_2}$ for the difference of the frequencies. The efficiency for both process depends on certain factors. The most important one of them is the second order susceptibility tensor $\overleftrightarrow{\chi}^{(2)}$ depending on the medium. Secondly, the phase-matching condition should be satisfied in the nonlinear material, which is described as the conservation of the momentum energy. Figure 2.1 shows the schematic illustration of these two conservations just for $\vec{P}^{(2)}_{\omega_1-\omega_2}$ component. In the material, as the photon momentum is also conserved $\hbar\vec{k}_3 = \hbar\vec{k}_1 - \hbar\vec{k}_2$ ($k_i = n(\omega_i)\omega_i/c$, $i = 1,2$ and 3, where $n(\omega_i)$ is the refractive index at frequency ω_i), the photon energy is conserved $\hbar\omega_3 = \hbar\omega_1 - \hbar\omega_2$ as well .

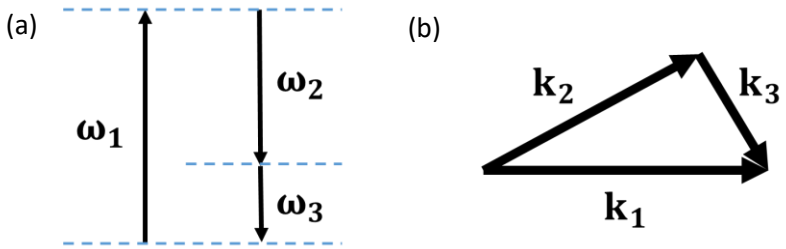

Figure 2.1: For $\vec{P}^{(2)}_{\omega_1-\omega_2}$ component, the energy (a) and momentum (b) conservations.

The phenomenon corresponding to the difference of two equal optical frequencies is called Optical Rectification (OR) (see Figure 2.2). By misuse of language, the difference of two optical frequencies that are almost equal, is also called OR. This is the case for THz generation, as the THz frequency is much smaller than the optical ones. In case of using a femtosecond pulse to excite the material, the generated OR field results in terahertz region since the bandwidth of femtosecond pulses are generally around 10 THz [95]: here the difference occurs between two spectral components of the broadband spectrum of the ultra-short laser pulse. OR was first demonstrated by Bass *et al.* in 1962 [98] by using KDP (potassium dihydrogen phosphate) and KD_dP (potassium dideuterium phosphate) crystals. After that, Morris and Shen [99] proposed and estimated far-infrared generation in $LiNbO_3$ (lithium niobate) crystal, and it has been proved by Yang *et al.* in 1971 [100] by using picosecond pulses (the generated signal band was 0.06-0.36 THz). Subsequently, free-space THz radiation from $LiTaO_3$ (lithium tantalate) crystal with a bandwidth of 1 THz was obtained by using femtosecond laser pulses in 1990 [101]. Afterwards, it becomes a more common way to generate THz waves since it is an easier method comparing to photoconductive antenna, *i.e.* it does not require antenna fabrication. The energy of common femtosecond pulses is enough to generate detectable terahertz radiation through OR in crystals.

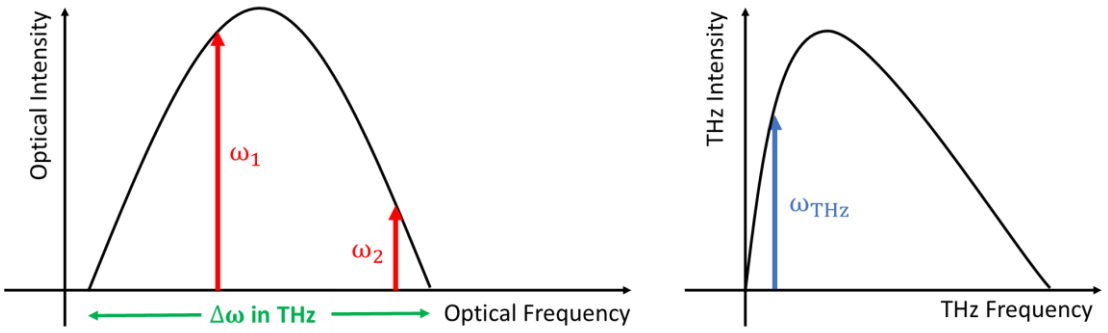

Figure 2.2: Representation of optical rectification for THz generation. A pair of optical frequency components (ω_1 and ω_2) generates a THz component (ω_{THz}) by OR.

The main disadvantage of OR method to generate THz waves is the low power conversion efficiency. The generated THz wave power lies within the range nW~sub-µW [95]. In addition, the efficiency of terahertz radiation also depends on the chosen crystal. The factors affecting efficiency are the nonlinearity of the crystal, absorption coefficient of the incident and THz waves, and the propagation length (coherence length) of optical rectification process [102]. The most commonly used crystal to generate THz waves is ZnTe (zinc telluride) because the optical group velocity roughly matches with the terahertz phase velocity at 800 nm [103]: therefore, each molecule of the crystal contributes additively to the THz generation. There are also other crystals commonly used [104]. For example, terahertz radiation with a bandwidth from 5 to 41 THz was generated by exciting with 50 fs pulses a GaSe crystal [105]. When working at 1.5 µm, DAST and other organic crystals exhibit a huge conversion efficiency, due to both a large nonlinearity and phase-matching [106,107]. Despite of the low power efficiency conversion of OR method, the signal-to-noise ratio (SNR) with an extreme bandwidth (up to 50 THz) can be as high as 5000/1 [95].

2.1.2 Photoconductive (PC) antenna

Photoconductive antennas (PC Antennas) are the most common way to generate (and detect) broad band THz waves, and the most efficient one at low power. They were first introduced by Auston and Smith in 1983 [108]. The classical dipole antenna structure proposed by Grischkowsky [109] consists of two metal electrodes (usually gold or aluminium) at the centre of a coplanar waveguide deposited on a semiconductor substrate as illustrated in Figure 2.3. The metal electrodes are separated with a photoconductive gap (PC gap) which is typically 5 – 10 µm wide [2].

Under the laser illumination in the PC gap between the metal electrodes, pairs of electron hole are photo-generated if the photon energy of the laser pulse is higher than the band gap of the semiconductor. These free carriers are accelerated by the electrical field induced a bias voltage (V_{bias}) applied to these electrodes [110] (see Figure 2.4). The bias electric field energy is stored in this gap, so the laser pulses serve as transient switches that release the energy in this region in a form of electromagnetic pulses. That is why it is important to use short laser pulses in terms of switch-on time and a short carrier life time for the switch-off time [2], in view of getting picosecond electromagnetic pulses whose spectrum spreads up to the THz range. Usually, low temperature-grown gallium arsenide (LTG-GaAs) is used as semiconductor material because its short carrier life time improves the response

speed of PC antenna [111], and their high carrier mobility and high voltage breakdown make them delivering high peak power THz pulses.

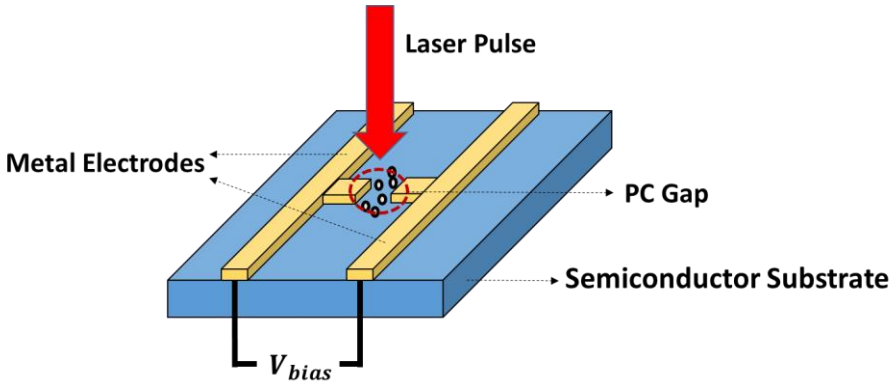

Figure 2.3: Schematic of a biased PC Antenna. Laser pulses generate carriers in the PC gap where there are accelerated by the bias voltage.

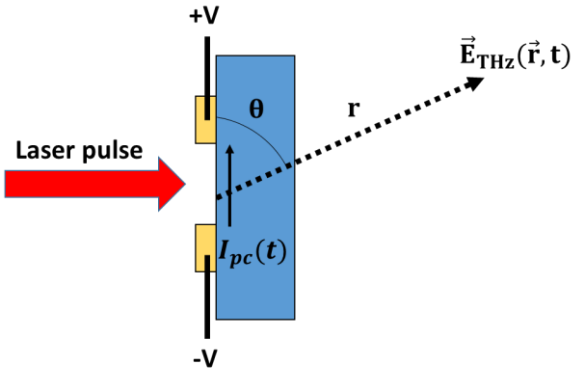

Figure 2.4: The side view of PC antenna with the radiated THz electric field

The THz electric field is proportional to the photocurrent $I_{PC}(t)$ generated between the metal electrodes. The THz electric field radiation is described at a distance r and time t [2]:

$$\vec{E}_{THz}(t) = \frac{\mu_0 w_0}{4\pi}\frac{\sin\theta}{r}\frac{\partial^2}{\partial {t_r}^2}\left(p(t_r)\right)\hat{\theta} \tag{2.8}$$

where μ_0 is the permeability of the free space, w_0 is the spot size of the laser beam, θ is the angle from the direction of the dipole and $p(t_r)$ is the dipole moment of the source at the retarded time ($t_r = t - r/c$, c is the speed of light) which was induced by the photocurrent in the PC gap (see Figure 2.4). In the far field region (r is much bigger than the wavelength of THz field), the radiated THz is proportional to the first derivative of the photocurrent:

$$\vec{E}_{THz}(t) \propto \frac{\partial I_{PC}(t)}{\partial t} \tag{2.9}$$

Time-dependent THz photocurrent ($I_{PC}(t)$) is described as the convolution of the laser pulse temporal shape and the impulse current response of the photoconductive antenna [112]:

$$I_{PC}(\mathrm{t}) = \mathrm{n}(\mathrm{t})\ \mathrm{q}\ \mathrm{v}(\mathrm{t}) = \int I_{laser}(\mathrm{t} - \mathrm{t}')\ \mathrm{q}\ \mathrm{v}(\mathrm{t}')\ \mathrm{dt}' \qquad (2.10)$$

where $I_{laser}(\mathrm{t})$ is the time-dependent laser pulse intensity profile, q is the electron charge, $\mathrm{n}(\mathrm{t})$ and $\mathrm{v}(\mathrm{t})$ are the density and the average velocity of carriers generated in PC gap, respectively.

The photo-excited zone size (about 10 µm) is much smaller than the THz wavelength (> 50 µm). Therefore, the THz radiates in a wide solid angle. A lens mounted on the semiconductor substrate is used to collimate this radiation and to enhance the THz field density. This lens is made of high-resistive silicon, therefore it overcomes the total internal reflection at the GaAs substrate face, otherwise most of the light would be trapped inside the substrate [113]. Preferably a hyper-hemispherical silicon lens is used (see Figure 2.5), with the illuminated gap located at the lens focus. Due to the rather small size of this lens, diffraction phenomena occur and counterbalance the focusing properties of the hyper-hemispherical lens. It is why a second lens (either a refractive lens made of Teflon or HDPE, or a parabolic mirror) is usually inserted in the setup after the hyper-hemispherical lens to make the THz beam parallel.

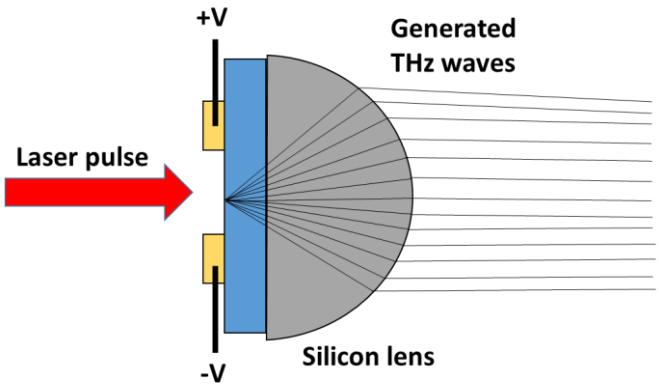

Figure 2.5: The ray diagram of THz wave with a collimated silicon lens

PC antenna exhibits a higher signal-to-noise ratio than rectification-based sources at low THz powers. They are also easy to operate; no need for phase-matching condition and no need for any thermal cooling system, *i.e*. they can operate at room temperature. Therefore, they are widely used for applications based on spectroscopy and imaging [114].

2.2 Detection of terahertz pulses

Terahertz detection devices are divided into two groups: coherent and incoherent detectors [115]. For coherent detection systems, both amplitude and phase of the THz signal are measured. The two most common techniques for these systems are introduced in this section which are electro-optic sampling (Section 2.2.1) and photoconductive antenna (Section 2.2.2) detections. On the other hand, incoherent detection systems allow direct detection of terahertz radiation. They measure the power of the radiation but they do not obtain the phase information of THz light. These detectors have remarkably higher sensitivities and broader bandwidth ranges (see section 2.2.3).

2.2.1 Electro-optic sampling

Electro-optic (EO) sampling is based on the well-known Pockels effect [116], and the first THz detection by this method was demonstrated by Wu and Zhang in 1995 [117]. This effect corresponds to frequency difference between a spectral component of the probe laser pulse at frequency $\omega + \omega_{THz}$ and a spectral component of the THz pulse at frequency ω_{THz}, so that $(\omega + \omega_{THz}) - \omega_{THz} = \omega$. In fact, because $\omega \gg \omega_{THz} \approx 0$, the preceding relation can be approximated by $\omega - 0 = \omega$, which renders for the Pockels effect, *i.e.* a change of the refractive index (rigorously of the index ellipsoid) of a dielectric crystal induced by the impinging THz field. Frequency difference and Pockels effect are second-order nonlinear optical phenomena. Therefore, THz field can be determined by measuring the change in the polarization.

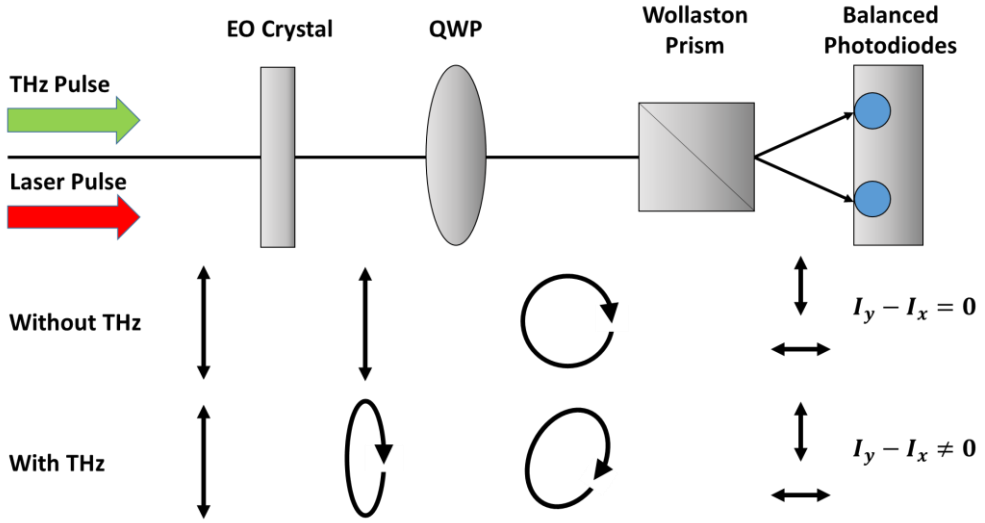

Figure 2.6: Electro-optic sampling

The most common experimental scheme for EO detection of a THz signal is illustrated in Figure 2.6. When there is no applied THz field in the EO crystal, a linearly polarized optical probe beam is made circularly-polarized by a quarter-wave plate (QWP), which can be placed either in front of or behind of the EO crystal. This beam is split into two orthogonal polarizations (x and y axes) by a Wollaston prism before being detected by a balanced-photodiodes system. The x and y components of the intensity in this condition are the same, so the difference in the optical beam intensities is almost zero and the balanced photodiodes give no signal. The application of a THz field to the EO crystal induces a birefringence through the Pockels effect, and now the polarization of the transmitted optical beam becomes elliptical since the two components of the optical field encounter two different phase in transmission because of the crystal ellipticity. The corresponding phase retardation ($\Delta\emptyset$) caused by the impinging THz field is measured for different time delays between the THz field and the optical beam. By varying the time delay, THz waveform can be mapped in time domain (the mapping technique will be discussed in Section 2.3) since the phase retardation is proportional to the THz electric field. The phase retardation is [2]:

$$\Delta\emptyset = \frac{\omega n_0^3 L r_{ij}}{c} E_{THz} \qquad (2.11)$$

where n_0 is the refractive index of the EO crystal at the frequency of the optical beam, L is the thickness of the EO crystal, r_{ij} is one unit EO coefficient in standard crystallographic coordinate system which varies for different crystal classes [97], ω and c are the angular frequency and the speed of light for the optical beam, respectively. The balanced photodiodes measure intensities of x and y components:

$$I_x = \frac{I_0}{2}(1 - \sin(\Delta\emptyset)) \approx \frac{I_0}{2}(1 - \Delta\emptyset) \tag{2.12}$$

$$I_y = \frac{I_0}{2}(1 + \sin(\Delta\emptyset)) \approx \frac{I_0}{2}(1 + \Delta\emptyset) \tag{2.13}$$

where I_0 is the intensity of the optical field. The signal of the balanced photodiodes is the intensity difference measured by the photodiodes, which is directly proportional to the amplitude of THz field as follows:

$$\Delta I = I_y - I_x = \frac{I_0 \omega n_0^3 L r_{ij}}{c} E_{THz} \ \alpha \ E_{THz} \tag{2.14}$$

Several parameters have to be considered and optimized for EO detection system. Firstly, the choice of EO crystal is vital. The most commonly used EO crystal is ZnTe because of velocity matching (THz and laser pulses propagate at the same speed) at 800 nm is almost realized and ZnTe is transparent at both optical and THz beams [103,118], even if its EO tensor coefficient (r_{41} = 4 pm/V [118]) is rather weak. Additionally, the thickness of the crystal has an impact on the detected bandwidth because phase-matching cannot be realized for all the THz frequencies of the broadband THz pulses. Typically, the detection THz bandwidth gets broader with a thinner crystal, as demonstrated for example with a GaP crystal [119]. Lastly, the detected signal depends on the orientation of EO crystal axes and on the polarization angle between the optical and THz beams. For example, for cubic crystals belonging to $\bar{4}3m$ point group, the optimum angle of these two beams are 0° and 90°[120].

2.2.2 Photoconductive antenna

The mechanism of PC Antenna to detect THz field is similar to PC Antenna emitter used to generate THz field [121]. The only major difference of PC Antenna detector from the emitter is that the metal electrodes are connected to a current meter instead of a voltage supplier (see Figure 2.7). Like in PC antenna receiver, the laser pulse illumination in the semiconductor creates charge carriers and allows the PC gap to conduct on a picosecond time scale. This causes a rapid change in the surface conductivity. The incident THz pulse, focused by a silicon lens to the PC gap, accelerates these carriers and gives rise to an electric current (I_d). In case of absence of THz pulse, these carriers recombine, and no current flows through the electrodes. To resolve THz signal, the carrier life time of the semiconductor should be smaller than the THz pulse [2]. Since the same laser is used to generate and to detect THz signal, the current is recorded in the time domain by varying the delay between the laser pulse and THz pulse to obtain THz waveform [47]. The recorded current is quite weak (sub-nA range [2]), so it is necessary to use a current amplifier.

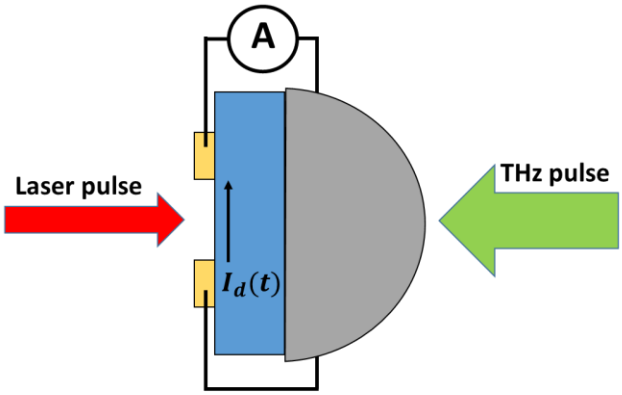

Figure 2.7: Side view of PC Antenna detector. The laser pulse and THz pulse shine onto the detector. The metal electrodes are connected to a current meter.

The detected electric current I_d at a time t is determined by the convolution of THz field E_{THz} and the surface conductivity σ_s [2]:

$$I_d(t) = E_{THz}(t) * \sigma_s(t) = \int E_{THz}(t')\sigma_s(t-t')dt' \qquad (2.15)$$

where t' is delay time between the laser pulse and terahertz pulse, and $\sigma_s(t) = e\,\mu_e\,n'(t)$ (e is the electron charge, μ_e is the constant electron mobility and $n'(t)$ is the time-dependent electron charge density [122]). The response function depends on the carrier life time. If it is very short, the surface conductivity is assumed a delta function. Therefore, the measured current is directly proportional to the amplitude of the THz electric field. In the opposite case, if the surface conductivity is a step function (the carrier life time is longer than the THz pulse), the current is measured as a time integrated THz pulse [110].

The bandwidth of detected THz pulse depends on the combination of the laser pulse duration and the carrier lifetime of the semiconductor. If they are short, the relative maximum bandwidth can be reached. For example, by using a 10 fs laser pulse together with LT-GaAs semiconductor, the bandwidth from 0.1 to 100 THz has been reported [123]. As a summary, there are two main advantages of using PC Antenna as a detector: dynamic range and sensitivity at low THz power. For example, in a THz-TDS system, a 5 THz bandwidth with a 90 dB dynamic range was demonstrated by using a PC antenna detector (LT-grown beryllium-doped InAlAs/InGaAs multilayer hetero-structure) [124]. The studies on PC Antenna show that this technique remain popular in detecting terahertz field.

2.2.3 Intensity measuring detectors

In the systems where narrowband THz pulses are detected, mostly incoherent detectors such as bolometers, Schottky diodes, nanotransistors, Golay cells, etc., are used [125,126]. These detectors directly measure the intensity of the THz radiation. They have sensitive components that absorb THz radiation, either by electron transition through a potential barrier, or by changing their physical properties via thermal energy.

Schottky diode is formed as metal-semiconductor junction which creates a potential energy barrier called Schottky barrier. Its working principle is based on carrier transport mechanism. When

the THz field has a sufficiently high energy, the electrons can cross the barrier. Advantages of using Schottky diodes detectors: they are capable of operating at room temperature and have a fast response time comparing to micro-bolometers and Golay cells [126]. Schottky diodes are also commercially available with different performances [127]. Its voltage responsivities typically ranges from 1000 to 4000 V/W [128]. They are sensitive for the frequency range from 0.1 to 1 THz with a noise equivalent power (NEP) of 11 $\mathrm{pW}/\sqrt{\mathrm{Hz}}$ [126]. The diodes operated at zero bias reduce the shot noise and improve the signal-to-noise ratio [129]. Nowadays, nanotransistors, *i.e*. field-effect transistors whose channel size ranges in the nanometer scale, become more and more popular, because they allow to manufacture sensor array for THz video camera applications, and they exhibit a rather good sensitivity. The incoming THz field, which is coupled to the electrodes of the nanotransistor, modifies the source-drain voltage and thus the mobility of the carrier. Simultaneously, it modulates the drain voltage. These both effects, together with plasma resonances in the channel at higher frequencies, combine to produce a rectified signal proportional to the THz intensity.

Other detection methods for THz radiation are based on thermal effect. The energy of THz radiation is sensed by an absorber which is attached to a resistive thermometer. The resulting temperature variation is converted to a change of electrical resistance by the thermometer. Then this change is read by an electronics that is calibrated in view of giving the absolute power of the incident radiation [130]. Absorption of the THz beam in the absorbing material is very broadband and extends up to the IR domain. These detectors are quite slow because of their dependence on the heating process. Such devices operate either at room or cryogenic temperatures. The latter include Hot Electron Bolometers (HEB) and Transition Edge Sensors (TES) which exhibit record high sensitivity [131]. The typical NEP can be as low as 5 x 10^{-20} $\mathrm{W}/\sqrt{\mathrm{Hz}}$ for TES [132]. Kinetic Inductance Detectors (KIDs) are also cryogenic detectors that show an amazing sensitivity. In principal, KIDs, under photon illumination, measure the change in quasi-particle density resulting from the breaking of Cooper pairs in the superconducting resonators at sub-Kelvin temperature[133,134]. This gives rise to the increase of kinetic inductance. However, the population of quasi particles are practically small. Therefore, a microwave resonant circuit is fabricated to sense this variation. The resonance frequency shift is proportional to the power of the incident radiation, and is measured by a dedicated electronics. Its NEP is $\sim 10^{-17}$ $\mathrm{W}/\sqrt{\mathrm{Hz}}$ [135]. More detail about KID detectors will be discussed in Chapter 3.

Thermal detectors at room temperature include micro-bolometers, pyroelectric detectors, Golay cells, and so on. The responsivity of Golay Cells is quite high (10^5 V/W) but they have a poor time response and can be damaged under strong radiation [126]. Pyoelectric detectors are even less sensitive. Micro-bolometers are interesting because they show a good NEP ($\sim$20 $\mathrm{pW}/\sqrt{\mathrm{Hz}}$) and can be processed as matrices. The related fabrication technology is difficult to handle, nevertheless commercial video-rate THz cameras with more than 1000 pixels are available.

2.3 Terahertz time-domain technique

Terahertz time domain spectroscopy (THz-TDS) is an optoelectronic system for generating and detecting THz pulses, and using them to characterize the response of materials and devices at THz frequencies. Usually, this system consists of a femtosecond laser, a translational stage, a THz emitter and a THz detector. The scheme of typical transmission configuration of THz-TDS is illustrated in Figure 2.8. The detector and emitter of THz pulses were discussed earlier in this chapter. The sample is placed

between parabolic mirrors which focus and collimate the THz waves. Additionally, a lock-in amplifier together with a mechanical chopper are used to improve the signal-to-noise ratio of THz-TDS system.

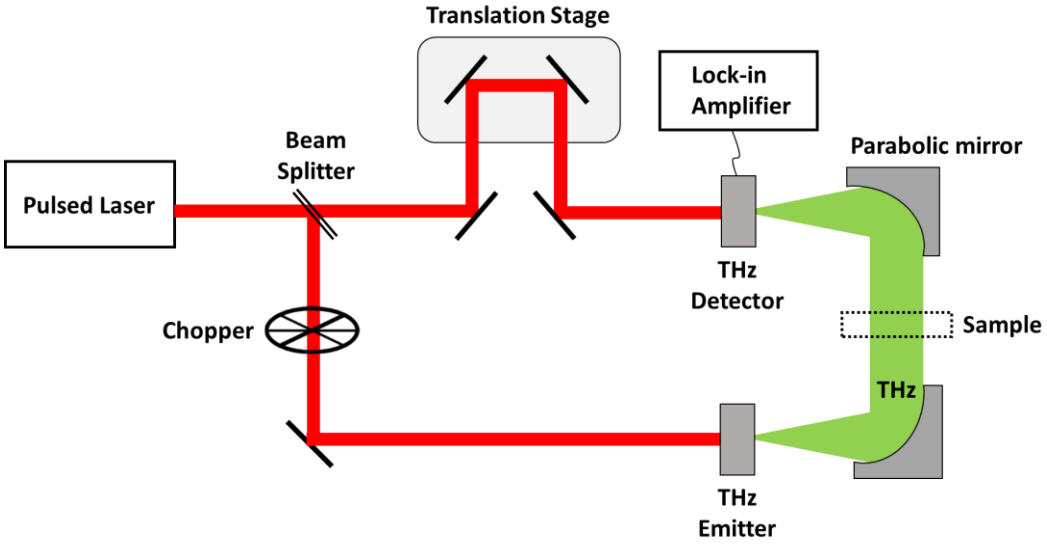

Figure 2.8: Typical THz-TDS system in transmission configuration.

The main idea of THz-TDS system is based on the probe-pump technique. The femtosecond laser pulse is split into two parts; the pump beam is used to generate THz waves in the emitter, while the probe one is used to gate the THz receiver. In the probe line, a translation stage provides relative time delay between the optical and THz pulses. Two beams are mixed in the detector and the THz field is recorded as a function of time by changing the arrival time of the pump beam to the detector in steps of Δt (see Figure 2.9). The time delay is defined by the displacement of the translation stage. The detected THz signal is quite weak, that is why the probe beam is modulated with a mechanical chopper placed before arriving the terahertz emitter. This modulation is read as a reference by a lock-in amplifier. Therefore, the lock-in amplifier can extract the buried signal from a noisy environment.

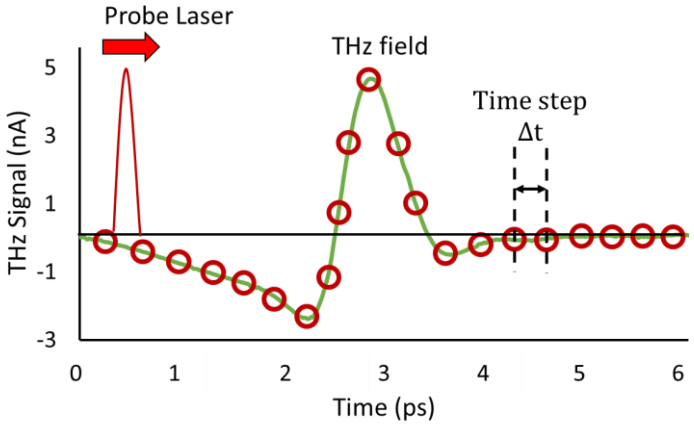

Figure 2.9: Pump-probe scheme. Each Δt steps of THz field is measured with the probe laser.

Since the terahertz field $E(t)$ is obtained in the time domain, a Fourier transform (FT) of this field gives both the amplitude $|E(\nu)|$ and phase $\varphi(\nu)$ of the signal $E(\nu)$ in the frequency domain. The frequency resolution in the frequency domain of THz field is calculated by:

$$\Delta\nu = \frac{1}{N\Delta t} \tag{2.16}$$

where N is the number of data recorded in time domain. Equation (2.16) shows that the spectral resolution is increased if it is scanned longer (more data points).

THz-TDS is applicable for extraction of transmission coefficients of the material in the THz region. THz pulses are recorded two times: with ($E_{sample}(\nu)$) and without the sample ($E_{ref}(\nu)$) [136]. These fields are written as:

$$E_{sample}(\nu) = \left|E_{sample}(\nu)\right|.\, e^{-i\varphi_{sample}(\nu)} \tag{2.17}$$

$$E_{ref}(\nu) = |E_{ref}(\nu)|.\, e^{-i\varphi_{ref}(\nu)} \tag{2.18}$$

where $\varphi_{ref}(\nu)$ and $\varphi_{sample}(\nu)$ are the phase of the signal without the sample and with the sample, respectively. Dividing these THz fields gives the complex transmission coefficient of the sample [137]:

$$T(\nu) = \frac{E_{sample}(\nu)}{E_{ref}(\nu)} \tag{2.19}$$

If the sample is a slab of homogeneous material with flat and parallel faces, the analytical expression of the complex transmission writes:

$$T_{theo}(\nu) = \frac{4(n-j\kappa)}{(n+1-j\kappa)^2} \frac{e^{-j\frac{2\pi\nu}{c}(n-1-j\kappa)d}}{1-\left(\frac{n-1-j\kappa}{n+1-j\kappa} e^{-j\frac{2\pi\nu}{c}(n-1-j\kappa)d}\right)^2} \tag{2.20}$$

Here d is the sample thickness. Determining the refractive index (n) and the extinction coefficient (κ), such as the coefficient of absorption is $\alpha = 4\pi\nu\,\kappa/c$, of the material from the experimental data involves solving the equation:

$$T(\nu) = T_{theo}(\nu) \tag{2.21}$$

Because of the complex exponential terms in Equation (2.20), $T_{theo}(\nu)$ exhibits an oscillatory behaviour that makes tricky to solve Equation (2.21). Smart codes have been proposed, which deliver the spectral curves $n(\nu)$ and $\alpha(\nu)$ with a great precision (see [138]).

2.4 Conclusion

In this chapter, we first introduced the sources used in this thesis for generating THz pulses, and the techniques used to detect these THz pulses. Especially, we have described the generation of THz waves in a nonlinear crystal through optical rectification, which is the process used in one of our methods for subwavelength THz imaging. The other method is based on detecting weak THz waves by using KIDs camera, In the following chapter, the detail of the camera will be presented together with results we obtained when using it as a “classical” TDS setup.

3. Kinetic Inductance Detector and Results

3.1 Superconducting detectors

Due to their high sensitivity and the low noise in the photon measurements, superconducting detectors have become a standard instrument for astronomical research particularly for millimetre and sub-millimetre wavelengths.

In a superconducting material, two charger carriers are present. When the temperature is lower or equal to the critical temperature (T_c) of the superconducting material, the material crystal lattice creates a force between the electrons thus the electrons are bounded in pairs. The bounded electrons are known as Cooper pairs and they carry the current without any resistance. When one of these pairs breaks up by photon absorption or by an increase of temperature of the crystal, it creates two unpaired quasi-particles, and their charge transport is resistive. The number of quasi-particles decreases exponentially when the temperature of the crystal lattice decreases. In a superconducting film, the surface impedance is dominated by the kinetic inductance of the Cooper pairs.

Superconducting detectors are based on different principles:

1. The first demonstration of a detector with a superconducting thermometer was demonstrated in 1942 [139]. In such detectors, an absorber stick against the superconducting material, which is at a temperature close to its critical temperature, absorbs the impinging THz beam energy. This increases the temperature of the superconducting material nearby or over its critical temperature [140]. Because Cooper pairs become de-associated, the resistivity of the material increases strongly as well, and its measurement delivers a value proportional to the impinging THz energy. These devices are named transition edge superconducting sensors (TES). TES detectors can be manufactured as large arrays that can be read by a superconducting quantum interference device (SQUID) amplifier. Although TES is one of the most sensitive detector (NEP of 10^{-20} W/$\sqrt{\text{Hz}}$ in [132]), it is limited by the heat capacity of the absorber and the low multiplexing factors (the number of the sensors for one readout signal) [141].

2. In hot electron bolometers (HEB), the energy of each impinging THz photon is larger than the binding energy of the Cooper pairs in the superconducting material, which must exhibit a low critical temperature. Thus THz photons break the Cooper pairs, which makes the resistivity of the material increase. Generally, the superconducting material is shaped as a bridge whose resistance varies with the illuminating THz power. HEB exhibit performance similar to TES.

3. A third type of superconducting cryogenic detector is the kinetic inductance detector (KID). This inductance depends on the temperature, and it can be used to measure temperature changes in superconducting films, *e.g.*, bolometric detectors [142]. Such detectors need operate close to T_c to determine the rapid change in the temperature variation of the kinetic inductance. However, a small change in the surface impedance Z_s induced by the population of quasi-particles ($\delta Z_s/\delta N_{qp}$) is independent of the temperature if this latter is

far below the critical temperature (approximately $T_c/10$). Such detectors can be integrated into large format arrays. The KID readout is based on the change of the resonant frequency, under illumination, of a circuit that includes the superconducting device. For KID arrays, high multiplexing techniques are employed. KID being the detector we used in this work, we will describe below the KID operation principle in detail.

3.2 Kinetic inductance detectors

The original idea of measuring kinetic inductance effect was first described by Mazin *et al.* in 2002 [143], "*Using kinetic inductance effect to read out the changes in quasi-particle population resulting from the absorption of pair-breaking photons rather than changes in the temperature of the phonons in a bolometric absorber*". Their idea was to use a superconductor material as an inductor in a resonant circuit. Therefore, the inductance in the circuit changes with the increase in the quasi-particle population. This results in the shift of the resonant frequency of the circuit. If all circuits are coupled to a common transmission line and each circuit has its own resonant frequency, it is possible to make large detector arrays [143]. This idea was later experimentally demonstrated by the same team [144,145]. Additionally, they showed that the arrays can be easily fabricated, and each detector can be read on one single transmission line.

A KID is a superconducting thin-film RLC resonator with a resonance frequency (f_0). In principal, a KID, under photon illumination (with an energy of $h\nu$), measures the change in quasi-particle density (n_{qp}) resulting from the breaking of Cooper pairs in the superconducting material below its superconducting critical temperature ($T \ll T_c$). Any photon with an energy greater than the binding energy of Cooper pairs can be measured by KIDs. The increase in the number of quasi-particles changes the complex part of the conductivity (σ_2) which is directly related to kinetic inductance (L_k) and the surface impedance (Z_s). This variation is detected using a microwave resonant circuit with a high quality factor (Q factor). The photon illumination leads to a shift in the resonance. Either the amplitude or the phase of the resonance, and their induced changes, can be measured in transmission, as shown in Figure 3.1. KIDs can be designed to make a multiplexing array in which all the resonators are electromagnetically coupled to a transmission line. The array design of KIDs is controlled in terms of geometry and number of resonators; all these resonators are set to discrete resonant frequencies.

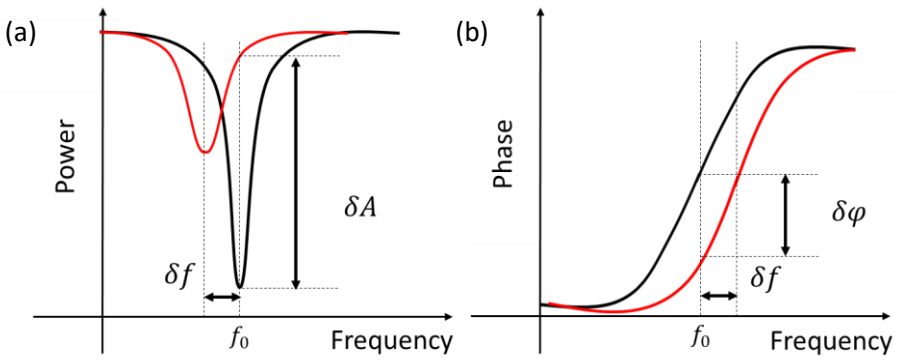

Figure 3.1: Measured transmitted amplitude (a) and phase (b) for one detector. f_0 represents the resonance frequency under dark condition (black lines). Photon absorption by the detector, the resonances are shifted a change in amplitude δA and in phase $\delta\varphi$ (red lines)

3.2.1 Kinetic Inductance Detector Properties

3.2.1.1 Conductivity

In a superconductor, electrons with opposite momentum can be bounded two-by-two, which form Cooper pairs, when the temperature T below the critical temperature T_c [146]. The binding energy of these pair is:

$$2\Delta \approx 3.5\, k_B\, T_c \tag{3.1}$$

where k_B is the Boltzmann constant. According to the famous BCS theory [147], the supercurrent is carried by Cooper pairs in the superconductor. These pairs have no resistance against dc electric field. However, under ac field, the impedance of the system is not zero and depends on the percentage of electrons that are not coupled, *i.e.* of the percentage of quasi-particles. These particles can already exist in the superconductor or can be generated by breaking up Cooper pairs when the incoming radiation energy is higher than the binding energy of these pairs at $0 < T < T_c$ (see Figure 3.2). The result of the population of quasi particle is:

$$N_{qp} = \frac{\eta h\nu}{\Delta} \tag{3.2}$$

where $\eta \approx 0.57$ is the efficiency to convert a Cooper pair into two quasi-particles with a photon energy $h\nu$ [148]. A commonly used metal film for KID is aluminium. As it is shown in Figure 3.2 , the energy of photon should be larger than the binding energy of Cooper pairs, *i.e.* $h\nu > 3.5\, k_B\, T_c$. For aluminium, the critical temperature is approximately 1.3 K so the minimum frequency can be detected with KIDs is roughly 100 GHz [149].

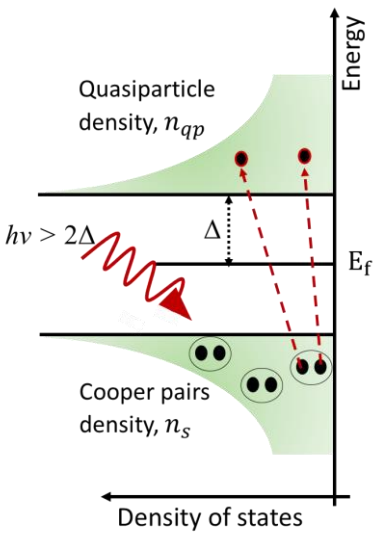

Figure 3.2: A photon whose energy is higher than 2Δ breaks the Cooper pairs and generate two quasi-particles. The density of Cooper pairs n_s and quasiparticles n_{qp} are changed inversely.

The density of quasi-particle n_{qp} depends on the temperature and the frequency. The population of the particles decreases from the total number of electron n_n to 0 when the temperature is down to T_c. Hence, the density of Cooper pairs increases, $n_s = n_n - n_{qp}$. The density changing of quasi-particles and Cooper pairs effect the surface impedance and correspondingly the complex conductivity of the superconductor. According to the two-fluid model, the current can flow through two paths, one path is with the quasi-particles and the other one is with the normal electrons [150]. Therefore, the complex conductivity in an electromagnetic field with an angular frequency ω is expressed [151]:

$$\sigma = \sigma_1 - j\sigma_2 = \frac{n_n e^2 \tau_n}{m_e} - j\frac{n_s e^2}{m_e \omega} \tag{3.3}$$

where m_e is the effective mass of an electron, e is the charge of an electron and τ_n is the electron-phonon relaxation time. In Eq. (3.3) , it is seen that the real part σ_1 is due to the normal component and the imaginary part σ_2 is the superconducting component of the material.

3.2.1.2 Kinetic inductance

The applied field in a superconductor strip can be stored in two different ways. One way is the magnetic energy stored in magnetic field ($\vec{H}$) because of the induced current (I):

$$E_m = \frac{1}{2}\mu_0 \int_V \vec{H}^2 dV = \frac{1}{2} L_m I^2 \tag{3.4}$$

where V is the volume of the superconductor and L_m is the magnetic inductance which is composed of:

$$L_m = L_{m,int} + L_{m,ext} \tag{3.5}$$

$L_{m,int}$ is the internal magnetic inductance which depends on the penetration depth of the field into the superconductor. $L_{m,ext}$ is the external magnetic inductance which originates from the magnetic field around the conductor. $L_{m,ext}$ is a geometric inductance because it is determined by the geometrical properties of the superconductor such as its length and cross section.

The other way to store energy is through the kinetic energy, E_{kin}. As it has been described before, the supercurrent is carried by Cooper pairs. When the electric field is assumed to be close to the surface of a superconductor, the Cooper pairs are accelerated by this field. The storage energy from the field is converted into the kinetic energy of Cooper pairs. As the superconductors are not dissipative, they release the stored energy in the opposite direction of the supercurrent, *i.e.* this energy is inductive and helps to provide the same supercurrent J_s [144]:

$$E_{kin} = \int_V \frac{m_e n_s \upsilon_0^2}{2} dV = \frac{m_e}{2 n_s e^2} \int_V J_s^2 dV = \frac{1}{2} L_{kin} I^2 \tag{3.6}$$

where υ_0 is the average velocity of the charge carriers, n_s is the Cooper pair density, J_s is the supercurrent ($J_s = n_s e \upsilon_0$) and L_{kin} is the kinetic inductance. As a result, the total inductance of the device is:

$$L_{total} = L_{kin} + L_{m,int} + L_{m,ext} \tag{3.7}$$

According to Eq. (3.6) , if the number of Cooper pairs decreases under the effect of photon absorption or due to the increase in the temperature in superconducting material, the value of the kinetic inductance increases. Therefore, the reactance part of the surface impedance Z_s increases because of the increase in the kinetic inductance. The relationship between Z_s and L_{kin} is the following:

$$Z_s = R_s + jX_s = R_s + j\omega L_{kin} \tag{3.8}$$

where R_s is the surface resistance. Surface impedance depends on the thickness of the superconducting film layer. Thickness of the film (d) is considered thin if d is much smaller than London penetration depth (λ_L, which is the distance that the magnetic field can penetrate into the superconducting material), otherwise the film is thick when $d >> \lambda_L$. For a thin film, the surface impedance is calculated as [152]:

$$Z_s = \frac{\sigma_1}{({\sigma_1}^2 + {\sigma_2}^2)d} + j\frac{\sigma_2}{({\sigma_1}^2 + {\sigma_2}^2)d} \tag{3.9}$$

3.2.1.3 Resonators

A KID has a superconducting resonant circuit where the resonator properties are affected by the change in surface impedance because of the incident photons. The change in surface impedance can be measured in amplitude, phase and resonance frequency. There are two types of commonly used KIDs: Microwave Kinetic Inductance Detectors (MKIDs) [144] and Lumped Element Kinetic Inductance Detectors (LEKIDs) [153]. The fabrication of multiplexing many resonant circuits are different for MKIDs and LEKIDs. For MKID, the multiplexing is achieved by using quarter-wave resonator, while for LEKID it is achieved by using discrete capacitors in each resonator circuit. The detector used in this work is lumped parallel resonator circuits, so the essentials of these circuits will be explained in the following.

3.2.1.3.1 Parallel RLC circuit

The parallel lumped resonators consist of a resistor (R), an inductor (L) and a capacitor (C), as shown in Figure 3.3. For each element in the circuit, applied voltage (V) is same but the current (I) is different.

The Kirchhoff's law applied to the circuit for a voltage oscillating at the angular frequency ω leads to:

$$I = V\left(\frac{1}{R} + \frac{1}{jL\omega} + jC\omega\right) = \frac{V}{Z} = GV \tag{3.10}$$

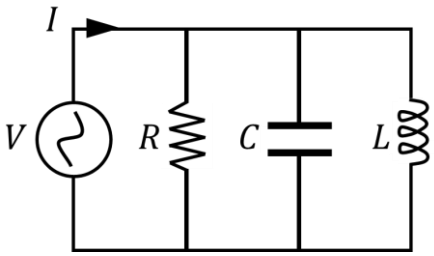

Figure 3.3: Parallel RLC circuit

The conductance *G* is maximum when:

$$\omega = \omega_0 = 2\pi f_o = \frac{1}{\sqrt{LC}} \tag{3.11}$$

where f_0 is the resonance frequency. In the LEKID circuit, the inductance L is in fact L_{total} (see Equation (3.7)). Thus:

$$\omega_0 = 2\pi f_o = \frac{1}{\sqrt{L_{total}C}} \tag{3.12}$$

When the frequency *f* of the voltage approaches f_0, the energies stored in the capacitor (W_C) and in the inductor (W_L) are equal:

$$W_C = \frac{1}{2}C < V^2 >= \frac{1}{4}CV^2 = W_L = \frac{1}{2}L < I^2 >= \frac{1}{4}LI^2 \tag{3.13}$$

At the resonance, the circuit impedance is:

$$Z_{RLC} = \left(\frac{1}{R} + \frac{1}{jL\omega_o} + jC\omega_o\right)^{-1} = \left(\frac{1}{R} - j\sqrt{\frac{C}{L}} + j\sqrt{\frac{C}{L}}\right)^{-1} = R \tag{3.14}$$

Any increase in the kinetic inductance decrease the resonant frequency in KIDs. These changes are proportional to the number of generated quasiparticles. Therefore, the resonant shift measures directly the energy of the incident radiation ($h\nu$) [154]. Nearby the resonance frequency of the circuit, and defining the shift $\Delta\omega = \omega - \omega_0$, Equation (3.14) becomes [153]:

$$Z_{RLC} \approx \frac{R}{1 + 2j\Delta\omega RC} = \frac{R}{1 + 2jQ_i x} \tag{3.15}$$

where $x = \Delta\omega/\omega_0$, Q_i is the internal quality factor for the circuit (see Section 3.2.1.3.2).

The KIDs are multiplexed on the same transmission line: this operation is possible because all the resonators have unique resonance frequencies ($f_1, f_2, \ldots, f_n$) by changing the capacitor values in the circuits (see Figure 3.4). The measurements are performed by the complex transmission scattering parameter S_{21}, which represents the transfer function of the measured signal. S_{21} is the ratio between

the input and output signal of the transmission line and has a real ($Re(S_{21})$) and an imaginary ($Im(S_{21})$) parts. The amplitude and phase transmission are [134]:

$$A = \sqrt{\left(Re(S_{21})\right)^2 + \left(Im(S_{21})\right)^2} \tag{3.16}$$

$$\varphi = atan\left(\frac{Im(S_{21})}{Re(S_{21})}\right) \tag{3.17}$$

Figure 3.5 shows the transmission through S_{21} parameters of an array of 132 resonators which are coupled to a single transmission line. The system is excited by a RF source and S_{21} is plotted here on a limited frequency range. All the sharp dips in Figure 3.5 are different resonances.

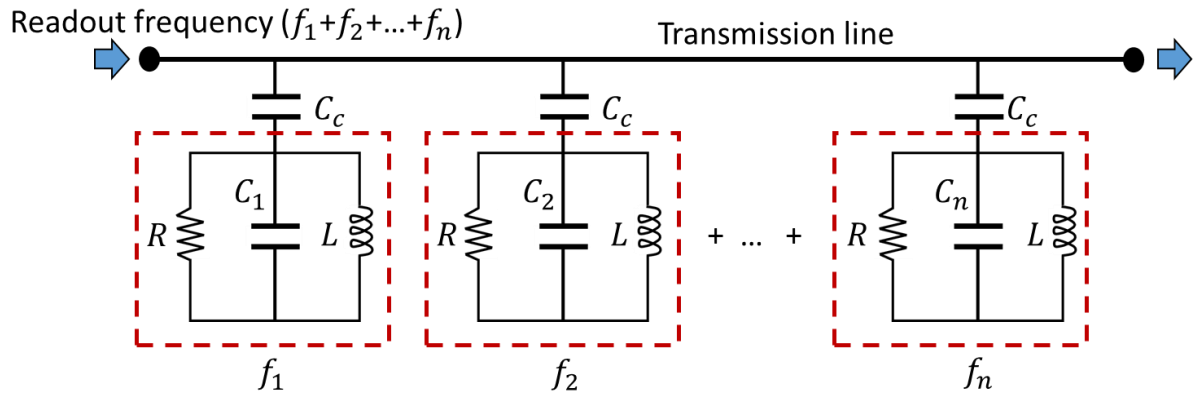

Figure 3.4: Circuit diagram for multiplexed LEKIDs with n resonators. Each parallel resonant circuit (red dashed line) are coupled to a transmission line. In the circuits, the inductance part is not changed, the resonance frequencies are varied with different capacitors ($C_1, C_2, \dots, C_n$).

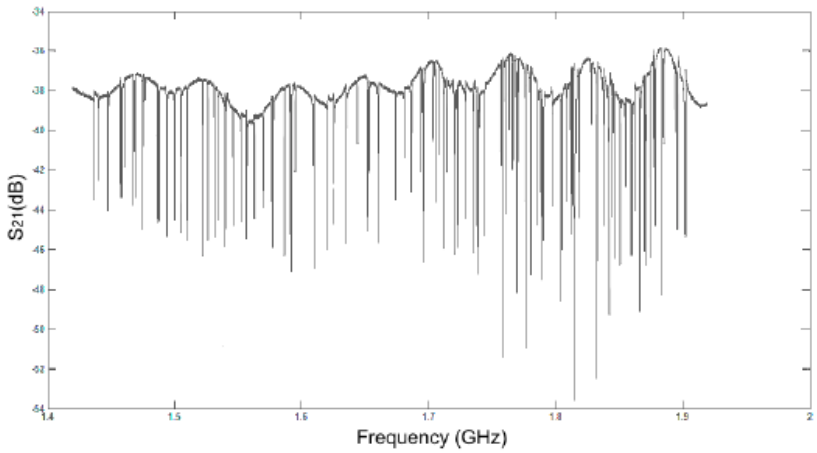

Figure 3.5: Experimental spectrum of the transmission scattering parameter (S_{21}). There are 129 resonances detected [155].

3.2.1.3.2 Quality factor

The quality factor Q is a dimensionless factor which is the ratio between the average energy stored in the resonator and the average dissipated power in the resistance. The internal quality factor Q_i of a resonator is:

$$Q_i = \omega_0 \frac{average\ energy\ stored}{average\ dissipated\ power} \tag{3.18}$$

The summation of the energy stored in the capacitor and inductor is the average energy stored in the RLC circuit, while the energy loss is equal to $< V^2 > / R = \frac{1}{2} V^2 R$. Since the voltage cross the capacitor and the inductor in the parallel circuit is same, the stored energy is $2W_C$. Therefore, the quality factor is:

$$Q_i = \omega_0 \frac{\frac{1}{2} CV^2}{\frac{1}{2} V^2 R} = \omega_0 RC \tag{3.19}$$

When the resonators are coupled to a transmission line as shown in Figure 3.4, there is an additional external impedance effect to the circuits. Therefore, the total quality factor is defined as:

$$\frac{1}{Q} = \frac{1}{Q_i} + \frac{1}{Q_C} \tag{3.20}$$

This new factor is called the coupling quality factor (Q_C), and it will add loss in the circuit. The value of Q_C depends on the coupling strength to the transmission line. The sensitivity of a resonator is determined by the performance of a high quality factor. High Q_C value means that low power is lost from the resonator to the transmission, so less coupling strength. Additionally, Q_i is associated with the superconducting film quality. Low dissipation in the resonator can be obtained by high Q_i value.

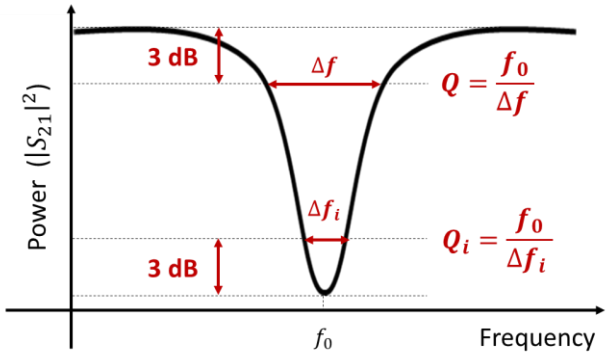

Figure 3.6: Representation of a typical resonance dip coupled to a transmission line. The different quality factors are determined by this curve.

The quality factors can be obtained from the S_{21} parameter. In Figure 3.6, the resonance frequency of the resonator coupled to a transmission line appears at the frequency f_0, and Δf is frequency bandwidth of the resonance at the classical half power bandwidth of a resonator (half of

the minimum value of $|S_{21}|^2$) which is used to calculate the value of Q. Similarly, Q_i is calculated from the frequency bandwidth of Δf_i.

KID unique design together with a high quality Q (up to a million [144]) provide a high sensitivity to variations in the number of quasi-particles. The increase in quasi-particles population under illumination is directly read out by the change in the inductance. The changes trigger measurable frequency shift in resonators. In practice, measurements are made up by monitoring the change in transmitted amplitude and phase of the fixed resonant frequency. The sensitivity of KID device depends on several parameters: choice of superconducting material, geometry of device, film thickness but not only. Material choice affects directly the sensitivity of the device in terms of cut off frequency and intrinsic device noise. The cut off frequency is determined by using Equation (3.1). Generally, aluminium film is used because of low cut off frequency (100 GHz). However, development of TiN films shows the increase in sensitivity by providing high kinetic inductance (NEP of $10^{-19}\ \mathrm{W}/\sqrt{\mathrm{Hz}}$) [156]. The sensitivity of KID increases with its quasi-particles lifetime, which is the average time at which quasi-particles remain at up energy level before forming a Cooper pair. This parameter depends not only on the material, but also depends on the film thickness and the quality of the deposition process during the fabrication [157]. The noise in a KID can be either intrinsic, because of random generation and recombination of quasi-particles, or can be extrinsic because of the readout electronic chain.

3.3 Interest of using KIDs for THz microscopy/imaging

As already explained in the introduction of this manuscript, nonlinear second order optical phenomena can occur in samples whose exhibit some non-centro-symmetric crystallinity as well as a nonlinear responsivity of their molecules. These phenomena include second harmonic generation (SHG) and THz optical rectification (OR), which occur simultaneously in the material as they originate in the square of the exciting laser field. If this latter has a central optical frequency ω_{laser}, we can write:

$$\vec{\mathrm{E}}_{\mathrm{laser}}(\vec{\mathrm{r}},\mathrm{t}) = \vec{\mathrm{E}}_{\mathrm{laser}}(\vec{\mathrm{r}})\cos(\omega_{\mathrm{laser}}\mathrm{t}) \tag{3.21}$$

Therefore, the square of the laser field is by following to second order nonlinear phenomena is:

$$\vec{\mathrm{E}}_{\mathrm{laser}}{}^{2}(\vec{\mathrm{r}},\mathrm{t}) = \vec{\mathrm{E}}_{\mathrm{laser}}{}^{2}(\vec{\mathrm{r}})\cos^2(\omega_{\mathrm{laser}}\mathrm{t}) = \vec{\mathrm{E}}_{\mathrm{laser}}{}^{2}(\vec{\mathrm{r}})\frac{1+\cos(2\omega_{\mathrm{laser}}\mathrm{t})}{2} \tag{3.22}$$

In this expression, the first and second terms of the ratio corresponds respectively to OR and SHG. Therefore, any material that permits the generation of SHG will also produce THz waves through OR. However, the efficiency of the nonlinear generation depends on the properties (refractive index and mostly absorption) of the materials at the generated nonlinear frequency (*i.e.* at SHG frequency or at THz frequency), as well as possible phase-matching. These values differ strongly in the visible and THz ranges. Thus it is expected that SHG and THz OR will deliver very complementary information on the sample.

The photon energy conservation in the related nonlinear phenomena is given by:

$$\begin{aligned} \hbar\omega_{laser} + \hbar\omega_{laser} &= \hbar\omega_{SHG} \\ \hbar\omega_{laser,1} - \hbar\omega_{laser,2} &= \hbar\omega_{THz} \end{aligned} \tag{3.23}$$

Each time a SHG photon is generated, a THz photon is generated as well. Because $\omega_{laser} \approx 1000 \times \omega_{THz}$, the energy of the THz photon is 1000 times weaker than the SHG one. Even if all the other parameters (phase matching condition, absorption, etc.) of the nonlinear interaction would have been the same, the generated THz signal would be 1000 weaker than the SHG one. When studying real heterogeneous materials in which the nonlinearity is weak and/or phase-matching is not realized, the efficiency of nonlinear generation becomes extremely small. In SHG experiments, this is compensated by using highly sensitive detectors, *i.e*. photomultiplier tubes, together with photon counting techniques, if necessary. For example, this is routinely applied to produce SHG or even THG (third harmonic generation) images of biological tissues [158]. This is a very popular technique used in hospitals and laboratories, and the images can be obtained with a superior quality. One study showed that the membranes of biological cells are strongly symmetrical thus generates a powerful SHG signal [159]. However, there are some liquid parts in the cells cannot be imaged by generating SHG signal due to their amorphous structure. Typically, in SHG imaging of biological samples, laser beams are focused onto the sample at the limit of diffraction (~0.5 µm), with average power of the order of 10-20 mW. With a pulse duration of 100 fs and a repetition rate of 100 MHz, this corresponds to a peak power density of 40 GW/cm^2. With such an exciting laser beam, one SHG photon is generated per pulse, *i.e*. 10^8 per second (~50 pW of average SHG power). If we assume the same conversion efficiency for THz OR, the average THz power is about 50 pW over 1000 (see above), *i.e.* 50 fW. Only cryogenic superconducting detectors exhibit the requested sensitivity performance. Indeed, standard THz-TDS system show a NEP of $0.6{\sim}6 \times 10^{-13}$ W/$\sqrt{\text{Hz}}$ which is equivalent to a minimum detectable power of $0.1{\sim}1$ pW with a 300 ms integration time [160]. Among superconducting THz detectors, the NEP of KIDs can be as low as 10^{-20} W/$\sqrt{\text{Hz}}$ [161] when installed in earth-based telescopes. KIDs have already been employed for passive THz imaging for security, but are generally used for astronomical research [162].

Thanks to our collaboration with the team of A. Monfardini at the Institut Néel in Grenoble, in the framework of the Labex FOCUS, we have access to a KID camera. We will perform some preliminary original tests of the use of such a camera to detect THz pulses delivered by a THz-TDS system, in order to demonstrate that a KID camera could be employed in THz OR microscopy.

The basic idea of measuring THz pulses with a KID camera is to generate very weak THz signals through OR in ZnTe crystals. Let us evaluate the THz power generated in such crystals. Using equations (3.22) and (2.6) the generated THz field in the crystal by two laser fields ($\vec{\mathrm{E}}_\mathrm{i}(\vec{\mathrm{r}},t) = \vec{\mathrm{E}}_\mathrm{i} e^{j(\vec{\mathrm{k}}_\mathrm{i}\vec{\mathrm{r}}-\omega_\mathrm{i}t)}$, $i = 1,2$) is

$$\vec{\mathrm{P}}^{(2)}(\vec{\mathrm{r}},t) = \varepsilon_0 \vec{\vec{\chi}}^{(2)} : \vec{\mathrm{E}}_1(\vec{\mathrm{r}},t)\vec{\mathrm{E}}_2^{*}(\vec{\mathrm{r}},t)\, {T_{laser}}^2 \tag{3.24}$$

where T_{laser} is the amplitude transmission (obtained by Fresnel's equations) of the electric field and equal to:

$$T_{laser} = \frac{2}{1 + n_{laser}} \tag{3.25}$$

In Equation (3.25), n_{laser} is the laser refractive index in the crystal. By solving the nonlinear Maxwell wave equation, THz field at angular frequency ω_{THz} is written inside the crystal [94]:

$$\vec{\mathrm{E}}_{\mathrm{THz}} = -\frac{{\omega_{\mathrm{THz}}}^2}{c^2} \frac{\vec{\vec{\chi}}^{(2)} : \vec{\mathrm{E}}_1 \vec{\mathrm{E}}_2^* \left(1 - e^{j\left(\vec{\mathrm{k}}_{\mathrm{THz}} - \left(\vec{\mathrm{k}}_1 - \vec{\mathrm{k}}_2\right)\right)\vec{\mathrm{r}}}\right)}{{\vec{\mathrm{k}}_{\mathrm{THz}}}^2 - \left(\vec{\mathrm{k}}_1 - \vec{\mathrm{k}}_2\right)^2} e^{-j\vec{\mathrm{k}}_{\mathrm{THz}}\vec{\mathrm{r}}} \left(\frac{2}{1 + n_{laser}}\right)^2 \tag{3.26}$$

By substituting $k = \omega n / c$ into Equation (3.26), the modulus of THz electric field E_{THz} becomes:

$$E_{THz} = \frac{\omega_{\mathrm{THz}}}{c} \frac{\left|\chi^{(2)} : E_1 E_2\right|}{n_{THz} + n_{laser}} \mathrm{sinc}\left(\frac{\omega_{\mathrm{THz}}}{2c}(n_{THz} - n_{laser})r\right) r \left(\frac{2}{1 + n_{laser}}\right)^2 \tag{3.27}$$

where n_{THz} is the refractive index of THz field in the crystal. Until here, we found the generated THz field inside of the crystal. To calculate the THz field outside of the crystal, Equation (3.27) is needed to be multiplied by the transmission coefficient. Finally, it becomes:

$$E_{THz} = \frac{\omega_{\mathrm{THz}}}{c} \frac{\left|\chi^{(2)} : E_1 E_2\right|}{n_{THz} + n_{laser}} \mathrm{sinc}\left(\frac{\omega_{\mathrm{THz}}}{2c}(n_{THz} - n_{laser})r\right) r \left(\frac{2}{1 + n_{laser}}\right)^2 \frac{2n_{THz}}{1 + n_{THz}} \tag{3.28}$$

In the case of phase matching, the refractive indexes of THz field and the laser are equal to $n_{THz} \approx n_{laser} = n$ (in the expression, the limit of $\mathrm{sinc}\,(x) \approx 1$ when x approaches zero), :

$$E_{THz} = \frac{4\omega_{\mathrm{THz}}}{c} \frac{\left|\chi^{(2)} : E_1 E_2\right|}{(1 + n)^3} r \tag{3.29}$$

The THz field is related to the power density $\widehat{D}_{laser}$ and the peak power $\hat{P}_{THz}$. Using Equation (2.5), the THz peak power is expressed as:

$$\hat{P}_{THz} = \frac{\mathrm{S}_{\mathrm{laser}} \left(\hat{E}_{THz}\right)^2}{2\mathrm{Z}} \tag{3.30}$$

where $\mathrm{S}_{\mathrm{laser}}$ is the illuminating area on the crystal. The Equation (3.29) can be written the peak power of the THz field and the peak power of the optical field $\hat{P}_{laser}$:

$$\hat{P}_{THz} = \frac{2\mathrm{Z}}{\mathrm{S}_{\mathrm{laser}}} \left(\frac{4\omega_{\mathrm{THz}}}{c} \frac{\chi^{(2)} \hat{P}_{laser}}{(1 + n)^3} r\right)^2 \tag{3.31}$$

In the OR process, the illuminating laser pulse with a mean laser power $\bar{P}_{laser}$, a pulse duration $\Delta \mathrm{t}_{\mathrm{laser}}$ and a repetition rate τ_{laser} generates THz field in the crystal. The generated THz field has the

same as the one of the laser pulse but the pulse duration of generated THz ($\Delta t_{THz} \sim 1$ ps) is different than the pulse duration of the laser. The mean power of THz field is $\bar{P}_{THz}$:

$$\bar{P}_{THz} = \frac{2Z}{S_{laser}} \frac{\Delta t_{THz}}{\tau_{laser} \Delta t_{laser}^2} \left(\frac{4\omega_{THz}}{c} \frac{\chi^{(2)} \bar{P}_{laser}}{(1+n)^3} r \right)^2 \tag{3.32}$$

To give an example, we can calculate the THz mean power generated in ZnTe crystal ($\chi^{(2)} =$ 3.7 pm/V [163], n~3 [104]). For this example, let us consider the properties of the laser to be used in Institut Néel, which will be introduced in the next section of the chapter: τ_{laser} =250 MHz and Δt_{laser} =100 fs. For the mean laser power of 20 mW with a beam waist of 2 mm on the crystal, the generated mean power of the THz field is calculated 0.5 pW using Equation (3.32). In a common THz-TDS setup, the THz beam is modulated by a chopper to improve the signal-to-noise ratio, so only half of its power is received by the detector, *i.e.* $\bar{P}_{THz} \approx 0.25$ pW. Additionally, if we take into account the absorption and the lack of perfect phase matching, the THz power is reduced by one order of magnitude, *i.e.* 25 fW. Let us continue this calculation by adapting it to an experimental setup detected with the KIDs camera. In this setup, a frequency filter is added to the KIDs camera to detect THz waves. This frequency filter is centred at 0.5 THz with a bandwidth of 35 GHz, as seen in Figure 3.7. The generated THz signal from ZnTe by optical rectification is obtained in our laboratory with the experimental setup will be described in Section 5.1 (black line in Figure 3.7). The integral of the whole ZnTe spectrum is 0.755, and the integration of the filter curve is 0.031. Therefore, the ratio of the total integrals is calculated ~ 25, meaning that only $1/25$ of the THz power is recorded. Therefore, the signal detected with the KIDs should be the order of 1 fW for this example. Other effects can reduce this power such as the transmission coefficient of the THz camera optics. As a conclusion, this mean power is very weak but within the range of the KIDs camera.

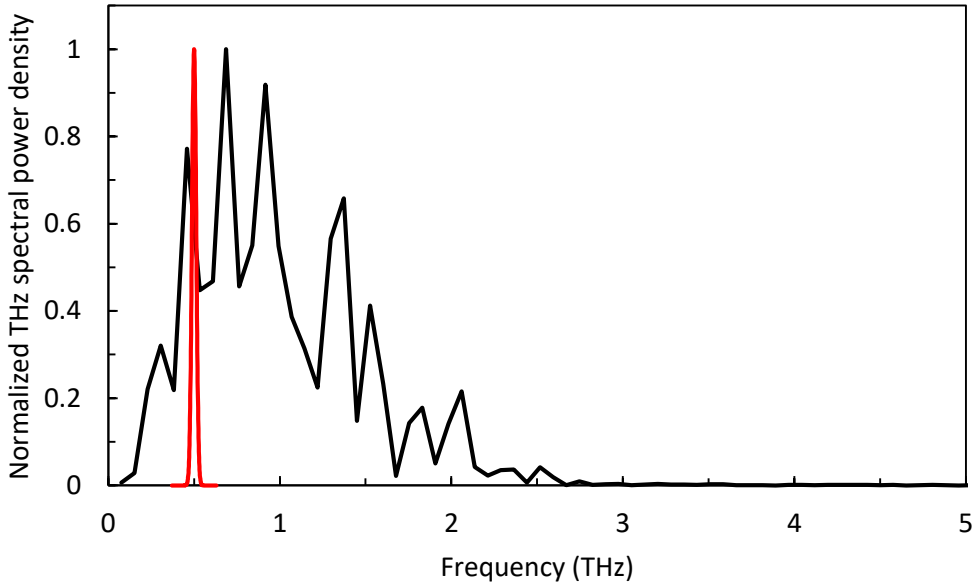

Figure 3.7: Generated THz signal from ZnTe crystal versus frequency (black line) with the transmission of the frequency filter (red line).

3.4 Results for detection of weak THz –TDS signals using KIDs

This study focuses on demonstrating the capability of KIDs to detect pulsed THz signals that are very weak. We used both optical rectification in ZnTe crystal and a PC antenna to generate THz waves. These THz sources pumped by a femtosecond laser generated waves that were detected by using KIDs. The energy of laser pulses was reduced to produce weak THz pulses. The measurements were carried on at Institut Néel in Grenoble, and some complementary experiments were performed at IMEP-LAHC in Chambery such as THz power calibration and investigation of some effects observed for PC antenna. The obtained results were published in the International Journal of Infrared Millimeter and THz Waves [1].

3.4.1 Experiment setup

The detector array used in this work is made of lumped element kinetic inductance detectors [153]. The geometry of each KID consists of the inductive part and an interdigital capacitor coupled to a transmission line as shown in Figure 3.8 [164]. The superconducting film in this detector is aluminium, and the array of aluminium is deposited on a high-resistivity silicon substrate. The array is back-illuminated through the silicon substrate. This method is more advantageous than illuminating the array directly because the silicon substrate has a lower impedance than the free space. This results in enlarging the detection bandwidth [165]. Reducing the aluminium film thickness down to 15 nm increase the KID's response [165]. The detector design of KIDs is based on a Hilbert-shaped inductor, which provides the pixels (KIDs) absorb the incoming photons in both polarizations (the detail of this design can be read in [166]). The KID resonators are 2.2×2.2 mm^2 pixels. The whole array includes $12 \times 12 = 144$ pixels but only 132 pixels are used because the substrate is cut at the corners (see Figure 3.9). The KID array is cooled down at 100 mK and placed with optics in a cryostat. Additionally, the resonance frequency of this array is designed between 0.8 – 1.2 GHz.

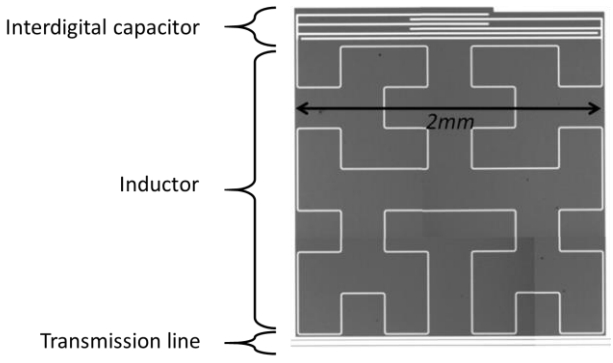

Figure 3.8: The geometric design of LEKID. The inductor part is shaped with Hilbert curve technique. The white line in the image is aluminium film, the grey surface in the image is the silicon substrate. The size of this image is 2x2 mm^2 (Image is taken from [149]).

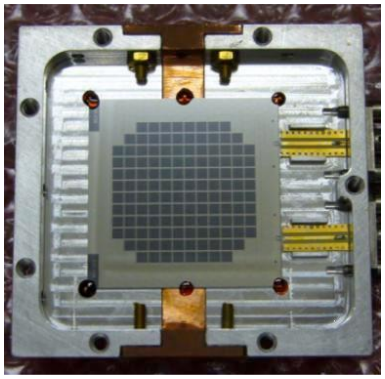

Figure 3.9: Photography of 132 pixels array mounted on its holder [164]

We used two different THz sources for the THz-TDS measurement with KIDs: a commercial photoconductive (PC) antenna and a ZnTe nonlinear crystal. The experimental setup used for the measurements is the same for both sources (red dashed line shows the position of the sources in Figure 3.10). The sources were pumped by a laser (Menlo C-fiber 780) emitting 100 fs pulses at 780 nm with an average power up to 210 mW, at 250 MHz repetition rate. In the setup, the chopper was used to see the magnitude changes in power to avoid background signal on KIDs. Half-wave plate (HWP) together with a polarizer allowed us to change the incoming average laser power exciting the sources, and another HWP was used to rotate the polarization of the laser beam on ZnTe to optimize the THz signal. The generated THz waves from the sources were collected by a $f/2$ teflon lens (diameter 5 cm, focal length 10 cm) and were focused on the KIDs by the $f/1.6$ optics [133]. Additionally, a grid filter from QMC instruments [167], centred at 375 GHz with a bandwidth of 35 GHz, filtered the entering light to the KIDs to detect just the THz waves.

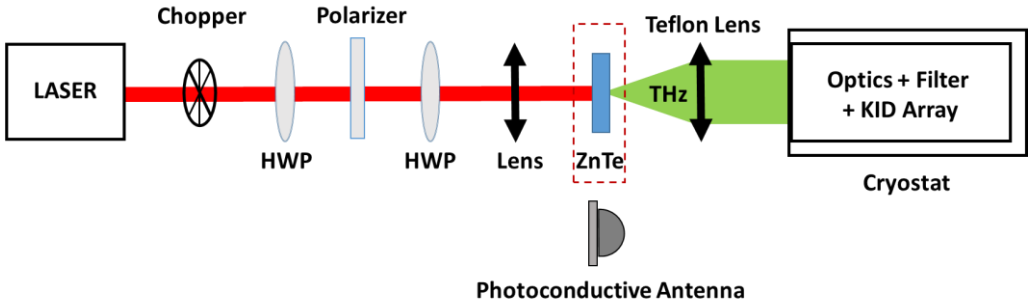

Figure 3.10: Experimental setup for THz-TDS measurement using KID detectors.

In the inside of the cryostat, there are some cold optics to focus the entering light on the KID array. To adapt our experiment setup with these optics, the simulation model (previously prepared at the Institut Néel by using Zemax) was modified by adding the Teflon lens and the THz source (see Figure 3.11). The real image of experimental setup is shown in Figure 3.12.

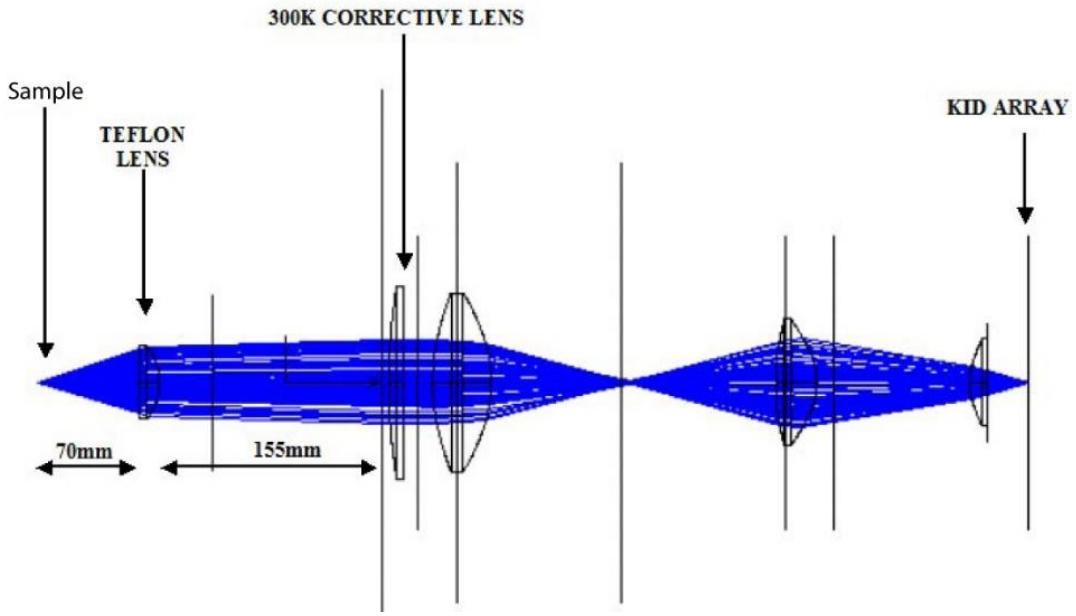

Figure 3.11: Snapshot of Zemax simulation

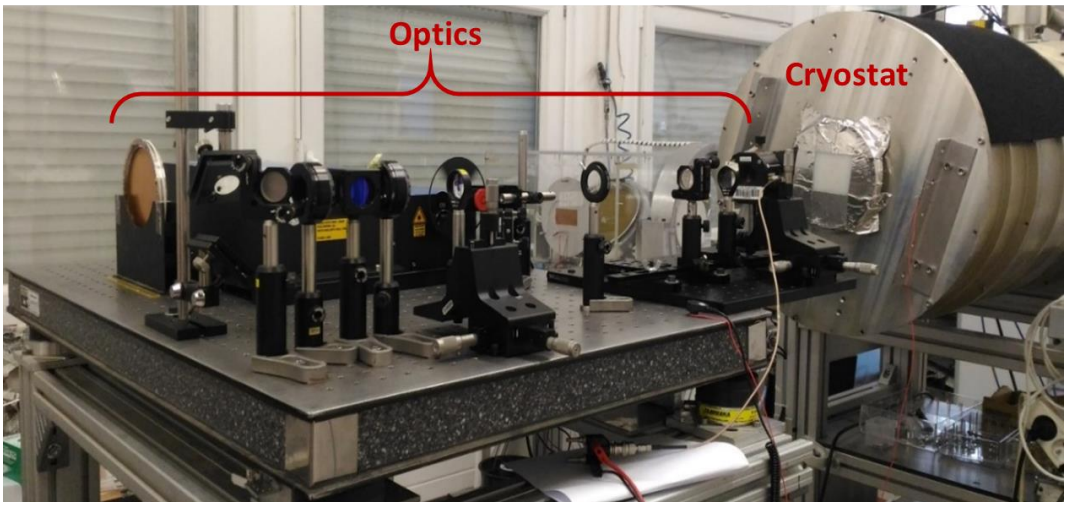

Figure 3.12: Picture of experimental setup.

3.4.1.1 THz Power Measurement with ZnTe crystal

The first experiment was performed with a nonlinear crystal, ZnTe (4.5 mm thickness, <111> crystal orientation). Using the experimental setup described in the previous section, the THz pulses were generated by optical rectification of femtosecond pulses with a beam waist of 2 mm and a mean power of 40 mW on the crystal. The laser beam was modulated at 5 Hz by an optical chopper, so the generated THz signal was modulated as well at the same frequency.

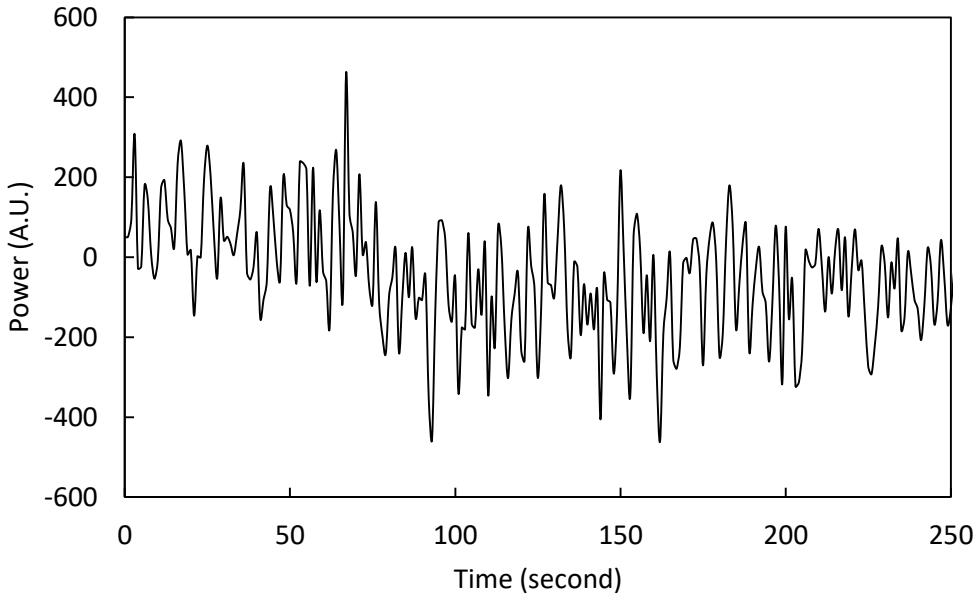

Figure 3.13: Detected THz power in time domain by one pixel in the KID array

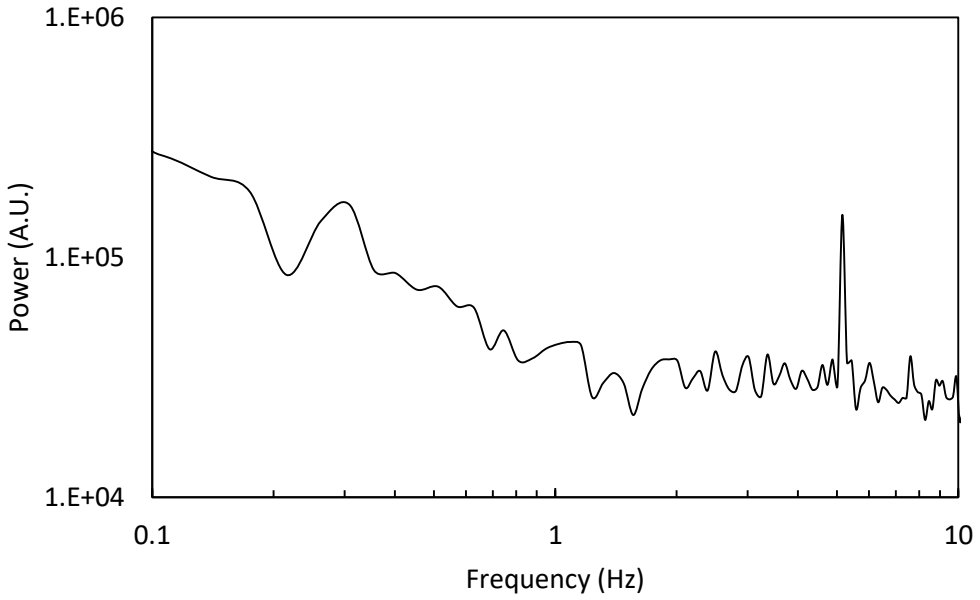

Figure 3.14: Detected THz power in frequency domain by one pixel in the KID array

Figure 3.13 shows the detected THz signal power in time domain by one single KID. The recorded signal is noisy, so the signal was converted into a frequency domain by Fourier transform to see clearly the magnitude changes in power (see Figure 3.14). The noise on the signal might be due to the background variation in the experimental room or the electronics.

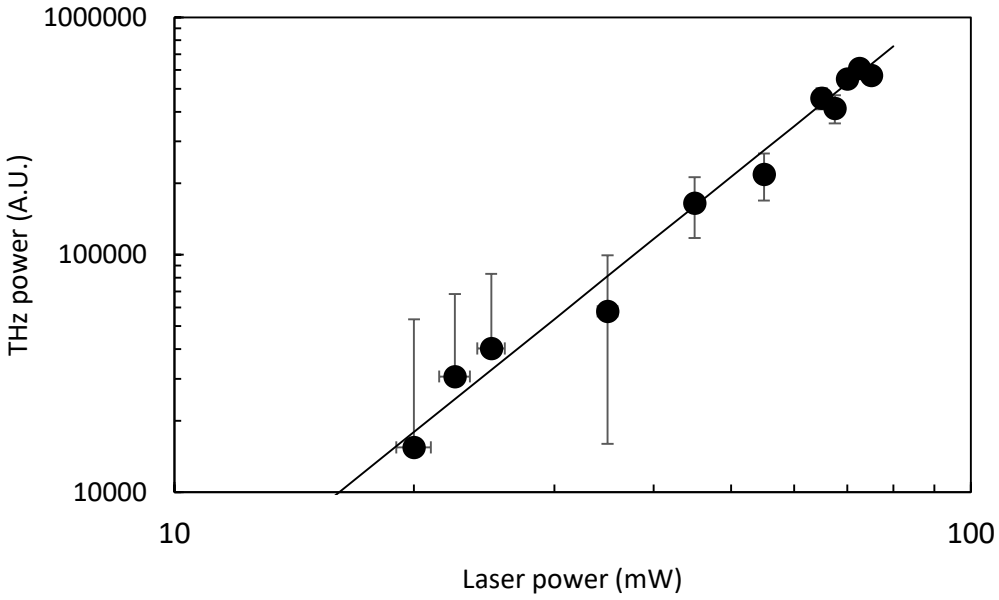

Figure 3.15: Measured average THz power generated by optical rectification in ZnTe for different average laser power

Generated THz power in ZnTe crystal by optical rectification was measured for the different average laser power ranging from 20 mW to 75 mW, and 3x3 pixels of the KID array were illuminated by this THz radiation. The measured power by KIDs are in arbitrary units (see Figure 3.15) but another THz setup bench was used to detect THz power generated from the same crystal to calibrate the power. In this setup which is described in [168], the crystal was pumped by an amplified Ti:sapphire laser (Coherent Libra) that delivers pulses of 45 fs duration with a mean pulse power of 260 mW at 800 nm, and at a repetition rate of 1 kHz. Thanks to the strong radiated THz power, we could record the THz power with a calibrated Schottky diode (VDI model WR1.9ZBD) [169]. To calibrate the power, we use Equation (3.32) to express the average THz powers in both setups. For the mean power of THz signal generated by the ZnTe crystal in the setup including the KIDs camera is:

$$\bar{P}_{THz,KIDs} = \frac{2\,Z\,\eta_{\mathrm{KIDs}}}{S_{\mathrm{laser,KIDs}}}\,\frac{\Delta t_{\mathrm{THz,KIDs}}}{\tau_{\mathrm{laser,KIDs}}\;\Delta t^2_{\mathrm{laser,KIDs}}}\left(\frac{4\omega_{\mathrm{THz}}}{c}\frac{\chi^{(2)}\bar{P}_{laser,KIDs}}{(1+n)^3}r\right)^2 \qquad (3.33)$$

where η_{KIDs} is the quantity representing the percentage of the collected light and the filter, which allows 1/25 of the total THz power (see Figure 3.7). For the other setup with a VDI diode as detector, the THz mean power generated by the same crystal is:

$$\bar{P}_{THz,VDI} = \frac{2\,Z\,\eta_{\mathrm{VDI}}}{S_{\mathrm{laser,VDI}}}\,\frac{\Delta t_{\mathrm{THz,VDI}}}{\tau_{\mathrm{laser,VDI}}\;\Delta t^2_{\mathrm{laser,VDI}}}\left(\frac{4\omega_{\mathrm{THz}}}{c}\frac{\chi^{(2)}\bar{P}_{laser,VDI}}{(1+n)^3}r\right)^2 \qquad (3.34)$$

where η_{VDI} is the responsivity of the VDI diode detector. Finally, the ratio of detected average THz power by VDI diode ($\bar{P}_{THz,VDI}$) and KIDs ($\bar{P}_{THz,KIDs}$) is expressed as:

$$\frac{\bar{P}_{THz,KIDs}}{\bar{P}_{THz,VDI}} = \frac{\eta_{\mathrm{KIDs}}}{\eta_{\mathrm{VDI}}} \frac{S_{\mathrm{laser,VDI}}}{S_{\mathrm{laser,KIDs}}} \frac{\Delta t_{\mathrm{THz,KIDs}}}{\Delta t_{\mathrm{THz,VDI}}} \frac{\tau_{\mathrm{rep,VDI}}}{\tau_{\mathrm{rep,KIDs}}} \left(\frac{\bar{P}_{laser,KIDs}}{\bar{P}_{laser,VDI}} \frac{\Delta t_{\mathrm{laser,VDI}}}{\Delta t_{\mathrm{laser,KIDs}}} \right)^2 \quad (3.35)$$

Equation (3.35) is used to calibrate the THz power measured with the KIDs camera. The calibration was done carefully by taking into account parameters in two experimental setups. The detected THz signal mean power from the ZnTe crystal by VDI diode is 1nW. Figure 3.16 shows the calibrated results on a log-log scale for one pixel with error bars corresponding to experimental standard deviation. The major uncertainties originate from THz pulse durations generated by the different lasers (with a 50% error), the VDI responsivity (with a 50% error), laser beam areas on the crystal (with a 10% error), the filter (with a 10% error), measured THz mean power with VDI (with a 10% error) and other optical uncertainty (with a 20% error). Therefore, the estimated error is roughly 200%. The minimum detected THz average power is calculated to be smaller than 0.2 fW (see Figure 3.16). This results shows how KIDs are very sensitive to detect weak THz waves.

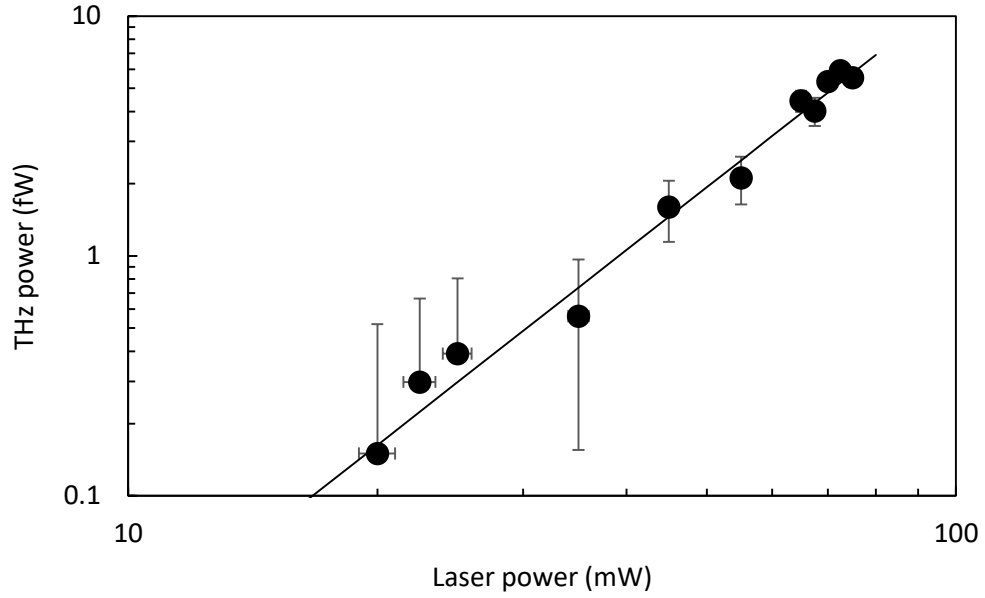

Figure 3.16: Measured average THz power generated by optical rectification in ZnTe versus average laser power.

Theoretically, the power of generated THz waves in ZnTe is directly proportional to the square of the power of the laser beam. As seen in Figure 3.16, the average THz power varies linearly with the average laser power but displays a slope of 2.6 on a log-log scale slightly different from theoretical slope of 2 expected from a square law one (solid line in Figure 3.16). This difference cannot be due to the nonlinear response of KIDs since its dynamic range is about $10^4 \sim 10^5$, *i.e.* its responsivity is linear over the range ~50 fW [170]. Also, only a narrow part of THz spectrum is recorded because the filter bandwidth used in front of the KIDs is 35 GHz. However, the free carriers generated by two-photon absorption can lead to the absorption of THz waves; this results in reshaping the THz pulse and changing the strength of the wave[171,172]. When the crystal is exposed to two-photon absorption, the intensity in the crystal with a thickness of l is given by $I = I_0/(1 + I_0\beta l)$, where β is the nonlinear absorption coefficient and I_0 is the incident intensity [172,173]. In the work of Harrel *et. al,* they

observed two photon absorptions in ZnTe above the excitation fluence of 17 µm/cm^2 [172]. In our experiment, the excitation fluences on the crystal range from 25 - 95 µm/cm^2, which are higher than their value. We then decided to change our THz emitter and used PC antenna whose centred spectrum is 500 GHz, *i.e.* closer to the KID working frequency.

3.4.1.2 THz Power Measurement with PC Antenna

In the second setup experiment, we replaced the ZnTe crystal with another THz source: a GaAs-based PC antenna from the Teravil company. In this method of THz generation, the laser beam is focused on the gap between two electrodes deposited on the PC antenna with a $f = 5$ cm lens. Then generated photocarriers are accelerated by applying a bias voltage to the electrodes. Since the carrier lifetime of GaAs is in the sub picosecond range, generated waves result in terahertz frequency (the details of this THz generation is in Section 2.1.2). The generated THz waves were collected by a silicon hyper-hemispheric dome attached to the GaAs wafer and directly detected by using KIDs as described before.

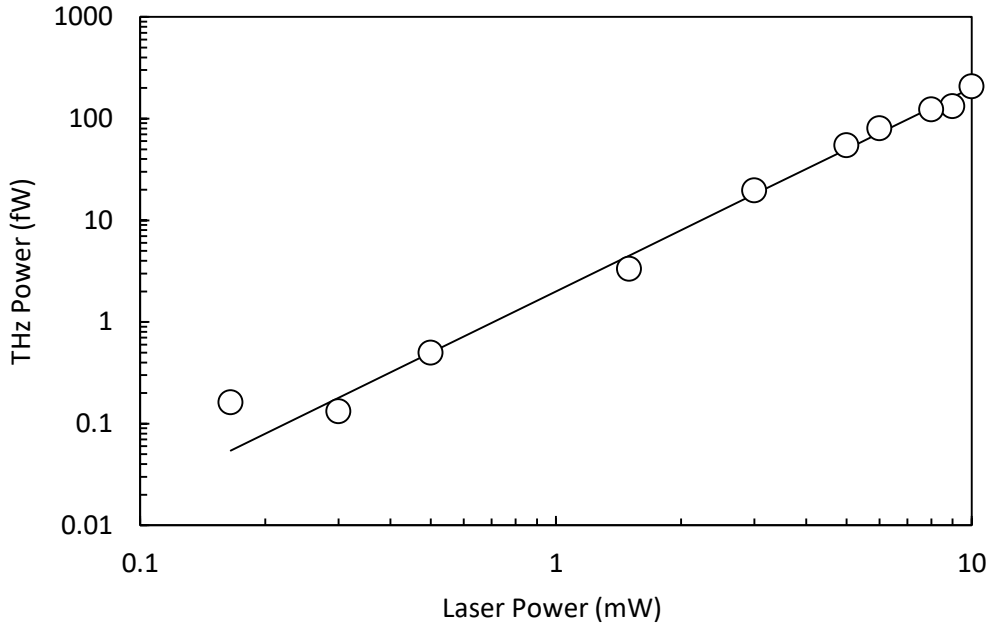

Figure 3.17: Measured average THz power generated by PC antenna versus average laser power (open circles). The data are fitted well by a square-law dependency (solid line).

Firstly, we focused the laser beam with an average power ranging from 0.15 to 10 mW on the PC gap between the electrodes with a fixed 15 V applied bias (nominal values are suggested by Teravil are: 40 V bias and 30 mW average laser power). The obtained results are shown in Figure 3.17 for one of the illuminated KID pixels. As theoretically expected (equations (2.6) and (2.7): $\vec{\mathrm{E}}_{\mathrm{THz}} \propto I_{laser}$), the detected THz power is proportional to the square of the applied laser power (solid line in Figure 3.17), and no deviation is detected due to either saturation, noise contribution or non-linearity of KIDs. For this experiment, the minimum detected THz power by using KIDs is 0.1 fW which is few times more than the recorded NEP value of such KIDs (6×10^{-17} W/$\sqrt{\mathrm{Hz}}$ in [164]) mounted at telescopes due to thermal contribution from the environment

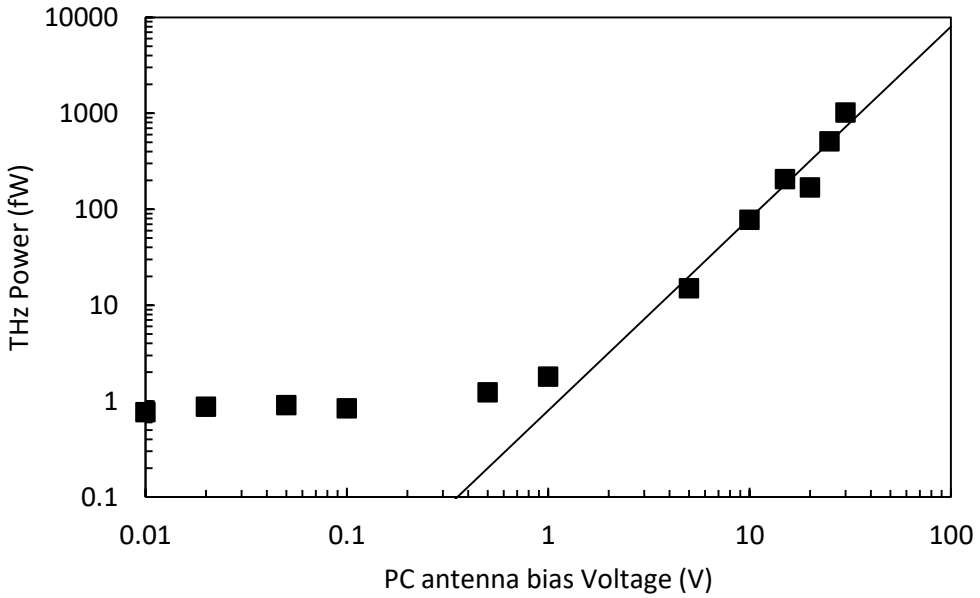

Figure 3.18: Measured average THz power generated by PC antenna versus PC antenna bias voltage (full square). The solid line is a square-law dependency fit.

In the second experiment with photoconductive antenna, we fixed the average laser power at 10 mW and varied the applied bias between the electrodes from 30 to 0 V (see Figure 3.18). When the bias voltage is higher than 1 V, the measured average THz power is proportional to the square of the applied voltage (solid line in Figure 3.18). However, at a bias voltage lower than 1 V, the THz signal remains constant. The measured THz power is well fitted by $P_{THz} = AV_{bias}^2 + 1.3$ (A is a constant value, V_{bias} is the applied bias). To investigate this unexpected behaviour, we used a simple THz-TDS system with the same PC antenna as an emitter and another PC antenna for the detection of THz waves instead of using KIDs. The reason for this behaviour can be as a result of either Schottky contact, the Dember effect or optical rectification in GaAs. Since GaAs is a non-centrosymmetric crystal, THz waves can be generated under laser illumination. These generated waves depend on the angular polarization but we didn't observe any magnitude differences in THz signal when the polarization of laser beam was rotated. Secondly, the other reason can be Schottky contact between the electrodes and the semiconductor surface in the photoconductive antenna. This contact creates electric fields around the anode and cathode. Theoretically these fields cancel out. However, they are unevenly distributed in the gap for commercial photoconductive antennas. Therefore, photo carriers generated by the laser beam can be accelerated by these fields. Figure 3.19 (a) shows the Schottky field contribution is zero when the laser pulse illuminates the center of the electrodes because around the electrodes Schottky fields are oppositely oriented. If the laser excitation is not centred or/and the photoconductive antenna structure is not symmetrical, Schottky field accelerate the carriers along the surface.

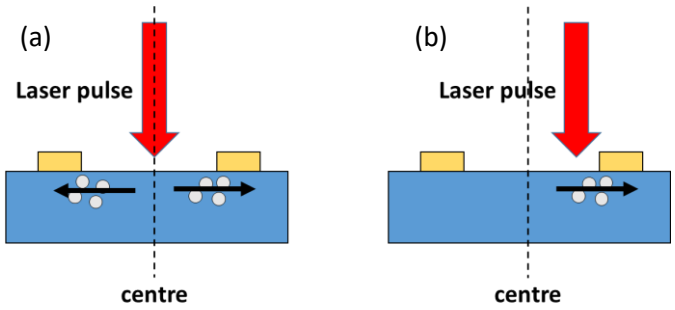

Figure 3.19: (a) In a symmetrical antenna structure, the laser illuminates the centre of PC Antenna, and Schottky fields around the electrodes is zero. (b) In an asymmetrical antenna structure, the laser illumination is not at the centre of PC antenna and the Photocarriers are accelerated by Schottky field and they give rise to THz signal.

The effect of Schottky contact can be observed when the bias voltage applied forward and reverse cases. In a PC antenna, the average velocity of carriers $\mathrm{v}(\mathrm{t})$ is considered constant. If the bias voltage reverse, the generated THz fields are identical in amplitude but the shape of the signal is flipped, *i.e.* the polarity of the signal changes. In case of Schottky contact on the antenna, the velocity is not constant. We assume that the velocity depends on the polarity of the field, so the field-dependent velocity $\mathrm{v}(I_{laser})$ is defined as [122]:

$$\begin{aligned} \mathrm{v}(I_{laser}) &= \mathrm{v}^{+} \quad \text{if } I_{laser} \geq 0 \\ \mathrm{v}(I_{laser}) &= \mathrm{v}^{-} \quad \text{if } I_{laser} < 0 \end{aligned} \tag{3.36}$$

The difference of the generated THz signals is observed for forward and reverse biases [174]:

$$\begin{aligned} I_{diff}(\mathrm{t}) &= I_{PC}^{+}(\mathrm{t}) + I_{PC}^{-}(\mathrm{t}) \\ &\propto \mathrm{q}\int I_{laser}^{+}(\mathrm{t}')\ \mathrm{v}(I_{laser}^{+})\,\mathrm{dt}' + \mathrm{q}\int I_{laser}^{-}(\mathrm{t}')\,\mathrm{v}(I_{laser}^{-})\,\mathrm{dt}' \end{aligned} \tag{3.37}$$

where $I_{laser}^{+}(\mathrm{t}') = I_{laser}(\mathrm{t})$ for the forward bias, and $I_{laser}^{-}(\mathrm{t}') = -I_{laser}(\mathrm{t})$ for the reverse bias. The rewriting of Equation (3.37) by using Equation (3.36) gives:

$$I_{diff}(\mathrm{t}) = \mathrm{q}(\mathrm{v}^{+} - \mathrm{v}^{-})\int |I_{laser}(\mathrm{t})|\mathrm{dt}' \tag{3.38}$$

If the field-dependent velocity is symmetric in positive and negative fields, $I_{diff}(\mathrm{t})$ is zero because $\mathrm{v}^{+} - \mathrm{v}^{-} = 0$. If it is not symmetric, then the difference of the signal is not zero and the nonlinear response of photoconductive antenna induced. This can happen under no bias or low bias voltages. In addition, the THz intensity depends on the laser position in this gap [175]. This effect was first confirmed by the voltage current relationship ($I(V)$) shown in Figure 3.20 under no laser illumination. Between +0.4 V and -0.4 V, there is a Schottky barrier, and the current remains constant. In addition, $I(V)$ curve shows that there is a symmetric relation for negative and positive bias, which means that the Schottky barriers are same for anode and cathode [122]. This effect can be seen also on the plot of generated THz power versus bias voltage in Figure 3.21: the THz power is not symmetric

for positive and negative bias voltages, and the minimum THz power was obtained at 0.3 V. This minimum power can vary from one experiment to another one with different laser positions in the gap and the centring of the silicon dome. Lastly, Dember effect can be the other reason for this unexpected behaviour. In this effect, generated photo carriers can be accelerated normally to the surface by the difference of mobility for holes and electrons (the difference creates dipole) [176]. These THz waves can be collimated by the silicon dome at an incidence angle of 50°-60°, which corresponds to the maximum of the emission of a dipole oriented perpendicular to the surface. This can also contribute to the THz signal, but not for a laser excitation at normal incidence. As a result, this unexpected behaviour observed in Figure 3.18 is likely attributed to a Schottky effect at the antenna electrodes, and a slight misalignment of the PC antenna. This hypothesis was confirmed by the employees of the Teravil company.

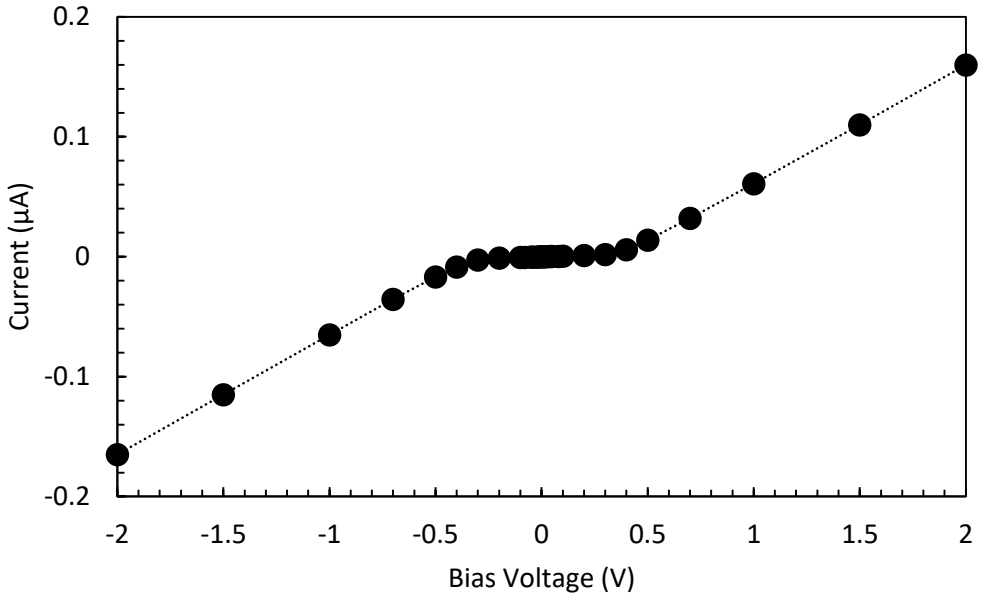

Figure 3.20: $I(V)$ curve of PC antenna under no laser illumination. The typical junction threshold is between 0.4 and –0.4 V.

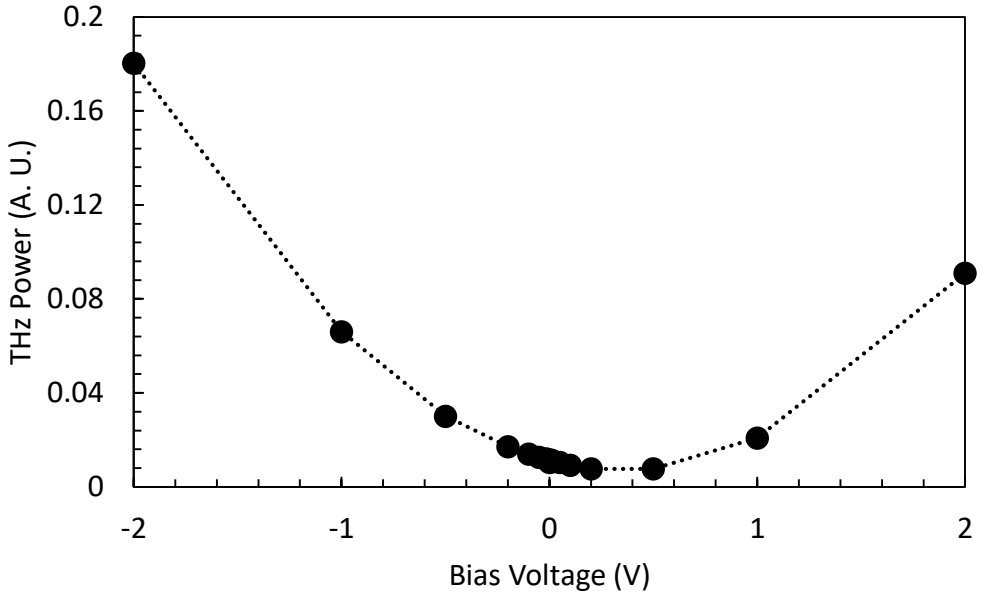

Figure 3.21: Measured THz power versus positive and negative bias voltages under a 6.7 mW laser excitation for PC antenna emitter. The minimum value of THz power is obtained at 0.3 V.

3.5 Conclusion

In this chapter, KID was explained by providing a basic theory to understand their response to light. We detected very weak THz pulses generated either by an optical rectification in a non-centrosymmetric material ZnTe pumped by femtosecond laser pulses, or by a photoconductive antenna. Detected THz power by the KID camera was calibrated with an another setup using calibrated VDI diode. The results show that the minimum average THz power was recorded smaller than 0.2 fW. Additionally, it was demonstrated that instead of following a square law with the bias voltage, the THz power generated by the photoconductive antenna remains constant when the bias voltage is less than 1 V. This unexpected behaviour was explained by Schottky contact between the electrodes and the semiconductor in the antenna. Since this preliminary result show the high sensitivity of KID to detect weak THz pulses, the KID camera can be employ for THz microscopy. In the next chapter, we will see the image results obtained with the KID camera and simulation results for the aperture used for the THz microscopy.

4. Imaging with a sub-wavelength hole by using KIDs

Spatial resolution in sub-wavelength range of THz imaging is required for applications such as biomedical diagnosis and semiconductor device inspection since the dimensions of the samples are often smaller than the THz wavelength [13,46]. Because one of the obstacles of THz imaging in the sub-wavelength regime is the lack of high-sensitivity detector, we present super-transmission THz microscopy which detects the THz radiation by using KID camera. This camera was developed for astronomical researches in the Institut Néel, so for the first time it is used for THz microscopy. We make use of this camera to record the very weak THz signal transmitted by a thin metal sheet with a sub-wavelength hole. In the microscopy method, a thin sample is placed against the metal sheet and is moved over the hole (see Figure 4.1). Therefore, the spatial resolution of the system is determined by the hole diameter. In this chapter, a simulation model to estimate the transmission through the hole is presented and the obtained experimental images are given.

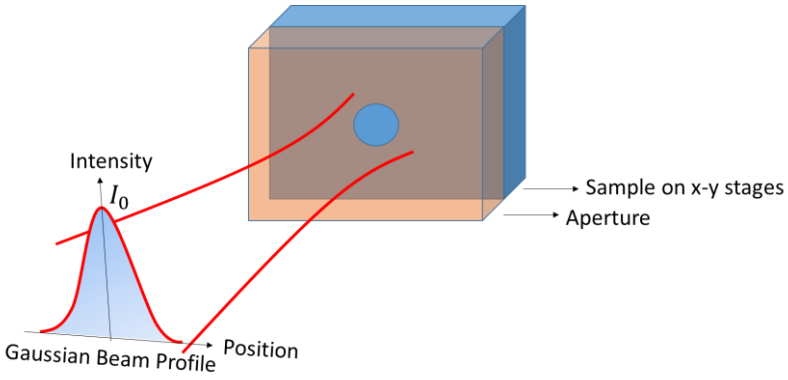

Figure 4.1: Scheme of the THz microscopy with a sub-wavelength diameter hole principle. The sample is on a x-y stage and against the aperture which is illuminated by a Gaussian THz beam.

As shown in Figure 4.1, if we assume that the beam propagates in the form of a Gaussian profile, the intensity distribution of the beam is given by [177]:

$$I(r) = I_0 \exp\left(\frac{-2r^2}{w_0^2}\right) \tag{4.1}$$

where r is the distance from the centre of the Gaussian beam, I_0 is the maximum intensity at the centre of the beam at that location, and w_0 is the beam waist of the beam where the intensity decreases by $1/e^2$ of its value. The transmitted Gaussian beam power through a circular aperture with a radius of a (smaller than w_0) in a zero-thickness sample is calculated by integration of the beam intensity over the cross-sectional area:

$$P_T = \int_0^a 2\pi a\, I_0 \exp\left(\frac{-2a^2}{w_0^2}\right) da = P_0\left(1 - \exp\left(\frac{-2a^2}{w_0^2}\right)\right) \tag{4.2}$$

where P_0 is the total power of Gaussian beam and is equal to $\pi w_0^2 I_0/2$. Let us notice that this expression gives only an estimation of the transmitted power. A rigorous calculation will be based on

the electromagnetic theory of diffraction. From Equation (1.2), the calculated transmission through the circular aperture for a Gaussian beam is described as below [178]:

$$T = 1 - \exp\left(\frac{-2a^2}{w_0^2}\right) \tag{4.3}$$

While analytical calculations have been published when the device thickness is null, and when the metal is perfectly conducting, actual devices cannot be described through these simplified hypothesises. Here we compute the transmitted THz signal with a finite element model (FEM) solver. In this solver, the entire volume of the simulation domain is divided into small regions called finite elements. This is obtained by meshing the domain. Generally, tetrahedral cells are used to mesh any geometry since such cells have the benefit of being flexible. Therefore, it is easy to model geometries containing complex structures. Usually, a denser mesh is designed where geometrical features are small, while bigger cells are employed in homogeneous regions. With the FEM solver, we can estimate the power transmitted through the hole used for our THz experiment. As the size of the hole is reduced, the transmission light through the hole decreases as well. We will also estimate the smallest hole dimension by comparing the transmitted power with the power sensitivity of the KID camera. Additionally, we can design different shaped apertures instead of a cylindrical hole. For example, the results show us that a conically tapered hole transmits more light than the cylindrical hole.

4.1 Simulation Model

In order to predict the transmission through a hole in a metal sheet, a simulation model was carried out using the High Frequency Structure Simulator (HFSS, version 18.1, produced by ANSOFT). The HFSS uses FEM to solve the Maxwell's equation at frequency domain:

$$\nabla \times \left(\frac{1}{\mu_r}\nabla \times \vec{E}(\omega)\right) - k_0^2 \epsilon_r \vec{E}(\omega) = \vec{J}_{source} \tag{4.4}$$

where $k_0^2 = \omega^2/c^2$, $\vec{J}_{source}$ represents the current density associated to any source, μ_r and ϵ_r are the relative permeability and permittivity respectively. HFSS uses 3D electromagnetic field solvers based on the FEM model to analyse 3D shape structures. The unit cell is defined as the tetrahedral elements, which is automatically generated and modified below the defined electrical length in HFSS. In order to obtain an accurate model, the adaptive meshing technique is used. At each step of adaptive meshing, the error in the numerical result is calculated by comparing with the previous step. If the error is larger than a chosen error value, a new mesh is computed. The computational process continues until the condition is satisfied or it stops when the assigned number of the repeating the process reaches its maximum. For our simulation models, we defined the error value as 2 %. According to the complexity of the simulation entities, the computation time of our models took ranging from 1 to 12 hours.

For the initial attempts, we were inspired by a study published by Kang *et al.*, which is related to power transmission through a λ/20 aperture in a very thin copper plate [179]. In their design using HFSS, they compare the transmission through a single sub-wavelength aperture in the case where a high permittivity dielectric cube is positioned (1) in front of the aperture or (2) is absent. Figure 4.2 (a)

illustrates their model designed using HFSS with the incoming and reflected THz field computed in a parallelogram of dimensions $t = 30\ \mu\text{m}$ and $L = 60\ \text{mm}$. In their computation, this parallelogram behaves as a rectangular waveguide by using a wave port (WP) excitation in HFSS: this boundary condition allows the energy to flow into and out of the problem space. The dimensions of the excitation port are chosen according to the operating frequency. In the computation by Kang *et al.*, the chosen dimensions are 19.05 mm and 9.525 mm for 14.61 GHz operating frequency, and the wave guiding distance is 40 mm. The parallel surfaces of the wave guiding box are assigned as Radiation Boundaries (RB) and Perfect Electric Conductor (PEC) to obtain quasi-plane wave excitation. Moreover, the other surfaces of the HFSS design are set as RB, in view of avoiding the multiple reflections at the boundaries of the air box and to provide open boundary conditions. Figure 4.2(b) shows the map of the transmitted electric field through a single sub-wavelength aperture calculated by Kang *et al*. We followed the same procedure as Kang *et al.*, and our results match well with the ones by Kang *et al.*, as shown in Figure 4.2(c) and Figure 4.2 (d). Additionally, HFSS can be used to extract the scattering parameters which describes the energy flow between the ports. The scattering parameter for the power transmission between the ports is calculated as ~85 dB for this simulation, meaning that the transmitted light $\sim 10^{-8}$ times weaker than the incident light because of the diffraction theory [52].

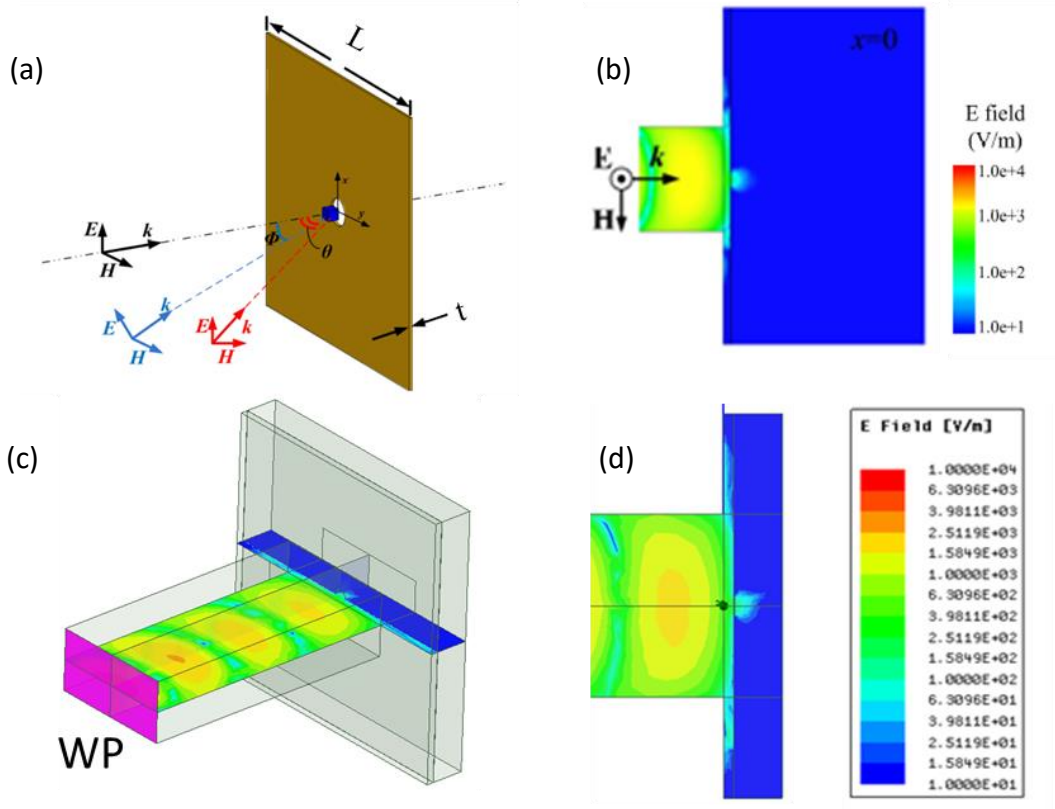

Figure 4.2: Comparison of the HFSS results by Kang et al. [179] and ours. (a) The HFSS geometry by Kang et al. includes a metal plate with a hole at its centre, and a high permittivity dielectric cube placed in front. (b) The transmitted electric field distribution through one single sub-wavelength aperture without the high permittivity dielectric cube computed by Kang et al. The radius of the hole is 1 mm and the frequency of the source is 14.61 GHz (c) Overview of our HFSS geometry. The front surface (pink coloured) is assigned as a WP excitation. (d) Distribution of the transmitted and reflected field that we computed.

This primarily result helped us to run and optimize our simulation model using HFSS. However, experimentally we do not use any structure to guide the waves up to the device. Therefore, we converted the model to be excited by a Gaussian beam excitation in HFSS. In our design, a metal plate with a cylindrical hole inside is illuminated by this excitation whose electric and magnetic field are parallel to the metal plate and whose wave vector is perpendicular to the metal plate (see Figure 4.3 (a)). The metal plate was assigned as a perfect electric conductor (PEC) because of the large dielectric constant of metal in the THz range, of the order of -30 000 and 100 000 for the real and imaginary parts of the dielectric constants of most metals, respectively [180]. The device is located in an air box: outer surfaces of the box are covered with perfectly matched layers (PMLs) (see Figure 4.3 (b)). PML is an another open boundary condition like RB but it is more advanced and give more accurate results than RB [181]. In Figure 4.3 (b), the waves enter the problem space from the surface S_{in}, and the transmitted field is detected over the surface S_{out}.

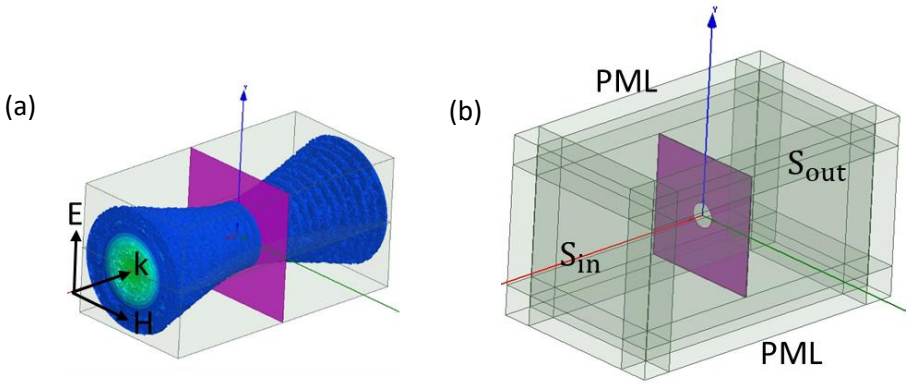

Figure 4.3: (a) Overview of the HFSS model including a Gaussian beam focused at the origin of the air box and the cylindrical hole made in a metal plate. (b) The air box is surrounded by PML boundary conditions.

To calculate the transmission through the hole using HFSS, Poynting vectors were integrated over the surfaces of S_{in} and S_{out} to find the incident and transmitted power, respectively. For these calculations, HFSS Field Calculator was used. The ratio of the transmitted and incident power gives the transmission coefficient [182]:

$$T = \frac{\int_{S_{out}} \left(\left(\vec{E}_{total} \times \vec{H}^{*}_{total} \right) \cdot \hat{n} \right) dS}{\int_{S_{in}} \left(\left(\vec{E}_{inc} \times \vec{H}^{*}_{inc} \right) \cdot \hat{n} \right) dS} \qquad (4.5)$$

where $\hat{n}$ is the unit vector normal to the surface; $\vec{E}_{inc}$, $\vec{H}_{inc}$, are the incident electric and magnetic fields and $\vec{E}_{total}$ and $\vec{H}_{total}$ are the total electric and magnetic fields, respectively. The incident field is the plane-wave field which exist in the absence of the device; the total field exist in the device only with a non-zero incident field. It is called "total field" because it is the summation of the reflected and the incident fields.

Using this simulation model, we can calculate the transmitted power through the hole for THz microscopy technique. Therefore, this can help us to estimate what is the smallest size of the hole that will allows us to detect and record a transmitted THz signal with the KID camera. In the following, we

will present the simulation results obtained by designing a conically tapered hole in a metal using HFSS for THz microscopy. When the angle of the cone is null, it corresponds to the cylindrical hole case.

4.1.1 Tapered hole device for THz microscopy

A conically tapered hole in a metal shows higher light transmission comparing to the cylindrical one [183]. This shaped device can be used to guide the wave and reduce the cut-off frequency. It can be perfectly adapted to THz microscopy; Schade *et al.* have applied the conically tapered hole to image biomedical tissues [72,184]. In their experiment, they placed the sample to be imaged in contact with the device and used a computer-controlled stage to move the sample. The experiment was performed using THz radiation delivered by a synchrotron. Comparing to their work, we propose a highly sensitive detector, a KID camera, instead of using a powerful radiation for sub-wavelength THz imaging. Figure 4.4 shows the schematic diagram of the device with a conically tapered cylindrical hole. The simulation model described in the previous section was used to design the aperture and calculate the transmitted power through the aperture for a specific wavelength. Using HFSS, we can optimize the device versus different parameters: input diameter (d_{in}), output diameter (d_{out}), thickness of the device (t) and tapered angle (TA).

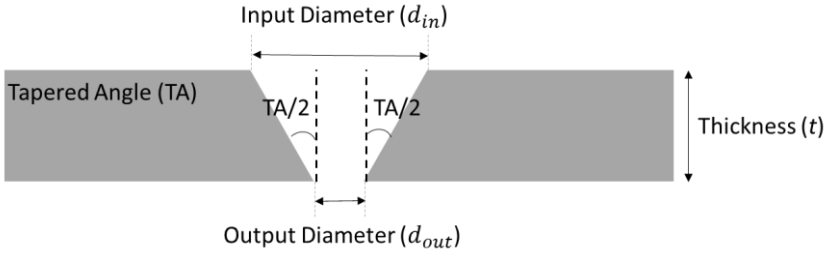

Figure 4.4: Diagram showing the conically tapered aperture

We followed the work of Liu *et al.* to confirm our simulation results [61]. In their work, Liu *et al.* experimentally compared the transmission through the conically tapered apertures with different tapered angles. For this, they kept the output diameter fixed but varied the input diameter of the device as a function of TA. Each device they studied has a fixed output diameter d_{out} of 400 µm in a 3-mm thick metal disk and the tapered angle takes the values TA = 0°, 30°, 60° and 90°. Therefore, the input diameters d_{in} are calculated for these angles: 400 µm, 2 mm, 3.86 mm and 6.4 mm. Liu *et al.* [61] defined the spectral field amplitude concentration factor $f_E(\nu)$, that is the transmission of the tapered hole normalized to the one of a thinner device with a cylindrical hole, namely:

$$f_E(\nu) = \frac{t_{TA}(\nu)}{t_{ref}(\nu)} \tag{4.6}$$

where ν is the frequency, $t_{TA}(\nu)$ is the transmitted amplitude spectrum measured through a hole with a tapered angle TA in a 3-mm thick device and $t_{ref}(\nu)$ is the measured spectrum for cylindrical reference hole with a diameter of 400 µm in a 0.075-mm thick metal plate. The results are shown in Figure 4.5. Theoretically, the cut-off frequency for the 400-µm diameter hole is calculated by using Equation (1.1) and we obtain ~440 GHz. In Figure 4.5, the waveguiding phenomenon is nicely observed for the cylindrical hole (purple line in Figure 4.5), but when the tapered angle increases, the

cut-off frequency decreases strongly (for example, when TA=90°, the corresponding cut-off frequency is 0.03 THz [61]). Additionally, transmission is stronger over for frequencies over the cut-off. The strongest transmission, through the 400-µm diameter hole, is calculated for the 30° tapered angle. As we deduce from Figure 4.5, the output power from the exit aperture depends on (1) the tapered angle of the cone, (2) the diameter of the aperture and (3) the beam wavelength.

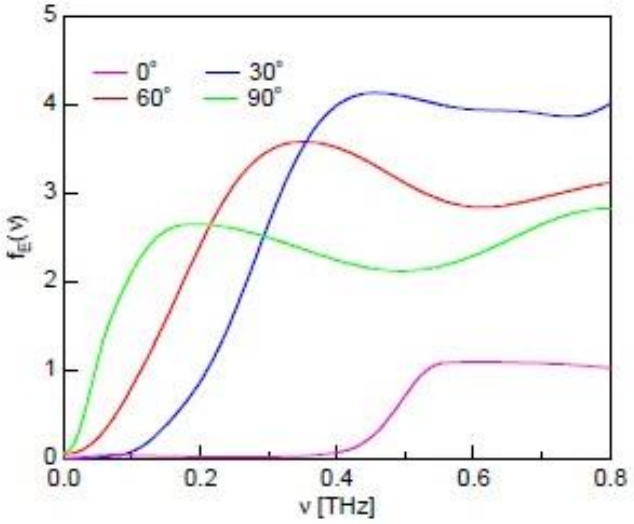

Figure 4.5: Spectra of the field amplitude concentration factors $f_E(v)$ are measured for each tapered angle devices. The output diameter of the devices are same, 400 µm (image taken from [61]).

To check our HFSS simulation procedure, we performed a simulation of the cylindrical hole, and we compared our simulation results with the experimental data Liu *et al.* [12] (see Figure 4.6). Our model includes a box filled with air, and a 3-mm thick metal plate with a 400-µm diameter cylindrical hole placed at the centre of the air box. This plate is illuminated by a Gaussian beam with a diameter of 8 mm. The HFSS simulation was performed for frequencies from 0.05 THz up to 0.8 THz, with a 0.05 THz frequency resolution. The initial tetrahedral size of the mesh cells was computed at 0.4 THz. Approximately 250 000 tetrahedral cells were created by HFSS to cover the whole investigated space. Poynting vector calculations for the transmission through the hole were applied in near field region. Since Liu *et al.* [61] measured the electric field, we took the square root of the calculated Poynting vector magnitude. Figure 4.6 shows the experimental data by Liu *et al.* [12] and our simulation result. As seen in Figure 4.6, a close agreement between the results is obtained.

Additionally, Liu *et al.* performed a numerical calculation by using 3D finite-difference time-domain (FDTD) simulations for every one of the TA studied [61]. They calculated the concentration values $f_E(v)$ in the frequency range of 0.05 - 0.8 THz, and obtained one maximum value in this frequency range. They calculated the maximum of the concentration values $f_E(v)$ in the frequency range of 0.05 - 0.8 THz. The comparison of Liu *et al.* computed results and ours is presented in Figure 4.7 for different tapered angles, together with the experimental data from Liu *et al*. Both FDTD and HFSS simulations fit well the experimental results. This validates our modelling calculation and thus we can now apply it to design and model the device for THz microscopy.

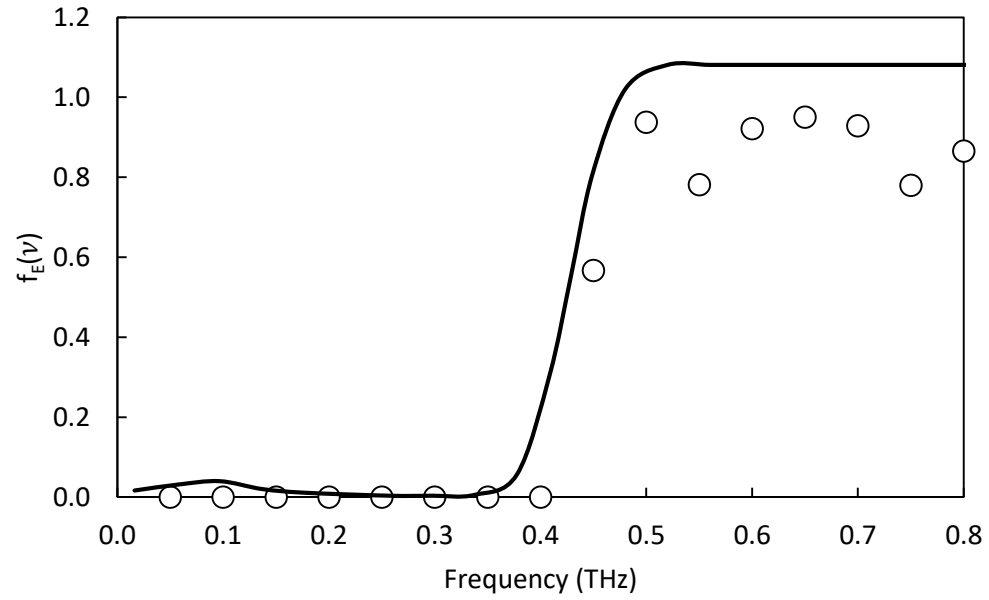

Figure 4.6: Comparison of our simulation model results obtained by using HFSS (open black circles) and the experimental results of Liu *et al.* [61] (continuous line).

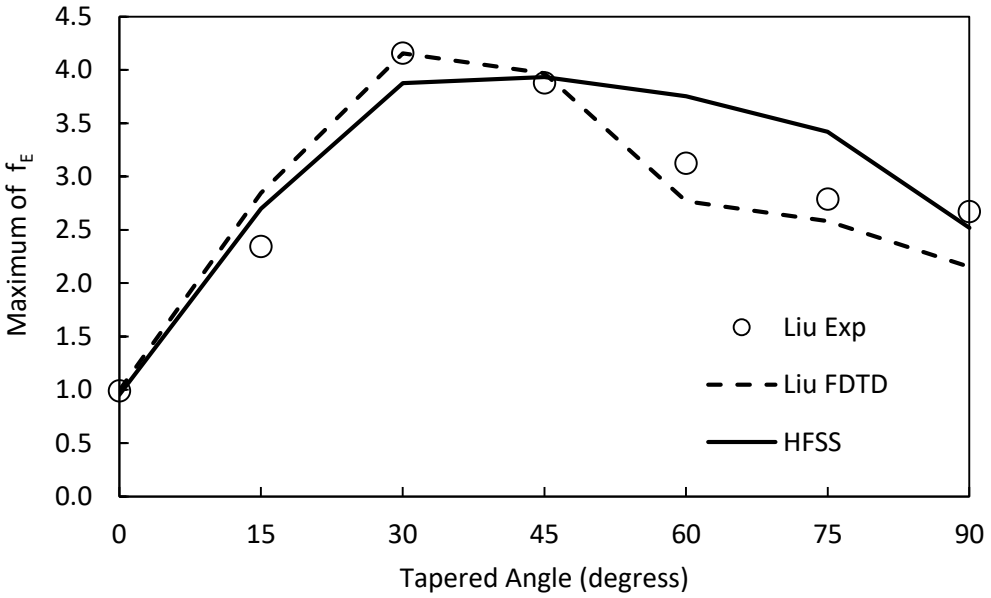

Figure 4.7: Comparison of our model (black continuous line), experimental results of Liu *et al.* (open black circles), simulation results of Liu *et al*. (black dashed line) (Liu *et al*. results are taken from [61])

The aim of this HFSS modelling for THz microscopy is to estimate the output power of the conical hole device and to optimize the shape of the conical hole. From this modelling we can also predict the smallest hole diameter that can be used by comparing the output power with the sensitivity of the KID camera. To perform the HFSS modelling, we use the same procedure as described above for the comparison with Liu *et al.* results, but we adjust the parameters to the ones of our experimental setup. In the experiment setup used for THz microscopy, we employ a microwave source equipped with a horn antenna that is supplied by the Institut Néel. The detailed information about

the simulation model for the horn antenna is given in Appendix A. This source delivers frequencies between 140 GHz and 210 GHz with 3 - 5 dBm (∼ 2 - 3 mW) output power. Therefore, we select a frequency of 200 GHz to design the aperture. In the experimental setup that will be shown in detail in the next section, the most of the incoming beam from the horn antenna was collected with parabolic mirror. In HFSS model and in the experimental setup, the incoming beam diameter at the device is equal to ∼ 8 mm. Figure 4.8 depicts the computed transmitted power for different tapered angles for an incoming power of 1 mW. The highest transmission through the hole was found with a tapered angle of 75°. The corresponding transmission coefficient T is ∼ 0.001, corresponding to ∼ 1.4 μW. This rather low transmitted power is nevertheless far above the KID's noise level 10^{-16} W [1].

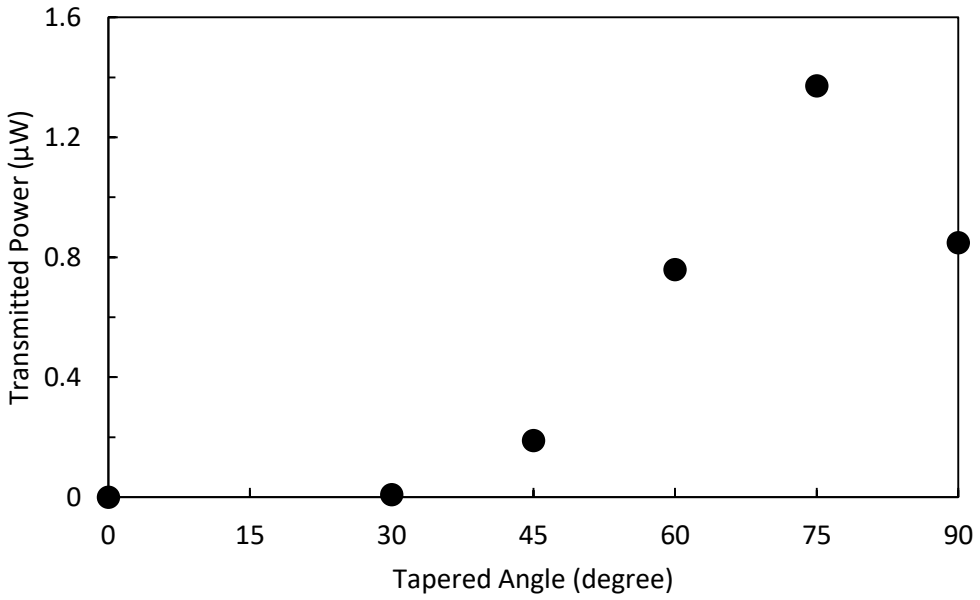

Figure 4.8: Transmitted Power versus different tapered devices for 1 mW input power at 200 GHz. Output diameter of each device are fixed at 400 μm.

The simulation model was performed for a 3-mm thick device. But when we performed the experiment, only a 2-mm thick device was available. However, as claimed by Liu *et al.* [61], the optimal tapered angle does not depend on the tapered length for specific wavelengths. Therefore, different output diameters (400 μm, 200 μm, 100 μm, 80 μm, 50 μm and 16 μm) were simulated for a 2-mm metal thickness using HFSS, and the results are shown in Figure 4.9. Here it is important to note that the FEM solver finely meshes the problem space to obtain accuracy. This might result in using most of the random access memory (RAM) on a computer, such as for the hole with a 16 μm diameter, the mesh size is the smallest one in these simulations. To avoid this problem and to reduce the memory use, the problem space was solved for quarter portion of the original model by assigning symmetrical boundaries: Symmetrical electric and magnetic boundaries are applied on two faces in the perpendicular direction of the incident electric and magnetic fields in HFSS, respectively. Based on the results plotted in Figure 4.9, we estimated that we could be able to detect the transmitted light from a hole with a diameter of 16 μm (∼ λ/94), whose power is almost 60 times larger than the minimum power that a KID camera can detect (typically 10^{-16} W). We could not simulate smaller holes because of the limited RAM in our computer, which is 64 GB.

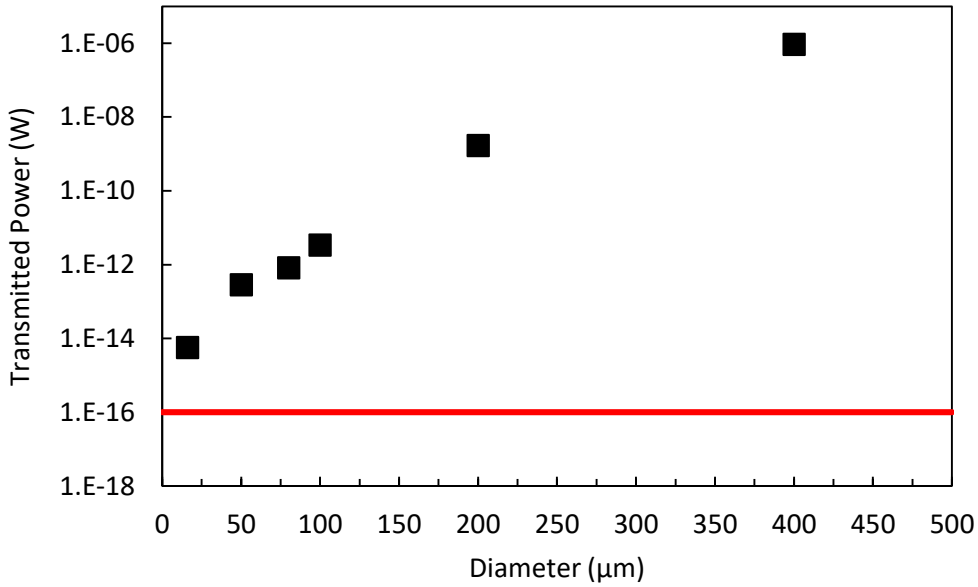

Figure 4.9. Transmitted power versus different hole diameters varying between 16 and 400 µm. The model was designed for 200 GHz at a 75° tapered angle. The red line gives the minimum power (NEP) that can be detected with the KID camera.

A frequency filter is needed to be placed in a KID camera to distinguish the light that comes from the hole from other lights in the experimental room. The filter that was placed in our first visit could allow the frequencies from 100 GHz to 180 GHz to pass through. Therefore, we needed to change the design of the device for 150 GHz as we designed it before for 200 GHz. As it is shown in Figure 4.10, the different tapered devices (90°, 75°, 60°, 45°, 30° and 0°) were designed by using HFSS for the output diameter aperture of 400 µm, and the transmitted power is higher at a TA of 90°. This can be also confirmed by the result of Liu *et al.* at 150 GHz (see Figure 4.5). Therefore, the devices for our THz microscopy experiment were fabricated with the tapered angle of 90°.

As a result of HFSS simulations, light transmission through the conically tapered hole is higher than with the cylindrical hole and reduces the cut-off frequency. For example, in the results obtained (Figure 4.10) the transmission ratio of tapered and cylindrical holes is 10 000 at 90°. The results also show that in the case of a small hole, the transmission light is calculated to be weak, as expected. Therefore, this proves that KIDs are necessary for sub-wavelength THz microscopy.

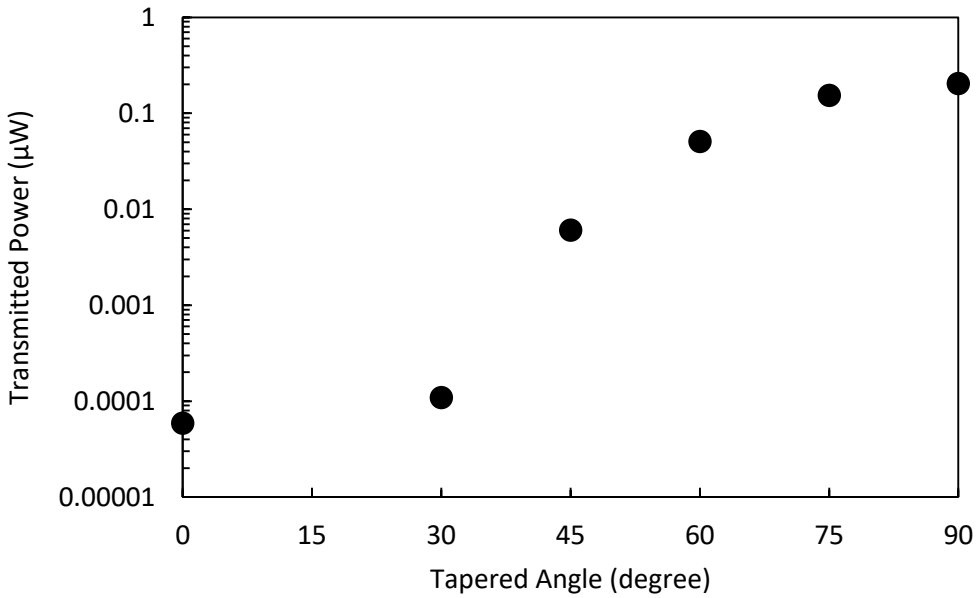

Figure 4.10. Transmitted Power versus different tapered angles for 1 mW input power at 150 GHz. Output diameter of each device are fixed at 400 µm.

4.2 Experimental Results

4.2.1 Experimental Setup

In the following, an overview of the experimental setup for THz microscopy used in the Institut Néel is presented with a detailed description of each component. Figure 4.11 shows the general layout of the experiment which includes the horn antenna 150-GHz microwave source, a parabolic mirror, a metal plate with a hole (the device), a sample, motorized stages, a Teflon lens and the KID camera (optics, filter and KID array in a cryostat).

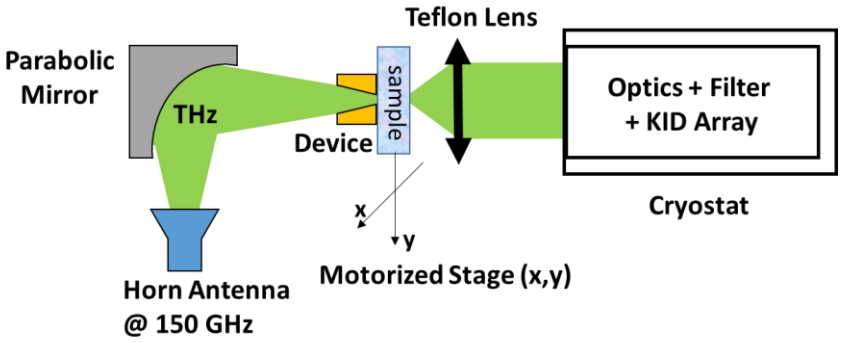

Figure 4.11. The experimental setup at the Institut Néel.

For the generation of the 150-GHz beam, a microwave source (signal generator "E8257D PSG Analog Signal Generator", produced by Agilent Technologies and a frequency multiplier) already existent in the Institut Néel is used. The signal from the source is radiated into the free space by a horn antenna (SGH-05 produced by Smiths Interconnect). This source delivers frequencies ranging from

140 to 220 GHz. A frequency filter is used in the front of the KID camera to reject frequencies below 100 GHz and over 180 GHz. Therefore, the source is set at 150 GHz. To avoid background signal on KIDs, the THz signal was modulated at 4 Hz by using the signal generator. The output power at the horn antenna is approximately 0.5 mW. To determine how the light spreads from the output of the horn antenna, a simulation was performed with HFSS (see Appendix A). The simulation shows that the beam spreads over 9 degrees from the optical axis. In our experiment, the parabolic mirror has a diameter of 5.08 cm and is placed 10 cm away from the horn antenna. The calculated beam width falling on the surface of the parabolic mirror is ~ 0.8 cm for a 9 degree-beam width, which is smaller than the diameter of the parabolic mirror used in the setup. This means that most of the beam is collected by the parabolic mirror.

The light collected by the 90 degree off-axis parabolic mirror was focused on the device (metal plate with the hole), which is used for THz microscopy. Different dimensioned conically tapered holes and cylindrical holes are used as devices for imaging. Figure 4.12 shows the devices with a conically tapered hole which were fabricated in the Istituto di Fotonica e Nanotecnologie (IFN) located in Milano, Italy. The conically tapered holes were manufactured in 2 mm thick silica using laser writing. Afterwards, they were covered with a layer of gold of thickness 80-nm by a sputtering technique. The 80 nm thickness is almost opaque in the THz frequency range [185]. In practice, it is difficult to make the perfect conical shapes in the substrate. It is why the shape of the output is slightly elliptical as seen in Figure 4.13. We have got only two devices with a tapered angle of 90 degrees: one in which the orthogonal dimensions are 140 µm and 180 µm (see Figure 4.13 (a)) and the other one with dimensions of 50 µm and 45 µm (see Figure 4.13 (b)). The input diameter of these devices are almost same, they are measured about 4.150 mm as shown in Figure 4.13 (c). Additionally, devices with a single cylindrical hole drilled in a 0.345 mm thick metal plate were used for imaging the samples. The cylindrical hole diameters of the aperture are: 350 µm and 560 µm. The results obtained with these devices are presented in the next section.

(a) 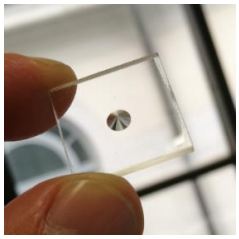 (b) 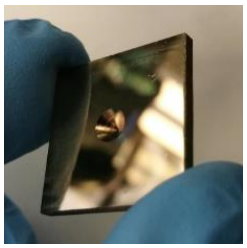

Figure 4.12. The photos of the two devices. The conically tapered hole in a silica without gold deposition (a) and with gold deposition (b)

In a next series of experiments, a sample is located against to the output side of the hole and it is moved by motorizes stages programmed in LabVIEW. Here it is important that the sample is in direct contact with the hole, otherwise the resolution will not be the hole diameter because of the propagation distance between the hole and the sample. In addition, the contribution of surface waves and plasmons around the hole are efficient in near field region at the microwave wavelength, and these surface waves can carry the signal between the metal plate and the sample. This may enhance the hole transmission (as described before in Chapter 1). This direct contact between the hole and the sample is firstly made by adjusting the position of the material by eye. It was then tested by a spring

system, made in our laboratory. We have tried different samples; they will be shown in the next section.

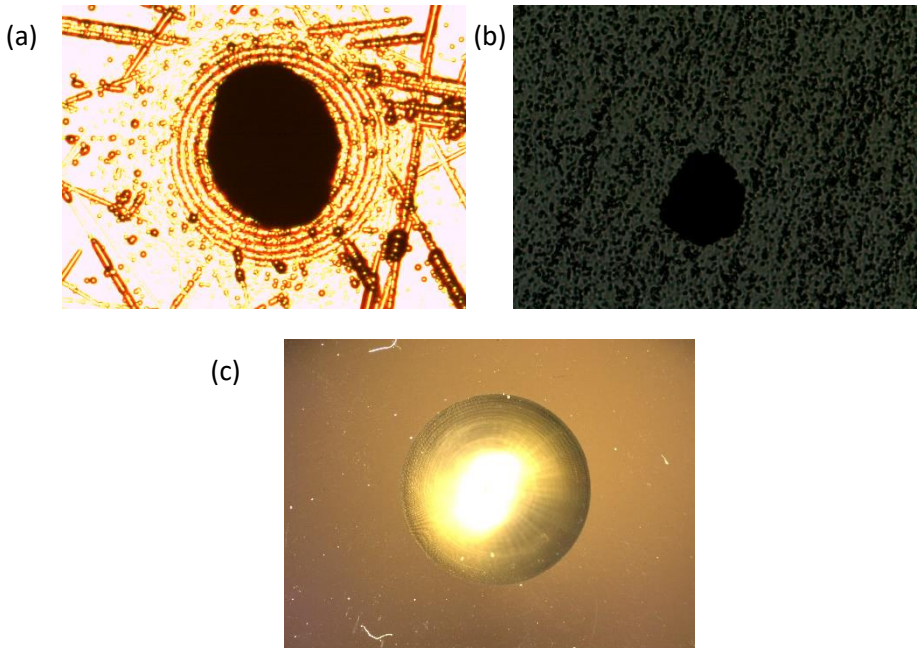

Figure 4.13: The microscopic photos of the tapered devices. The elliptical output holes with orthogonal dimensions of 180 and 140 µm (a) and 50 and 45 µm (b). The circular input hole with a diameter of 4.150 mm (c).

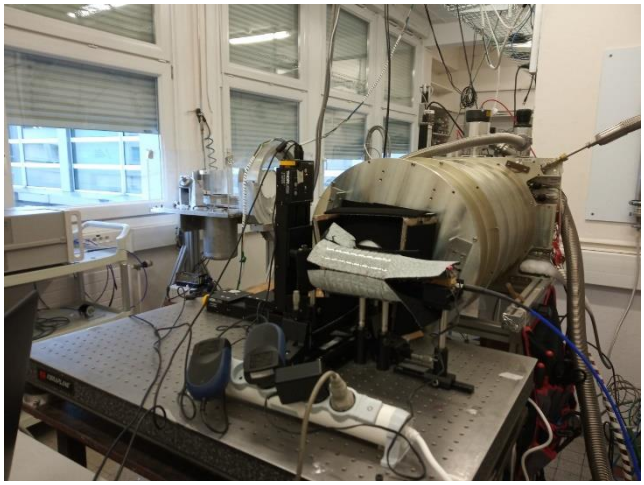

Figure 4.14: Photo of the experimental setup. Microwave absorbers were used to shield the setup.

Another component of the setup is a Teflon Lens with a focal length of 7.62 cm, placed between KID camera and the sample to collect and collimate the THz waves. Additionally, the optics inside the KID camera shown in the previous Chapter is same for this experiment (see Figure 3.11). Lastly, some of the light coming from the horn antenna can reach the KID camera without passing through the hole. For example, some light can be reflected or scattered on the optical table and then detected by the KID camera. To overcome this problem, the experiment was shielded by microwave absorbers (producer: ECCOSORB, model: AN72). Figure 4.14 shows the photo of the experimental

setup, the setup is placed on an optical table which is against to KID camera. In the next section, the imaging results obtained by using KIDs are presented.

4.2.2 Imaging with using KIDs

We performed THz imaging experiments three times at the Institut Néel, and we spent only one week for each visit because the KID camera is not always available. In our first visit, we worked on our experimental setup and how to process the data obtained from the pixels in the KID array. In the second and the third visits, we recorded signals and the results are presented in this section. For these experiments, we used two tapered conically hole and two cylindrical hole devices.

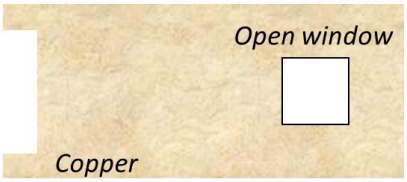

Figure 4.15: The first sample used for THz microscopy: an open square window with a width of 4 mm in a 1.6 mm thick copper plate.

For our second visit to the Institut Néel, we used the two conically tapered hole displayed in Figure 4.13 (a) and (b). Firstly, the sample that was imaged by moving it behind the hole was a 4 mm wide open window made in a copper plate with a thickness of 1.6 mm (see Figure 4.15). It was scanned along one axis forwards and backwards with the biggest conically tapered device whose output hole dimensions with 180 µm – 140 µm. The obtained data from one pixel are shown in Figure 4.16; we plot the data delivered by the pixel of the camera which exhibits the largest signal response among all the pixels. Thanks to the modulated THz signal, the power magnitude change is recorded as a function of time, the signal modulation can be seen between 50-55 seconds in Figure 4.17. As it is seen in Figure 4.16, we observed that the data has a wavy behaviour at the same time the motorized stage moves, and this wavy behaviour stops when the motor stops. This helped us to estimate the start and the finish times of the experiment.

As seen in Figure 4.16, when the motorized stage starts to move to scan the sample, the obtained power data makes a wavy behaviour because of the background variation in the experimental room. To calculate the change in power magnitude, THz power from the source was modulated by the signal generator. This way helped us to transform the data to an image. The distance scanned is 9 mm with a velocity speed of 0.05 mm/second. Figure 4.18 shows the image of the sample scanned along one axis forward and backward directions. The two images of the same sample are identical for both directions. Around the edge of the image, diffraction light can be seen.

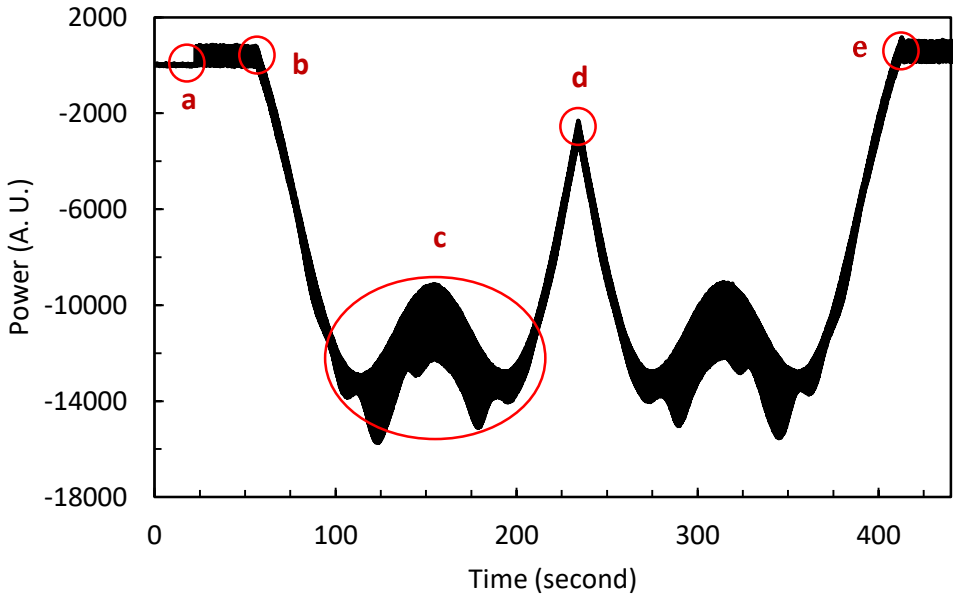

Figure 4.16: Power versus time for one pixel in the KID array. a: no THz illumination, b: the motorized stage starts to move and the data starts to make wavy behaviour, c: the hole is passing in front of the 4 mm wide open window so more signal is obtained, d: the motorized stage stops and scans in the backward direction, e: the experiment finishes, motorized stage stops, the wavy behaviour of the data stops as well

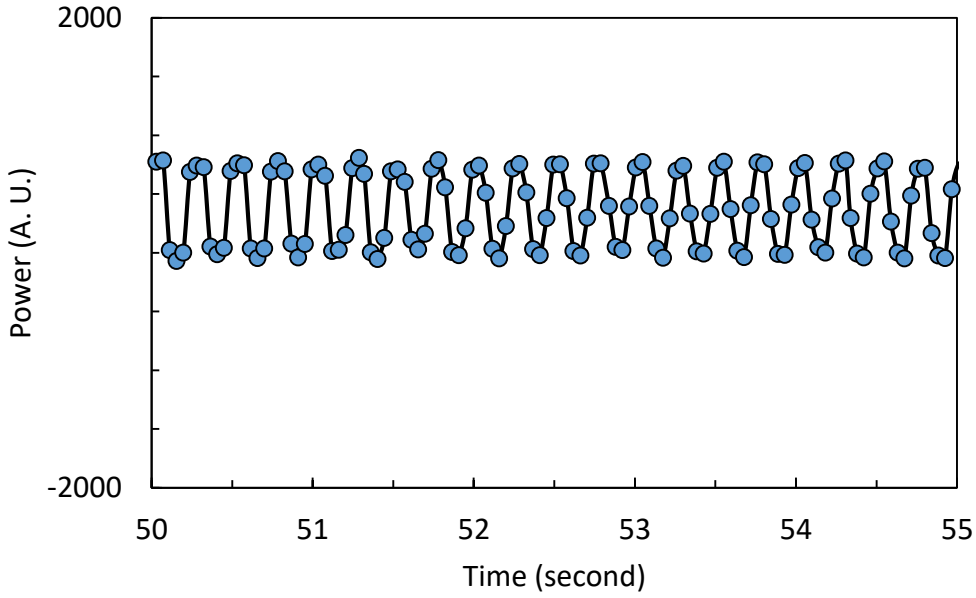

Figure 4.17: From Figure 4.16, zoom of the time range from 50 to 55 seconds.

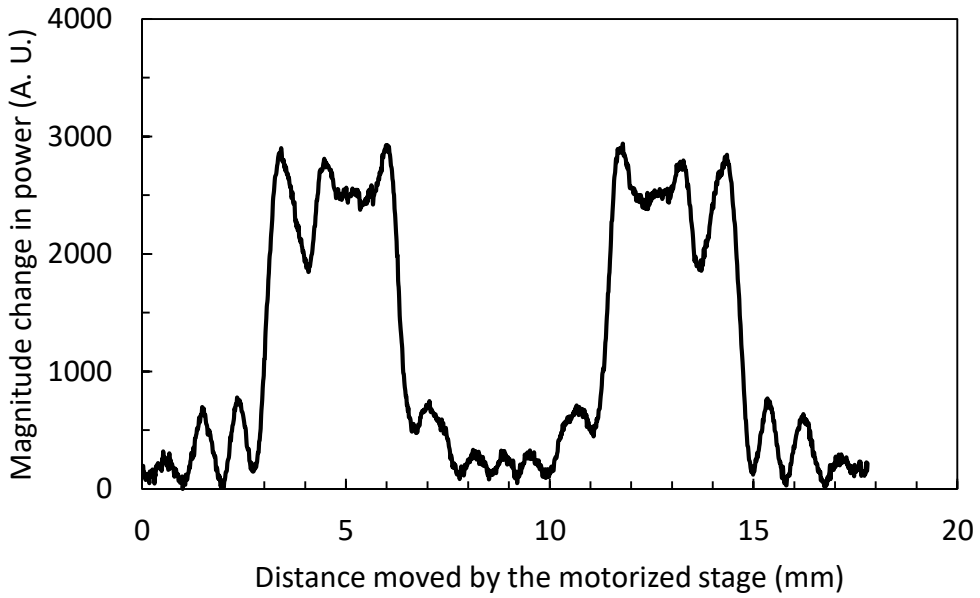

Figure 4.18: Image of a 4 x 4 mm^2 open window made in a copper plate scanned in the forward and backward directions along one axis using the tapered hole with exit aperture dimensions of 180 – 140 µm. The result is obtained by one pixel in the KID array.

When the tapered device starts to scan the area from the opaque side to the open side of the sample, the transition curve between these regions is not sharp and depends on the beam diameter, which is the resolution of the setup. Ideally, for our experiment, the resolution should be the output hole diameter of the tapered device. If the sample and the hole are in perfect contact, the transmitted power variation with the displacement x of the hole results from a shadowing effect and writes:

$$P(x) = P_0\left(1 - \alpha\left(\frac{\sin\alpha}{2}\right)\right) \text{ with } \cos\left(\frac{\alpha}{2}\right) = \frac{x}{R} \tag{4.7}$$

where R is the radius of the hole. This function $P(x)$ is almost linear with x and varies from P_0 to zero over the distance $2R$. For the $R = 200$ µm hole, the total variation of the signal should occur over 400 µm, which is definitively not observed in Figure 4.18, even if the curve is perturbed by oscillations due to diffraction at the edge of the window sample. If there exists a distance between the hole and the sample, we can expect that the beam transmitted by the beam is Gaussian, and thus the transmitted data in Figure 4.18 are fitted with the well-known expression given by [186]:

$$P(x) = \frac{P_0}{2}\left(1 - erf\left(\frac{\sqrt{2}(x - x_0)}{\omega_0}\right)\right) \tag{4.8}$$

where P_0 is the maximal power, x is the position of the sample, x_0 is the position of the shift, erf is the error function and ω_0 is the value of the half of the resolution. Here again, the calculated resolution for this experiment is 400 µm which is almost 2 times larger than the hole diameter. It means that the sample and the hole were not against each other during the measurement, and that the THz beam waist at the sample location is about twice the hole width. The conclusion is that the

distance between the sample and the hole device is a critical parameter. Since the gold film deposited on the conically tapered holes are very fragile and can be damaged during the experiment by friction, we needed to put a small distance between the hole and the sample. In our third visit to the Institut Néel, we overcome this problem by using a hole drilled in a metal plate. So no metal deposition was necessary, and the sample could therefore be in physical contact with the hole.

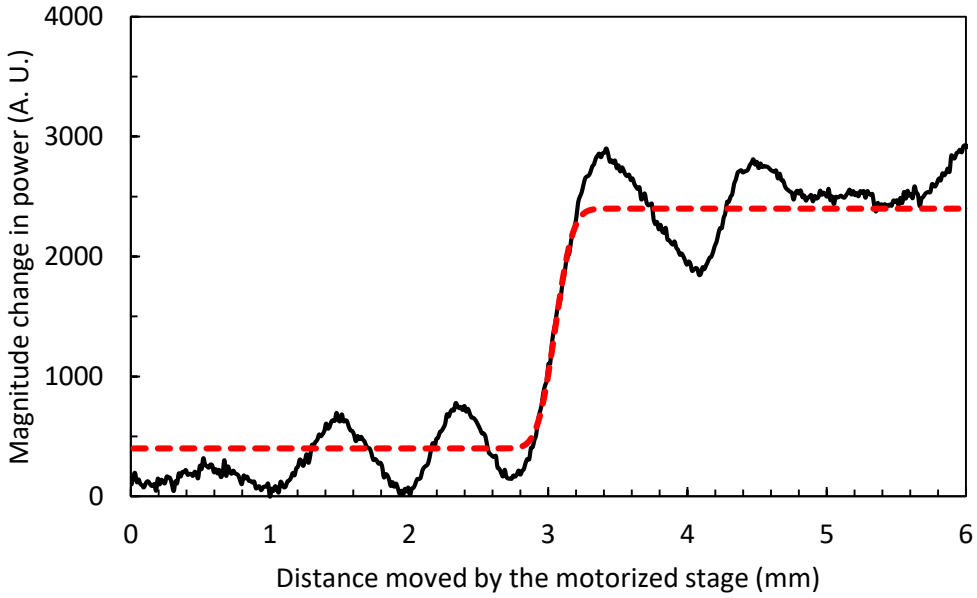

Figure 4.19: The data of image taken from Figure 4.18 between 0 – 6 mm (continuous black line) is fitted with Equation (4.8) (red dashed line)

Still during the second visit, the sample shown in Figure 4.15 was also scanned with the gold-covered tapered device whose elliptical output hole dimensions are 50-45 µm. Figure 4.20 shows the result; the data fits well with Equation (4.8), and the resolution is calculated as 2.4 mm, which is 48 times more than the hole diameter! This resolution result proves that the sample and the hole should be in direct contact to get the resolution depending only on the hole diameter. The resolution is worse for the smaller hole since a smaller hole will diffract light more than a larger hole (previous device). In addition, the data in Figure 4.20 shows that the scanning of the sample is not complete and a section of the image is missing. This is because the data obtained from our second visit to the Institut Néel were analysed after the experiment was completed. However, even with this result, we can see that the transmitted power through the smaller tapered hole is more intense than with the larger tapered hole. This disagreement can be due to the alignment of the optics, which might be different for each hole. For example, when the hole needs to be changed, the handmade shielding needs to be removed and put it back again.

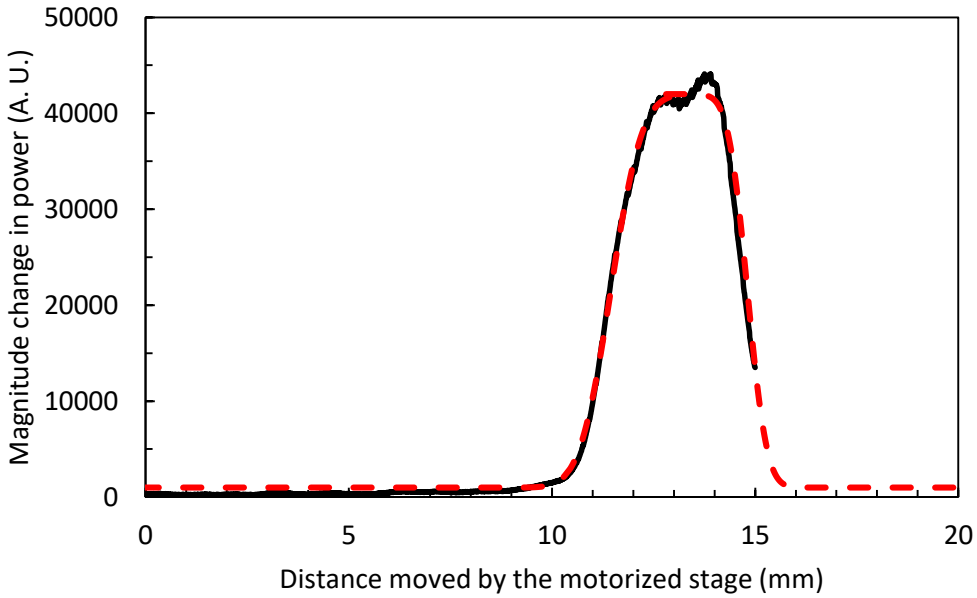

Figure 4.20: Obtained image with the tapered device whose output hole dimensions with 50 µm – 45 µm (continuous black line). The data is fitted with Equation (4.8) (red dashed line).

Also, during the second visit, we made use of the hole drilled in a metal sheet. The same sample was scanned by a 350 µm diameter cylindrical hole drilled in copper plate with a thickness of 0.345 mm. The record is shown in Figure 4.21. The resolution of the image is calculated to be only 4 mm, indicating that we may have the same problem we faced before in the previous experiment: the sample and the hole are not against each other and the resolution depends on the propagation distance between the hole and the sample. That is why in our third visit in Institut Néel, we aimed to overcome this problem by putting a spring mechanism to push the sample against the hole.

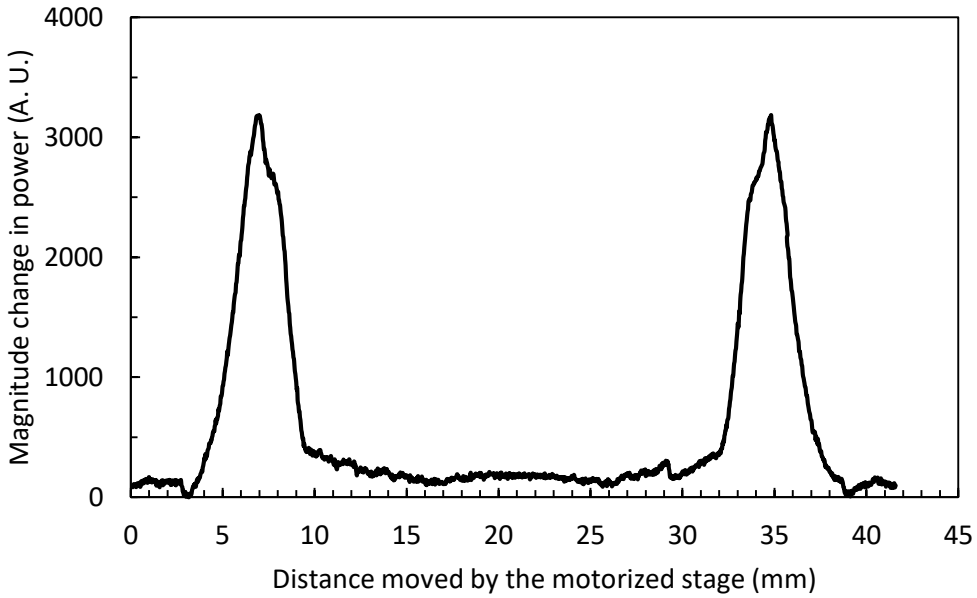

Figure 4.21: The sample scanned with a 350 µm cylindrical hole drilled in a metal sheet.

In our last experiment of the second visit, the smallest tapered hole whose output hole dimensions is 50 µm – 45 µm was used to scan the same sample but with a 800 µm thick metal wire placed approximately in the middle of the open window (see Figure 4.22). The sample is scanned with the wire and without the wire at the same distance from the hole. As it is seen in Figure 4.23, there is less power when the metal wire is scanned but the hole is not completely blocked by the sample. Because probably there is a distance between the hole and the wire. In additionally, when the sample is scanned without the wire, the power is increased. That might be because of the fact that the sample is tilted towards to the hole.

Figure 4.22: The second sample used for THz microscopy, which is the same sample in Figure 4.15 except with a 800 µm diameter wire located approximately in the middle of the open window.

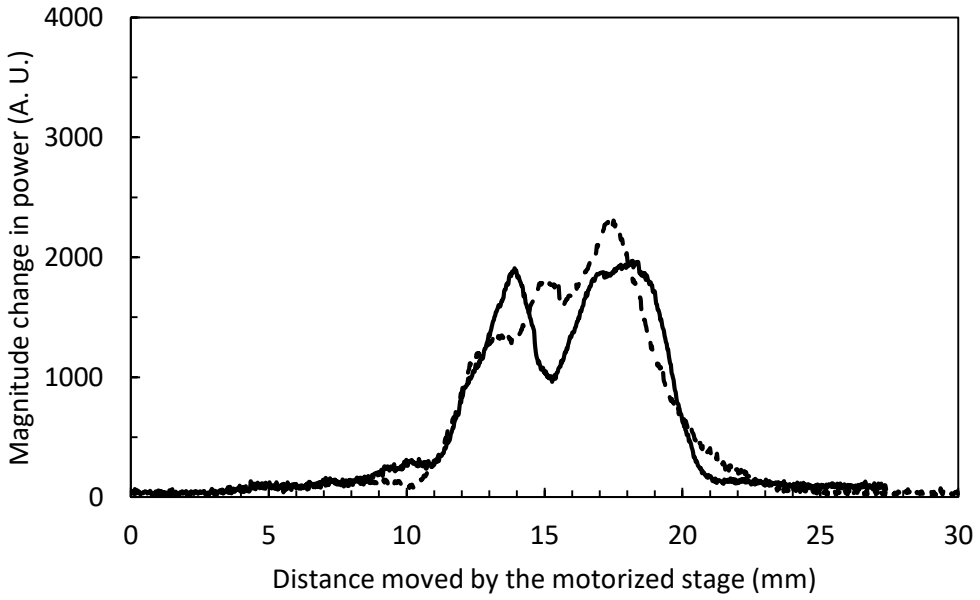

Figure 4.23: 800 µm metal wire is placed in the middle of the 4 mm open window. The sample is scanned with wire (continuous black line) and without wire (dashed black line).

As a summary of our measurements during the second visit to the Institut Néel, we faced some important problems to take into account for the next visit. Firstly, the main problem of the resolution of the images origins from the hole and the sample not being in direct contact. Therefore, we could not define the resolution of the images depending on the hole diameter. The scanned position of the images was only estimated because there is no communication between the motorized stage and the KID camera. The shielding of the experiment setup was hand made from microwave absorbers, and we could still see some background signals that were not coming through the hole on certain pixels. Among all these problems, we will improve the contact between the sample and the hole with a mechanism. We expect in our third visit to the Institut Néel to prove the resolution concept

of our THz microscopy technique. Also, we simultaneously processed the obtained data to evaluate the images. This bring us to our last visit and the images we obtained will now be discussed.

In our third and the last visit to the Institut Néel, we did not use the tapered hole devices because we observed that the gold films on the devices were damaged during the measurements. Therefore, we used a cylindrical hole with a diameter of 560 µm drilled in a 0.345 mm thick metal plate. In this visit, we aimed to prove that the resolution of the image depends on the hole dimensions. For our third visit, we simultaneously analysed the data to avoid the problem we faced in Figure 4.20.

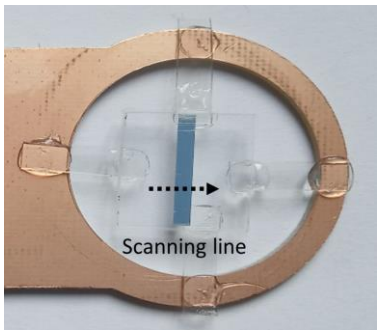

Figure 4.24: Photo of holding mechanism of the sample.

Another sample with its holding mechanism was fabricated especially for this visit. Glass substrates with a thickness of 1 mm were cut into 1.5 x 1.5 mm squares, and a 200 µm thick aluminium foil was deposited in strips of 1 mm or 2 mm wide onto the substrates. These samples were held at the four sides with some plastics as shown in Figure 4.24. With this sample, we expected to have less diffraction around the sample (see Figure 4.18), and with this new holding mechanism for the sample, we expected the sample would be pushed from its four sides to avoid any tilting and could be placed in direct contact with the hole.

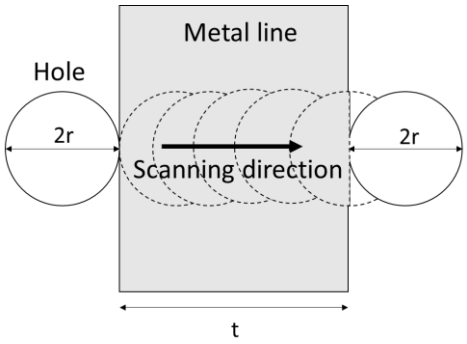

Figure 4.25: The expected zone with a transmission power drop is equal to (2 x 2r) + t

The sample shown in Figure 4.24 is scanned along one axis. The width of the low transmission region should be the summation of the two times the dimension (2r) of the cylindrical hole device and one time the width of the metal strips (t) (see Figure 4.25). For example, the 1 mm wide metal strip was scanned with the cylindrical hole device, so the expected image should be about 2.1 mm wide (calculation: 2x0.56 mm + 1 mm). Figure 4.26 shows the obtained image from 1 mm wide metal line. As expected, the experimental power drop caused by blocking the signal with the metal line is 2 mm wide. This result shows that the hole and the sample are in direct contact, and the resolution of our

THz microscopy technique depends on the hole diameter device. This expected result was checked in the same condition with 2 mm wide aluminium sample. The image obtained in Figure 4.27 is about 3.15 mm wide. The results show that the mechanism to hold the samples worked very well for imaging; it proved the resolution concept of our THz microscopy technique. In addition, in the middle of the images obtained in Figure 4.26 and Figure 4.27, there is a certain amount of increase in the power. Because of the limited time we had to work with the KIDs, we could not find an answer for this behaviour.

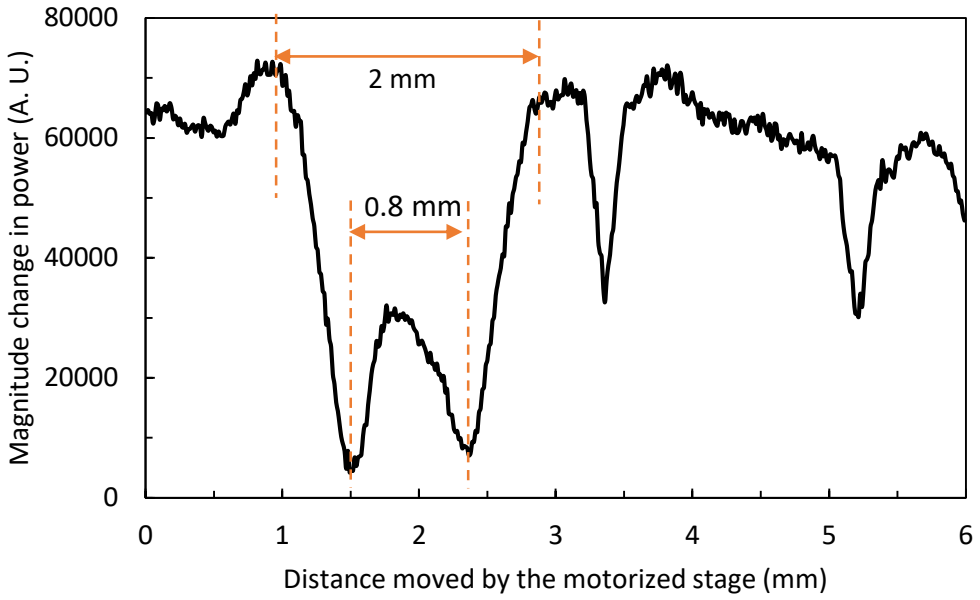

Figure 4.26: Image of the 1 mm wide metal strip deposited on glass scanned by a cylindrical hole device (with a diameter of 560 µm in a 0.345 thick metal plate).

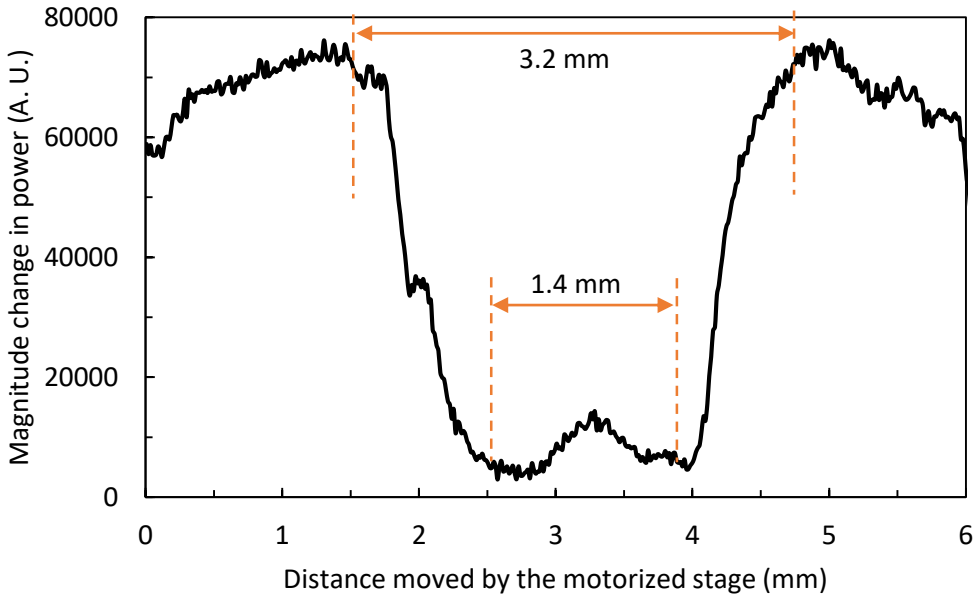

Figure 4.27: Image of the 2 mm wide metal strip deposited on glass scanned by a cylindrical hole device.

4.3 Conclusion

In this chapter we have established a simulation model of transmission through a sub-wavelength size hole made in a metal sheet using HFSS. Our calculated results were validated by comparison with published data. This simulation model was designed to estimate the transmitted power through a hole that was used as a device for our THz microscopy technique. The model shows that conically tapered hole has higher light transmission than a cylindrical hole. With this device and taking into account the KID sensitivity, the resolution of our microscopy can be as small as 16 µm (λ/125 for 150 GHz). In reality, we had at our disposal only 50-µm tapered hole devices, we easily detected the signal through this hole with the KID camera. Therefore, if we had smaller hole devices, we could achieve a better image resolution thanks to the sensitivity of the KID camera. The resolution of the observed images we obtained was not limited by the hole dimension because the hole and the sample were not against each other. Therefore, propagation distance between the hole and the sample changes the resolution of our microscopy technique. In the last experiments, we fabricated in our laboratory a mechanism to hold the sample with 4 springs around it. This time, we observed that the resolution of the images is the hole diameter as expected. We could not find solutions to certain problems: for example, as the shield for the experimental setup is hand-made, we probably need a better coverage to completely avoid the parasitic light to illuminate the camera. Another problem is that we estimated the scanned position of the sample from analysing of the data. This could be improved with a program that provides communication between the motorized stage and the KID camera. Lastly, KID camera is not always available, so we had some very limited time slots to align the experimental setup and to perform the measurements. If we had more time to work with the KID camera, we could improve the images obtained.

5. ORTI: Optical Rectification TeraHertz Imaging

In this chapter, we use a sub-wavelength resolution THz imaging method, named Optical Rectification Terahertz Imaging (ORTI), which use the THz radiation generated by a femtosecond laser in a sample that exhibits some non-centro-symmetry. This technique was previously proposed by Sotome *et al.* to image the different domains of ferroelectric materials [91,92]. However, their aim was not to do microscopy. Subsequently, our team used this technique to produce sub-wavelength THz microscopy by imaging a caster sugar grain (see Figure 1.19) [93]. In this technique, the illuminated laser beam in a non-centrosymmetric dielectric crystal generates THz frequency by optical rectification. An image in the THz range is then obtained by scanning the sample in front of the laser beam, following the scan lines depicted in Figure 5.1.

Here, we employ a focused laser beam on the sample to reach a sub-wavelength resolution. This is the one of the great advantages of the ORTI technique: the resolution is limited by the spot size of the laser beam, not by the THz frequency. For the image of caster sugar grain in Figure 1.19, Sanjuan *et al.* recorded the peak amplitudes of terahertz waveforms as a function of position at the crystal with a lateral resolution of 50 µm. As the sample is placed in classical THz-TDS system, we complete this work by recording the THz waveforms for each position of the sample. Therefore, by Fourier transformation of the THz signals, one can obtain the image with a wide THz spectrum. In other words, the image result in a hyperspectral-like image. This image can supply information on the crystallinity, absorption, homogeneity and chemical composition of the sample in the spectral image. In this chapter, we present a simple calculation for the resolution dependency on the diffraction of THz waves, and we give the imaging results obtained by using ORTI.

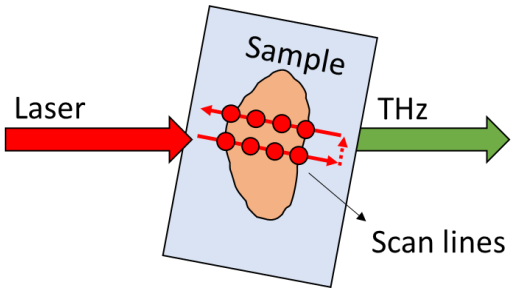

Figure 5.1: Demonstration of ORTI image: the laser beam focus on the sample, and the generated THz waves are recorded for each position on the scan lines of the laser.

As it is mentioned before, the expected resolution of the ORTI technique is limited by the spot size of the laser beam. When the spot size of the laser beam in the crystal is much smaller than the wavelength of THz waves, the THz waves can be considered as generated by a point source. In the ideal case of a punctual source, the radiated waves are circular. In actual experiments, the THz beam will be spread over a large diffraction angle. By using a Gaussian beam approximation, the diffraction angle of THz waves can be calculated. Here, we assume that the pumping laser beam has a Gaussian shape, and thus the THz generated beam is also supposed to be a Gaussian one. If the Gaussian beam travels in z direction, the expression of the THz beam electric field is written in cartesian coordinates [178]:

$$E(x,y,z) = \frac{w_0}{w(z)} \exp\left(-\frac{r^2}{w^2(z)}\right) \exp\left(j\left(\arctan\left(\frac{z}{z_0}\right) - \frac{z_0}{z}\frac{r^2}{w^2(z)}\right)\right) \exp(-jkz) \qquad (5.1)$$

where w_0 is the THz beam waist at $z = 0$ and it is equal to the laser beam waist, r is the distance from the centre of the beam and equal to $\sqrt{x^2 + y^2}$. In addition, the waist $w(z)$ and the Rayleigh range z_0 are given by:

$$w(z) = w_0 \sqrt{1 + \frac{4z^2}{k^2 {w_0}^4}} \qquad (5.2)$$

$$z_0 = k\frac{{w_0}^2}{2} = \pi\frac{{w_0}^2}{\lambda} \qquad (5.3)$$

In Equation (5.1), the first two terms specify the amplitude of the wave, and they define the amplitude variation with distance z and the shape of the Gaussian beam, respectively. The other terms in Equation (5.1) contain the phase of the wave inserted in the exponentials. Now, we can analyse the amplitude diffraction patterns of the Gaussian beam as a function of the beam waist.

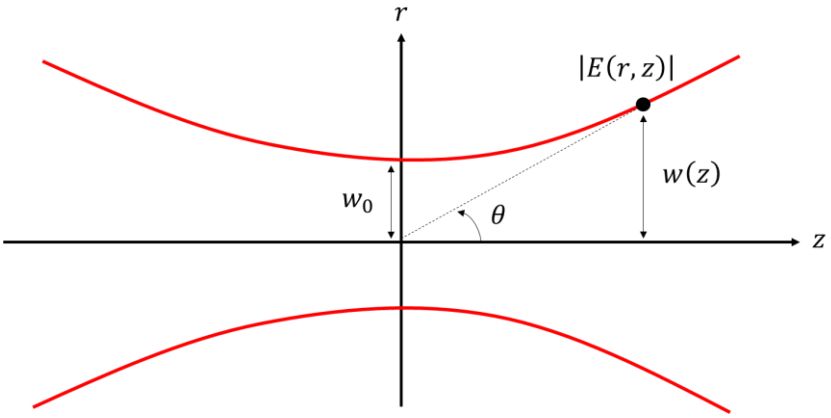

Figure 5.2: Propagation of a fundamental Gaussian beam

The amplitude of the electric field in Equation (5.1) is given by the following:

$$|E(r,z)| = \frac{w_0}{w(z)} \exp\left(-\frac{r^2}{w^2(z)}\right) = \frac{1}{\sqrt{1 + \frac{\lambda^2 z^2}{\pi^2 w_0^4}}} \exp\left(-\frac{r^2}{w_0^2 + \frac{\lambda^2 z^2}{\pi^2 w_0^2}}\right) \qquad (5.4)$$

Gaussian beam diverges at an angle of θ (see Figure 5.2), which is defined as $\tan\theta = r/z$. Therefore, the electric field modulus in Equation (5.4) becomes:

$$|E(\theta,z)| = \frac{1}{\sqrt{1+\frac{\lambda^2 z^2}{\pi^2 w_0^4}}} \exp\left(-\frac{z^2\tan^2\theta}{w_0^2+\frac{\lambda^2 z^2}{\pi^2 w_0^2}}\right) \tag{5.5}$$

Using Equation (5.5), the diffraction pattern of THz electric fields can be plotted as a function of different laser beam waists (the generated THz beam waist is considered to be equal to the laser beam waist in the crystal). Figure 5.3 shows the calculated results of THz field at 1 THz for different laser beam waists $w_0 = 0.03$, 0.3 and 1 mm at $z = 100$ mm.

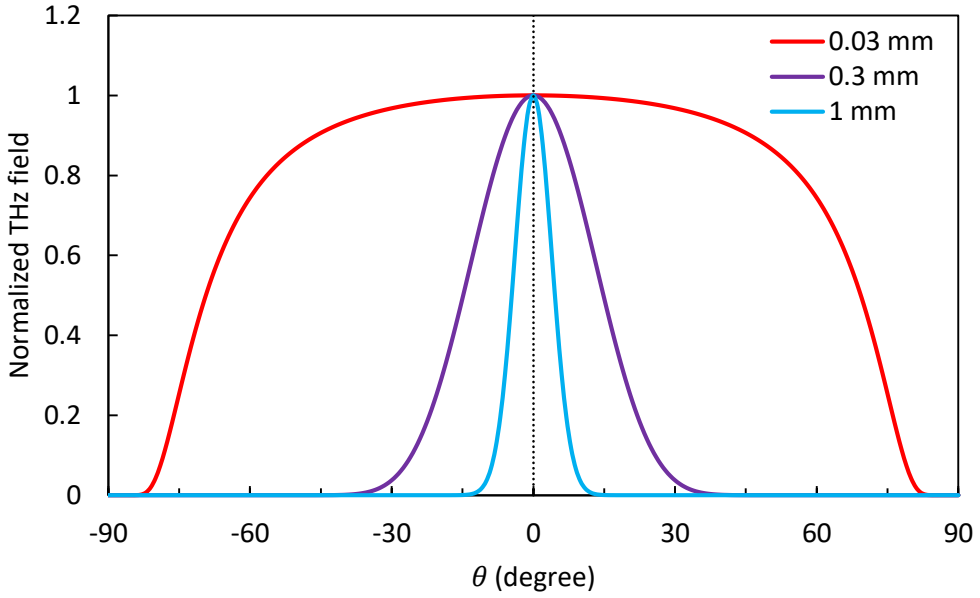

Figure 5.3: Normalized THz electric field at a distance of 100 mm from the centre of the beam versus the divergence angle θ. The diffraction patterns are plotted for three different beam waists.

In the far-field region where $\gg z_0$, we can compute the edge of the beam (*i.e*. the radius and thus the angle for which the field is 1/e as compared to its value at the optical axis) with the following equation:

$$\theta = \arctan\left(\frac{w(z)}{z}\right) = \arctan\left(\frac{\lambda}{\pi w_0}\right) \tag{5.6}$$

Here, θ is the divergence angle of the beam in far-field. Figure 5.4 shows the calculated angles for different beam waists for 1 THz Gaussian electric field. When w_0 is 0.1 mm, the beam propagates in a cone-shape with a half-cone angle of about 50°. Therefore, the beam can be considered as spherical.

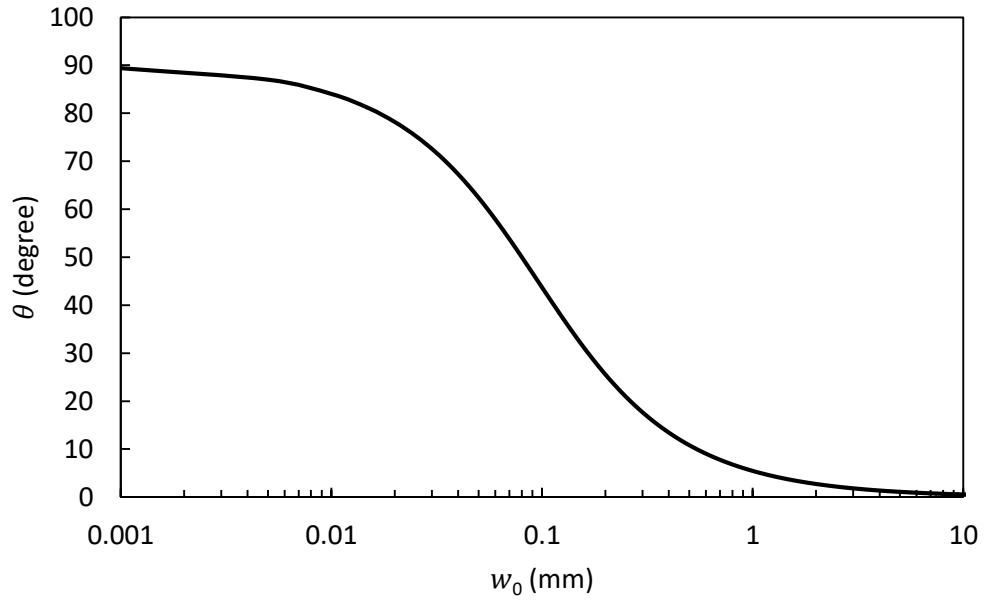

Figure 5.4: Calculation of the beam diverge angle as a function of beam waist.

In ORTI technique, the collection of the generated THz signal in the crystal depends on the optics. If R is considered as the radius of the collection optics, we find the amount of collected light using Equation (5.4):

$$S(R,z) = 2\pi \int_{r=0}^{R} |E(r,z)| r dr = \pi w_0 w(z) \left(1 - \exp\left(-\frac{R^2}{w^2(z)}\right)\right) \qquad (5.7)$$

Notice that, the second term is always positive and smaller than 1. Until now, we found that the Gaussian beam with smaller beam waist results in a larger divergence angle. Obviously, a collection optics with a higher R in Equation (5.7) can collect more signal and improve the resolution in our imaging technique.

In this Chapter, we present ORTI images obtained by two different setups. Our team previously imaged a sugar grain with a resolution of 50 µm by using a classical THz-TDS system including an amplifier laser [93]. In the first section in the Chapter, we imaged the thickness difference of two parts of an $LiNbO_3$ crystal with the same experimental setup used in their work. However, the amplifier laser delivers the pulses with a high peak energy. When the laser beam waist is reduced, it brings a risk of damaging the sample as the peak optical density increases on the sample. Therefore, we set another experimental setup with a simple laser oscillator delivering weaker pulse energy, as will be shown in the second section of the chapter. The new laser has higher repetition rate, so it allows to improve the noise ratio by averaging over more optical pulses. Additionally, a sensitive PC antenna is placed near the sample to detect the THz waves. With this new setup, we imaged ZnTe and periodically poled KTP crystals, and these results were presented in some conferences and submitted to a paper.

5.1 Imaging results using the first experimental setup

ORTI technique is installed in a typical THz-TDS system, so we can obtain the spectrum of the image. For this, we recorded THz waveforms for each position of the sample. In this section, the experimental setup will be described, and the imaging result will be shown.

Figure 5.5 shows the experimental setup used for the first ORTI technique (used in [93]), just with a small difference in the method of collecting the generated THz waves. An Ti:Sapphire amplified laser system (Coherent Libra) delivers optical pulses of 50 fs duration with an energy of 5 mJ at 800 nm, and at a repetition rate of 1 kHz. The pump laser beam is modulated by a mechanical chopper at 160 Hz, which synchronizes the lock-in amplifier detection. In the experiments, the power on the sample was controlled by a first half-wave plate (HWP) and a polarizer. In addition, a second HWP was placed to rotate the laser polarization. To obtain a smaller laser beam waist on the sample, the pump beam was focused by a lens. The sample to be imaged was placed on a translation stage to control laser excitation position on the sample. After the generated terahertz waves from the sample were collimated by parabolic mirrors, the terahertz beam was focused onto a 200 µm thick <111> ZnTe crystal for electro-optic detection. The main reason for using <111> ZnTe crystal is because the detection sensitivity in the ZnTe crystal is independent of the THz polarization [187]. It means that the ZnTe axis does not need to be rotated to optimize the THz signal, which can be optimized by just rotating the pump and probe laser beams. The laser probe beam illuminates the ZnTe simultaneously with the THz beam, and it is circularly polarized thanks to quarter wave plate (QWP). After the crystal, the laser beam becomes elliptically polarized because of the Pockels effect. It is split into two polarization components by a Wollaston Prism (WP). Therefore, these two beams are directed to two diodes of the balanced detector. The normalized difference of these two beams is made by the balanced detector electronics and is read by a lock-in amplifier. This difference can be optimized by rotating the elliptically polarized beam by a means of HWP just before WP. This setup is a typical THz-TDS system, so the waveform is obtained by varying the time delay between the pump and probe beams.

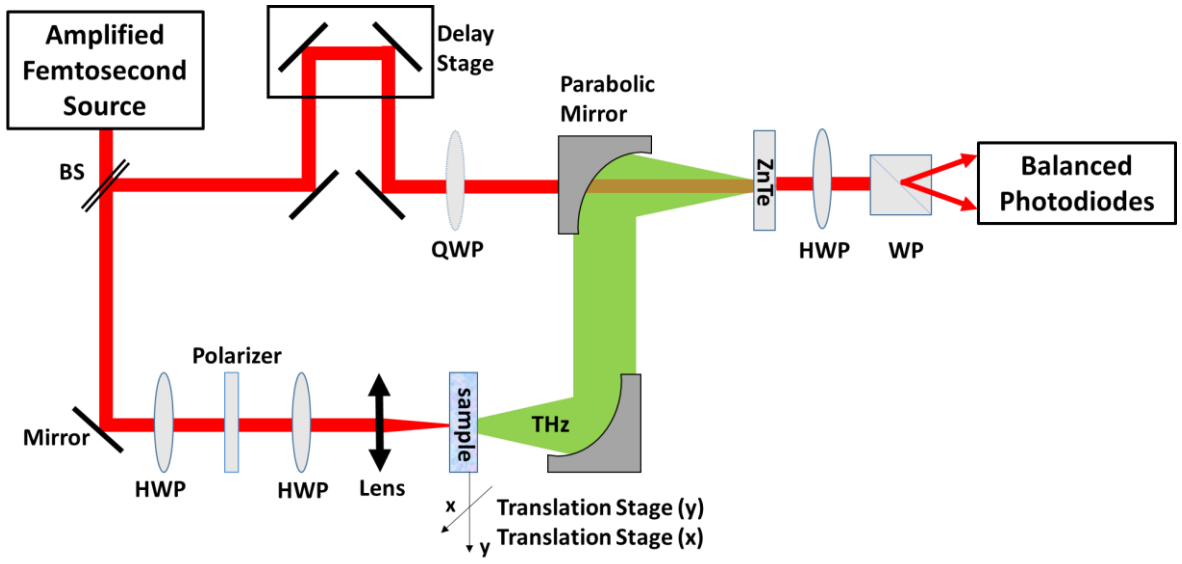

Figure 5.5: Optical layout of the first ORTI experimental setup

We initially started to work with this setup shown in Figure 5.5. After that, we decided to use another setup (discussed in Section 5.2), because the small beam waist at the crystal leads to high power densities with the amplified system. Let us evaluate the performance of the ORTI experiment fed with 1) an amplified laser system and 2) a non-amplified one. The relationship is described between the peak magnitude of the THz electric field and the laser field by using equations (3.24), (2.4) and (2.5):

$$\hat{E}_{THz} \propto \left(\hat{E}_{laser}\right)^2 \propto \frac{\hat{P}_{laser}}{\mathrm{S_{laser}}} \propto \frac{\bar{P}_{laser}\tau_{\mathrm{rep}}}{\Delta \mathrm{t_{pulse}} \mathrm{S_{laser}}} \tag{5.8}$$

The energy emitting from one pulse (U_{laser}) on the crystal is formulized by the average power of the laser over the repetition time rate of the laser:

$$U_{laser} = \bar{P}_{laser}\tau_{\mathrm{rep}} \tag{5.9}$$

Then, the average THz field generated by the laser energy is given by:

$$\bar{E}_{THz} = \frac{\Delta \mathrm{t_{pulse}} \hat{E}_{THz}}{\tau_{\mathrm{rep}}} = \frac{U_{laser}}{\tau_{\mathrm{rep}} \mathrm{S_{laser}}} \tag{5.10}$$

For example, we can consider the amplified and the non-amplified laser beams used in this thesis are focused with the same laser spot size on the crystal with a diameter of 50 µm. Table 1 shows the properties of the lasers and the calculated $\bar{E}_{THz}$ by using Equation (5.10). The amplified laser generates more THz field compared to the non-amplified one but we cannot illuminate most materials with the whole amplified energy. For typical dielectric materials such as Al_2O_3 and SiO_2, their laser-induced damage threshold (LIDT) with 100-fs pulses at 800 nm is about 1∼2 J/cm^2 [188]. The minimum average laser power that can be applied by the amplified laser is calculated to be 50 mW for these materials, which leads to a lower $\bar{E}_{THz}$ by a factor of 10^4. However, these materials can be illuminated with much higher average laser power with the non-amplified laser. Therefore, the non-amplified system should deliver stronger signals than the amplified one.

Table 1: Calculation of $\bar{E}_{THz}$ for two different lasers

Lasers	Repetition rate (s)	Maximum average laser power (W)	Calculated $\bar{E}_{THz}$ (W/cm^2)
Non-amplified laser	4×10^{-9}	0.1	5×10^3
Amplified laser	1×10^{-3}	5	2.5×10^5

In the next section, the setup is used for a preliminary study to image a $LiNbO_3$ crystal with an uneven thickness. We also discuss in the image of $LiNbO_3$ how the phase matching condition effects the generated THz signal.

In addition, we had the opportunity to study THz generation by OR in a langatate (LGT) crystal. This complementing work is presented in Appendix B. These original results are also described in a paper that will be submitted soon for publication in a journal.

5.1.1 Imaging with $LiNbO_3$

Lithium niobate ($LiNbO_3$) is a widely used crystal for generating THz waves through OR. Because of its large effective nonlinearity, it has 6.5 times higher figure of merit than the popular ZnTe crystal used for THz wave generation [107]. However, the THz refractive index of $LiNbO_3$ (n_{THz}) is almost 3 times larger than the optical group velocity refractive index (n_g). Therefore, the generated THz waves propagates along a cone with an angle ($\cos^{-1}(n_g/n_{THz})$) as compared to the laser beam propagation, which is analogue to the Cherenkov effect. Generating single-cycle THz field is accomplished by the tilted-pulse-front pumping technique, which was proposed first by Hebling *et al.* [189] for achieving an efficient phase-matching. In this section, we imaged a $LiNbO_3$ crystal with a varied thickness by the ORTI technique. This primarily study helped us to show the effect of the phase matching condition in ORTI, as well as to lead us to develop our next experimental setup.

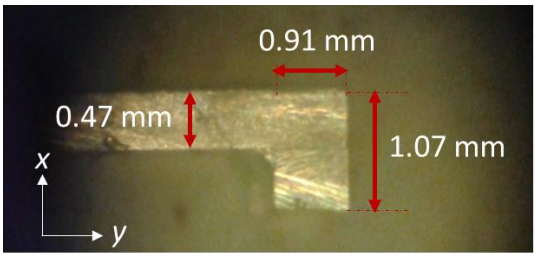

Figure 5.6: Dimensions of $LiNbO_3$ crystal used to be imaged.

The dimensions of the sample are shown in Figure 5.6 with two perpendicular directions, denoted *x* and *y*. The crystal has a thinner region (0.47 mm) and a thicker one (1.073 mm), and both regions were illuminated by the laser beam propagating along *x* direction. Figure 5.7 (a) shows the generated THz signals in these regions by optical rectification. As the thicknesses of these regions are different, a time difference between the two generated THz peaks appears. The thickness difference of the two regions is simply equal to $\Delta d = \Delta t \frac{c}{(n-1)}$, where $\Delta t \approx 11$ ps is the recorded time difference of THz peaks and n is the refractive index of the crystal. The thickness difference is calculated correctly with the refractive index of the crystal at the THz frequency, which means that the THz waves were generated at the entrance of the crystal.

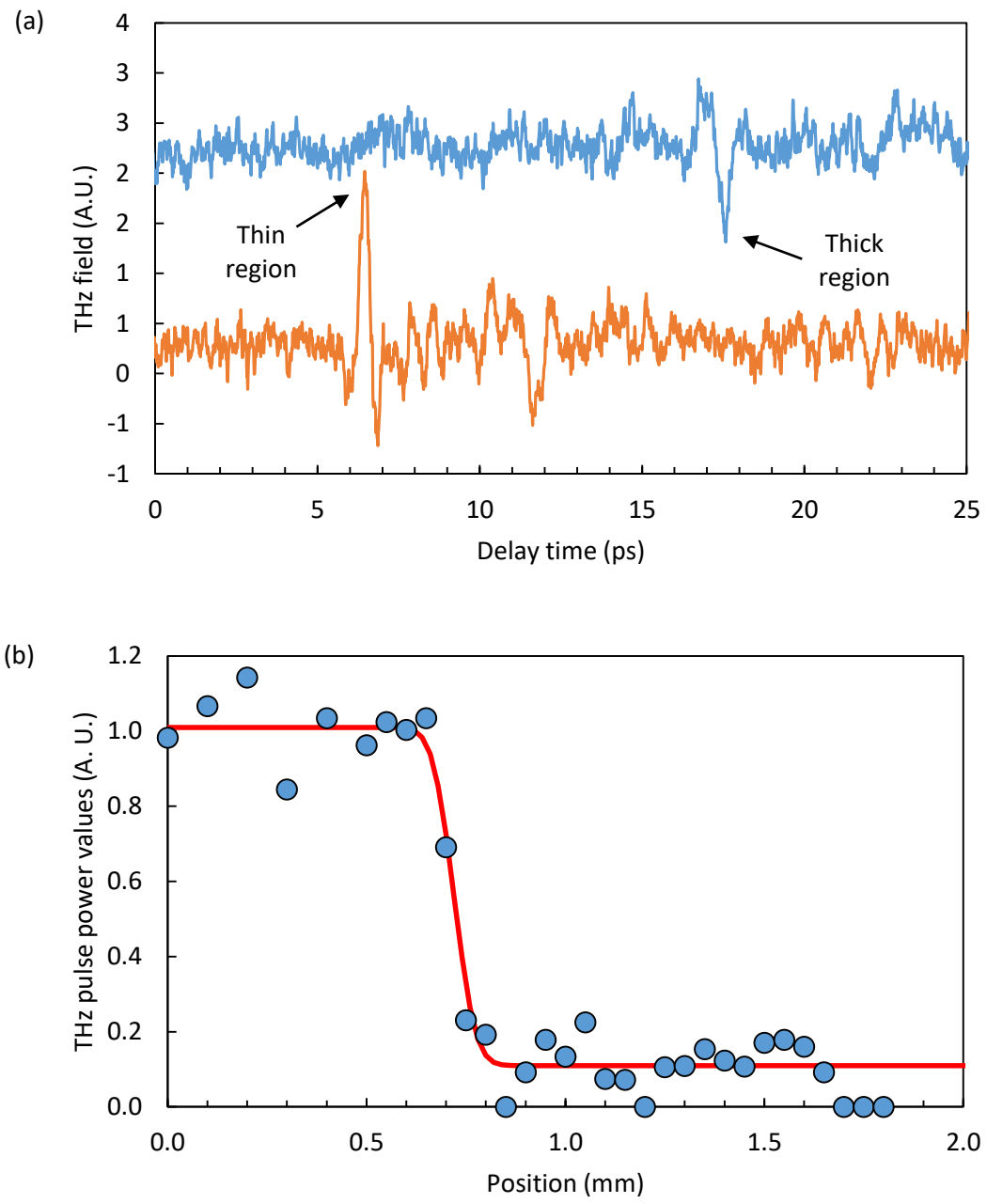

Figure 5.7: (a) Generated THz signal waveforms from the thinner area (orange line, peak 1) and the thicker area (blue line) of the LiNbO3 crystal. (b) Generated THz pulse peak amplitude (blue circles) in the LiNbO3 crystal versus position along one axis. The data are fitted with Equation (4.8) (red line)

ORTI imaging of $LiNbO_3$ crystal was performed along the *y* direction by recording the THz signals. Firstly, the THz signal is generated in the thinner region then scanned along the y axis towards the thicker region. Figure 5.7 (b) shows the ORTI image obtained by the square of the measured amplitudes of the THz signals along the scanning axis. By using Equation (4.8), we calculated the beam waist of the laser as 60 µm which corresponds to 100 µm lateral resolution (see calculated fit as a dashed line in Figure 5.7). As it is seen in Figure 5.7 (b), less THz signal from the thicker area of the $LiNbO_3$ crystal is obtained comparing to the thinner region. This can be due to phase-matching condition in the crystal. As it is discussed before in Section 2.1.1 of the manuscript, the phase matching

is fulfilled when the group velocity of the pump frequency is equal to the phase velocity of the generated THz frequency, *i. e.* energy conservation for photons. Even a crystal with a high nonlinear coefficient can suffer from the poor phase matching. For example, the $LiNbO_3$ crystal has a higher nonlinear coefficient than the common crystals (ZnTe, GaP, GaAs) but almost three times larger refractive index in THz range than in the infrared range [190]. If a phase matching condition is satisfied in a crystal, the intensity of the generated THz wave increases as the square of the length of the nonlinear crystal. Otherwise, the generated THz wave and optical wave cancel each other out and the THz intensity become low. Here, we can formulize the intensity of the generated THz wave by optical rectification for position r in the crystal by using Equation (3.27) at angular frequency ω_{THz}:

$$I(\omega_{\mathrm{THz}}, r) \propto \mathrm{sinc}^2\left(\frac{\omega_{\mathrm{THz}}}{2c}(n_{THz} - n_{laser})r\right) r^2 \exp(-\alpha_{THz} r) \tag{5.11}$$

where n_{THz}, n_{laser} and α_{THz} are the THz refractive index, the refractive index of the femtosecond source (λ=800 nm) and the THz absorption coefficient in $LiNbO_3$ crystal; the values are 6.5, 2.25 and 25 cm^{-1} for 0.5 THz, respectively [191]. Figure 5.8 shows the generated THz intensity while being scanned along the *y*-axis of the $LiNbO_3$ crystal. The ratio of the intensity of THz signals generated from the thinner and the thicker regions of the crystal regions was determined to be almost 9.2 experimentally, with a theoretical value of 8.8 according to Figure 5.8. The agreement between the theory and the experiment is almost perfect, and the result demonstrates that the generated THz signal from the thicker region is weaker than the thinner region of the crystal because of the phase matching condition in the crystal. Additionally, the change of thickness in the sample can be estimated by using Equation (5.11) for the ORTI images.

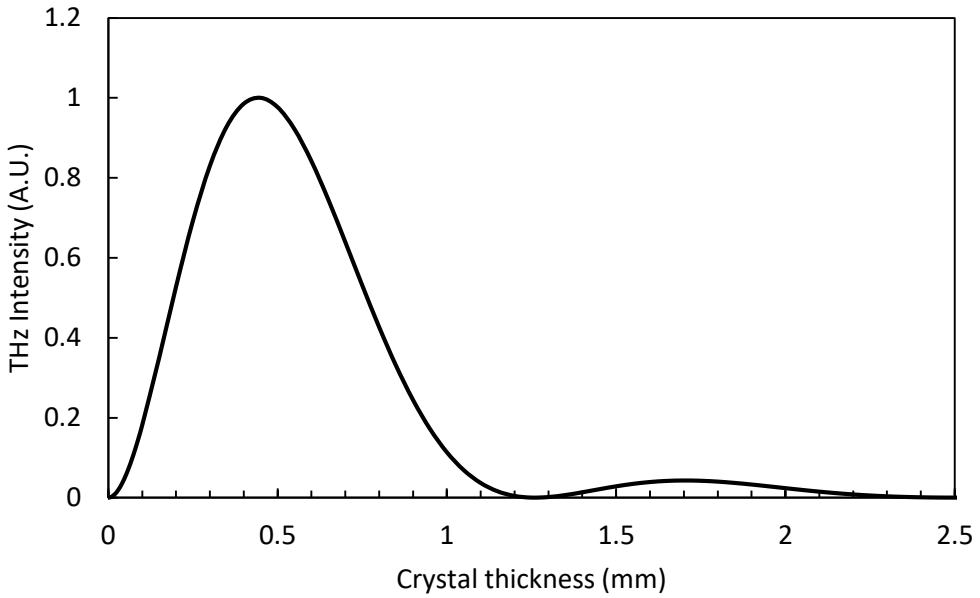

Figure 5.8: Calculated THz intensity for LiNbO3 crystal by using Equation (3.27)

This primarily result showed us the importance of the phase-matching condition in the transmission mode of ORTI technique. The phase-matching can be advantageous for some crystals as the optical and THz waves interfere constructively. If a sample cannot satisfy the phase-matching

condition perfectly, the generated THz signal might not be high enough to be detected. This might be solved by imaging the sample in reflection mode. In addition, we decided to build another setup because of high peak pulse energy provided by the amplified laser on the sample. Since the aim of this study is to reach a subwavelength resolution, we needed to reduce the laser beam waist on the crystal. However, the repetition rate of the laser is high, even with very low average laser power (0-1 mW) we observed that the samples were damaged. In the following, we will see the ORTI images obtained by the new experimental setup.

5.2 Imaging results done by second experimental setup

In this section, we introduce a new experimental setup mainly used for this thesis. The previous setup included an amplifier laser to generate THz waves through the nonlinear material and an electro-optic detection to record the THz signal. However, the problem of using an amplified laser is that the high energy peak pulses can cause damage to the sample when the laser beam waist is smaller, *i.e*. greater image resolution. In the new experimental setup, a simple laser oscillator delivering weaker pulse energy but at higher repetition rate is used; this brings less damage risk of the sample and enables the signal-to-noise level to be increased by adding more optical pulses, which compensates for the weaker pumping peak power. In addition, we used a photoconductive antenna that was mounted as a detector near the sample. With this new experimental setup, we recorded THz waveforms at each point of the sample, and thus we produced a hyper-spectral image.

Figure 5.9 shows the second THz-TDS imaging setup used in this work. The setup includes a femtosecond laser (Femtolaser Synergy M1) emitting optical pulses with a 15 fs duration at a repetition rate of 100 MHz. The THz microscopy system is again a typical pump-and-probe setup, in which the laser beam is separated into two beams with a beam splitter (BS). The pump beam was modulated by an optical chopper with a frequency of 130 Hz used as a reference of a lock-in amplifier. The laser average power on the sample was 140 mW maximum, and it can be decreased by the placement of optical densities. In the measurements, the laser beam was focused by a lens placed on a linear stage to vary the distance between the lens and the sample and thus to adjust the beam waist on the samples. Two different lenses were used: one is a lens with a focal length of 3 cm, and the other is a microscope objective with a magnification factor of 4 (parfocal length of 4.5 cm). The THz signal was generated within the sample located on a stage controlled by a computer. The transmitted THz signal through the sample was collimated with a Teflon lens (focal length, 1.5 cm). In addition, this Teflon lens is thick enough (2.5 cm) to block the remaining laser light transmitted through the sample. Afterwards, the THz signal was focused onto a low-temperature grown GaAs THz antenna (producer: Teravil company). This antenna involves a High-Density Polyethylene (HDPE) silicon lens to focus the incoming THz wave in between its gold metal electrodes. Let us notice that the PC antenna detector is only sensitive to one polarization direction of the THz beam [192] so the detected THz signal was optimized by rotating the pump beam with a HWP before the crystal. On the probe path, the laser beam was focused onto the antenna with a lens (focal length, 5 cm). The detection of THz signal in time-domain was obtained by varying the time between the probe and the pump with a delay line mechanism. After, this signal was transformed to the frequency domain with a Fast Fourier Transform.

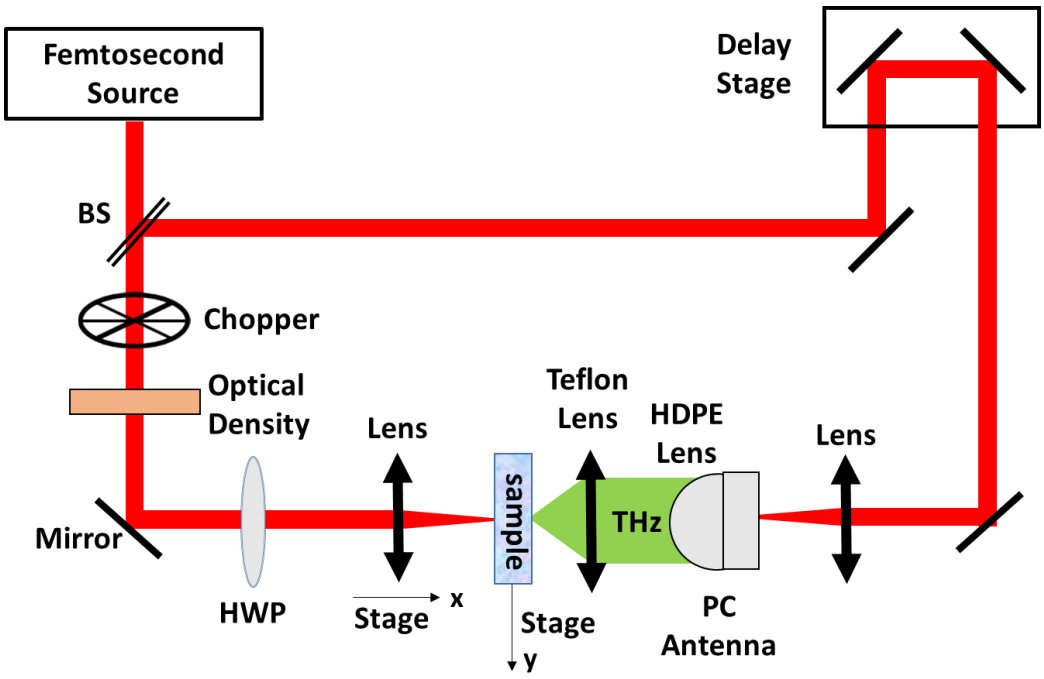

Figure 5.9: Optical layout of the second ORTI experimental setup

The ORTI images of the samples were obtained by recording the generated THz signal for each position on the sample. The moving of samples was controlled with a motorized stage in perpendicular direction of the laser beam. Two different samples were used to image by using this setup: 2 slivers of a ZnTe <111> crystal and a periodically poled KTP crystal. In the following, we will see the obtained 1D images. All the images in this section were either presented in conferences (IRMMW-THz 2019 in Paris/France, RJUSE 2019 in Nizhny Novgorod/Russia, SNAIA 2019 in Paris/France), published as a conference paper [193] and submitted to a journal [194].

5.2.1 Imaging the ZnTe slivers

The new experimental setup shown in Figure 5.9 was firstly used to image a high nonlinear crystal, ZnTe. For this, two grains of about 300 µm thick ZnTe crystals with <111> orientation were stuck next to each other on a rubber tape. Firstly, we optimized the generated THz wave from the first grain by rotating the HWP in the setup, and then the grains were scanned along one axis with a step size of 10 µm. Additionally, we recorded the THz waveforms at each point so a hyperspectral-like image can be obtained with these transmitted spectra. After this, another ZnTe crystal was scanned along two axes with ORTI.

Figure 5.10 shows the obtained ORTI image along one axis of the sample at different THz frequencies, together with a photography of the two grains of ZnTe. As we expected, the spatial resolution of the image in Figure 5.10 (a) is independent of the generated THz frequency, which shows that it depends only on the laser beam waist on the sample. Here, the beam waist on the samples was measured using a razor blade technique and was calculated as 25 µm (corresponding to 41 µm lateral resolution by using equation $2w\sqrt{ln2}$, w=25 µm).

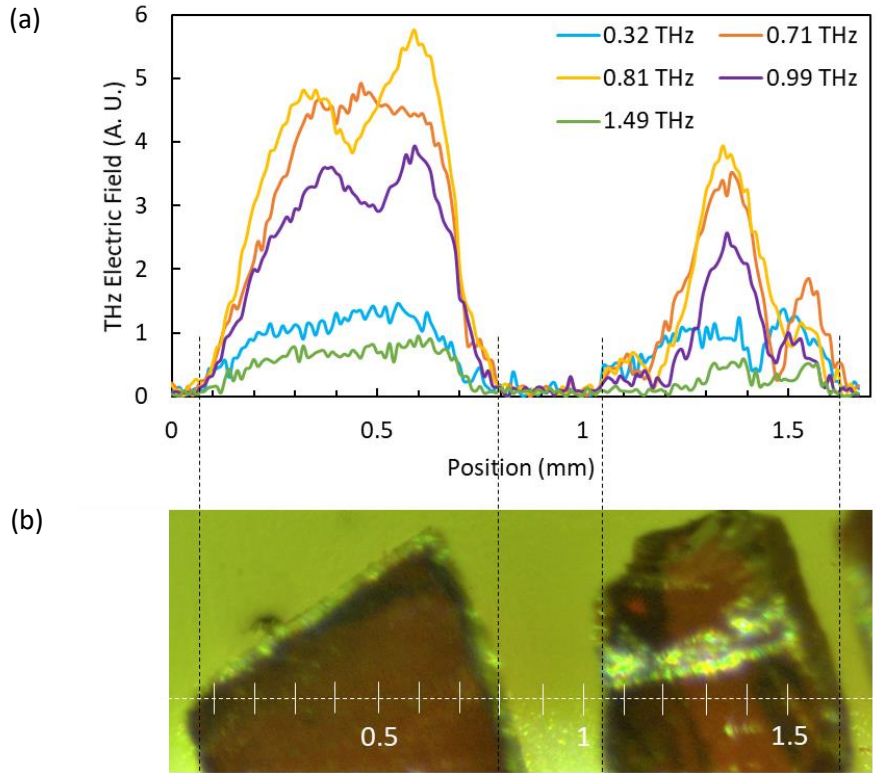

Figure 5.10: (a) THz signal versus position along the scanning line on the ZnTe grains at different frequencies: 0.32, 0.71, 0.81, 0.99 and 1.49 THz. (b) Photography of two grain ZnTe crystals: the white dashed line is the scanning line.

Moreover, some areas of the crystal in the image give a weaker THz signal for certain wavelengths (see the 0.5 mm position in Figure 5.10 (a)). This observation has several possible explanations:

1. Fabry-Pérot resonances inside the crystal at THz frequencies: the thickness of the samples is about 0.3 mm, so their optical thickness is $d_{eff} = n_{THz} d \approx 1.005$ mm. Interference (Fabry-Pérot) resonances occur at frequencies $f_m = \left(m + \frac{1}{2}\right) \times 149$ GHz. Figure 5.11 shows the calculated transmission of the ZnTe slab versus frequency, together with data extracted around the crystal at position of 0.5 mm in Figure 5.10 (data were normalized to the maximum in the range 0.2-0.7 mm).

2. Phase-matching effects: the phase matching function in Equation (3.27) is plotted in Figure 5.11 for ZnTe with a 0.3-mm thick sample. Due to the long coherence, the result does not show any special spectral feature, and thus the lack of phase-matching cannot explain our results.

3. Scratches, cracks or thickness variation along the crystal cannot explain the observation around the crystal at position of 0.5 mm, because their effect should be visible whatever is the frequency.

In conclusion, Fabry-Pérot effects are more likely the reason of the feature observed around the crystal at position of 0.5 mm. Between 1.1 and 1.2 mm positions, we observe another dip in the

curves. Here, the dip is seen whatever the frequency is. Therefore, it is certainly due to a scratch at the sample surface or a crack inside the crystal (cracks could appear when we broke the ZnTe wafer to produce slivers).

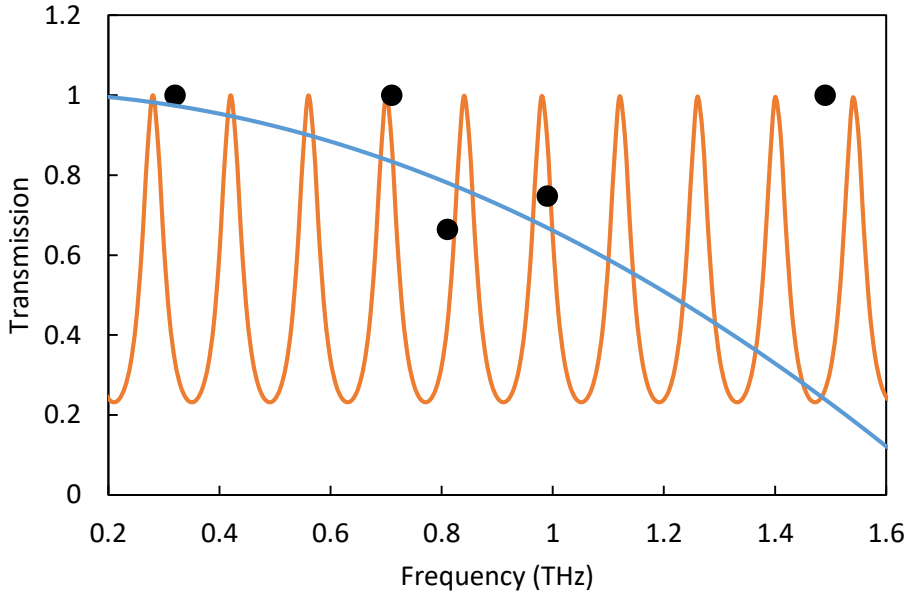

Figure 5.11: Fabry-Pérot effect (orange line), phase matching effect (blue line) and experimental results (black circles)

In the next experiment, we imaged a corner of the ZnTe <111> cut crystal with a thickness of 200 µm. The ORTI image of this sample is shown in Figure 5.12 (a). We aimed to obtain a 2D image of the sample, for this: a vertical translation stage to move the sample was added in the setup. Like in the previous experiment, the sample is located in the same position far from the lens used to focus the laser beam on the sample, so the lateral resolution is also 41 µm. The THz waveforms were recorded for each 5 µm step. Figure 5.12 (b), (c) and (d) show the obtained ORTI image at 0.3, 0.5 and 0.8 THz frequencies, respectively. The shape of the edge is nicely reproduced by the ORTI images. As expected, the resolution is independent on the THz frequency. Nevertheless, at 0.8 THz, the image is noisier and less contrasted because the signal is weaker than at 0.3 and 0.5 THz. The difficulty of this experiment is that the whole experiment took 8 hours. Therefore, we continued to scan the other samples only in one axis. In the next section, the ORTI images of the periodically poled crystal will be given in 1D.

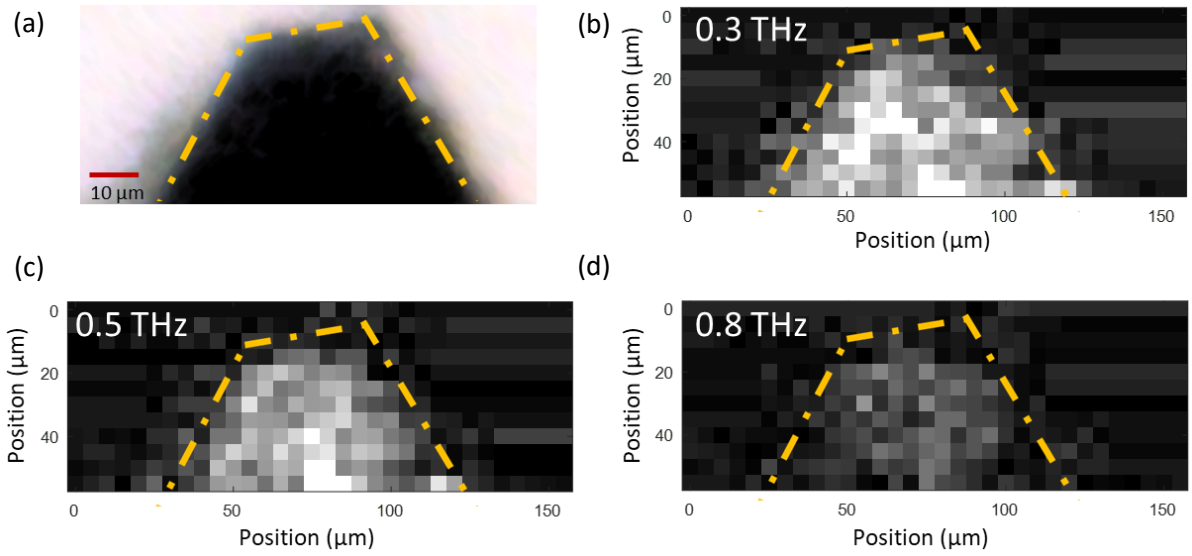

Figure 5.12: Photography of ZnTe <111> cut crystal : the yellow dashed line respresents the border of the sample (a). ORTI image of the sample at 0.3 (b), 0.5 (c) and 0.8 (d) THz frequencies.

5.2.2 Imaging with PPKTP

Potassium titanyl phosphate ($KTiOPO_4$, KTP) is one of the most used crystals in nonlinear optical applications because it exhibits high nonlinearity, low absorption in the range of 340 nm to 4500 nm, high damage threshold of 30 GW/cm² (8-11 ns pulse at 1064 nm wavelength) and wide wavelength range for SHG phase matching [195–197]. In addition, KTP is a ferroelectric crystal which makes it possible to form periodic polarization reversing by applying an intense electric field, which inverts the crystal structure in periodic domains. These periodically poled KTP (PPKTP) crystals are used for generating efficient frequency conversion at preferred wavelength [198,199], for tuneable optical parametric oscillators [200] and for mode-locking operation [201]. It is important to control the formation and quality of the domains of the periodically poled crystals in order to achieve a high performance from the devices. The ferroelectric domain patterns could indeed be affected by different factors such as crystal impurities, and shape and crystal defects occurring during fabrication. Therefore, imaging the domains is indispensable to inspect the domain properties. Until now, various methods have been developed to image the ferroelectric domains [202] such as X-ray imaging [203,204], atomic force microscopy [205] and piezoresponse force microscopy [206]. Additionally, second harmonic generation (SHG) microscopy is widely used for imaging the domains [207,208]. However, it is difficult to identify the polarization direction of the domains due to the loss of phase information in the intensity detection of the second harmonic wave. On the contrary, the polarization direction can be directly determined by terahertz imaging technique. The ORTI, which is based upon mapping out the terahertz radiation by irradiating femtosecond pulses in non-centrosymmetric crystals, has been used before to image the domains of the crystals by Sotome *et al.* [91,92]. In their work, the aim was not the microscopy. Here, in this section, we use the ORTI technique to image the domains of a PPKTP crystal with a sub-wavelength resolution. To distinguish one domain to its neighbouring domain, we expect that THz field generation should be inverted. In this section, we give general information about the structure of periodically poled crystals, then present the ORTI images of a PPKTP crystal with a different lateral resolution which is determined by the adjacent domains.

Why a periodical structure?

In any nonlinear optic process, the nonlinear propagation equation includes the linear Helmholtz equation together with a nonlinear polarization term, which depends on the pumping field. The general solution for such an equation is the sum of a free wave and of a forced wave. The free wave is the solution of the linear Helmholtz equation, while the forced term is a particular solution of the whole nonlinear equation. The free wave propagates with a wavevector $k_o = \frac{\Omega}{c} n_\Omega$, where Ω is the nonlinear angular frequency and n_Ω is the refractive index at this nonlinear frequency. The forced wave is driven by the nonlinear term, and thus its wavevector k_g is that of the nonlinear polarization (in this general introduction, we do not give an explicit expression of k_g as it depends on the involved nonlinear phenomenon). Both free and forced waves propagate simultaneously and interfere inside the crystal. The interference phenomenon is driven by the wavevector difference $\Delta k = k_g - k_0$. Depending on the phase difference ΔkL, where *L* is the crystal length, the generated nonlinear beam can be strong, or weak, or even null. Strong signals are achieved when $\Delta k = 0$, *i.e*. phase-matching, for which both forced and free waves interfere positively. When $\Delta k \neq 0$, the generated nonlinear signal first increases with the thickness L, then decreases, and so on, with a periodicity equal to the nonlinear phenomenon coherence length L_C ($L_c = \pi/\Delta k$). To avoid the oscillating behaviour, a smart technique has been proposed by Armstrong *et al.* [209] at the early times of nonlinear optics. The idea is to take a crystal of thickness equal to L_C . Thus the signal is maximum at the output of this crystal. Then one adds a similar crystal in which the crystallographic orientation in inverted, such as the nonlinear polarization is also inverted. Instead of starting to decrease due to destructive interferences, the signal increases. By adding several inverted layer in the stack, intense nonlinear signals can be produced. Therefore, the crystal orientation of the sample must be periodically converted physically along in a period of the crystal length depending on the wavelength of the light and the temperature of the crystal [196]. The intensity of the generated wave at the frequency Ω is [210] :

$$I(\Omega) \sim L^2 \, sinc^2 \left(\frac{\Delta k . L}{2} \right) \tag{5.12}$$

where *L* is the propagation position in the crystal.

Figure 5.13 shows the generated wave intensity as a function of the coherence length in the crystal for three different cases of the phase matching. If Δk is zero, the phase-matching (PM) is perfectly satisfied and the intensity of the generated wave increases as the square of the propagation distance. If Δk is nonzero, non-phase matching (non-PM) occurs, so the intensity oscillates periodically with the distance. However, in the case of quasi phase matching (QPM), the orientation of the crystal is periodically modulated and the intensity increases at the each twice of the coherence length.

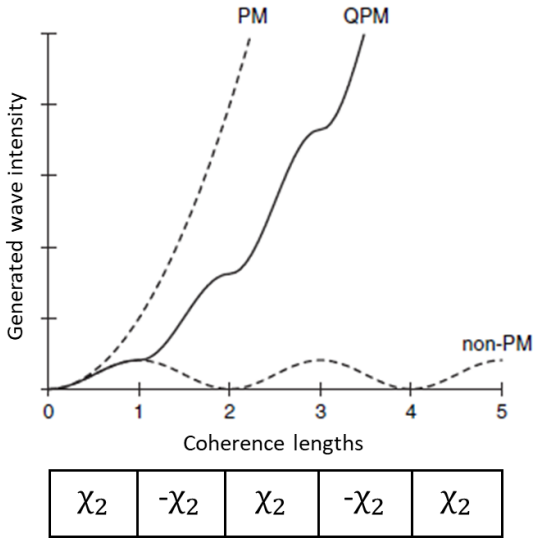

Figure 5.13: Generated wave intensity versus coherence length along the crystal for the cases of phase matching (PM), quasi phase matching (QPM) and non-phase matching (non-PM) (Figure taken from [211])

5.2.2.1 THz generation in KTP crystal

Periodically-poled crystals have been used for a long time to generate THz radiation through quasi-matching between the pump laser beam and the THz one [212]. Here our goal is different: we desire to image the domains of a PP crystal. Thus the pumping beam will scan the lateral side of the crystal instead of propagating along its axis as in quasi-phase-matching experiments. The experimental setup is the same as in Figure 5.9. The polarization of the generated THz beam will be inverted between two neighbour domains. Let us demonstrate why.

KTP belongs to the point group symmetry mm2 [213] ,and it has five independent nonzero tensor elements. So the second order nonlinear tensor gets the form:

$$d = \begin{pmatrix} 0 & 0 & 0 & 0 & d_{15} & 0 \\ 0 & 0 & 0 & d_{24} & 0 & 0 \\ d_{31} & d_{32} & d_{33} & 0 & 0 & 0 \end{pmatrix} \tag{5.13}$$

where d_{ij} is the nonlinear coefficients in Cartesian coordinates. Obtained second order nonlinear polarization at THz frequency is:

$$\vec{P}_{THz}^{NL} = \varepsilon_0 d \begin{pmatrix} E_x^2(\omega) \\ E_y^2(\omega) \\ E_z^2(\omega) \\ 2E_y(\omega)E_z(\omega) \\ 2E_x(\omega)E_z(\omega) \\ 2E_x(\omega)E_y(\omega) \end{pmatrix} = \varepsilon_0 \begin{pmatrix} 2d_{15}E_x(\omega)E_z(\omega) \\ 2d_{24}E_y(\omega)E_z(\omega) \\ d_{31}E_x^2(\omega) + d_{32}E_y^2(\omega) + d_{33}E_z^2(\omega) \end{pmatrix} \tag{5.14}$$

Here $E(\omega)$ is the magnitude of the electric field of the laser beam at optical frequency ω, and *x,y,z* represent the crystallographic axes. Each domain of the crystal periodicity Λ , for which the orientation of the crystal is flipped in the *z*-axis, is shown in different colours in Figure 5.14.

Assuming that the linearly polarized laser beam propagates along the *y*-axis and makes an angle of ϕ with *x*-axis. Figure 5.14 shows the cases for "up" and "down" which means that the crystallographic *z*-axis of each domain is oriented along *z* and *-z*. For "up" case, the electric field of laser beam is described as:

$$\vec{E}(\omega) = E(\omega)\begin{pmatrix}\cos\phi\\0\\\sin\phi\end{pmatrix} \tag{5.15}$$

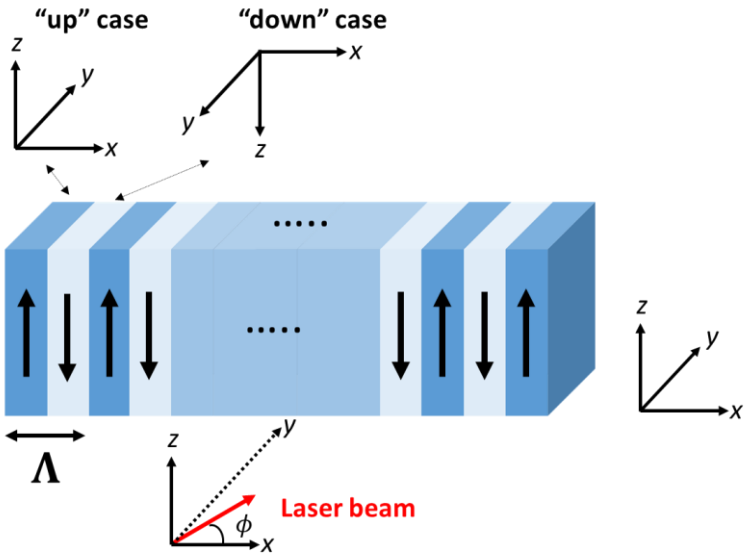

Figure 5.14: Periodically poled KTP crystal and crystallographic axes

Substituting Eq. (5.15) into Eq. (5.14), the generated second order nonlinear polarization is:

$$\vec{P}_{THz}^{NL} = \varepsilon_0 E^2(\omega)\begin{pmatrix}d_{15}\sin(2\phi)\\0\\d_{31}\cos^2\phi + d_{33}\sin^2\phi\end{pmatrix} \tag{5.16}$$

On the other hand, for "down" case, the z component of the electric field of the laser beam is oriented along *–z*, so Equation (5.15) becomes:

$$\vec{E}(\omega) = E(\omega)\begin{pmatrix}\cos\phi\\0\\-\sin\phi\end{pmatrix} \tag{5.17}$$

Using Eq. (5.17) , we obtain the second order nonlinear polarization as:

$$\vec{P}_{THz}^{NL} = \varepsilon_0 E^2(\omega) \begin{pmatrix} -d_{15} \sin(2\phi) \\ 0 \\ d_{31} \cos^2 \phi + d_{33} \sin^2 \phi \end{pmatrix} \tag{5.18}$$

Because the THz field is detected by PC antenna, this antenna is sensitive just the *z* component of the THz field. Therefore, we need to change the sign of the *z* component of the nonlinear polarization in Eq. (5.18). Now, the second order nonlinear polarization for the "down" case is defined in laboratory frame as:

$$\vec{P}_{THz}^{NL} = \varepsilon_0 E^2(\omega) \begin{pmatrix} -d_{15} \sin(2\phi) \\ 0 \\ -d_{31} \cos^2 \phi - d_{33} \sin^2 \phi \end{pmatrix} \tag{5.19}$$

Equations (5.16) and (5.19) show that the sign of the THz field varies from positive to negative values when scanning the laser along the *x*-axis. In case of the detection of *z* component of the THz field, the generated THz signal depends on two different tensor elements d_{31} and d_{33} for the crystal orientation along *z*-axis. While choosing the laser polarization angle ϕ as 90°, the THz field depends on only d_{33}, and it depends on only d_{31} for ϕ as 0°. Additionally, the z component of THz field shows that whatever the laser polarization angle is, there is always generated THz radiation. On the other hand, the *x* component of THz field depends on only one tensor element d_{15}, and it can be determined when the laser polarization angle ϕ is equal to 45°.

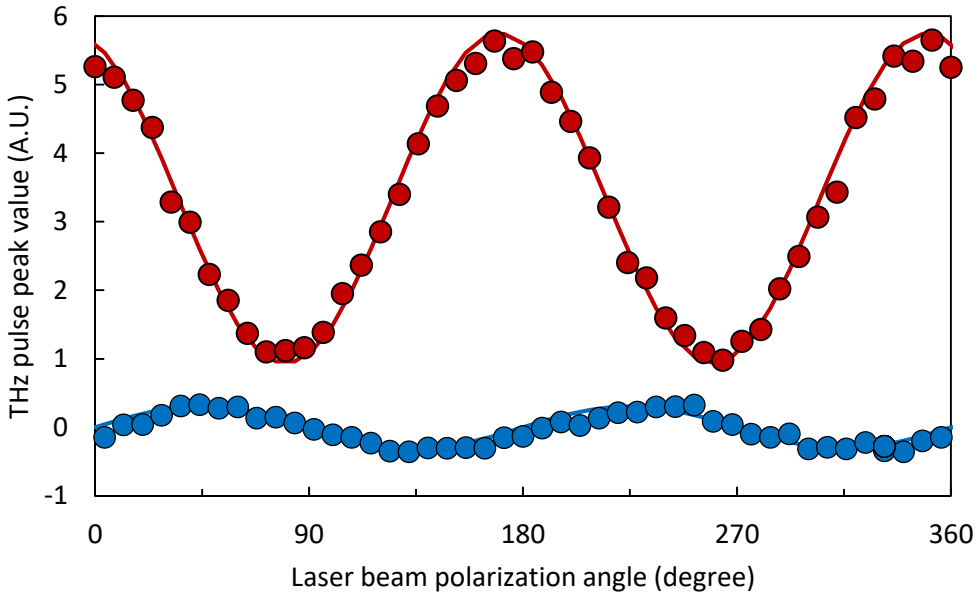

Figure 5.15: THz peak values as a function of the laser beam polarization angle. Red circles and blue circles are the experimental data for z component of THz field and x component of THz field, respectively. Red line and blue line are the fitted lines.

In our experiment, the thickness of PPKTP crystal is 440 µm. Phase matching condition is in the constructive part for this thickness [196]. We recorded generated THz peak values in one domain of PPKTP crystal for each laser polarization angle ϕ. The measured data are seen in Figure 5.15 with red circles for the detection of the *z* component of the THz field and blue circles for the *x* component.

To record the *x* and *z* components of the generated THz field, the sample was rotated by 90°. For KTP crystal, the second order nonlinear tensor elements are $d_{15} = 2.04$ pm/V, $d_{31} = 2.76$ pm/V and $d_{33} = 18.5$ pm/V (at 880-nm light) [214]. The signal from the *x* component of THz filed is weaker since the tensor element d_{15} is the lowest one comparing the other tensor elements. The experimental data were fitted by using Equation (5.16) and the tensor ratios d_{33}/d_{15} and d_{33}/d_{31} . The results in Figure 5.15 show a good agreement between theory and experiment.

5.2.2.2 Imaging PPKTP domains

The PPKTP crystal used in our experiments has a thickness of 440 µm (along the *y*-axis), a width of 1030 µm (along the *z*-axis) and a length of 9740 µm (along the *x*-axis). The next measurement was performed to compare the generated THz beams in two neighbouring domains of the periodic structure of KTP crystal. Figure 5.16 (a) and (b) show the obtained THz waveforms and the spectrums for these beams. As we expect, the polarization of the generated THz waves are inverted as the crystal orientation is flipped inverted.

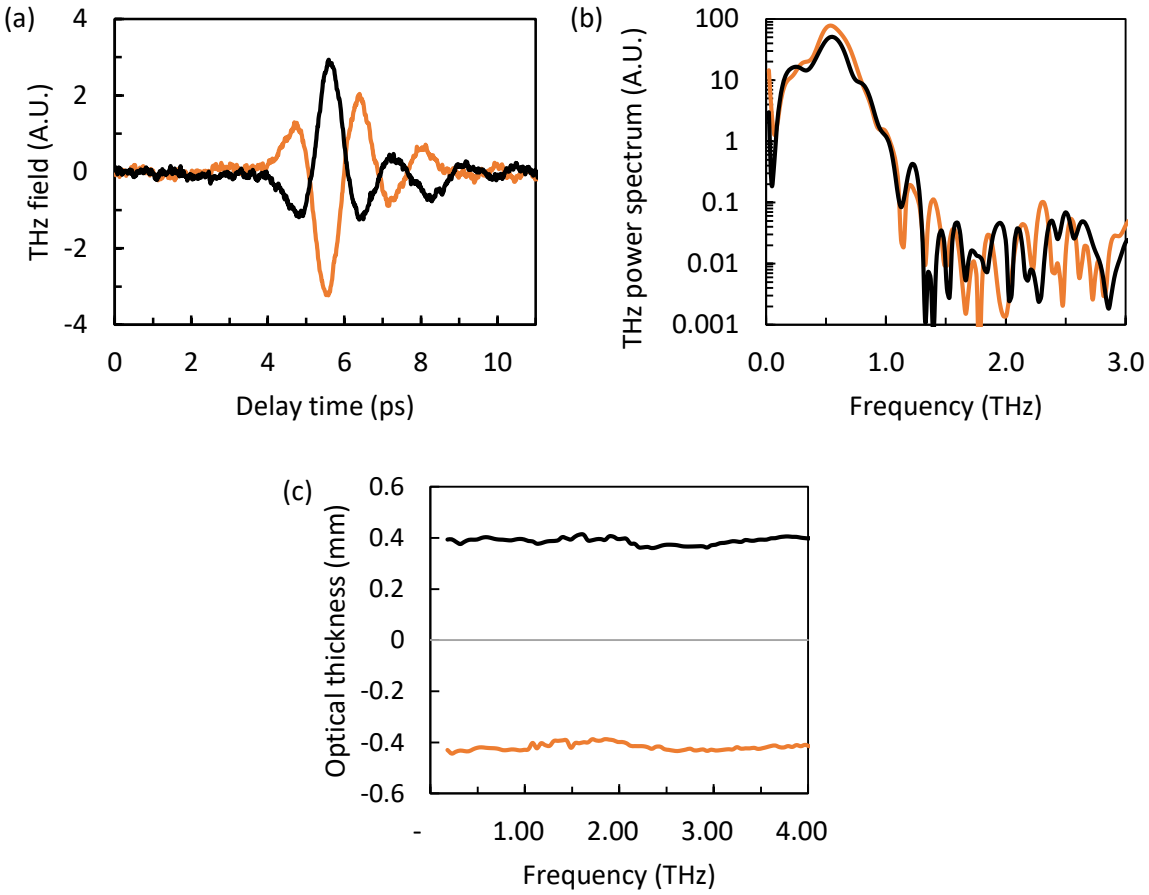

Figure 5.16: Obtained THz waveforms (a), spectrums (b) and optical thickness (c) in two different domains. The same colour for the waveform and the spectrum represent the measurement in the that domain.

Optical thickness (or distance) in a medium is the product of the geometrical thickness of the sample ($L = 1.03$ mm) and the refractive index of the medium ($n_{THz} \approx 4$ [195]), *e.g.* $d = n_{THz}L \approx$

4.12 mm for PPKTP crystal. The optical thickness is used to determine the phase of the light. As the obtained Fourier-transformed signal include the phase information, corresponding optical thickness with the obtained phase that is dividing the phase of the Fourier-transformed signal by ω_{THz}/c. Figure 5.16 (c) shows the calculated optical thickness by Fourier-transformed signal, which is around $d = 2 \times 0.4$ mm $= 0.8$ mm between two domains. This value is quite different than the theoretical calculated one, *i.e.* 4.12 mm. It means that the THz signal is mainly generated close to the output surface of the crystal.

In our experiment, we imaged different domains of a 440-µm thick-PPKTP crystal. The periodicity (Λ) of the crystal is 500 µm. The propagation of the laser beam was along *y*-axis, and the detection of THz beams was along *z*-axis. The average laser power on the crystal is 44.5 mW. We recorded the peak values of THz field when crystal was moved step by step along the x-axis. For these measurement we used a microscope objective (magnification 4x, numerical aperture 0.1 and focal length 45 mm). Figure 5.17 shows these measured peak values versus the crystal position along the *x* direction. As expected the signal varies from positive to negative from one domain to another.

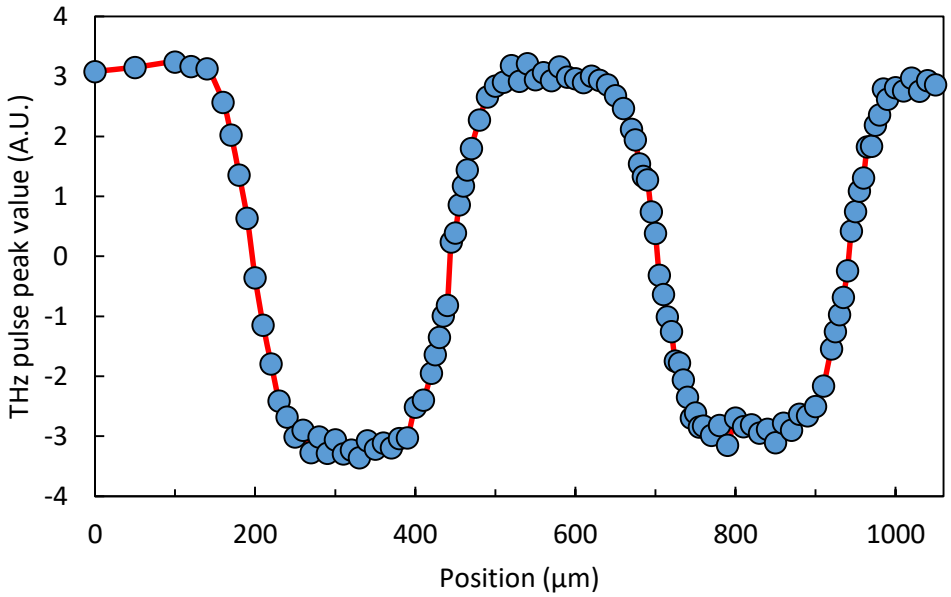

Figure 5.17: Peak amplitude of generated THz signal (circles) by optical rectification in the PPKTP crystal versus position along the *x*-axis. The experimental data (circle) was fitted using Equation (5.24) (red line).

In the image shown in Figure 5.17, the sample was not at the focus point for the microscope objective. The resolution of the image can be easily determined at the point where the laser beam crosses from one domain to next. Assuming the laser beam as a Gaussian, the generated THz beam in one domain is cancelled partly by the generated THz beam from its neighbouring domain. Using Equation (5.4), the electric field amplitude of the Gaussian laser beam can be rewritten:

$$E_{laser}(x', y') = E_{laser}\ e^{-\frac{x'^2+y'^2}{a^2}} \tag{5.20}$$

where x' is the centre of the laser beam profile, and a is the beam radius. The overlap of these two generated THz fields $S_{THz}(x)$ at a distance of x from the centre of the laser beam is shown as:

$$S_{THz}(x) = \int_{-\infty}^{\infty} e^{-\frac{y'^2}{a^2}}\, dy' \left[\int_{0}^{\infty} e^{-\frac{(x-x')^2}{a^2}}\, dx' - \int_{-\infty}^{0} e^{-\frac{(x-x')^2}{a^2}}\, dx'\right]$$
$$\rightarrow S_{THz}(x) \propto \left[\int_{0}^{\infty} e^{-\frac{(x-x')^2}{a^2}}\, dx' - \int_{-\infty}^{0} e^{-\frac{(x-x')^2}{a^2}}\, dx'\right] \quad (5.21)$$

Here we say that $x' - x = u$ so $dx' = du$, and the limit for the integral in Equation (5.21) changes $-x$ by substituting $x' = 0$ into $x' - x = u$, now the expression is:

$$S_{THz}(x) = \int_{-x}^{\infty} e^{-\frac{u^2}{a^2}}\, du - \int_{-\infty}^{-x} e^{-\frac{u^2}{a^2}}\, du = \int_{-x}^{\infty} e^{-\frac{u^2}{a^2}}\, du - \int_{x}^{\infty} e^{-\frac{u^2}{a^2}}\, du \quad (5.22)$$

Then, we call that $u/a = u'$, so $du = a\, du'$. The integral in Equation (5.22) becomes:

$$S_{THz}(x) = a\left[\int_{-x/a}^{\infty} e^{-u'^2}\, du' - \int_{x/a}^{\infty} e^{-u'^2}\, du'\right] \quad (5.23)$$

We can express equation (5.23) with error functions:

$$S_{THz}(x) \propto \operatorname{erfc}\left(-\frac{x}{a}\right) - \operatorname{erfc}\left(\frac{x}{a}\right) \quad (5.24)$$

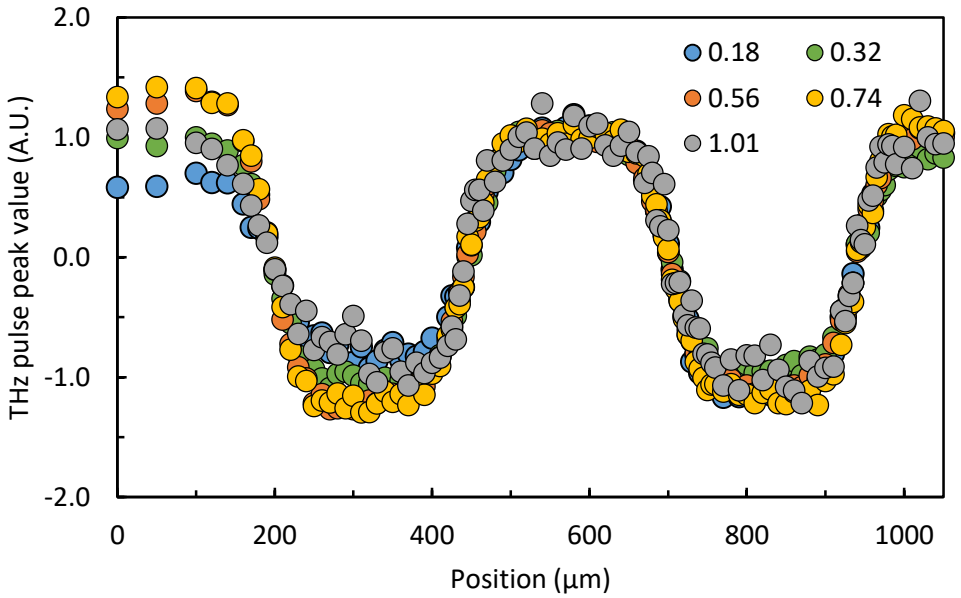

Figure 5.18: The experimental data of spectral component of THz field versus position along the *x*-axis for 0.18 THz, 0.32 THz, 0.56 THz, 0.74 THz and 1.01 THz.

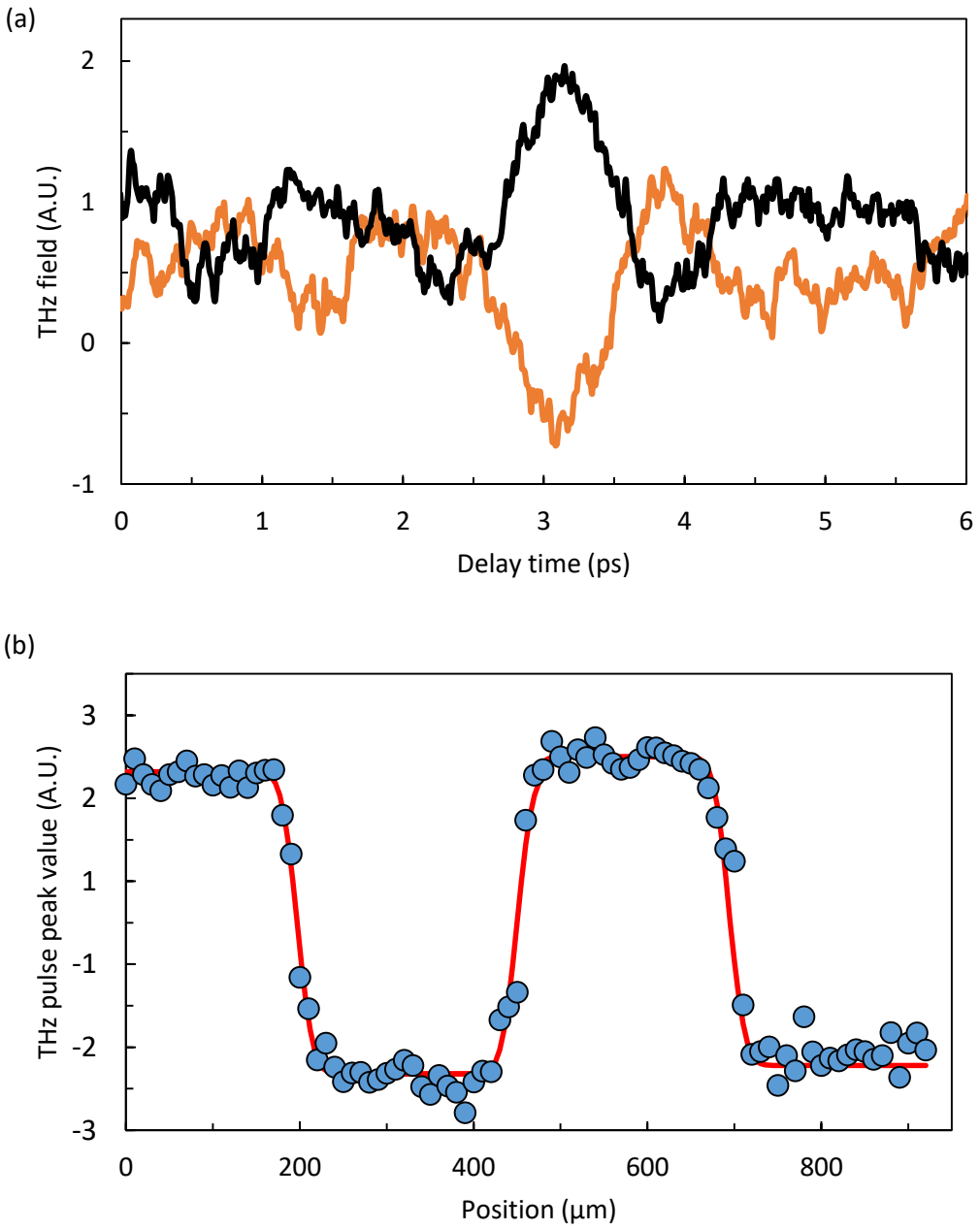

Figure 5.19: (a) THz waveforms (black and orange continuous lines) in two different domains. (b) Recorded THz pulse peak values versus position along *x*-axis. The experimental data (blue circles) was fitted using Eq. (5.24) (red continuous line).

Equation (5.24) is fitted nicely with the experimental data which is shown in Figure 5.17 (red line). The calculating beam waist is a=39 μm, so following the Rayleigh criteria, the lateral (Rayleigh) resolution for this image is $\delta = 2a\sqrt{ln2}$ = 65 μm. Figure 5.18 shows the experimental data by normalized Fourier transform for the magnitude of the THz field versus the position (*z*) for five different frequencies; 0.18 THz, 0.32 THz, 0.56 THz, 0.74 THz and 1.01 THz. This result demonstrates that the resolution of the image does not depend on the frequencies but depends on the laser beam size on the crystal.

The next imaging experiment was performed when the sample is rotated by 90°, so the x component of THz field will be recorded. Since the tensor element (d_{15}) is known to be the lowest compared to the other tensor elements, the average laser power is increased to 110 mW. Like in the previous experiment, we observed that the THz fields from two different domains are inverted (see Figure 5.19 (a)). The THz fields are recorded along *x*-axis (see Figure 5.19 (b)), and the calculated beam waist for this record is 20 µm by using Equation (5.24) so the spatial resolution is $\delta = 33$ µm.

Another experiment was performed by moving the microscope objective forward and backward directions in order to vary the beam waist on the sample. The results are shown in Figure 5.20, the beam waists were calculated again by fitting the experimental data with expression (5.24) to (blue circles in Figure 5.20). The calculated waists were ranged from 47 µm to 6 µm, and the corresponding lateral resolution are from 78 µm to 10 µm. The best lateral resolution we obtained from our setup is shown in Figure 5.20 (d): let us notice that it is the smallest laser beam waist that we can obtain with the present objective. A resolution reduced even to a few microns may be achieved by using another lens or a microscope objective.

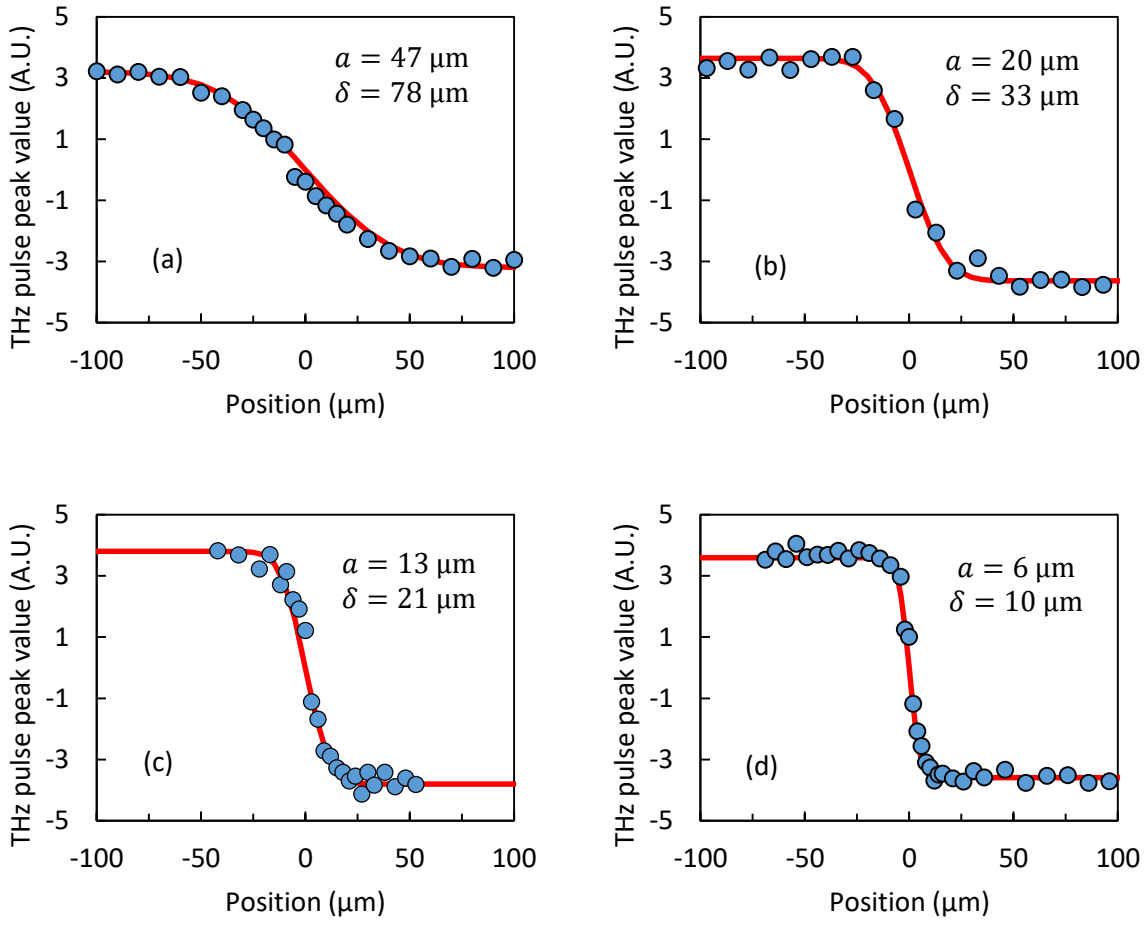

Figure 5.20: The peak values of the THz waveforms versus position on the sample for different laser beam waists. The measured data (blue circles) are fitted using Equation (5.24) (red continuous line)

For the best resolution obtained in Figure 5.20 (d), we performed a Fourier transform of the recorded waveform at each position of the measurement. This supplies us with the profile of the PPKTP domain recorded for different frequencies. Figure 5.21 presents these profiles obtained at 0.68,

0.47, 0.2 and 0.14 THz. The fits, with only the beam waist as adjustable variable, are in good agreement with the experimental data obtained at all the different THz frequencies: the best laser sport size value is 6 µm. As expected, it shows that the resolution is independent of the generated THz frequencies. For this lateral resolution, we achieve λ/44, λ/64, λ/150 and λ/214 for 0.68, 0.47, 0.2 and 0.14 THz, respectively. For THz frequencies lower than 0.14 THz, the image is noisy as it is the limit of the THz spectrum generated by the PPKTP crystal.

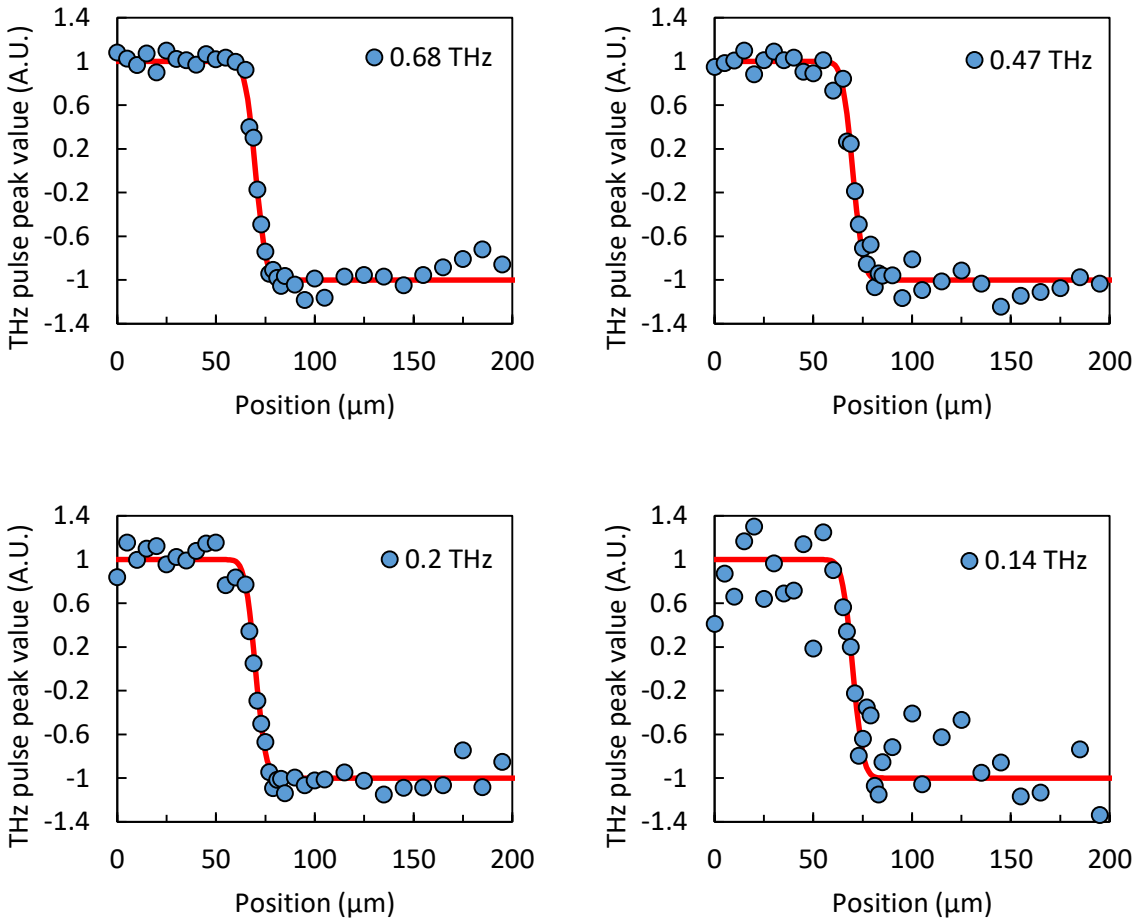

Figure 5.21: : The peak values of THz waveforms versus position on the sample for 0.68, 0.47, 0.2 and 0.14 THz. The experimental data (blue circles) are fitted using Equation (5.24) (red continuous line) with a 6 µm beam waist value.

PPKTP crystal is scanned with the smallest beam waist obtained in our setup, 6 µm. The blue circles in Figure 5.22 (a) correspond to the first experiment performed, and after analysing the data, some points between the position of 380 µm and of 430 µm on the crystal display a lower THz field than the neighbouring positions. Therefore, the experiment was repeated (the red circles in Figure 5.22 (a)) to scan along that area. It was observed that the reduction in the peak values were same for the repeated experiment, and it does not depend on the generated THz frequencies. If this THz signal reduction was due to the crystal thickness in that area, this dip would be varied for different frequencies [215]. Thus, the reduction of the THz signal is not due to a thinner sample thickness. The reason for this is that a scratch on the crystal causes weaker OR signal. The photography of the

scanning line and the scratch on the crystal can be seen in Figure 5.22 (b). This result shows us that ORTI method is a sensitive tool to detect the defaults on the sample.

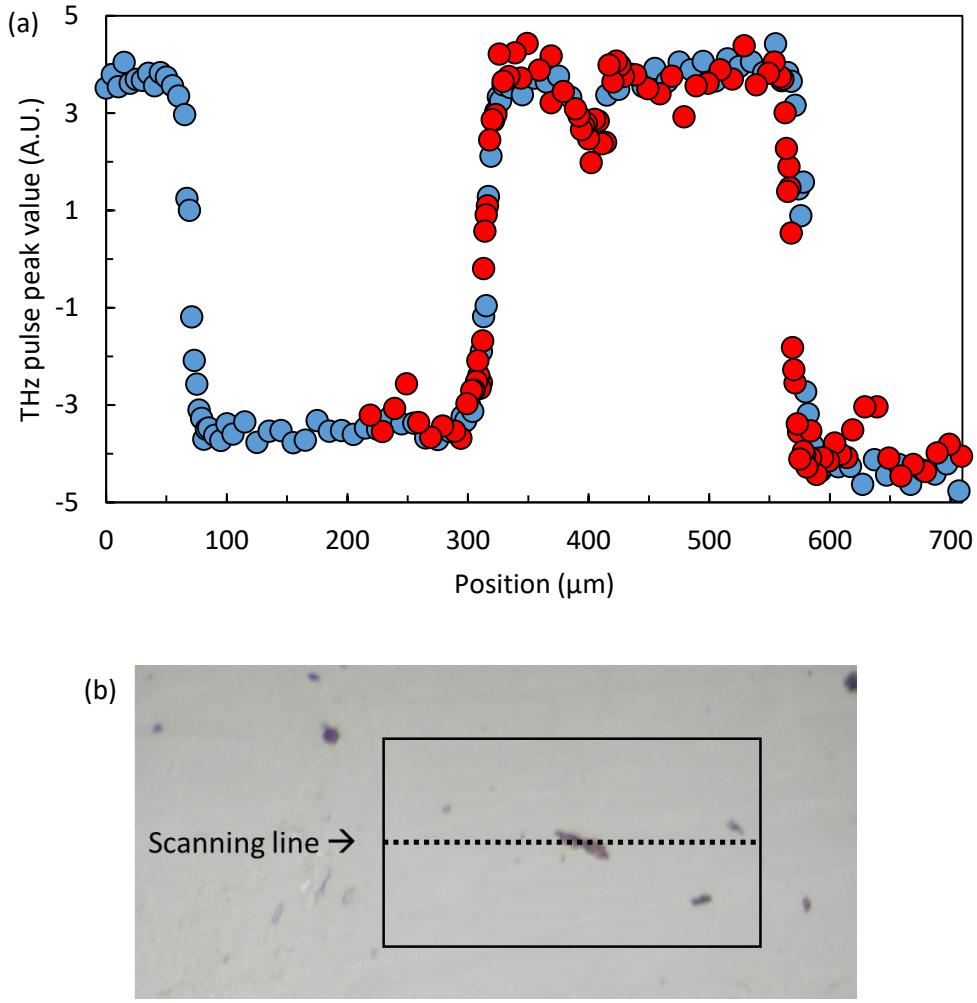

Figure 5.22: ORTI image of the PPKTP crystal scanned with the smallest laser beam waist in our setup, 6 µm. The first scanning result is represented with the blue dots; the repeated experiment is represented with the red dots (a). Photography of the imaging area on the crystal, the default can be seen in the scanning line (b).

The default area on the crystal (the one displayed in Figure 5.22 (b) was imaged with the ORTI technique with average laser power of 25 mW, 11 mW and 3 mW (corresponding to 14.7 GW/cm², 6.5 GW/cm² and 1.8 GW/cm² respectively).The imaging results are presented in Figure 5.23 (a). Even with the lowest optical density the default on the crystal can be seen. However, KTP crystal suffer from the saturation which is caused by two photon absorption [216]. Therefore, the expected linear relationship between the magnitude of THz electric field (E_{THz}) and the average laser power (P_{laser}^{ave}) does not fit well with the experimental data seen in Figure 5.23 (b).

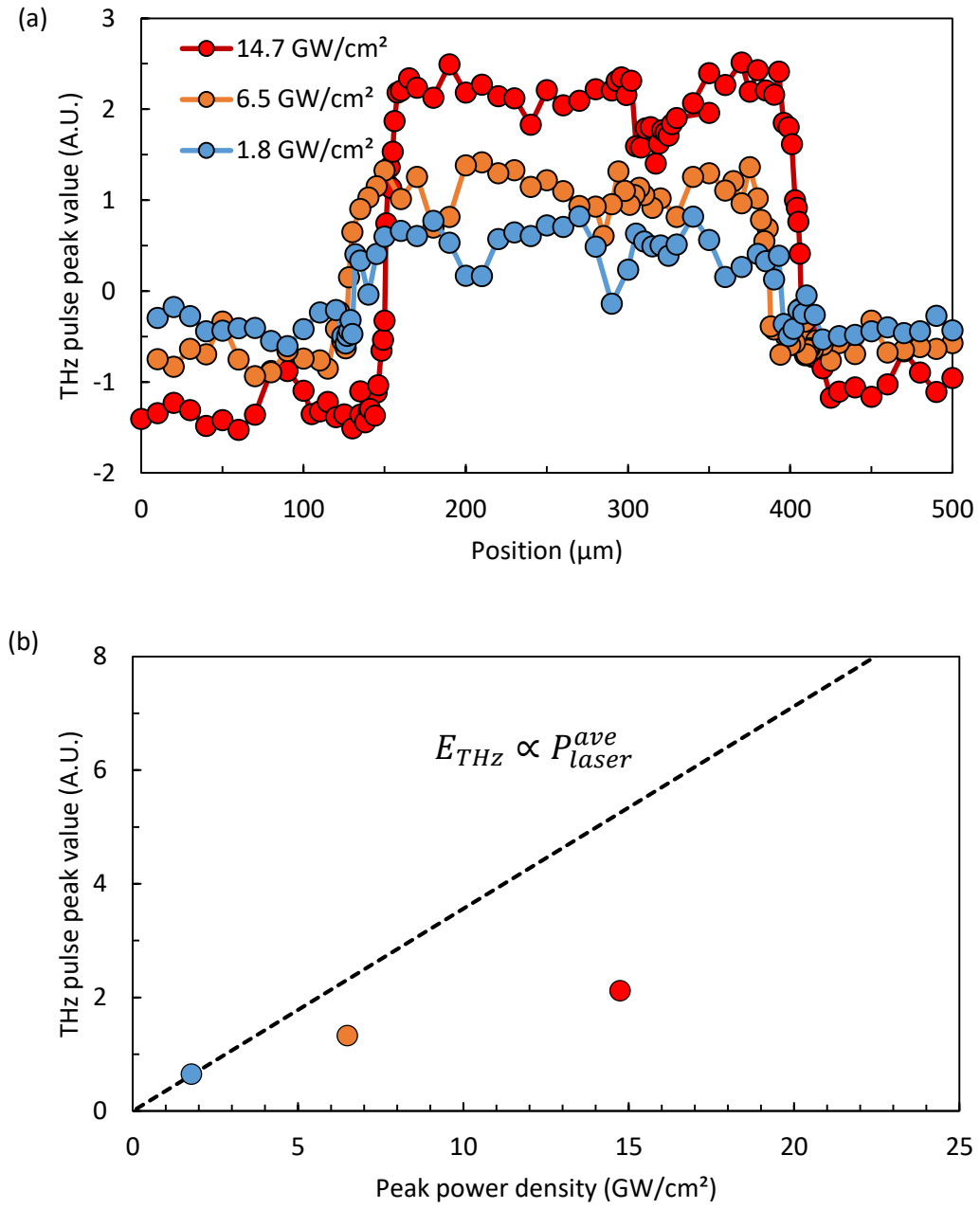

Figure 5.23: (a) ORTI image of the default area on the PPKTP crystal scanned under different optical densities. (b) The relationship between the generated THz electric field from KTP crystal and the illuminating average laser power does not fit with the experimental data. This can be due to two photon absorption observed in KTP.

ORTI method was demonstrated for imaging the domains of PPKTP crystal. As the crystal orientation of the domain was inverted along the crystal, the generated THz field in the crystal was observed inverted as well. This helped us to separate the neighbouring domains. Table 2 shows the comparison between microscopy techniques used to image domains of most common periodically poled crystals. To achieve the properties needed for practical applications, it is important to visualize the ferroelectric domains to optimize, as well as to characterize the problems in their fabrication process. Especially small domain periods for blue and violet light generation, an imaging method which

is non-destructive but high resolution of distinguish the domains is necessary. Simple optical microscope cannot distinguish the ferroelectric domains. Besides, they need the crystal to be etched with specific materials which is a destructive technique [202]. X-ray imaging can provide high resolution of imaging the domains but with no depth resolution. Another popular technique is piezoresponse force microscopy, which images the ferroelectric domain with the help of a sharp tip but has a limited scan area. Scanning electron microscopy has an advantage of lateral resolution less than 1 µm. However, the charged ferroelectric domains can cause deformations on the crystal image after the effect of electron beam. Additionally, it can only visualize the surface of the crystal, so the inhomogeneity cannot be observed at depth. Using second harmonic generation microscopy, the structural information at depths of several tens of µm can be provided. Unfortunately, this imaging requires phase matching for efficient operation of the process and cannot give information about the crystal orientation of the domains due to the intensity detection of the second harmonic wave. Contrary to the SHG technique, ORTI measures the THz electric field generated from the crystal so it can distinguish the orientation of the periodic domains. Additionally, the resolution of ORTI images is limited by the optical wave so a resolution of a few microns can be achieved. It has not been shown in this work but it could be possible to image the inside of the crystal. Although, ORTI is a new microscopic technique to image periodically poled crystals, it displays the features obtained in other microscopic techniques.

Table 2: Comparison of different imaging techniques used for periodically poled crystals.

Imaging method	Lateral resolution	Limitation	References
Scanning electron microscopy	<1 µm	No structural information	[217]
X-ray imaging	~ 50 nm	No structural information	[218]
Piezoresponse force microscopy	5-10 nm	Small lateral dimension (100 x100 µm^2)	[206], [219]
Second-harmonic generation	1 µm	Phase matching	[207], [208]
Optical rectification terahertz imaging	10 µm	Phase matching	[91,92], [93]

5.2.3 Polycrystalline sample

A sugar crystal was imaged by our team using ORTI (see Figure 1.19) [93]. We used again sugar to make a polycrystalline sample; we mixed sugar with some water on a glass layer and allowed the water to be vaporized at room temperature. Thus, the sugar with a varied thickness was stuck on a glass. To scan the sample, the experimental setup shown in Figure 5.9 was used, and the glass was placed in front of the laser beam before the sugar. For the measurements, the laser polarization angle was optimized for the first position (position 0) in the sugar sample and scanned along one axis with a laser beam waist of about 70 µm at a mean laser power of 60 mW. Theoretically, if there are any crystals with different orientations on the scanning line, we should be able to see them when the laser polarization angle changed. For this, the laser polarization angle was rotated with an angle of 90° to scan the same scanning line along the sugar. Figure 5.24 shows the ORTI image of the scanned sugar sample along one axis for two different laser polarizations (ϕ=0°, 90°). The results show that for the

sample position between 0 - 420 µm, there is no generated THz signal when the laser position angle is 90° whereas there is still generated THz signal between the position of 1300 – 2080 µm. It means that there are certainly two possible crystals along the scanning line. Additionally, between the position of 420 – 1160 µm, there is no detected THz signal when ϕ=90°. It might be a crystal with a same crystal orientation as the first crystal but with different properties such as thickness or crystal quality.

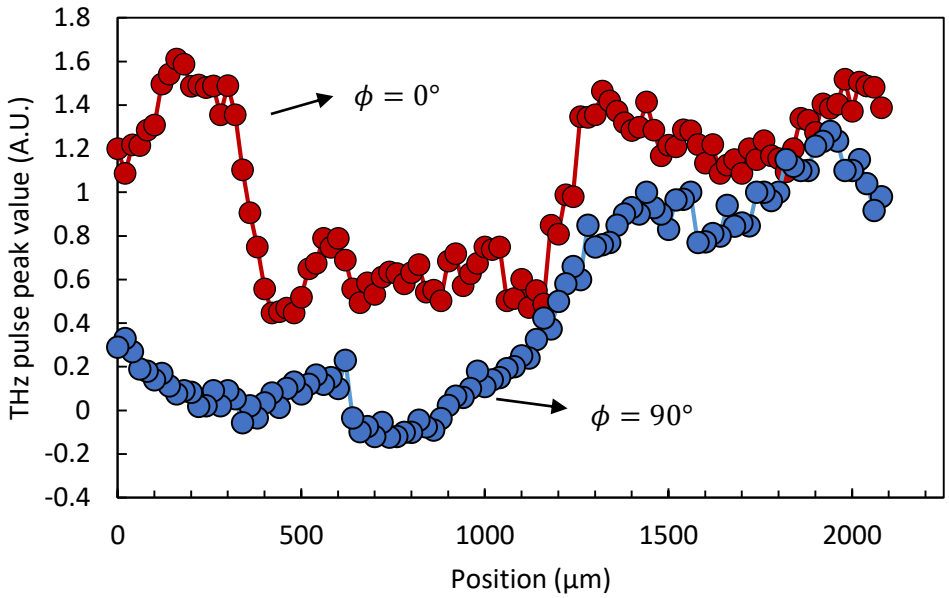

Figure 5.24: ORTI image of the sugar sample for two laser polarization angles of 0° (red) and 90° (blue)

The thickness variation along the scanning line of the sugar sample can be observed by the time shift between the THz waveforms. Figure 5.25 (a) shows the THz waveforms for three different positions when $\phi = 0°$. The time shift between the waveforms at the position 240 µm and 1420 µm is 0.24 ps, corresponding to a thickness difference of 42 µm between the two regions (refractive index of sugar is $\sim$ 1.7 [220]). Additionally, there is no obvious time shift between the positions at 240 µm and 760 µm, so the different amount of generated THz signals between these regions might be due to the crystal quality. In Figure 5.25 (b), the THz waveforms for the same three positions are plotted when the laser polarization angle was rotated with an angle of $90°$. It can be seen that there is still THz generation from the position at 1420 µm but no THz generation from the other plotted positions. This result shows the existence of crystals with different crystal axes.

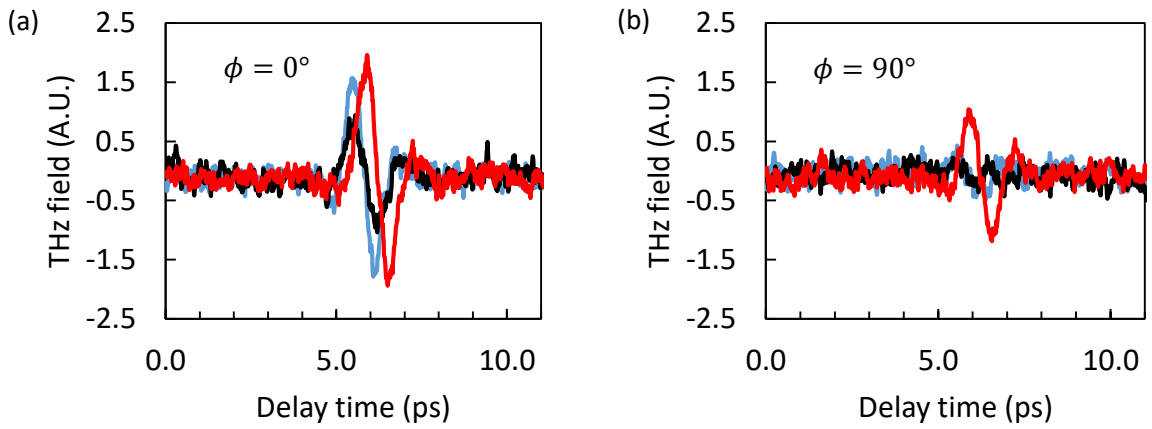

Figure 5.25: THz waveforms at (a) $\phi = 0°$ and (b) $\phi = 90°$ for the scanning line positions at 240 µm (blue line), at 760 µm (black line) and at 1420 µm (red line)

We tried to image the scanning area of the sugar sample with a commercial microscope to distiguish crystal axes of the sugar srytals (see Figure 5.26). For this, we used two light polarizers. As it is known that if two polarizers are placed perpendicular to the each other, the light tranmission through these polarizers is completely extinguished. But if a transparent object is replaced between these polarizers, any polarization effect in the object will enhance the transmission. Using this method, the sugar sample was placed between two polarizers and viewed under a commercial microscope. One of the polarizer was fixed and the two images were taken when the other polarizer is rotated by 90° or parallel to the first polarizer. Figure 5.26 shows the microscope images for two different states of the polarizer. At the position between 0 – 2500 mm in the image, there are some areas that have different light transmission.

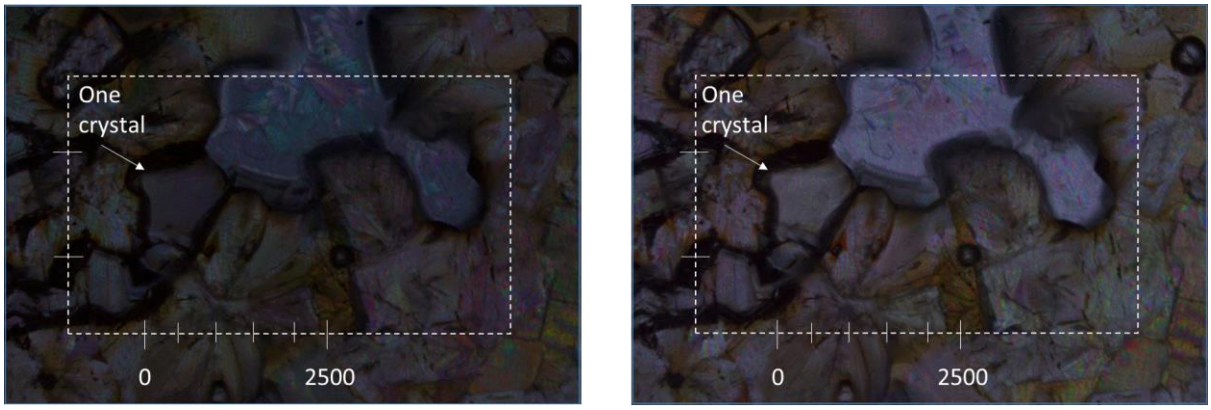

Figure 5.26: Microscopic images of scanning area of sugar sample. The position between the 0 – 2500 mm is the estimated scanning area. In the images, one possible crystal is pointed.

A polycrystalline sample was made of sugar, and ORTI was used to scan this sugar sample along one axis. The ORTI image was performed for two different laser polarization angles to be able to see the existence of the different crystal orientations. We expect three groups of crystals with different axes along the scanning line. Therefore, THz waveforms were plotted by selecting one position from each of the suspected regions for two different laser polarization angles. The results show that this imaging technique is very sensitive to the crystal orientation and the thickness

differences between the crystals. Lastly, the existence of the crystals with different axes was confirmed by imaging the sugar sample with a commercial microscope.

5.3 Performance and limit of ORTI

The performance of the ORTI technique can be addressed in terms of correspondence between the THz image and the actual composition/morphology of the sample, and of spatial resolution.

5.3.1 Correspondence between the recorded image and the actual sample properties

As we already explained, the ORTI signal depends on the nonlinear efficiency at a given location on the sample, which is mostly related to the chemical composition and to the crystallinity of the sample at this point. However, the THz signal may be disturbed by other effects, which could make the image not directly related to the sample composition/crystallinity. Thus it could lead to a misinterpretation of the achieved ORTI image. This could be due to reliefs at the sample surface that scatters/diffracts the laser beam and/or the THz beam, and also to phase-matching effect. The first problem can be solved by smartly preparing the sample, for example with an appropriate polishing if the material is solid and hard. Here we will focus our study on the phase matching effect. When phase-matching is not realized, the signal could decrease with the sample thickness instead of increasing, which may be wrongly interpreted as absorption. For most of natural materials, the phase-matching condition between the laser beam and the THz one is not realized. Therefore, the THz intensity will oscillate with the sample thickness at a given frequency, and simultaneously will be damped because of absorption. The period of the oscillations corresponds to the so-called coherence length. For a THz signal which varies linearly with the sample thickness, this thickness must be smaller than the coherence length.

To study this effect, we have to write the nonlinear propagation equation of the THz field inside the sample. Let us consider two spectral components of the laser pulse spectrum, which will interact to generate a THz frequency. The two laser fields ($\omega_i, i = 1,2$, ω and $\omega + \omega_{\mathrm{THz}}$) propagating into the crystal are written in cartesian coordinates (x, y, z):

$$\vec{\mathrm{E}}_{\mathrm{i}}(\vec{\mathrm{r}}, t) = \vec{\mathrm{E}}_{\mathrm{i}}\, e^{j(\vec{\mathrm{k}}_{\mathrm{i}}\vec{\mathrm{r}} - \omega_{\mathrm{i}} t)}\, T_{laser} \tag{5.25}$$

where T_{laser} is the amplitude transmission coefficient (see Equation (3.25)), $\vec{\mathrm{k}}_{\mathrm{i}} = \mathrm{k}_{\mathrm{i,x}}\,\hat{\mathrm{x}} + \mathrm{k}_{\mathrm{i,z}}\,\hat{\mathrm{z}}$, and x is the direction normal to the surface. The Helmholtz propagation equation in a nonlinear isotropic media for the THz field $\vec{\mathrm{E}}_{\mathrm{THz}}(\vec{\mathrm{r}}, t)$ is [94,221]:

$$\Delta\vec{\mathrm{E}}_{\mathrm{THz}}(\vec{\mathrm{r}}) + \frac{\omega_{THz}^2}{c^2}\tilde{\mathrm{n}}_{THz}^2\vec{\mathrm{E}}_{\mathrm{THz}}(\vec{\mathrm{r}}) = -\frac{\omega_{THz}^2}{c^2}\left(\overleftrightarrow{\chi}^{(2)}\vdots\vec{\mathrm{E}}_1(\vec{\mathrm{r}})\,\vec{\mathrm{E}}_2^{*}(\vec{\mathrm{r}})\right) T_{laser}{}^2 \tag{5.26}$$

THz electric field $\vec{\mathrm{E}}_{\mathrm{THz}}(\vec{\mathrm{r}}, t)$ is the summation of the free and forced waves [221]:

$$\vec{\mathrm{E}}_{\mathrm{THz}}(\vec{\mathrm{r}},t)=\vec{\mathrm{E}}_{\mathrm{free,THz}}e^{j\left(\vec{\mathrm{k}}_{\mathrm{THz}}\vec{\mathrm{r}}-\omega_{\mathrm{THz}}t\right)}+\vec{\mathrm{E}}_{\mathrm{forced,THz}}e^{j\left(\Delta\vec{\mathrm{k}}\,\vec{\mathrm{r}}-\omega_{\mathrm{THz}}t\right)} \tag{5.27}$$

$\vec{\mathrm{E}}_{\mathrm{free,THz}}$ and $\vec{\mathrm{E}}_{\mathrm{forced,THz}}$ is solved with and without the linear term of polarization. Then, the solution of $\vec{\mathrm{E}}_{\mathrm{THz}}(\vec{\mathrm{r}},t)$ polarized along y-axis [221] without taking into account the Fabry-Pérot oscillations is found as [221]:

$$\begin{aligned}\mathrm{E}_{\mathrm{THz,y}}(x)=\mathrm{E}_{\mathrm{f,y}}\,e^{j\frac{\omega_{\mathrm{THz}}}{c}n_G x}\,e^{-\frac{2\omega+\omega_{\mathrm{THz}}}{c}\kappa_\omega x}\times\\ \left[1-e^{j\frac{\omega_{\mathrm{THz}}}{c}(n_{THz}-n_G)x}e^{-\frac{\omega_{THz}}{c}\left(\kappa_{\omega_{THz}}+\frac{2\omega+\omega_{\mathrm{THz}}}{\omega_{THz}}\kappa_\omega\right)x}\right]\end{aligned} \tag{5.28}$$

where

$$\mathrm{E}_{\mathrm{f,y}}=\frac{\left(\overleftrightarrow{\chi}^{(2)}:\vec{\mathrm{E}}_1\vec{\mathrm{E}}_2^{*}\right)_y}{\tilde{n}_G^2-\tilde{n}_{\omega_{THz}}^2-\left(\frac{2\omega+\omega_{\mathrm{THz}}}{\omega_{\mathrm{THz}}}\kappa_\omega\right)^2} \tag{5.29}$$

Here $\tilde{n}_G$ is the group index at the laser wavelength. A tilde indicates that the value is complex, and κ is the imaginary part of the refractive index. The modulus of the generated THz field is:

$$\begin{aligned}\left|\mathrm{E}_{\mathrm{THz,y}}(x)\right|^2=\left|\mathrm{E}_{\mathrm{f,y}}\right|^2e^{-2\frac{\omega_{\mathrm{THz}}}{c}(\kappa_{OR}-\kappa_{\omega_{THz}})x}\times\\ \left[\left(1-e^{j\frac{\omega_{\mathrm{THz}}}{c}\kappa_{OR}x}\right)^2+4e^{-\frac{\omega_{THz}}{c}\kappa_{OR}x}\sin^2\left(\frac{\omega_{\mathrm{THz}}}{2c}\Delta nx\right)\right]\end{aligned} \tag{5.30}$$

with $\kappa_{OR}=\kappa_{\omega_{THz}}+\frac{2\omega+\omega_{\mathrm{THz}}}{\omega_{\mathrm{THz}}}\kappa_\omega$ and $\Delta n=n_{THz}-n_G$. In the absence of loss, this expression leads to the very known *sinc* expression of the THz field. The signal is maximum when the term between brackets is maximum. This value is determined by taken the derivative of the bracket term versus *x*, and it is solution of the following equation:

$$e^{-\frac{\omega_{\mathrm{THz}}}{c}\kappa_{OR}x}=\cos\left(\frac{\omega_{\mathrm{THz}}}{c}\Delta nx\right)+\frac{\Delta n}{\kappa_{OR}}\sin\left(\frac{\omega_{\mathrm{THz}}}{c}\Delta nx\right) \tag{5.31}$$

This expression has to be solved numerically. Nevertheless, in transparent or moderately absorbing materials, $\kappa_{OR}\ll 1$. It follows:

$$e^{-\frac{\omega_{\mathrm{THz}}}{c}\kappa_{OR}x}\approx\frac{\Delta n}{\kappa_{OR}}\sin\left(\frac{\omega_{\mathrm{THz}}}{c}\Delta nx\right) \tag{5.32}$$

Moreover, the exponential term is close to 1 for mm-thick samples. Therefore, the first maximum of the generated THz signal occurs at:

$$\frac{\Delta n}{\kappa_{OR}} \sin\left(\frac{\omega_{\mathrm{THz}}}{c}\Delta n x\right) \approx 1$$
$$\rightarrow \quad \sin\left(\frac{\omega_{\mathrm{THz}}}{c}\Delta n x\right) \approx \frac{\kappa_{OR}}{\Delta n} \tag{5.33}$$

If phase-matching is not realized, *i.e.* Δn is quite larger, at least larger than κ_{OR}, we get:

$$\sin\left(\frac{\omega_{\mathrm{THz}}}{c}\Delta n x\right) \approx 0 \;\rightarrow\; x_{max} = \frac{\pi}{2}\frac{c}{\Delta n \omega_{\mathrm{THz}}} = \frac{c}{4\Delta n f_{THz}} \tag{5.34}$$

Because of the sinc-like behaviour of the THz field versus thickness, the THz field increases linearly with the thickness up to around $x_{max}/2$. Thus ORTI can be successfully performed at a given frequency with samples whose thickness is smaller than:

$$x_{ORTI} = \frac{x_{max}}{2} = \frac{c}{8\Delta n f_{THz}}$$
$$x_{ORTI}(\mu\mathrm{m}) \approx \frac{37.5}{\Delta n f_{THz}} \tag{5.35}$$

At 1 THz, with $\Delta n = 0.1$, we obtain $x_{ORTI} = 375$ µm. Therefore, ORTI is possible with thin samples that are commonly examined in classical microscopy. If samples exhibit a large dispersion (Δn large) millimeter-thick and eventually cm-thick samples can be characterized.

5.3.2 Estimation of the best achievable spatial resolution

Let us now treat the lateral resolution. One may think that it suffices to focus more tightly the laser beam to obtain a smaller laser spot and thus a better lateral resolution. However, a stronger concentration of the pump beam means a higher laser power density, which can burn or destroy the sample if the power density is larger than the damage threshold of the sample material. If, while focusing more and more, one diminishes the laser power to work below the damage threshold, the generated THz signal could be below the detection threshold of the THz receiver. One has indeed to remember that the detector is sensitive to the whole number of THz photons, which itself is proportional to the laser power, and not to the laser power density. We address this problem in the following paragraph.

As explained in this thesis, the generated THz field is proportional to the laser field to the square. This latter value is also proportional to the laser power density. So we write:

$$E_{THz} \propto \chi^{(2)} E_{laser}^2 \propto \chi^{(2)} \frac{P_{laser}}{S_{laser}} \tag{5.36}$$

Here for the sake of simplicity, we use only the magnitude of the involved values and coefficients. Until now, we deal with peak values of the fields. The radiated THz power is:

$$P_{THz} \propto S_{THz} E_{THz}^2 \propto S_{laser} E_{THz}^2 \propto \frac{\left(\chi^{(2)} P_{laser}\right)^2}{S_{laser}} \tag{5.37}$$

We already took into account the fact that the surface of THz emission, *i.e.* the THz beam spot size at the crystal, is equal to the illuminated region ($S_{laser} = S_{THz}$). Since the illuminating laser beam area is much smaller than the wavelength of THz waves, THz waves are considered as generated by a punctual source and they propagate as circular waves with a power density decreasing as 1/ R^2, where R is the distance from the source to the collection optics. The detected THz wave is the one collected at a distance R by the collection optics of section S_{lens}:

$$P_{THz,D} \propto \frac{P_{THz}}{R^2} S_{lens} \propto P_{THz} \Omega_{\text{lens}} \propto \frac{\left(\chi^{(2)} P_{laser}\right)^2}{S_{laser}} \Omega_{\text{lens}} \propto \left(\chi^{(2)} D_{laser}\right)^2 S_{laser} \Omega_{\text{lens}} \tag{5.38}$$

where Ω_{lens} is the solid angle of the optics, describing as an entrance of the collecting optics and D_{laser} is the laser power density [93]. The laser beam waist at the crystal w_{laser} will help us to define the resolution ($S_{laser} \propto w_{laser}^2$):

$$\begin{aligned} & P_{THz,D} \propto \left(\chi^{(2)} D_{laser}\right)^2 w_{laser}^2 \Omega_{\text{lens}} \\ \rightarrow \quad & w_{laser} \propto \sqrt{\frac{P_{THz,D}}{\Omega_{\text{lens}}}} \frac{1}{\chi^{(2)} D_{laser}} \end{aligned} \tag{5.39}$$

In the measurement, $P_{THz,D}$ must be bigger than the threshold of the detector, *i.e.* its noise equivalent power (NEP). As well, the power density at the sample must be weaker than the damage threshold D_{damage} . Therefore:

$$w_{laser} > \sqrt{\frac{NEP}{\Omega_{\text{lens}}}} \frac{1}{\chi^{(2)} D_{damage}} = w_{resolution} \tag{5.40}$$

This expression gives the limit in resolution that is achievable with the ORTI technique. It is noticeable that the square-root in the preceding expression depends only on the set up parameters, while the other term depends only on the sample characteristics. Thus, for a given set up, the resolution depends on the sample and we cannot an absolute value of this resolution.

Let us comment the influence of the different parameters:

- ***NEP*** of the detector: This parameter defines on the sensitivity of the detector camera, and NEP of the detector should be smaller than the power of the generated THz signal from the sample. In the case of using materials with a low non-linear coefficient (such as biological samples) it is important that the detector should be highly sensitive, *i.e.*, low NEP.

- Scalar nonlinear coefficient $\boldsymbol{\chi}$ of the sample: In ORTI technique, the sample to be imaged should include some non-centrosymmetric regions. If the scalar nonlinear coefficient χ of the sample is high, the resolution of the image can be even better.

- Sample damage threshold $\boldsymbol{D_{damage}}$: It is defined as the ability limit of material can stand under laser illumination without being damaged. It depends on the laser properties (peak power energy, repetition rate and pulse duration of the laser) and the spot size of the laser on the sample. Ultra-short laser pulses are preferable as the peak power of the pulses could be extremely high, while the pulse energy remains rather low, and thus minimizes the thermal effects.

- Solid angle of the optical system $\boldsymbol{\Omega_{lens}}$: Another important parameter is the collection optics of the generated THz signal from the sample source. It is obvious that the maximum THz signal should be collected by the detection optics.

- Absorption of THz ($\boldsymbol{\kappa_{THz}}$) or optical wave in the sample: Higher absorption of the optical wave or the generated THz waves in the crystal might result in weaker OR signal, which might not be detected. In the case of opaque samples at optical and/or laser frequencies, ORTI performed in reflection could be of interest.

- Phase matching: As explained above, phase matching could lead to artifact when dealing with thick samples. Therefore, ORTI is maybe more adapted to thin samples. On the other hand, if phase matching could realize, or almost realized, in given samples, the THz signal will be stronger, and the detection as well as the resolution will be improved.

- Other nonlinear phenomena in the crystal: Two photon absorption is a third order nonlinear phenomena and can limit the THz efficiency. For example, the saturation of generated THz signals in crystals was be observed because of two photon absorption in Figure 5.23.

5.4 Conclusion

In this Chapter, we imaged some samples by using ORTI technique. The image results also gave us information about the parameters required to be taken into account while using this technique. For example, the image result of $LiNbO_3$ crystal showed us the importance of the phase matching condition in the crystal. If phase-matching can be satisfied in the crystal, enough THz signal can be generated to be detected. However, in most of the cases, phase-matching will not be realized, and moreover the nonlinear efficiency of actual materials will be low. It is why a very sensitive detector should be used to detect the weak THz waves, *e.g.* a KID camera. When dealing with absorbing materials, it is preferable to arrange an ORTI experiment in reflection. The reflection mode for the ORTI technique has not been demonstrated in our work but it could easily be applied. In the work of Coutaz, *et a*l. [221], the detected reflected THz signal for a 100-µm thick <111> ZnTe crystal is calculated 25 times weaker than the transmitted THz field. This low field could be still measured by the THz-TDS thanks to its high dynamics, or a KID camera could be used to detect much weaker THz signals.

In this thesis, we used a setup including an amplified laser to image samples in ORTI experiment. However, due to strong peak pulse delivering from the amplified laser setup, we built another setup using a simple femtosecond laser source and efficient photoconductive detector. With this setup, we imaged the ZnTe slivers, the PPKTP crystal and polycrystalline sample, and we observed that the resolution of the ORTI images is independent of the generated THz frequencies but limited

by the laser beam waist. It means that the resolution can be improved even to a few microns. Until now, the best lateral resolution was obtained 10 μm (λ/214 for 0.14 THz) by scanning the domains of PPKTP crystal. Additionally, we formulize that the limited laser beam can be used to image the samples by ORTI technique. The factor determining the minimum laser beam waist can be categorized in two groups. Depending on the experimental setup, the sensitivity of the detector (NEP) and the collecting optics (Ω_{lens}) for generated THz waves are important. Also, the factors depend on the samples are the damage threshold ($\widehat{\mathrm{D}}_{\mathrm{damage}}$), the nonlinear coefficient ($\chi^{(2)}$) and the absorption coefficient of the sample (κ_{THz}).

As a conclusion, ORTI technique is different than the other subwavelength THz imaging because the THz waves are directly generated in the sample. The ORTI images can give information on the crystal quality (homogeneity along the crystal), defaults, absorption of the sample, crystal axes, thickness differences along the sample, and chemical composition of the sample in the spectral image.

6. General conclusion and future work

6.1 General conclusion

The work carried out during this thesis focused on developing ideas for subwavelength THz imaging. Two different methods have been presented. The first one is based on using a KIDs camera to detect THz waves for the first time for THz microscopy. The second enables subwavelength resolution using the ORTI technique. The benefits of using THz waves and the limits encountered in THz subwavelength microscopy are reported in Chapter 1, as are several original techniques in the literature to overcome these limitations. Then, in Chapter 2, different methods used in this thesis were described theoretically including THz generation and detection, and THz spectroscopy. The generation of THz waves by optical rectification is explained theoretically, which is the main technique used for ORTI imaging.

Scanning a sample by using a small hole made in a metallic sheet is a very efficient and easy way to reach a subwavelength resolution. The biggest challenges of this method is to detect the weak waves transmitted through the hole. We used a highly sensitive KIDs camera to detect these weak waves for THz microscopy. In Chapter 3, we firstly focused on measuring the minimum power of THz pulses that can be detected by this camera. For this, we used two different THz sources including (1) THz waves generated through optical rectification in a non-centrosymmetric material ZnTe *via* excitation by femtosecond laser pulses and (2) THz waves generation from photoconductive antenna. The results show the minimum power of THz pulses detected to be 0.2 fW. In addition, we observe the generated THz waves with the PC antenna emitter when the bias of the antenna is zero. This unexpected result is explained by the effect of Schottky contact between the metal electrodes of the antenna.

In Chapter 4, a KIDs camera is used to image samples in the THz range. The aperture used in THz microscopy was designed using HFSS. The simulation results show that the light transmission through the conically shaped tapered hole is greater than through cylindrical hole. Besides, taking into account the KID's power sensitivity, the diameter of the tapered hole can be as small as 16 µm under 150 GHz illumination light according to the simulation results (corresponding resolution is λ/125). In the imaging experiments with KIDs, the sample is placed against the hole and moved over it. Since the measurements are very sensitive; problems occurred because of:

- The sample and hole not completely touching each other
- Removing of the gold deposition on the tapered hole device
- Failure of the coverage of the experimental setup
- The motorized stage and the KID camera not in communication

Although, all these reasons make it difficult to obtain an expected image with KIDs, we obtained some results:

- We demonstrated that a KID camera can be used for THz microscopy.

- A signal high above the noise signal was detected with a 50 µm diameter tapered hole. It means that even a smaller dimensioned hole can be used.

- We managed to fabricate a mechanism to place the sample against the hole with 4 springs, and this helped us to obtain an image with a resolution defined by the hole dimension of the device.

Imaging a sample using the self-generated THz waves is a novel microscopy technique. In Chapter 5, we use ORTI which is performed in a standard THz-TDS by using a simple femtosecond laser source and an commercial photoconductive detector. Other THz microscopy techniques can have more advanced equipment and are usually performed by illuminating the sample with specific THz waves (*e.g*. s-SNOM, AFM and aperture-based techniques). However, with ORTI, the sample can generate THz with a wide spectrum which results in a hyperspectral-like image. These spectral images provide information about the chemical composition, the absorption and the homogeneity of the sample. ORTI was previously used for imaging periodic domains of ferroelectric crystals [90,92] but not proposed as a subwavelength THz imaging technique. In this project, the results prove that ORTI provides subwavelength resolution. By imaging the ZnTe crystal at different frequencies with ORTI, we show that the resolution is indeed independent of the generated THz frequencies but dependent of the illuminating laser beam waist and can therefore reach even a few microns.

In a non-centrosymmetric crystal, the theory to generate THz waves by optical rectification depends on second order nonlinear coefficients of the crystal. We achieved a good agreement between the experiment and the theory by using the ratio of the coefficients of the PPKTP crystal. In two neighbouring domains of the PPKTP crystal, the crystal orientations are flipped. When THz waves are generated in those domains, the THz signals are inverted to each other. The sign changing in THz signals helps us to distinguish ferroelectric domains in ORTI. The sharpness between two adjacent domains gives the resolution of ORTI image. Until now, we have reached a resolution of 10 µm by scanning the ferroelectric domains of the PPKTP crystal, corresponding to λ/214 for 0.14 THz. In addition, this ORTI image obtained with a 10 µm resolution also enabled us to see a scratch on the crystal.

The resolution of the ORTI image depends on (and can be improved by) experimental and sample parameters: scalar nonlinear coefficient χ and damage threshold D_{damage} of the sample, NEP of the detector, and solid angle of the optical system Ω_{lens}. Besides, the efficiency of the THz field generated from the sample is achieved with the phase-matching condition of the sample**.** We scanned the $LiNbO_3$ crystal with uneven thickness and observed different generated THz signals due to varied phase-matched conditions. Additionally, a polycrystalline sample made with sugar was imaged in ORTI experiment. The results show that ORTI technique is sensitive the crystal with different orientations.

As a summary, we investigated two different techniques for THz microscopy. The ORTI technique showed a good way to achieve subwavelength THz resolution, and the KIDs camera was presented for the first time in THz microscopy, with the ability to detect THz pulses at a power of 0.2 fW. The results reported here give an intriguing perspective in order to further develop these two techniques.

6.2 Future work

There are several improvements that can be done for the imaging techniques proposed in this thesis. To go further with THz imaging using the KIDs camera, it is necessary to improve the experimental setup. The problem of coverage of the experimental setup needs to be solved in terms of the material and the fit over the experiment. The experimental setup should only allow the incoming light passing through the hole of the device for the microscopy, and every gap outside of the hole should be covered. Additionally, the communication between the KIDs camera and the motorized stage used to move the sample to be scanned should be supplied with a software. Our method was based on the estimation of the position on the sample. With the correct software, we can ensure the accurate position in the scanned area of the sample. Beside all these improvements in the experimental setup, the tapered holes could be used to reach a subwavelength resolution of the image. We have demonstrated that the light transmission through the tapered device with an output diameter of a 50 µm was detected by the KIDs camera. The output diameter can be even smaller than 50 µm, and therefore the image resolution could be improved. However, another fabrication process to make these devices should be used: for example, instead of gold deposition of the silica substrate, a tapered hole could be drilled in a metal. This would help to avoid the problem of removing the gold deposition on the aperture substrate while moving the sample over the hole. Besides, in order to image the biological samples with ORTI, the KIDs camera should be used since the generated THz signal from the samples are very weak. Finally, the optics in front of the KID camera were designed for radio astronomy use. Optimizing them for microscopy application could improve the setup efficiency.

THz subwavelength resolution (10 µm) was achieved in this thesis with ORTI technique. This resolution can be even improved to a few microns. For this, it is necessary to use different lenses or microscope objectives to reduce the laser beam waist on the sample. In addition, the experimental setup can be developed to detect all diffracted THz waves to improve the resolution of the images. Since the SHG technique can be used for imaging the inside the crystals, the ORTI technique could also be used for 3D images. This can be very easily applied in the setup and can be an alternative method to visualize the inside of the periodically poled crystals. In this thesis, the ORTI technique has been demonstrated for detecting the transmitted THz waves through the samples. Since the broken symmetry along the surface of the sample can generate THz waves, another experimental setup can be installed to detect these reflected waves generated from the sample surface. This setup can be used for imaging thick samples, samples with unsatisfied phase conditions and biological samples. Although, we have shown very interesting results for two different techniques, a lot of developments are still needed in order to be easily applied in industry and in daily life.

Appendices

Appendix A: Horn antenna simulation

The simulation model of the horn antenna was designed by using HFSS. This antenna can be operated at any frequency in the range of 140 GHz to 220 GHz. The pyramidal horn is associated with a feeding rectangular G-band waveguide whose dimensions are 1.2954 mm x 0.6477 mm. The schematic of the designed 3D geometry with the dimensions of A, B and C is shown in Figure A.1. In the HFSS model, the outer surfaces of the horn antenna are assigned as PEC boundaries. Wave port is used as excitation for the antenna simulation and shown G-band in Figure A.1. The horn antenna is located inside a box filled with vacuum, the surfaces of the vacuum box is assigned as Radiation boundary in HFSS.

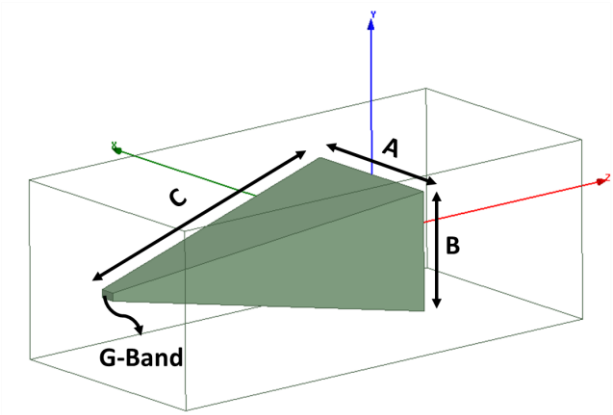

Figure A.1: Designed pyramidal horn in HFSS. The length of A, B and C are 12.548 mm, 9.550 mm and 26.314 mm, respectively (The values are given in the manual of the horn antenna).

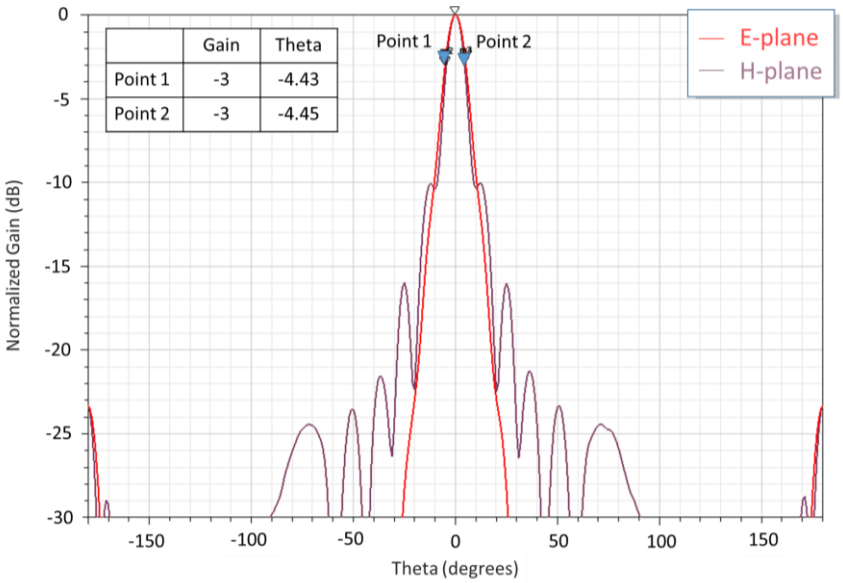

Figure A.2: Normalized radiation pattern at 180 GHz

The simulation model horn antenna was performed at a frequency of 180 GHz. Actually, we perform our experiment at 150 GHz because this simulation model was designed before knowing the information about the filter used for KIDs, and the filter allows frequencies between 100 GHz to 180 GHz. We assume that the results obtained by this simulation model should be close enough the model if it was analysed at 150 GHz. Figure A.2 shows the normalized radiation pattern for E- and H-planes. The beam width is measured at -3 dB level of the main lobe. For this horn antenna simulation, the width is approximately equal on the E-plane and on H-plane, which is calculated to be 9 degrees.

Appendix B: THz generation in LGT through optical rectification

In this part of the thesis, we present for the first time the THz generation by optical rectification of a femtosecond laser pulse in a langatate ($La_3Ga_{5.5}Ta_{0.5}O_{14}$, LGT) crystal. As the *Z*-cut LGT is studied here, the THz waves should be emitted regardless of the impinging polarization state, this will be shown theoretically in the following. In addition, we explore the absorption coefficient and refractive index in the THz range and investigate quantitatively the damage threshold of the crystal. Finally, the LGT crystal will be discussed as a possible THz emitter by comparing with one of the most common used crystals for generating THz waves: ZnTe. The results were presented as a poster in a France-Germany Terahertz Conference 2019 (FGTC, Kaiserslautern/Germany) and will be submitted to a journal.

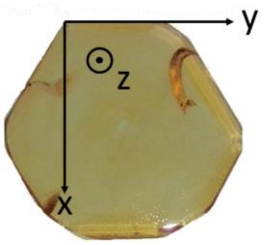

Figure B.1: Z-cut LGT crystal with Cartesian coordinates.

LGT crystals have been grown for the first time at the University of Moscow and show specific physical properties that make them very attractive in numerous applications [222]: their piezoelectric constant (d_{11}) is three times higher than in quartz [223,224], no phase changes up to its melting point (1470°C) [225] and sixth times higher damage threshold than $LiNbO_3$ [226]. Up to now, nonlinear properties of LGT have been already demonstrated for second harmonic generation (SHG), sum frequency generation (SFG) and difference frequency generation (DFG) with efficiency close to KTP crystal [227]. Let us notice that THz waves are generated simultaneously with generation of second harmonic waves, but with a different efficiency. LGT crystals belong to the hexagonal symmetry group 32 [225,228], so the second order nonlinear tensor writes:

$$\overleftrightarrow{d} = \begin{pmatrix} d_{11} & d_{11} & 0 & d_{14} & 0 & 0 \\ 0 & 0 & 0 & 0 & -d_{14} & d_{11} \\ 0 & 0 & 0 & 0 & 0 & 0 \end{pmatrix} \tag{B.1}$$

In our experiments, a *Z*-cut LGT was used, which means that the wave propagation is along the *z*-axis (optical axis) (see Figure B.1). Therefore, the crystal must show an isotropic behavior at normal incidence. The electric field of the pumping laser is:

$$\vec{E}(\omega) = E(\omega)\begin{pmatrix} \cos\phi \\ \sin\phi \\ 0 \end{pmatrix} \tag{B.2}$$

where ϕ is the polarization angle of the laser beam. Like in Equation (5.14), the emitted THz field is calculated theoretically by using Equation (B.1) :

$$\vec{P}_{THz}^{NL} = \varepsilon_0 d_{11} E^2(\omega) \begin{pmatrix} 1 \\ \sin 2\phi \\ 0 \end{pmatrix} \quad \text{(B.3)}$$

Equation (B.3) shows that the THz electric field depends on one nonlinear coefficient, namely d_{11}, and can be generated whatever is the polarization angle of the incident laser beam. The minimum amplitude of the THz field is proportional to $E^2(\omega)\ d_{11}$.

B.1. Obtained THz Signal and Spectrum

The LGT crystal is placed at the sample location in the experimental setup shown in Figure 5.5. The incident laser beam excites a 3-mm thick *Z*-cut LGT crystal (see Figure B.1) to drive the generation of THz radiation. Figure B.2 shows the terahertz waveform and its spectrum generated by OR in the LGT crystal. The laser beam waist is 0.75 mm and the average power of the laser is 285 mW on the crystal, *i.e*. a peak power density of ~0.37 TW/cm^2. The generated THz spectrum ranges from 0.04 THz to 1.4 THz with a 40 dB dynamic range, and the maximum of the spectrum is around 0.3 THz.

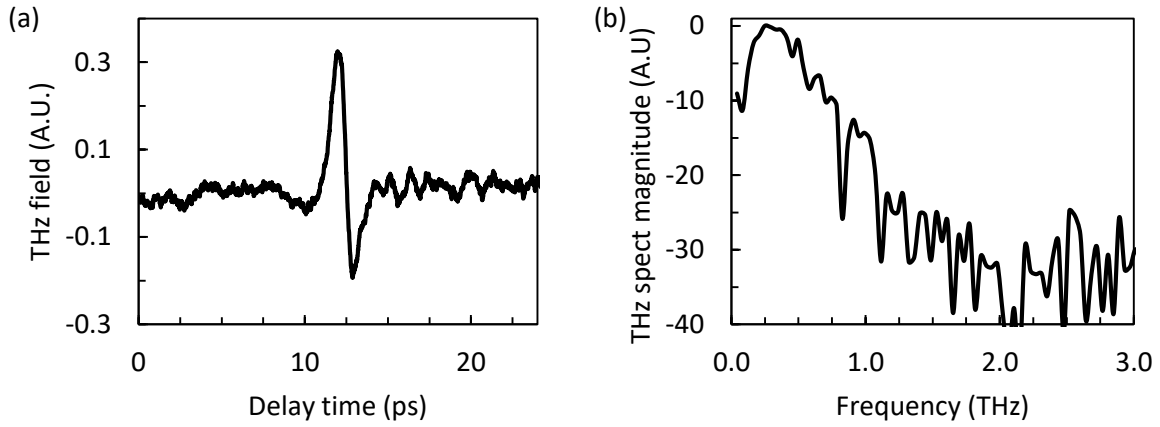

Figure B.2: Terahertz waveform (a) and terahertz spectrum (b) generated by optical rectification in the LGT crystal

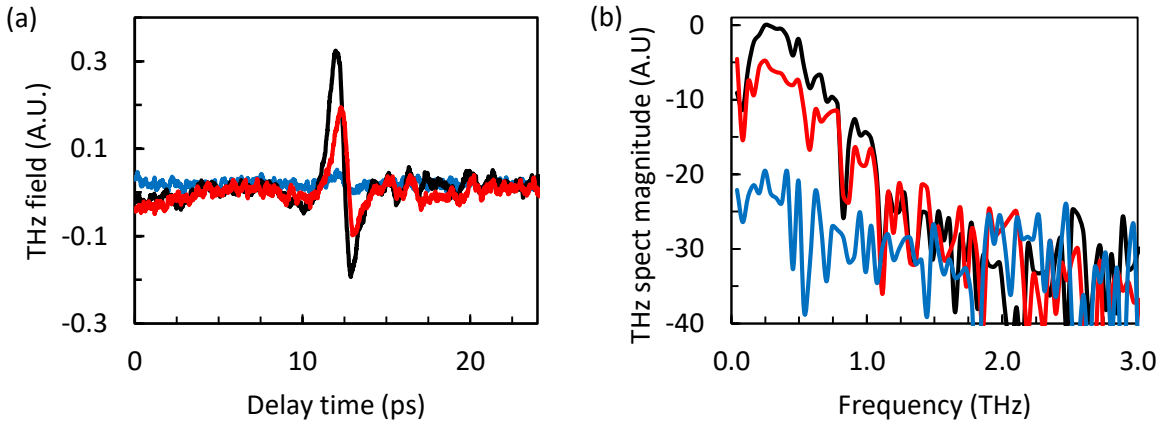

Figure B.3: Terahertz waveforms (a) and terahertz spectrums (b) generated in the LGT crystal by using optical rectification of a femtosecond laser pump beam with an average power of a 20 mW (~0.02 TW/cm^2; blue line), 168 mW (~0.21 TW/cm^2; red line) and 285 mW (~0.37 TW/cm^2; black line).

The THz signal from LGT crystal was recorded under different average laser powers. Even with a lower average power (20 mW), and THz signal can be detected (see Figure B.3). The polarization state of terahertz waves generated in the LGT crystal was studied for different azimuthal angles (crystal orientations). Figure B.4 shows the THz pulse peak field amplitude versus the polarization angle of the pumping laser beam for different azimuthal angles of the crystal (30°, 35°, 52.5° and 80°). The data curves (point in Figure B.4) are normalized and fitted nicely with the transfer function (η) of the set-up [229]. This function is the ratio of the intensity of the THz signal and the average THz signal, which depends on:

$$\eta \propto \cos(3\Theta_0 + 4\gamma + \arctan(2\Theta_0 - 4\gamma)) \qquad \text{(B.4)}$$

where Θ_0 is the azimuthal angle and γ is the angle of the half-wave plate. The results show that the THz efficiency in the LGT crystal are same whatever the crystal orientation is. The LGT crystal can be used as an electro-optic sensor because the rotation of the LGT axis is not necessary to optimize THz signal, it can be just optimized by rotating the pump and probe laser beams. [187].

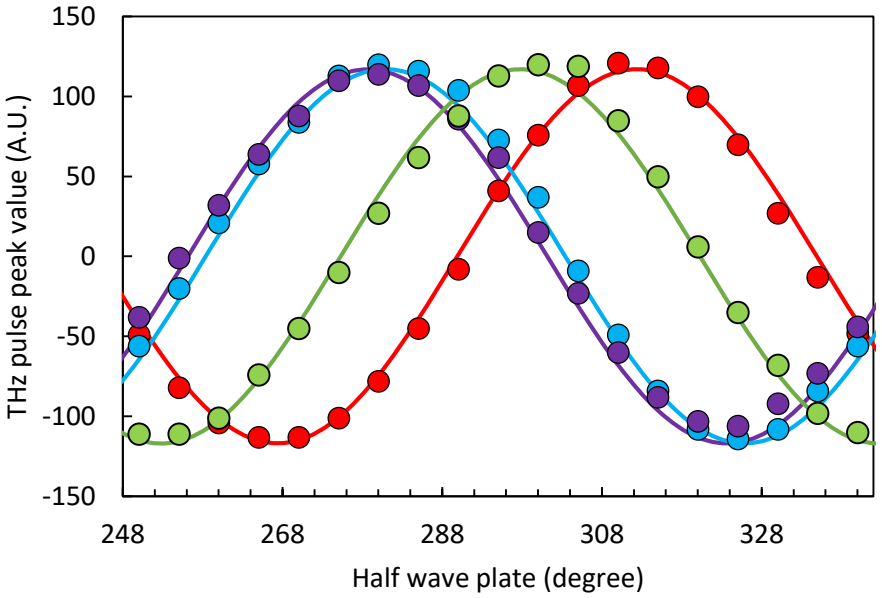

Figure B.4: THz signals generated in the LGT crystal for four different azimuthal angles 30°(blue), 35° (purple), 52.5°(green) and 80°(red) versus half-wave plate angle. The data are fitted with Equation (B.1) (continuous lines)

B.2. Absorption Coefficient and Refractive Index in THz

THz characterization of both refractive index and absorption coefficient of the material can be obtained by determining the amplitude and phase of the recorded THz-TDS signals, (see Section 2.3). To perform the experiment, the sample should be more or less transparent. For the measurement, we used the experimental setup shown in Figure 5.9. In that setup, we moved the Teflon lens and put a LTG-GaAs photoconductive antenna (from Teravil) as a THz emitter in the sample location. The LGT crystal with a thickness of 0.43 mm was placed between the PC antennas which were separated by a distance of 12 cm.

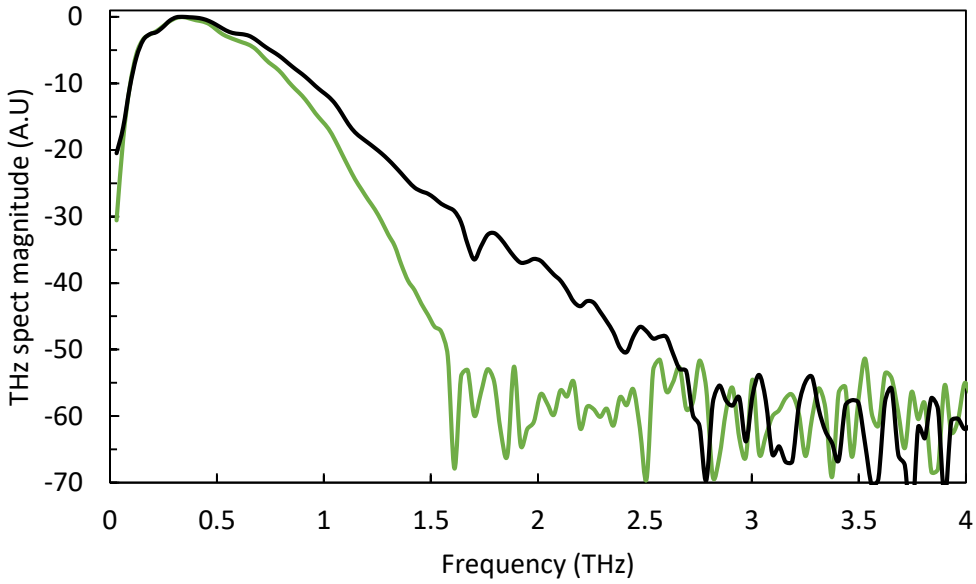

Figure B.5: The measured THz spectrum with (black line) and without (green line) the LGT crystal.

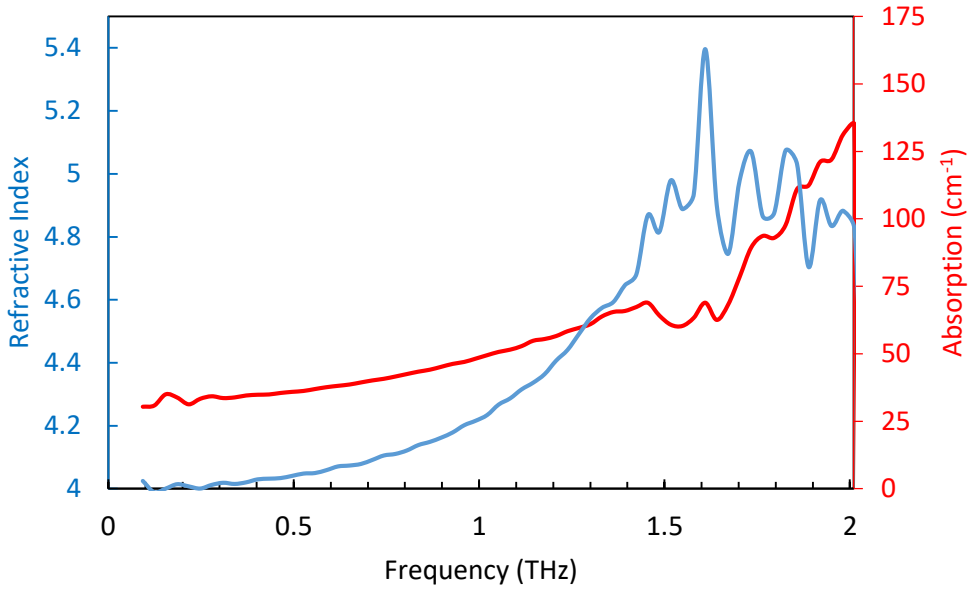

Figure B.6: Index of refraction (blue line) and absorption coefficient values (red line) of the LGT crystal.

The THz electric field were monitored with and without the LGT crystal (see Figure B.5). The ratio of the reference and obtained spectra gives the complex transmission coefficient of the sample $T(\nu)$ shown in Equation (2.19), which is used to calculate the index of refraction and absorption coefficient spectra. To determine the values, we used a software which has already been developed in our laboratory. As a result, the LGT crystal is transparent from 0.04 THz to 1 THz. The obtained refractive and the absorption coefficients are plotted in Figure B.6. The values were measured for two axes of the LGT crystal by rotating the sample 90°. As expected, the crystal shows an isotropic behaviour on both axes. A resonance, certainly of vibrational origin, is seen at 1.6 THz: this resonance

leads to a high absorption in the THz range, and will limit the THz application of LGT to frequencies typically below 1 THz.

B.3. Damage threshold and comparison with ZnTe crystal

THz generation efficiency in 3 mm thick LGT was compared with a 4 mm thick ZnTe crystal. The experiment was performed using the experimental setup shown in Figure 5.5. Both crystals were illuminated by a laser beam with a same beam waist of 0.735 mm, and the peak power densities on the crystals were varied from 0.03 TW/cm^2 to 0.37 TW/cm^2. The experimental data were obtained by recording the peak value of the THz pulse on the lock-in amplifier. As the results are seen in Figure B.7, the ZnTe crystal generates more signal than the LGT crystal but does not present a linearity between the generated THz field and the power of the laser beam (the fitted curve: $E_{THz,ZnTe} \propto 440\ P_{laser} + 50$). However, a good linearity was obtained for the LGT crystal (the fitted curve: $E_{THz,LGT} \propto 86\ P_{laser}$) and no saturation was observed until 0.37 TW/cm^2 which is the maximum value delivered by our setup. Additionally, the nonlinear coefficient d_{11} for the LGT crystal in Equation (B.3) is extracted by comparing with the nonlinear coefficient of the ZnTe crystal. The ZnTe crystal might be already in the saturation zone for these applied peak power densities [168], that is why we fitted the first experimental data for the ZnTe crystal to give an order of the estimated the nonlinear coefficient d_{11}. For the ZnTe crystal, the relationship between the THz field generated in the crystal and the laser power is:

$$E_{THz,ZnTe} \propto d_{14} {E_{laser}}^2 \qquad \text{(B.4)}$$

where $d_{14} = 61$ pm/V [230]. Therefore, the nonlinear coefficient for the LGT crystal d_{11} is around order of $15 - 3$ pm/V. However, we need to take into account the ratio of the thicknesses of the crystals, *i.e.* 4/3. As a result, the nonlinear coefficient d_{11} is in the order of 12 – 2 pm/V for the LGT crystal.

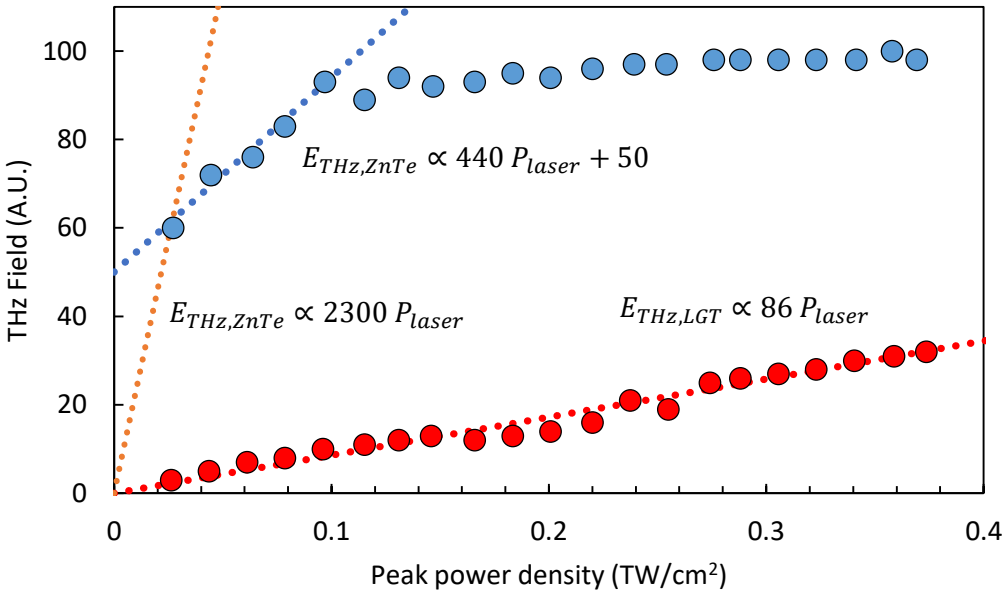

Figure B.7: THz signals obtained by the ZnTe crystal (blue circles) and the LGT crystal (red circles) versus peak power density. The experimental data of the LGT crystal shows a good linearity (red dashed line).

We also compared the damage threshold of the ZnTe crystal and the LGT crystal. The experiment was performed with the same laser average power (285 mW, the maximum laser power in our setup) but varied the spot size of the laser beam on the crystals. After damaging the samples, the size of the damaged regions was measured with a commercial microscopy available in our laboratory. The photos of the damaged areas on the crystals and the values of the crystal damage threshold are given in Figure B.8. As a result, the applied peak power density on the LGT crystal is higher than the ZnTe crystal, *i.e.*, the LGT crystal has higher damage threshold than the ZnTe crystal (15 times higher).

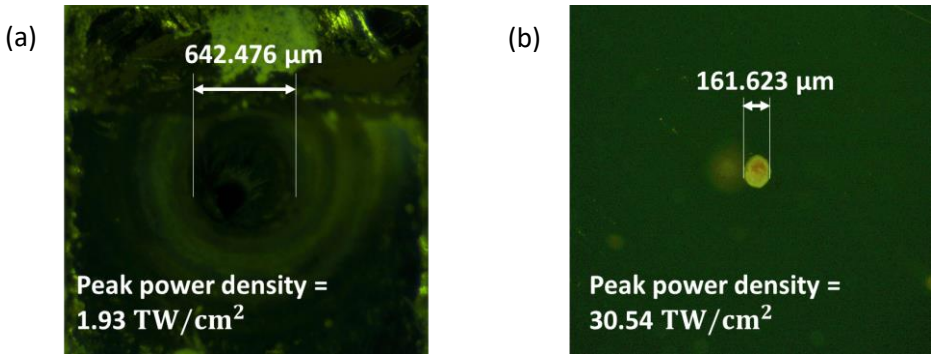

Figure B.8: The photos of damaged place with the applied peak power density on (a) the ZnTe crystal and (b) the LGT crystal

B.4. Conclusion

For the first time, the THz generation in a LGT crystal by optical rectification is demonstrated. It is found that the THz efficiency in the LGT crystal is independent of the crystal orientation. The crystal is compared with the one of the most common crystals used for the THz generation, ZnTe. Although, the THz signal in ZnTe is generated more than the LGT crystal, it is observed that the generated THz field is saturated in ZnTe crystal. However, no saturation is observed for the LGT crystal. Lastly, the damage threshold of both crystals were compared, and the LGT has higher damage threshold than the ZnTe.

Bibliography

1. G. Soylu, F. Sanjuan, E. Hérault, J.-F. Roux, F. Levy-bertrand, M. Calvo, A. Monfardini, and J.-L. Coutaz, "Detection of weak terahertz pulsed signals using kinetic inductance detectors," J. Infrared Millim. Terahertz Waves **40**(1), 31–37 (2019).

2. Y.-S. Lee, *Principles of Terahertz Science and Technology* (Springer US, 2009).

3. S. S. Dhillon, M. S. Vitiello, E. H. Linfield, A. G. Davies, M. C. Hoffmann, J. Booske, C. Paoloni, M. Gensch, P. Weightman, G. P. Williams, E. Castro-Camus, D. R. S. Cumming, F. Simoens, I. Escorcia-Carranza, J. Grant, S. Lucyszyn, M. Kuwata-Gonokami, K. Konishi, M. Koch, C. A. Schmuttenmaer, T. L. Cocker, R. Huber, A. G. Markelz, Z. D. Taylor, V. P. Wallace, J. A. Zeitler, J. Sibik, T. M. Korter, B. Ellison, S. Rea, P. Goldsmith, K. B. Cooper, R. Appleby, D. Pardo, P. G. Huggard, V. Krozer, H. Shams, M. Fice, C. Renaud, A. Seeds, A. Stohr, M. Naftaly, N. Ridler, R. Clarke, J. E. Cunningham, and M. B. Johnston, "The 2017 terahertz science and technology roadmap," J. Phys. D. Appl. Phys. **50**(4), 043001 (2017).

4. D. H. Auston, "Picosecond optoelectronic switching and gating in silicon," Appl. Phys. Lett. **26**(3), 101–103 (1975).

5. C. Fattinger and D. Grischkowsky, "Point source terahertz optics," Appl. Phys. Lett. **53**(16), 1480–1482 (1988).

6. C. Fattinger and D. Grischkowsky, "Terahertz beams," Appl. Phys. Lett. **54**(6), 490–492 (1989).

7. M. Van Exter, C. Fattinger, and D. Grischkowsky, "Terahertz time-domain spectroscopy of water vapor," Opt. Lett. **14**(20), 1128–1130 (1989).

8. M. Van Exter and D. R. Grischkowsky, "Characterization of an optoelectronic terahertz beam system," IEEE Trans. Microw. Theory Tech. **38**(11), 1684–1691 (1990).

9. D. H. Auston, K. P. Cheung, J. A. Valdmanis, and D. A. Kleinman, "Cherenkov radiation from femtosecond optical pulses in electro-optic media," Phys. Rev. Lett. **53**(16), 1555–1558 (1984).

10. Q. Wu, T. D. Hewitt, and X.-C. Zhang, "Two-dimensional electro-optic imaging of THz beams," **69**(8), 1026–1028 (1996).

11. H. Hamster, A. Sullivan, S. Gordon, W. White, and R. W. Falcone, "Subpicosecond, electromagnetic pulses from intense laser-plasma interaction," Phys. Rev. Lett. **71**(17), 2725–2728 (1993).

12. N. Karpowicz, J. Dai, X. Lu, Y. Chen, M. Yamaguchi, H. Zhao, X.-C. Zhang, L. Zhang, C. Zhang, M. Price-Gallagher, C. Fletcher, O. Mamer, A. Lesimple, and K. Johnson, "Coherent heterodyne time-domain spectrometry covering the entire “terahertz gap,”" Appl. Phys. Lett. **92**(1), 011131 (2008).

13. M. Tonouchi, "Cutting-edge terahertz technology," Nat. Photonics **1**(2), 97–105 (2007).

14. P. U. Jepsen, D. G. Cooke, and M. Koch, "Terahertz spectroscopy and imaging – Modern techniques and applications," Laser Photonics Rev. **5**(1), 124–166 (2011).

15. J. P. Guillet, B. Recur, L. Frederique, B. Bousquet, L. Canioni, I. Manek-Honninger, P. Desbarats, and P. Mounaix, "Review of terahertz tomography techniques," J. Infrared Millim. Terahertz

Waves **35**(4), 382–411 (2014).

16. C. Jordens and M. Koch, "Detection of foreign bodies in chocolate with pulsed terahertz spectroscopy," Opt. Eng. **47**(3), 0037003 (2008).

17. G. Kim, J. Kim, S. Jeon, J. Kim, K.-K. Park, and C.-H. Oh, "Enhanced continuous-wave terahertz imaging with a horn antenna for food inspection," J. Infrared Millim. Terahertz Waves **33**(6), 657–664 (2012).

18. Y. Lee, S. Choi, S. Han, D. H. Woo, and H. S. Chun, "Detection of foreign bodies in foods using continuous wave terahertz imaging," J. Food Prot. **75**(1), 179–183 (2012).

19. G. Ok, H. Jung, H. Sook, and S. Choi, "Foreign-body detection in dry food using continuous sub-terahertz wave imaging," Food Control **42**, 284–289 (2014).

20. M. C. Kemp, "Explosives detection by terahertz spectroscopy — A bridge too far?," IEEE Trans. Terahertz Sci. Technol. **1**(1), 282–292 (2011).

21. B. H. Liu, H. Zhong, N. Karpowicz, Y. Chen, and X. Zhang, "Terahertz spectroscopy and imaging for defense and security applications," Proc. IEEE **95**(8), 1514–1527 (2007).

22. Y. Jin, G. Kim, C. Shon, S. Jeon, and J. Kim, "Analysis of petroleum products and their mixtures by using terahertz time domain spectroscopy," J. Korean Phys. Soc. **53**(4), 1879–1885 (2008).

23. K. Kawase, Y. Ogawa, and Y. Watanabe, "Non-destructive terahertz imaging of illicit drugs using spectral fingerprints," Opt. Express **11**(20), 2549–2554 (2003).

24. J. F. Federici, B. Schulkin, F. Huang, D. Gary, R. Barat, F. Oliveira, and D. Zimdars, "THz imaging and sensing for security applications — explosives, weapons and drugs," Semicond. Sci. Technol. **20**(7), S266–S280 (2005).

25. B. R. Appleby and R. N. Anderton, "Millimeter-wave and submillimeter-wave imaging for security and surveillance," Proc. IEEE **95**(8), 1683–1690 (2007).

26. D. Arnone, C. Ciesla, and M. Pepper, "Terahertz imaging comes into view," Phys. World **13**(4), 35–40 (2000).

27. A. J. Fitzgerald, E. Berry, N. N. Zinnov'Ev, S. Homer-Vanniasinkam, R. E. Miles, J. M. Chamberlain, and M. A. Smith, "Catalogue of human tissue optical properties at terahertz frequencies," J. Biol. Phys. **29**(2–3), 123–128 (2003).

28. E. Leiss-Holzinger, K. Wiesauer, H. Stephani, B. Heise, D. Stifter, B. Kriechbaumer, S. J. Spachinger, C. Gusenbauer, and G. Withalm, "Imaging of the inner structure of cave bear teeth by novel non-destructive techniques," Palaeontol. Electron. **18**(1), 1T (2015).

29. E. Pickwell, B. E. Cole, A. J. Fitzgerald, V. P. Wallace, and M. Pepper, "Simulation of terahertz pulse propagation in biological systems," Appl. Phys. Lett. **84**(12), 2190–2192 (2004).

30. R. M. Woodward, B. E. Cole, V. P. Wallace, R. J. Pye, D. D. Arnone, E. H. Linfield, and M. Pepper, "Terahertz pulse imaging in reflection geometry of human skin cancer and skin tissue," Phys. Med. Biol. **47**(21), 3853–3863 (2002).

31. A. J. Fitzgerald, V. P. Wallace, M. Jimenez-Linan, L. Bobrow, R. J. Pye, A. D. Purushotham, and D. D. Arnone, "Terahertz pulsed imaging of human breast tumors," Radiology **239**(2), 533–540

(2006).

32. E. Pickwell and V. P. Wallace, "Biomedical applications of terahertz technology," J. Phys. D. Appl. Phys. **39**(17), R301–R310 (2006).

33. K. Fukunaga, Y. Ogawa, S. Hayashi, and I. Hosako, "Terahertz spectroscopy for art conservation," IEICE Electron. Express **4**(8), 258–263 (2007).

34. J. B. Jackson, J. Bowen, G. Walker, J. Labaune, G. Mourou, M. Menu, and K. Fukunaga, "A survey of terahertz applications in cultural heritage conservation science," IEEE Trans. Terahertz Sci. Technol. **1**(1), 220–231 (2011).

35. A. J. L. Adam, P. C. M. Planken, S. Meloni, and J. Dik, "TeraHertz imaging of hidden paint layers on canvas," Opt. Express **17**(5), 3407–3416 (2009).

36. K. Fukunaga, I. Hosako, Y. Kohdzuma, T. Koezuka, M.-J. Kim, T. Ikari, and X. Du, "Terahertz analysis of an East Asian historical mural painting," J. Eur. Opt. Soc. - Rapid Publ. **5**, 10024 (2010).

37. J. Caumes, A. Younus, S. Salort, B. Chassagne, B. Recur, A. Ziéglé, A. Dautant, and E. Abraham, "Terahertz tomographic imaging of XVIIIth Dynasty Egyptian sealed pottery," Appl. Opt. **50**(20), 3604–3608 (2011).

38. J. W. Bowen, "Terahertz spectroscopy and imaging at the nanoscale for biological and security applications," in *Nano-Optics for Enhancing Light-Matter Interactions on a Molecular Scale* (2012), pp. 287–303.

39. R. Ulbricht, E. Hendry, J. Shan, T. F. Heinz, and M. Bonn, "Carrier dynamics in semiconductors studied with time-resolved terahertz spectroscopy," Rev. Mod. Phys. **83**(2), 543–586 (2011).

40. T. Kiwa, M. Tonouchi, M. Yamashita, and K. Kawase, "Laser terahertz-emission microscope for inspecting electrical faults in integrated circuits," Opt. Lett. **28**(21), 2058–2060 (2003).

41. H. Nakanishi, S. Fujiwara, K. Takayama, I. Kawayama, H. Murakami, and M. Tonouchi, "Imaging of a polycrystalline silicon solar cell using a laser terahertz emission microscope," Appl. Phys. Express **5**(11), 112301 (2012).

42. T. S. Hartwick, D. T. Hodges, D. H. Barker, and F. B. Foote, "Far infrared imagery," Appl. Opt. **15**(8), 1919–1922 (1976).

43. D. H. Auston and M. C. Nuss, "Electrooptic generation and detection of femtosecond electrical transients," IEEE J. Quantum Electron. **24**(2), 184–197 (1988).

44. B. B. Hu and M. C. Nuss, "Imaging with terahertz waves," Opt. Lett. **20**(16), 1716–1718 (1995).

45. D. M. Mittleman, R. H. Jacobsen, and M. C. Nuss, "T-Ray imaging," IEEE J. Sel. Top. Quantum Electron. **2**(3), 679–692 (1996).

46. X.-C. Zhang, "Terahertz wave imaging: horizons and hurdles," Phys. Med. Biol. **47**(21), 3667–3677 (2002).

47. W. L. Chan, J. Deibel, and D. M. Mittleman, "Imaging with terahertz radiation," Reports Prog. Phys. **70**(8), 1325–1379 (2007).

48. P. H. Siegel, "Terahertz technology," IEEE Trans. Microw. Theory Tech. **50**(3), 910–928 (2002).

49. T. Globus, I. Sizov, J. Ferrance, A. Jazaeri, J. Bryant, A. Moyer, B. Gelmont, M. Kester, and A. Bykhovski, "Sub-terahertz vibrational spectroscopy for microRNA based diagnostic of ovarian cancer," Converg. Sci. Phys. Oncol. **2**(4), 045001 (2016).

50. S. Hunsche, M. Koch, I. Brener, and M. C. Nuss, "THz near-field imaging," Opt. Commun. **150**(1–6), 22–26 (1998).

51. E. H. Synge, "A suggested method for extending the microscopic resolution into the ultra-microscopic region," Philos. Mag. **6**(35), 356–362 (1928).

52. H. A. Bethe, "Theory of diffraction by small holes," Phys. Rev. **66**(7–8), 163–182 (1944).

53. S. Collin, F. Pardo, and J.-L. Pelouard, "Waveguiding in nanoscale metallic apertures," Opt. Express **15**(7), 4310–4320 (2007).

54. T. W. Ebbesen, H. J. Lezec, H. F. Ghaemi, T. Thio, and P. A. Wolff, "Extraordinary optical transmission through sub-wavelength hole arrays," Nature **391**(6668), 667–669 (1998).

55. F. J. Garcia de Abajo, "Light transmission through a single cylindrical hole in a metallic film," Opt. Express **10**(25), 1475–1484 (2002).

56. T. D. Nguyen, Z. V. Vardeny, and A. Nahata, "Concentration of terahertz radiation through a conically tapered aperture," Opt. Express **18**(24), 25441–25448 (2010).

57. S. Liu, O. Mitrofanov, and A. Nahata, "Near-field terahertz imaging using sub- wavelength apertures without cutoff," Opt. Express **24**(3), 2728–2736 (2016).

58. D. M. Pozar, *Microwave Engineering* (John Wiley & Sons, Inc, 2011).

59. J. Weiner, "The physics of light transmission through subwavelength apertures and aperture arrays," Reports Prog. Phys. **72**(6), 064401 (2009).

60. D. S. Bulgarevich, M. Watanabe, and M. Shiwa, "Single sub-wavelength aperture with greatly enhanced transmission," New J. Phys. **14**, 053001 (2012).

61. S. Liu, Z. V. Vardeny, and A. Nahata, "Concentration of broadband terahertz radiation using a periodic array of conically tapered apertures," Opt. Express **21**(10), 12363–12372 (2013).

62. K. Ishihara, K. Ohashi, T. Ikari, H. Minamide, H. Yokoyama, J. Shikata, and H. Ito, "Terahertz-wave near-field imaging with subwavelength resolution using surface-wave-assisted bow-tie aperture," Appl. Phys. Lett. **89**(20), 201120 (2006).

63. E. X. Jin and X. Xu, "Finitte-difference time-domain studies on optical transmission through planar nano-apertures in a metal film," Jpn. J. Appl. Phys. **43**(1), 407–417 (2004).

64. X. Shi and L. Hesselink, "Mechanisms for enhancing power throughput from planar nano-apertures for near-field optical data storage," Jpn. J. Appl. Phys. **41**(3B), 1632–1635 (2002).

65. K. Tanaka and M. Tanaka, "Simulation of an aperture in the thick metallic screen that gives high intensity and small spot size using surface plasmon polariton," J. Microsc. **210**(3), 294–300 (2003).

66. H. Cao, A. Agrawal, and A. Nahata, "Controlling the transmission resonance lineshape of a single subwavelength aperture," Opt. Express **13**(3), 763–769 (2005).

67. F. J. Garcia-Vidal, H. J. Lezec, T. W. Ebbesen, and L. Martin-Moreno, "Multiple paths to enhance optical transmission through a single subwavelength slit," Phys. Rev. Lett. **90**(21), 213901 (2003).

68. M. J. Lockyear, A. P. Hibbins, J. R. Sambles, and C. R. Lawrence, "Enhanced microwave transmission through a single subwavelength aperture surrounded by concentric grooves," J. Opt. A Pure Appl. Opt. **7**(2), S152–S158 (2005).

69. A. J. Huber, F. Keilmann, J. Wittborn, J. Aizpurua, and R. Hillenbrand, "Terahertz near-field nanoscopy of mobile carriers in single semiconductor nanodevices," Nano Lett. **8**(11), 3766–3770 (2008).

70. O. Mitrofanov, I. Brener, R. Harel, J. D. Wynn, L. N. Pfeiffer, K. W. West, and J. Federici, "Terahertz near-field microscopy based on a collection mode detector," Appl. Phys. Lett. **77**(22), 3496–3498 (2000).

71. O. Mitrofanov, M. Lee, J. W. P. Hsu, L. N. Pfeiffer, K. W. West, J. D. Wynn, and J. F. Federici, "Terahertz pulse propagation through small apertures," Appl. Phys. Lett. **79**(7), 907–909 (2001).

72. U. Schade, K. Holldack, P. Kuske, G. Wüstefeld, and H. W. Hübers, "THz near-field imaging employing synchrotron radiation," Appl. Phys. Lett. **84**(8), 1422–1424 (2004).

73. K. Ishihara, T. Ikari, H. Minamide, J. Shikata, K. Ohashi, H. Yokoyama, and H. Ito, "Terahertz near-field imaging using enhanced transmission through a single subwavelength aperture," Jpn. J. Appl. Phys. **44**(29), L929–L931 (2005).

74. C.-M. Chiu, H.-W. Chen, Y.-R. Huang, Y.-J. Hwang, W.-J. Lee, H. Huang, and C.-K. Sun, "All-terahertz fiber-scanning near-field microscopy," Opt. Lett. **34**(7), 1084–1086 (2009).

75. B. Knoll, F. Keilmann, A. Kramer, and R. Guckenberger, "Contrast of microwave near-field microscopy," Appl. Phys. Lett. **70**(20), 2667–2669 (1997).

76. S. Mastel, M. B. Lundeberg, P. Alonso-Gonzalez, Y. Gao, K. Watanabe, T. Taniguchi, J. Hone, F. H. L. Koppens, A. Y. Nikitin, and R. Hillenbrand, "THz nanofocusing with cantilevered THz-resonant antenna tips," Nano Lett. **17**(11), 6526–6533 (2017).

77. N. C. J. Van der Valk and P. C. M. Planken, "Electro-optic detection of subwavelength terahertz spot sizes in the near field of a metal tip," Appl. Phys. Lett. **81**(9), 1558–1560 (2002).

78. H. T. Chen, R. Kersting, and G. C. Cho, "Terahertz imaging with nanometer resolution," Appl. Phys. Lett. **83**(15), 3009–3011 (2003).

79. K. Moon, H. Park, J. Kim, Y. Do, S. Lee, G. Lee, H. Kang, and H. Han, "Subsurface nanoimaging by broadband terahertz pulse near-field microscopy," Nano Lett. **15**(1), 549–552 (2015).

80. M. Eisele, T. L. Cocker, M. A. Huber, M. Plankl, L. Viti, D. Ercolani, L. Sorba, M. S. Vitiello, and R. Huber, "Ultrafast multi-terahertz nano-spectroscopy with sub-cycle temporal resolution," Nat. Photonics **8**(11), 841–845 (2014).

81. M. Wachter, M. Nagel, and H. Kurz, "Tapered photoconductive terahertz field probe tip with subwavelength spatial resolution," Appl. Phys. Lett. **95**(4), 041112 (2009).

82. T. L. Cocker, V. Jelic, M. Gupta, S. J. Molesky, J. A. J. Burgess, G. De Los Reyes, L. V Titova, Y. Y.

Tsui, M. R. Freeman, and F. A. Hegmann, "An ultrafast terahertz scanning tunnelling microscope," Nat. Photonics **7**(8), 620–625 (2013).

83. T. L. Cocker, D. Peller, P. Yu, J. Repp, and R. Huber, "Tracking the ultrafast motion of a single molecule by femtosecond orbital imaging," Nature **539**(7628), 263–267 (2016).

84. I. Brener, D. Dykaar, A. Frommer, L. N. Pfeiffer, J. Lopata, J. Wynn, K. West, and M. C. Nuss, "Terahertz emission from electric field singularities in biased semiconductors," Opt. Lett. **21**(23), 1924–1926 (1996).

85. M. Yamashita, K. Kawase, C. Otani, T. Kiwa, and M. Tonouchi, "Imaging of large-scale integrated circuits using laser terahertz emission microscopy," Opt. Express **13**(1), 115–120 (2005).

86. R. Lecaque, S. Gresillon, and C. Boccara, "THz emission Microscopy with sub-wavelength broadband source," Opt. Express **16**(7), 4731–4738 (2008).

87. F. Blanchard, A. Doi, T. Tanaka, H. Hirori, H. Tanaka, Y. Kadoya, and K. Tanaka, "Real-time terahertz near-field microscope," Opt. Express **19**(9), 8277–8284 (2011).

88. P. Klarskov, H. Kim, V. L. Colvin, and D. M. Mittleman, "Nanoscale laser terahertz emission microscopy," ACS Photonics **4**(11), 2676–2680 (2017).

89. J. M. Atkin, S. Berweger, A. C. Jones, and M. B. Raschke, "Nano-optical imaging and spectroscopy of order, phases, and domains in complex solids," Adv. Phys. **61**(6), 745–842 (2012).

90. Y. Kinoshita, N. Kida, M. Sotome, R. Takeda, N. Abe, M. Saito, T. Arima, and H. Okamoto, "Visualization of ferroelectric domains in boracite using emission of terahertz radiation," Jpn. J. Appl. Phys. **53**(9), 09PD08 (2014).

91. M. Sotome, N. Kida, S. Horiuchi, and H. Okamoto, "Visualization of ferroelectric domains in a hydrogen-bonded molecular crystal using emission of terahertz radiation," Appl. Phys. Lett. **105**(4), 041101 (2014).

92. M. Sotome, N. Kida, S. Horiuchi, and H. Okamoto, "Terahertz radiation imaging of ferroelectric domain topography in room-temperature hydrogen-bonded supramolecular ferroelectrics," ACS Photonics **2**(9), 1373–1383 (2015).

93. F. Sanjuan, G. Gaborit, and J.-L. Coutaz, "Sub-wavelength terahertz imaging through optical rectification," Sci. Rep. **8**(1), 13492 (2018).

94. J.-L. Coutaz, R. Boquet, N. Breuil, L. Chusseau, P. Crozat, J. Demaison, L. Duvillaret, G. Gallot, F. Garet, J.-F. Lampin, D. Lippens, J. Mangeney, P. Mounaix, G. Mouret, and J.-F. Roux, *Optoélectronique Térahertz* (EDP Sciences, 2008).

95. P. Shumyatsky and R. R. Alfano, "Terahertz sources," J. Biomed. Opt. **16**(3), 033001 (2011).

96. C. L. Tang, "Nonlinear Optics," in *Handbook of Optics Volume II - Devices, Measurements and Properties*, M. Bass, ed. (McGraw-Hill, Inc, 1995).

97. R. W. Boyd, *Nonlinear Optics* (Academic Press, Inc, 2008).

98. M. Bass, P. A. Franken, J. F. Ward, and G. Weinreich, "Optical rectification," Phys. Rev. Lett. **9**(11), 446–449 (1962).

99. J. R. Morris and Y. R. Shen, "Far-infrared generation by picosecond pulses in electro-optical materials," Opt. Commun. **3**(2), 81–84 (1971).

100. K. H. Yang, P. L. Richards, and Y. R. Shen, "Generation of far-infrared radiation by picosecond light pulses in LiNbO3," Appl. Phys. Lett. **19**(9), 320–323 (1971).

101. B. B. Hu, X.-C. Zhang, D. H. Auston, and P. R. Smith, "Free-space radiation from electro-optic crystals," Appl. Phys. Lett. **56**(6), 506–508 (1990).

102. X.-C. Zhang and J. Xu, *Introduction to THz Wave Photonics* (Springer US, 2010).

103. Q. Wu and X.-C. Zhang, "Design and characterization of traveling-wave electrooptic terahertz sensors," IEEE J. Sel. Top. Quantum Electron. **2**(3), 693–700 (1996).

104. M. C. Hoffmann and J. Andras Fulop, "Intense ultrashort terahertz pulses: generation and applications," J. Phys. D. Appl. Phys. **44**(8), 083001 (2011).

105. R. Huber, A. Brodschelm, F. Tauser, and A. Leitenstorfer, "Generation and field-resolved detection of femtosecond electromagnetic pulses tunable up to 41 THz," Appl. Phys. Lett. **76**(22), 3191–3193 (2000).

106. A. Schneider, M. Stillhart, and P. Günter, "High efficiency generation and detection of terahertz pulses using laser pulses at telecommunication wavelengths," Opt. Express **14**(12), 5376–5384 (2006).

107. M. Jazbinsek, U. Puc, A. Abina, and A. Zidansek, "Organic crystals for THz photonics," Appl. Sci. **9**(5), 882 (2019).

108. D. H. Auston and P. R. Smith, "Generation and detection of millimeter waves by picosecond photoconductivity," Appl. Phys. Lett. **43**(7), 631–633 (1983).

109. M. Van Exter, C. Fattinger, and D. Grischkowsky, "High-brightness terahertz beams characterized with an ultrafast detector," Appl. Phys. Lett. **55**(4), 337–339 (1989).

110. P. U. Jepsen, R. H. Jacobsen, and S. R. Keiding, "Generation and detection of terahertz pulses from biased semiconductor antennas," J. Opt. Soc. Am. B **13**(11), 2424–2436 (1996).

111. S. Gupta, M. Y. Frankel, J. A. Valdmanis, J. F. Whitaker, G. A. Mourou, F. W. Smith, and A. R. Calawa, "Subpicosecond carrier lifetime in GaAs grown by molecular beam epitaxy at low temperatures," Appl. Phys. Express **59**(25), 3276–3278 (1991).

112. L. Duvillaret, F. Garet, J.-F. Roux, and J.-L. Coutaz, "Analytical modeling and optimization of terahertz time-domain spectroscopy experiments using photoswitches as antennas," IEEE J. Sel. Top. Quantum Electron. **7**(4), 615–623 (2001).

113. J. Van Rudd and D. M. Mittleman, "Influence of substrate-lens design in terahertz time-domain spectroscopy," J. Opt. Soc. Am. B **19**(2), 319–329 (2002).

114. Y. C. Shen, P. C. Upadhya, E. H. Linfield, H. E. Beere, and A. G. Davies, "Ultrabroadband terahertz radiation from low- temperature-grown GaAs photoconductive emitters," Appl. Phys. Lett. **83**(15), 3117–3119 (2003).

115. F. Sizov, "Terahertz radiation detectors: the state-of-the-art," Semicond. Sci. Technol. **33**(12), 123001 (2018).

116. F. Von Pockels, *Lehrubuch Des Kristalloptic* (B.G.Teubner, 1906).

117. Q. Wu and X.-C. Zhang, "Free-space electro-optic sampling of terahertz beams," Appl. Phys. Lett. **67**(24), 3523–3525 (1995).

118. Q. Wu and X.-C. Zhang, "Ultrafast electro-optic field sensors," Appl. Phys. Lett. **68**(12), 1604–1606 (1996).

119. Q. Wu and X.-C. Zhang, "7 terahertz broadband GaP electro-optic sensor," Appl. Phys. Lett. **70**(14), 1784–1786 (1997).

120. P. C. M. Planken, H.-K. Nienhuys, H. J. Bakker, and T. Wenckebach, "Measurement and calculation of the orientation dependence of terahertz pulse detection in ZnTe," J. Opt. Soc. Am. B **18**(3), 313–317 (2001).

121. K. Sakai, *Terahertz Optoelectronics* (Springer-Verlag Berlin Heidelberg, 2005).

122. C. T. Que, F. Miyamaru, S. Tanaka, M. Tani, and M. Hangyo, "Temporal rectification response of an asymmetric photoconductive antenna with Schottky contact," Jpn. J. Appl. Phys. **46**(2), 597–600 (2007).

123. H. Shimosato, M. Ashida, T. Itoh, S. Saito, and K. Sakai, "Ultrabroadband detection of terahertz radiation from 0.1 to 100 THz with photoconductive antenna," in *Ultrafast Optics V* (2007), pp. 317–323.

124. N. Vieweg, F. Rettich, A. Deninger, H. Roehle, R. Dietz, T. Göbel, and M. Schell, "Terahertz-time domain spectrometer with 90 dB peak dynamic range," J. Infrared Millim. Terahertz Waves **35**(10), 823–832 (2014).

125. F. Sizov, "THz radiation sensors," Opto-Electronics Rev. **18**(1), 10–36 (2010).

126. R. A. Lewis, "A review of terahertz detectors," J. Phys. D. Appl. Phys. **52**(43), 433001 (2019).

127. "Virginia Diodes," .

128. L. Liu, J. L. Hesler, H. Xu, A. W. Lichtenberger, and R. M. Weikleii, "A broadband quasi-optical terahertz detector utilizing a zero bias Schottky diode," IEEE Microw. Wirel. Components Lett. **20**(9), 504–506 (2010).

129. A. Semenov, O. Cojocari, H.-W. Hübers, F. Song, A. Klushin, and A.-S. Müller, "Application of zero-bias quasi-optical Schottky-diode detectors for monitoring short-pulse and weak terahertz radiation," IEEE Electron Device Lett. **31**(7), 674–676 (2010).

130. F. Simoens, "THz Bolometer Detectors," in *Physics and Applications of Terahertz Radiation* (Springer US, 2014).

131. P. L. Richards, "Bolometers for infrared and millimeter waves," J. Appl. Phys. **76**(1), 1–24 (1994).

132. M. Kenyon, P. K. Day, C. M. Bradford, J. J. Bock, and H. G. Leduc, "Background-limited membrane-isolated TES bolometers for far-IR/submillimeter direct-detection spectroscopy," Nucl. Instruments Methods Phys. Res. A **559**(2), 456–458 (2006).

133. A. Monfardini, L. J. Swenson, A. Bideaud, F. X. Désert, S. J. C. Yates, A. Benoit, A. M. Baryshev, J. J. A. Baselmans, S. Doyle, B. Kelvin, M. Roesch, C. Tucker, P. Ade, M. Calvo, P. Camus, C. Giordano, R. Guesten, C. Hoffmann, S. Leclercq, P. Mauskopf, and K. F. Schuster, "NIKA: A

millimeter-wave kinetic inductance camera," Astron. Astrophys. **521**, A29 (2010).

134. A. Monfardini, A. Benoit, A. Bideaud, L. Swenson, A. Cruciani, P. Camus, C. Hoffmann, F. X. Désert, S. Doyle, P. Ade, P. Mauskopf, C. Tucker, M. Roesch, S. Leclercq, K. F. Schuster, A. Endo, A. Baryshev, J. J. A. Baselmans, L. Ferrari, S. J. C. Yates, O. Bourrion, J. Macias-Perez, C. Vescovi, M. Calvo, and C. Giordano, "A dual-band millimeter-wave kinetic inductance camera for the IRAM 30 m telescope," Astrophys. J. Suppl. Ser. **194**(2), 24 (2011).

135. J. Hubmayr, J. Beall, D. Becker, H.-M. Cho, M. Devlin, B. Dober, C. Groppi, G. C. Hilton, K. D. Irwin, D. Li, P. Mauskopf, D. P. Pappas, J. Van Lanen, M. R. Vissers, Y. Wang, L. F. Wei, and J. Gao, "Photon-noise limited sensitivity in titanium nitride kinetic inductance detectors," Appl. Phys. Lett. **106**(7), 073505 (2015).

136. L. Duvillaret, F. Garet, and J.-L. Coutaz, "A reliable method for extraction of material parameters in terahertz time-domain spectroscopy," IEEE J. Sel. Top. Quantum Electron. **2**(3), 739–746 (1996).

137. M. Bernier, F. Garet, and J.-L. Coutaz, "Determining the complex refractive index of materials in the far-infrared from terahertz time-domain data," in *Terahertz Spectroscopy - A Cutting Edge Technology*, J. Uddin, ed. (Intech-Open Science, 2017), pp. 119–141.

138. J.-L. Coutaz, F. Garet, and V. Wallace, *Principles of Terahertz Time-Domain Spectroscopy* (Stanford Pan Publishing, 2018).

139. D. H. Andrews, W. F. Brucksch, W. T. Ziegler, and E. R. Blanchard, "Attenuated superconductors I. for measuring infra-red radiation," Rev. Sci. Instrum. **13**, 281–292 (1942).

140. K. D. Irwin and G. C. Hilton, "Transition-Edge Sensors," in *Cryogenic Particle Detection* (2005), pp. 63–150.

141. S. W. Henderson, J. R. Stevens, M. Amiri, J. Austermann, J. A. Beall, S. Chaudhuri, H.-M. Cho, S. K. Choi, N. F. Cothard, K. T. Crowley, S. M. Duff, C. P. Fitzgerald, P. A. Gallardo, M. Halpern, M. Hasselfield, G. Hilton, S.-P. P. Ho, J. Hubmayr, K. D. Irwin, B. J. Koopman, D. Li, Y. Li, J. McMahon, F. Nati, M. D. Niemack, C. D. Reintsema, M. Salatino, A. Schillaci, B. L. Schmitt, S. M. Simon, S. T. Staggs, E. M. Vavagiakis, and J. T. Ward, "Readout of two-kilopixel transition-edge sensor arrays for Advanced ACTPol," Proc. SPIE **9914**, 99141G (2016).

142. D. G. McDonald, "Novel superconducting thermometer for bolometric applications," Appl. Phys. Lett. **50**(12), 775–777 (1987).

143. B. A. Mazin, P. K. Day, J. Zmuidzinas, and H. G. Leduc, "Multiplexable kinetic inductance detectors," AIP Conf. Proc. **605**, 309–312 (2002).

144. P. K. Day, H. G. Leduc, B. A. Mazin, A. Vayonakis, and J. Zmuidzinas, "A broadband superconducting detector suitable for use in large arrays," Nature **425**(6960), 817–821 (2003).

145. B. A. Mazin, "Microwave kinetic inductance detectors," PhD Thesis (2004).

146. L. N. Cooper, "Bound electron pairs in a degenerate fermi gas," Phys. Rev. **104**(4), 1189–1190 (1956).

147. J. Bardeen, L. N. Cooper, and J. R. Schrieffer, "Microscopic theory of superconductivity," Phys. Rev. **106**(1), 162–164 (1957).

148. A. G. Kozorezov, A. F. Volkov, J. K. Wigmore, A. Peacock, A. Poelaert, and R. Den Hartog, "Quasiparticle-phonon downconversion in nonequilibrium superconductors," Phys. Rev. B **61**(17), 11807–11819 (2000).

149. M. Calvo, J. Goupy, A. D'Addabbo, A. Benoit, O. Bourrion, A. Catalano, and A. Monfardini, "Superconducting kinetic inductance detectors for astronomy and particle physics," Nucl. Instruments Methods Phys. Res. A **824**, 173–176 (2016).

150. C. J. Gorter and H. Casimir, "On superconductivity I.," Physica **1**, 306–320 (1934).

151. M. Tinkham, *Introduction to Superconductivity* (2004).

152. A. D'Addabbo, "Applications of kinetic inductance detectors to astronomy and particle physics," PhD Thesis (2014).

153. S. Doyle, "Lumped element kinetic inductance detectors," PhD Thesis (2008).

154. J. Baselmans, "Kinetic inductance detectors," J. Low Temp. Phys. **167**(3–4), 292–304 (2012).

155. A. Monfardini, R. Adam, A. Adane, P. Ade, P. Andre, A. Beelen, B. Belier, A. Benoit, A. Bideaud, N. Billot, O. Bourrion, M. Calvo, A. Catalano, G. Coiffard, B. Comis, A. D'Addabbo, F.-X. Désert, S. Soyle, J. Goupy, C. Kramer, S. Leclercq, J. Macias-Perez, J. Martino, P. Mauskopf, F. Mayet, F. Pajot, E. Pascale, N. Ponthieu, V. Réveret, L. Rodriguez, G. Savini, K. Schuster, A. Sievers, C. Tucker, and R. Zylka, "Latest NIKA results and the NIKA-2 project," J. Low Temp. Phys. **176**, 787–795 (2014).

156. H. G. Leduc, B. Bumble, P. K. Day, B. H. Eom, J. Gao, S. Golwala, B. A. Mazin, S. Mchugh, A. Merrill, D. C. Moore, O. Noroozian, A. D. Turner, and J. Zmuidzinas, "Titanium nitride films for ultrasensitive microresonator detectors," Appl. Phys. Lett. **97**(10), 102509 (2010).

157. N. Boudou, A. Benoit, O. Bourrion, M. Calvo, F.-X. Désert, J. Macias-Perez, A. Monfardini, and M. Roesch, "Kinetic inductance detectors for millimeter and submillimeter astronomy," Comptes Rendus Phys. **13**(1), 62–70 (2012).

158. I. Freund and M. Deutsch, "Second-harmonic microscopy of biological tissue," Opt. Lett. **11**(2), 94–96 (1986).

159. P. Theer, W. Denk, M. Sheves, A. Lewis, and P. B. Detwiler, "Second-harmonic generation imaging of membrane potential with retinal analogues," Biophys. J. **100**(1), 232–242 (2011).

160. M. Naftaly and R. Dudley, "Methodologies for determining the dynamic ranges and signal-to-noise ratios of terahertz time-domain spectrometers," Opt. Lett. **34**(8), 1213–1215 (2009).

161. J. Zmuidzinas, "Superconducting Microresonators: Physics and Applications," in *Annual Review of Condensed Matter Physics* (2012), **3**, pp. 169–214.

162. K. Wood, A. Bideaud, S. Doyle, A. Papageorgiou, E. Pascale, and S. Rowe, "The "KIDcam" passive THz imager; recent developments," 39th Int. Conf. Infrared Millim. Terahertz Waves (Tucson/Arizona), (2014).

163. S. L. Dexheimer, *Terahertz Spectroscopy: Principles and Applications* (Crc Press, 2008).

164. M. Roesch, A. Benoit, A. Bideaud, N. Boudou, M. Calvo, A. Cruciani, S. Doyle, H. G. Leduc, A. Monfardini, L. Swenson, S. Leclercq, P. Mauskopf, and K. F. Schuster, "Development of lumped

element kinetic inductance detectors for NIKA," arXiv **1212.4585**, (2012).

165. M. Calvo, A. Benoît, A. Catalano, J. Goupy, A. Monfardini, N. Ponthieu, E. Barria, G. Bres, M. Grollier, G. Garde, J.-P. Leggeri, G. Pont, S. Triqueneaux, R. Adam, O. Bourrion, J.-F. Macias-Pérez, M. Rebolo, A. Ritacco, J.-P. Scordilis, D. Tourres, A. Adane, G. Coiffard, S. Leclercq, F.-X. Désert, S. Doyle, P. Mauskopf, C. Tucker, P. Ade, P. André, A. Beelen, B. Belier, A. Bideaud, N. Billot, B. Comis, A. D'Addabbo, C. Kramer, J. Martino, F. Mayet, F. Pajot, E. Pascale, L. Perotto, V. Revéret, A. Ritacco, L. Rodriguez, G. Savini, K. Schuster, A. Sievers, and R. Zylka, "The NIKA2 instrument , a dual-band kilopixel KID array for millimetric astronomy," J. Low Temp. Phys. **184**(3–4), 816–823 (2016).

166. M. Rösch, "Development of lumped element kinetic inductance detectors for mm-wave astronomy at the IRAM 30 m telescope," PhD Thesis (2012).

167. "http://www.terahertz.co.uk/qmc-instruments-ltd," .

168. F. Sanjuan, G. Gaborit, and J.-L. Coutaz, "Influence of two-photon absorption anisotropy on terahertz emission through optical rectification in zinc-blende crystals," J. Infrared Millim. Terahertz Waves **39**(4), 378–386 (2018).

169. G. Gaborit, J. Oden, J.-F. Roux, J.-L. Coutaz, M. Yamashita, Y. Sasaki, and C. Otani, "Time-domain characterization of THz power detectors," 38th Int. Conf. Infrared Millim. Terahertz Waves (Mainz/Germany), (2013).

170. J. J. A. Baselmans, J. Bueno, S. J. C. Yates, O. Yurduseven, N. Llombart, K. Karatsu, A. M. Baryshev, L. Ferrari, A. Endo, D. J. Thoen, P. J. de Visser, R. M. J. Janssen, V. Murugesan, E. F. C. Driessen, G. Coiffard, J. Martion-Pintado, P. Hargrave, and M. Griffin, "A kilo-pixel imaging system for future space based far-infrared observatories using microwave kinetic inductance detectors," Astron. Astrophys. **601**, A89 (2017).

171. S. Vidal, J. Degert, M. Tondusson, E. Freysz, and J. Oberle, "Optimized terahertz generation via optical rectification in ZnTe crystals," J. Opt. Soc. Am. B **31**(1), 149–153 (2014).

172. S. M. Harrel, R. L. Milot, J. M. Schleicher, and C. A. Schmuttenmaer, "Influence of free-carrier absorption on terahertz generation from ZnTe (110)," J. Appl. Phys. **107**(3), 033526 (2010).

173. Z.-Y. Zhao, S. Hameau, and J. Tignon, "THz generation by optical rectification and competition with other nonlinear processes," Chinese Phys. Lett. **25**(5), 1868–1870 (2008).

174. M. Tani, Y. Hirota, C. T. Que, S. Tanaka, R. Hattori, M. Yamaguchi, S. Nishizawa, and M. Hangyo, "Novel terahertz photoconductive antennas," Int. J. Infrared Millimeter Waves **27**(4), 531–546 (2006).

175. W. Shi, L. Hou, and X. Wang, "High effective terahertz radiation from semi-insulating-GaAs photoconductive antennas with ohmic contact electrodes," J. Appl. Phys. **110**(2), 023111 (2011).

176. G. Klatt, F. Hilser, W. Qiao, M. Beck, R. Gebs, A. Bartels, K. Huska, U. Lemmer, G. Bastian, M. B. Johnston, M. Fischer, J. Faist, and T. Dekorsy, "Terahertz emission from lateral photo-Dember currents," Opt. Express **18**(5), 4939–4947 (2010).

177. K. Uehera and H. Kikuchi, "Transmission of a Gaussian beam through a circular aperture," Appl. Opt. **25**(24), 4514–4516 (1986).

178. B. E. A. Saleh and M. C. Teich, *Fundamentals of Photonics* (Wiley-Interscience, 2007).

179. L. Kang, V. Sadaune, and D. Lippens, "Numerical analysis of enhanced transmission through a single subwavelength aperture based on Mie resonance single particle," Prog. Electromagn. Res. **113**, 211–226 (2011).

180. J. W. Lee, M. A. Seo, D. S. Kim, S. C. Jeoung, C. Lienau, J. H. Kang, and Q.-H. Park, "Fabry–Perot effects in THz time-domain spectroscopy of plasmonic band-gap structures," Appl. Phys. Lett. **88**(7), 071114 (2006).

181. F. Nataf, "Absorbing boundary conditions and perfectly matched layers in wave propagation problems," Direct Inverse Probl. Wave Propag. Appl. **14**, 219–232 (2013).

182. I. Bardi, R. Remski, D. Perry, and Z. Cendes, "Plane wave scattering from frequency-selective surfaces by the finite-element method," IEEE Trans. Magn. **38**(2), 641–644 (2002).

183. F. Keilmann, "Scanning tip for optical radiation," U.S. Pat. **4,994,818**, (1991).

184. U. Schade, K. Holldack, M. C. Martin, and D. Fried, "THz near-field imaging of biological tissues employing synchrotron radiation," Ultrafast Phenom. Semicond. Nanostructure Mater. IX **5725**, 46–52 (2005).

185. M. Walther, D. G. Cooke, C. Sherstan, M. Hajar, M. R. Freeman, and F. A. Hegmann, "Terahertz conductivity of thin gold films at the metal-insulator percolation transition," Phys. Rev. B **76**(12), 125408 (2007).

186. R. Diaz-Uribe, M. Rosete-Aguilar, and R. Ortega-Martinez, "Position sensing of a Gaussian beam with a power meter and a knife edge," Rev. Mex. Fis. **39**(3), 484–492 (1993).

187. G. Gaborit, F. Sanjuan, and J.-L. Coutaz, "Second order nonlinear optical processes in [111] cubic crystals for terahertz optoelectronics," Lith. J. Phys. **58**(1), 24–37 (2018).

188. L. Gallais, D.-B. Douti, M. Commandré, G. Bataviciute, E. Pupka, M. Sciuka, L. Smalakys, V. Sirutkaitis, and A. Melninkaitis, "Wavelength dependence of femtosecond laser-induced damage threshold of optical materials," J. Appl. Phys. **117**(22), 223103 (2015).

189. J. Hebling, G. Almási, I. Z. Kozma, and J. Kuhl, "Velocity matching by pulse front tilting for large-area THz-pulse generation," Opt. Express **10**(21), 1161–1166 (2002).

190. J. Hebling, A. G. Stepanov, G. Almasi, B. Bartal, and J. Kuhl, "Tunable THz pulse generation by optical rectification of ultrashort laser pulses with tilted pulse fronts," Appl. Phys. B **78**(5), 593–599 (2004).

191. M. Unferdorben, Z. Szaller, I. Hajdara, J. Hebling, and L. Pálfalvi, "Measurement of refractive index and absorption coefficient of congruent and stoichiometric lithium niobate in the Terahertz range," J. Infrared Millim. Terahertz Waves **36**(12), 1203–1209 (2015).

192. F. Garet, L. Duvillaret, and J.-L. Coutaz, "Evidence of frequency-dependent THz beam polarization in time-domain spectroscopy," Proc. SPIE **3617**, 30–37 (2019).

193. G. Soylu, E. Hérault, F. Laurell, B. Boulanger, and J.-L. Coutaz, "Sub-wavelength THz imaging through optical rectification," 44th Int. Conf. Infrared Millim. Terahertz Waves (Paris/France), (2019).

194. G. Soylu, E. Hérault, B. Boulanger, F. Laurell, and J.-L. Coutaz, "Sub-wavelength THz imaging of the domains in periodically-poled crystals through optical rectification," J. Infrared Millim. Terahertz Waves (Submitted), (2019).

195. V. D. Antsygin, A. B. Kaplun, A. A. Mamrashev, N. A. Nikolaev, and O. I. Potaturkin, "Terahertz optical properties of potassium titanyl phosphate crystals," Opt. Express **22**(21), 25436–25443 (2014).

196. C.-R. Wang, Q.-K. Pan, F. Chen, G. Lanskii, N. Nikolaev, A. Mamrashev, Y. Andreev, and A. Meshalkin, "Phase-matching in KTP crystal for THz wave generation at room temperature and 81 K," Infrared Phys. Technol. **97**, 1–5 (2019).

197. J. D. Bierlein and H. Vanherzeele, "Potassium titanyl phosphate: properties and new applications," J. Opt. Soc. Am. B **6**(4), 622–633 (1989).

198. P. E. Perkins and T. S. Fahlen, "20-W average-power KTP intracavity-doubled Nd: YAG laser," J. Opt. Soc. Am. B **4**(7), 1066–1071 (1987).

199. M. Pierrou, F. Laurell, H. Karlsson, T. Kellner, C. Czeranowsky, and G. Huber, "Generation of 740 mW of blue light by intracavity frequency doubling with a first-order quasi-phase-matched KTiOPO4 crystal," Opt. Lett. **24**(4), 205–207 (1999).

200. J.-P. Fève, O. Pacaud, B. Boulanger, B. Ménaert, J. Hellström, V. Pasiskevicius, and F. Laurell, "Widely and continuously tunable optical parametric oscillator based on a cylindrical periodically poled KTiOPO4 crystal," Opt. Lett. **26**(23), 1882–1884 (2001).

201. S. J. Holmgren, V. Pasiskevicius, and F. Laurell, "Generation of 2.8 ps pulses by mode-locking a Nd:GdVO4 laser with defocusing cascaded Kerr lensing in periodically poled KTP," Opt. Express **13**(14), 5270–5278 (2005).

202. E. Soergel, "Visualization of ferroelectric domains in bulk single crystals," Appl. Phys. B **81**(6), 729–752 (2005).

203. Z. W. Hu, P. A. Thomas, and W. P. Risk, "Studies of periodic ferroelectric domains in KTiOPO4 using high-resolution x-ray scattering and diffraction imaging," Phys. Rev. B **59**(22), 14259–14264 (1999).

204. P. Pernot-Rejmankova, P. A. Thomas, P. Cloetens, F. Lorut, J. Baruchel, Z. W. Hu, P. Urenski, and G. Rosenman, "Periodically poled KTA crystal investigated using coherent X-ray beams," J. Appl. Crystallogr. **33**(4), 1149–1153 (2000).

205. C. Canalias, V. Pasiskevicius, A. Fragemann, and F. Laurell, "High-resolution domain imaging on the nonpolar y-face of periodically poled KTiOPO4 by means of atomic force microscopy," Appl. Phys. Lett. **83**(4), 734–736 (2003).

206. A. Gruverman, M. Alexe, and D. Meier, "Piezoresponse force microscopy and nanoferroic phenomena," Nat. Commun. **10**, 1661 (2019).

207. S. I. Bozhevolnyi, J. M. Hvam, K. Pedersen, F. Laurell, H. Karlsson, T. Skettrup, and M. Belmonte, "Second-harmonic imaging of ferroelectric domain walls," Appl. Phys. Lett. **73**(13), 1814–1816 (1998).

208. M. Flörsheimer, R. Paschotta, U. Kubitscheck, C. Brillert, D. Hofmann, L. Heuer, G. Schreiber, C. Verbeek, W. Sohler, and H. Fuchs, "Second-harmonic imaging of ferroelectric domains in

LiNbO3 with micron resolution in lateral and axial directions," Appl. Phys. B **67**(5), 593–599 (1998).

209. J. A. Armstrong, N. Bloembergen, J. Ducuing, and P. S. Pershan, "Interactions between light waves in a nonlinear dielectric," Phys. Rev. **127**(6), 1918–1939 (1962).

210. B. B. Boulanger and J. Zyss, "Nonlinear optical properties," in *International Tables for Crystallography* (2013), **D**, pp. 181–222.

211. G. News, *Introduction to Nonlinear Optics* (Cambridge University Press, 2011).

212. Y.-S. Lee, T. Meade, V. Perlin, H. Winful, and T. B. Norris, "Generation of narrow-band terahertz radiation via optical rectification of femtosecond pulses in periodically poled lithium niobate," Appl. Phys. Lett. **76**(18), 2505–2507 (2000).

213. P. F. Bordui, "Inorganic crystals for nonlinear optical frequency conversion," Annu. Rev. Mater. Sci. **23**, 321–379 (1993).

214. H. Vanherzeele and J. D. Bierlein, "Magnitude of the nonlinear-optical coefficients of KTiOPO4," Opt. Lett. **17**(14), 982–984 (1992).

215. A. Schneider, M. Neis, M. Stillhart, B. Ruiz, R. U. A. Khan, and P. Günter, "Generation of terahertz pulses through optical rectification in organic DAST crystals: theory and experiment," J. Opt. Soc. Am. B **23**(9), 1822–1835 (2006).

216. V. A. Maslov, V. A. Mikhailov, O. P. Shaunin, and I. A. Shcherbakov, "Nonlinear absorption in KTP crystals," Quantum Electron. **27**(4), 356–359 (1997).

217. S. Zhu and W. Cao, "Direct observation of ferroelectric domains in LiTaO3 using environmental scanning electron microscopy," Phys. Rev. Lett. **79**(13), 2558–2561 (1997).

218. A. Grigoriev, D. Do, D. M. Kim, C.-B. Eom, B. Adams, E. M. Dufresne, and P. G. Evans, "Nanosecond domain wall dynamics in ferroelectric Pb(Zr,Ti)O3 thin films," Phys. Rev. Lett. **96**(18), 187601 (2006).

219. L. Li, L. Xie, and X. Pan, "Real-time studies of ferroelectric domain switching: a review," Reports Prog. Phys. **82**(12), 126502 (2019).

220. D. Lee, J.-H. Kang, J.-S. Lee, H.-S. Kim, C. Kim, J. H. Kim, T. Lee, J.-H. Son, Q.-H. Park, and M. Seo, "Highly sensitive and selective sugar detection by terahertz nano-antennas," Sci. Rep. **5**, 15459 (2015).

221. J.-L. Coutaz, "Terahertz generation through optical rectification in reflection: Modeling," (To be submitted), (n.d.).

222. B. V Mill and Y. V Pisarevsky, "Langasite-type materials: From discovery to present state," Proc. 2000 IEEE/EIA Int. Freq. Control Symp. Exhib. 133–144 (2000).

223. J. Stade, L. Bohaty, M. Hengst, and R. B. Heimann, "Electro-optic, piezoelectric and dielectric properties of Langasite (La3Ga5SiO14), Langanite (La3Ga5.5Nb0.5O14) and Langataite (La3Ga5.5Ta0.5O14)," Cryst. Res. Technol. **37**(10), 1113–1120 (2003).

224. S. A. Sakharov, A. N. Zabelin, O. A. Buzanov, D. V Roshchupkin, and M. Y. Barabanenkov, "Physical properties of lanthanum gallium tantalate crystals for high-temperature application,"

IEEE Ultrason. Symp. 1–4 (2005).

225. J. Bohm, R. B. Heimann, M. Hengst, R. Roewer, and J. Schindler, "Czochralski growth and characterization of piezoelectric single crystals with langasite structure: La3Ga5SiO14 (LGS), La3Ga5.5Nb0.5O14 (LGN), and La3Ga5.5Ta0.5O14 (LGT) part I," J. Cryst. Growth **204**(1–2), 128–136 (1999).

226. H. Kong, J. Wang, H. Zhang, X. Yin, X. Cheng, Y. Lin, X. Hu, X. Xu, and M. Jiang, "Growth and characterization of La3Ga5.5Ta0.5O14 crystal," Cryst. Res. Technol. **39**(8), 686–691 (2004).

227. E. Boursier, P. Segonds, B. Boulanger, C. Félix, J. Debray, D. Jegouso, B. Ménaert, D. Roshchupkin, and I. Shoji, "Phase-matching directions, refined Sellmeier equations, and second-order nonlinear coefficient of the infrared Langatate crystal La3Ga5.5Ta0.5O14," Opt. Lett. **39**(13), 4033–4036 (2014).

228. A. A. Kaminskii, B. V Mill, G. G. Khodzhabagyan, A. F. Konstantinova, A. I. Okorochkov, and I. M. Silvestrova, "Investigation of trigonal (La1-xNdx)3Ga5Si014 crystals," Phys. Status Solidi **80**, 387–398 (1983).

229. G. Gaborit, A. Biciunas, M. Bernier, and J.-L. Coutaz, "Emitting and receiving terahertz vectorial antennas based on cubic electro-optic crystals," IEEE Trans. Terahertz Sci. Technol. **5**(5), 828–835 (2015).

230. M. Ebrahim-Zadeh and I. T. Sorokina, *Mid-Infrared Coherent Sources and Applications* (Springer Netherlands, 2008).

Publications and Conferences

Publications

1. G. Soylu, F. Sanjuan, E. Hérault, J.-F. Roux, F. Levy-bertrand, M. Calvo, A. Monfardini, and J.-L. Coutaz, "Detection of weak terahertz pulsed signals using kinetic inductance detectors," J. Infrared, Millimeter, Terahertz Waves **40**(1), 31–37 (2019).

2. G. Soylu, E. Hérault, B. Boulanger, F. Laurell, and J.-L. Coutaz, "Sub-wavelength THz imaging of the domains in periodically-poled crystals through optical rectification," J. Infrared Millim. Terahertz Waves **41**, 1144–1154(2020)

3. G. Soylu, F. Aljammal, G. Gaborit, E. Herault, M. Dumortier, H. Cabane and J.-L. Coutaz, "Optical rectification in a langatate crystal for terahertz generation," (To be submitted)

Conferences

1. G. Soylu, F. Sanjuan, E. Hérault, J.-F. Roux, F. Levy-Bertrand, M. Calvo, A. Monfardini and J.-L. Coutaz, "Detection of terahertz time-domain signals with KIDs," 43th International Conference on Infrared, Millimeter, Terahertz Waves (IRMMW-THz), Nagoya/Japan, 2018 (accepted as a keynote talk and presented by: E. Hérault)

2. G. Soylu, F. Sanjuan, E. Hérault, J.-F. Roux, F. Levy-Bertrand, M. Calvo, A. Monfardini and J.-L. Coutaz, "Measuring terahertz signals delivered by time-domain systems with KID detectors," GDR NanoTeraMIR, Montpellier/France, 2018

3. G. Soylu, F. Aljammal, G. Gaborit, E. Herault, M. Dumortier, H. Cabane and J.-L. Coutaz, "Terahertz generation in langatate crystal by optical rectification," French-German THz conference, Kaiserslautern/Germany, 2019

4. G. Soylu, E. Hérault, B. Boulanger, F. Laurell and J.-L. Coutaz, "Sub-wavelength THz imaging through optical rectification," 44th International Conference on Infrared, Millimeter, Terahertz Waves (IRMMW-THz), Paris/France, 2019

5. G. Soylu, E. Hérault, F. Sanjuan, G. Gaborit and J.-L. Coutaz, "Towards sub-wavelength THz imaging through nonlinear optical techniques," Russia-Japan-USA-Europe Symposium on Fundamental & Applied Problems (RJUSE), Nizhny Novgorod/Russia, 2019 (presented by J.-L. Coutaz)